Vers la compréhension de l'abondance des cyanures / isocyanures : collisions inélastiques et transfert radiatif

Mario Hernandez-Vera

To cite this version:

Mario Hernandez-Vera. Vers la compréhension de l'abondance des cyanures / isocyanures : collisions inélastiques et transfert radiatif. Physique [physics]. Université du Havre; Instituto superior de Tecnologias Y Ciencias Aplicadas de Cuba, 2014. Français. NNT : 2014LEHA0013 . tel-01131371

HAL Id: tel-01131371
https://theses.hal.science/tel-01131371

Submitted on 13 Mar 2015

THÈSE

Présentée pour obtenir le grade de
DOCTEUR DE l'UNIVERSITÉ DU HAVRE

par
Mario HERNANDEZ-VERA

Sujet de la thèse :

Toward the understanding of cyanide/isocyanide abundances: Inelastic collisions and radiative transfer calculations.

École doctorale Sciences Physiques, Mathématiques et de l'Information pour l'Ingénieur

Soutenue le 16 décembre 2014 au Laboratoire Ondes et Milieux Complexes

devant le jury composé de :

M. Majdi HOCHLAF	Rapporteur
M. Maurice MONNERVILLE	Rapporteur
M. Jacek KŁOS	Examinateur
M. Laurent PAGANI	Examinateur
M. Alexandre FAURE	Examinateur
M. Fabien DUMOUCHEL	Examinateur
M. François LIQUE	Directeur de thèse
M. Jesús RUBAYO	Co-Directeur de thèse

Acknowledgments

These three years in Le Havre have been a great experience because of the excellent people that I have met. Without these persons, it would have been very difficult to achieve all the results and goals of my PhD work.

My special thanks to Dr. François Lique for his constant support, for all the interesting projects and for giving me the opportunity to work in his group. I would also want to express my gratitude to his family, for its solidarity and for helping me all these years.

I want to thanks my old colleagues from Havana, specially Prof Dr. Jesus Rubayo Soneira, whose guide and support was decisive at the start of my career.

I would like to thanks Yulia Kalugina, Fabien Dumouchel and Mathieu Lanza for all the scientific discussions.

I would also like to thanks our secretary, Carole, for her skills and her patience to deal with the bureaucracy.

Finally, I want to express my profound thanks to Borja, Raounak, Simon, Nezha, Céline, Guillaume, Xue Zhou, Sylvain and all the others friends and colleagues of LOMC for their friendship and support.

Abstract

Cyanide and isocyanide species are ubiquitous in the interstellar medium (ISM). We have studied the collisional excitation of three kind of species: the metal cyanides/isocyanides which are the most common metal-bearing molecules in the ISM; the silicon cyanide/isocyanide, and the simplest hydrogen cyanide molecule which is one of the best tracers of the dense interstellar gas. Modelling of molecular emission spectra of these species from interstellar clouds requires the calculation of rate coefficients for excitation by collisions with H_2, the most abundant molecule in the cold ISM. Thus, we have used the coupled states approximation to study the rotational (de-)excitation of AlCN($^1\Sigma$), AlNC($^1\Sigma$), MgCN($^2\Sigma$), MgNC($^2\Sigma$), SiCN($^2\Pi$) and SiNC($^2\Pi$) molecules by collisions with He, as a model of H_2. We have also considered the rotational (de-)excitation of HCN($^1\Sigma$) molecules by ortho-H_2 and para-H_2 molecules using the close coupling approach. In all cases, new highly correlated potential energy surfaces have been employed. Significant differences between the rate coefficients of the isomers were observed. These differences confirm that specific calculations have to be performed for each isomer in order to obtain the necessary level of details in astrophysical applications. We have also assessed the impact of our collisional rates coefficients in the molecular emission simulations using radiative transfer calculations.

Contents

List of Figures

List of Tables

Chapter 1

General Introduction

1.1 Molecular astrophysics

Observers of the night-time sky of XIX century ignored the significant amount of cold matter hidden in the large spaces amongst the stars. Presently, we know that this tenuous medium, the so-called "interstellar-medium" (ISM), is formed of gas (atoms, molecules, ions, and electrons) and dust (tiny solid particles). Despite its large spatial dimensions, it accounts for only 10–15 % of the total mass of our galaxy [1]. Most of the interstellar matter comes from the ejections of the stars, continuously via stellar winds, or instantaneously via supernova explosions. Stars also affect the interstellar matter through their radiation and gravitational field. At the same time, the chemical and physical conditions of the interstellar matter define the birthplace of stars and impact their future characteristics. Therefore, the dynamics and the chemistry of ISM are of fundamental interest in modern astrophysics.

The interstellar matter manifests itself by different optical phenomena. Through their absorption and scattering, small dust grains give rise to extinction of light from distant stars. Besides, observed starlight polarization is believed to be caused by selective absorption of magnetically aligned interstellar dust grains [2]. On the other hand, molecular and atomic gases manifest themselves through the formation of absorption lines in stellar spectra and through emissions of light.

The first interstellar molecules (CH, CH^+ , and CN) were discovered in the late 1930s [3–5], through optical absorption lines they produce in stellar spectra. The important atomic hydrogen was observed by the detection of its hyperfine 21 cm line [6] in 1951. Twenty years later, the observations of the Aerobee-150 rocket, above the Earths atmosphere, allow detecting the most abundant interstellar molecule, H_2, in the far-UV spectrum of the stars ζ Persei [7]. One year later, the second most abundant molecule, the carbon monoxyde (CO), was identified in a UV stellar spectrum [8].

Optical and UV absorption lines are very useful tools for the survey of space, but they do not allow astronomers to probe the interior of dense molecular clouds. Indeed, the interstellar dust obscures the bright sources necessary to make absorption measurements. The structure of dense interstellar clouds can be explored using "radio astronomy" since radio waves are not subject to interstellar extinction. One of the main advantages is that radio telescopes can operate from the ground and look through the atmosphere of the Earth at millimeter wavelengths or at submillimeter wavelength through windows of transparency in the atmosphere. As two examples of these telescopes, we can mention the Atacama Large Millimeter/submillimeter Array (ALMA) interferometer and the Green Bank Telescope (GBT). Additionally to these telescopes, there have been a number of satellite observatories like Herschel or Hubble. At present, these sophisticated devices allow observations with very high spatial and spectral resolution.

Most molecules have been detected at radio and millimeter wavelengths. The multitude of rotational lines of the molecular species, each with their own characteristic critical density[1] and frequency, provide a powerful tool to study the physical and chemical properties of molecular clouds. CO has become the primary tracer of molecular interstellar gases [9–11] through its $j = 1 \rightarrow 0$ rotational transition at a radio wavelength of 2.6 mm. Weakly polar molecules such as CO radiate slowly, especially from low-lying excited rotational states, and so their emission lines are easily observed in lower density portions of dense clouds. Otherwise, because of the larger dipole moment of their emitting species, rotational lines of molecules like CH or HCO^+ have higher critical densities than CO and can also probe dense gas in molecular clouds. Molecules are also considered as the signature of important astrophysical processes. For example, line profiles of HCO^+ and CS transitions could be good tracers of infall motion caused by gravitational collapse and possibly leading to stars formation [12]. SiO is an important tracer of outflow in young stars [13].

The estimations of the molecular abundances is an essential step to understand the ISM. Presently, there are two possibilities to estimate the molecular abundances in the ISM: (1) considering predictions of astrochemical models, (2) modeling the molecular lines from astrophysical observations. The first option considers large networks of elemental reactions and grain-gas interactions to describe the chemical state evolution of the clouds [14]. Method (2) is based on the spectro-

---

[1] The critical density is defined as the ratio between the Einstein's spontaneous decay coefficient (in s^{-1}) and the collisional de-excitation rate coefficient (in $cm^3\ s^{-1}$).

scopic observations and it is important to test the success of chemical models. In principle, there must be a good agreement among both methods, but the discrepencies are often large [14]. The interpretation of the molecular lines requires accurate molecular data, such as the collisional rate coefficients that are essential to understand molecular excitation and emissions from the ISM.

1.2 Inelastic molecular collisions

Accurate collisional rate coefficients are obtained using different quantum approaches. Quantum effects, like tunneling, resonances and propensity rules which govern many collision-induced transitions, have been predicted by theory and confirmed experimentally [15,16]. These effects reveal the real quantum nature of the microscopic process that cannot be correctly described by pure classical considerations.

In the frame of the Born-Oppenheimer approximation, we can study the molecular collision process in two fundamental steps. First, we solve the electronic Schrödinger equation for a fixed configuration of the nuclei. Hence, we compute the electronic energies for a set of nuclei configurations, in order to derive the potential energy surface (PES). In the second step, we use the PES to solve the Schrödinger equation for the nuclei. This allow us characterizing the nuclei dynamics during a molecular collision.

In 1960 Arthurs and Dalgarno [17] developed the quantum time-independent Closed-Coupling Approach (CC). They used the advances in the nuclear dispersion theory and the tensorial algebra introduced by Fano and Racah [18] to simplify the numerical calculations of the potential matrix. Their theory, later generalized to the ro-vibrational excitations, showed advantages over the previous approaches of Curtis [19] and Takayanagi [20]. However, these calculations are frequently expensive and time consuming because of the large number of channels to consider. This problem has been tackled in some cases through the coupled states and sudden approaches that were the subject of many important theoretical works [21,22] some decades ago. Many of these formulations take CC as the starting point in their physical considerations. In particular, small molecules have been suitable models for testing different formalisms because it is easy to identify the energy transfer mechanisms in these cases.

The study of molecular collisions was also pushed forward by the progressive development of computing technology. Theoreticians are not longer satisfied with qualitative models of the phenomena. The current trend emphasizes detailed dynamical information, including rigorous computation of cross sections at a state-to-state level (including the fine and hyperfine structure of the molecules). At present, potential interaction energy surfaces can be computed with high accuracy using *ab initio* methods of quantum chemistry. Some codes, both open source and commercial software, like MOLPRO [23] and GAUSSIAN [24], are available to compute highly correlated PES and to study the molecular structure. In turn, PES can be implemented in codes designed for modeling collisional processes, such as MOLSCAT [25] and Hibridon packages [26], which have been tested in many molecular systems. Thereby, full quantum calculations are possible for small collisional systems like C_2H + He [27], C_4 + He [28] SiS + H_2 [29] or more complex organic molecules such as ortho-H_2CO+H_2 [30] or CH_3OH+He [31].

Moreover, sophisticated experimental methods are also available to study molecular collisions. In the past decades, the development of molecular beam methods has revolutionized the field of reactive and inelastic collisions [32]. In particular, merged neutral beams technique show possibility to explore collisions at temperatures as low as 10 mK [33]. The motion of neutral molecules in a beam can be manipulated with inhomogeneous electric and magnetic fields [34]. These methods may be used in conjunction with a variety of other techniques to prepare atoms or molecules in excited initial states. Spectroscopic detection methods usually involve either laser-induced fluorescence (LIF) or resonant photo-ionization (REMPI). At present, it is possible to analyze the collisional products for each dispersion angle and for specific quantum state [35].

1.3 The interstellar cyanide/isocyanide compounds

The CN radical was among the first molecules detected toward the star ζ Ophiuchi [36, 37] in the 1940s. Later on, observations have demonstrated that CN compounds are widely distributed in the ISM. They have been detected in different physical conditions in multiple regions like diffuse clouds [38], prestellar cores [39] and protoplanetary disks [40].

Millimeter-wavelength emission of CN molecule is widely used as probe of dense molecular gas and of photon-dominated regions in the Galactic ISM [41]. Moreover, CN has a non-zero Zeeman splitting factor that is large enough to measure the weak magnetic fields one can find in the ISM. Then, as a tracer of high density gas, the CN thermal lines are a unique tool that allow measurement of the magnetic field strengths in star forming regions [42, 43]. Cyanide compounds can also be used for estimating the electron density in the gas [44] which is a crucial parameter for modeling both the physics and chemistry of molecular clouds.

In the ISM, CN could be synthesized by different chemical processes like the following neutral reactions [45, 46],

$$\mathrm{N} + \mathrm{CH} \rightarrow \mathrm{CN} + \mathrm{H} \tag{1.1}$$

$$\mathrm{N} + \mathrm{C_2} \rightarrow \mathrm{CN} + \mathrm{C} \tag{1.2}$$

The CN radical which can also react at temperatures as low as 10-15 K with other molecules seems to be essential in the formation of cyanopolynes or other important hydrocarbons in cold environments [47, 48]. Furthermore, some reactions that involve the CN radical are considered as "key" processes due to their impact on the abundances of other observed species. For example, chemical models predict that the reaction $CN + C_4H_2 \rightarrow HC_5N + H$ could affect the abundance of five interstellar species in the circumstellar gas of the carbon star IRC+10216 [14].

Thus, CN contributes to the formation of many important species in astrophysics. Among them, HCN stands out for its utility. After the first detection of hydrogen cyanide in the space by Snyder & Buhl (1971) [49], this molecule was observed in different regions like diffuse clouds [50], dark interstellar clouds [51] and protoplanetary disks [52].

This molecule can be formed in different chemical processes such as ion/molecule reactions [53],

$$\mathrm{CN} + \mathrm{H_3}^+ \rightarrow \mathrm{HCN}^+ \tag{1.3}$$

dissociative recombination [54],

$$\begin{aligned} HCNH^+ + e^- &\rightarrow H + HCN \\ &\rightarrow H + HNC \\ &\rightarrow H + H + CN \end{aligned} \tag{1.4}$$

or neutral reactions [55] like

$$\begin{aligned} N + C_2H &\rightarrow CCN + H \\ &\rightarrow HCN + C \\ &\rightarrow HNC + C \end{aligned} \tag{1.5}$$

Hydrogen cyanide is considered as a good tracer of high-density regions due its high dipole moment and critical density [12]. Moreover, the HCN:CN ratio appears to be a good probe of gas layers affected by photochemistry [56] and could indicate the effects of dust settling and grain growth. Additionally, determining the physical structure of galaxies via the use of HCN molecular emission may be a powerful tool at high redshift. For example, observations towards high redshift galaxies reveal ratios of molecular column densities such as HCN/HCO^+ and HCN/CO to be very different from those found in the Milky Way or in nearby galaxies. These differences have been interpreted as an indication of either high ionization rates or high star-formation rates [12,57]

Others interesting CN-bearing molecules observed in the ISM are the metal cyanides/isocyanides. These species are the most common metal-containing molecules in circumstellar gas. They seem to find the best conditions for their formation in the envelope of asymptotic giant branch (AGB) stars. For example, AlNC [58], MgCN [59], MgNC [60], FeCN [61] and KCN [62] have been observed in the circumstellar envelope of the carbon star IRC+10216. MgNC was also detected in the circumstellar gas of the proto-planetary nebulae CRL 2688 [63] and CRL 618 [64].

The synthesis of this molecule could be driven by the radiative association of metals M^+ and cyanopolyynes [65, 66]

$$M^+ + HC_{2n+1}N \rightarrow MN(C_{2n+1})H^+ + hv \tag{1.6}$$

followed by the dissociative recombination

$$\begin{aligned} MN(C_{2n+1})H^+ + e^- &\rightarrow M(C_{2n+1}N) + H \\ &\rightarrow M(CN) + C_{2n}H \\ &\rightarrow M + HC_{2n+1}N \end{aligned} \tag{1.7}$$

Despite the dominant role as metals carriers, the abundance and chemical evolution of metal cyanides and isocyanides in the interstellar medium (ISM) are still not completely understood. As a matter of fact, the extent to which metals contribute to dust formation and their diffusion in the stellar outflows remains poorly known.

In addition, the abundance of silicon is one of the most important diagnostics for studying dust in the ISM. Only oxygen and carbon form a higher fraction of grain mass, but the large abundances and volatility of these elements make it difficult to determine their precise dust-phase abundances. Accurate abundance determination of silicon bearing molecules in the ISM will enable a better understanding of the interstellar silicon chemistry and the extend to which it is incorporated in dust. In this thesis we will study the collisional excitation of the SiCN and SiNC radicals. These species were originally detected by observations toward the carbon star IRC+10216 [67, 68]. The synthesis of SiCN/SiNC is not clear and some authors have suggested [69] that the similarity of the spatial distributions of species as different as C_4H, SiC_2, MgNC, SiCN and SiNC, could be better explained by grain chemistry rather than by gas phase reactions.

All cyanide molecules discussed so far have an isomeric stable counterpart (HCN/HNC, AlCN/AlNC, MgCN/MgNC, SiCN/SiNC) [70,71]. Isomer pairs are often observed in the same environments, indicating connected formation pathways and that energetic differences and selective formation/destruction pathways control the relative abundances. However, favoring the lower energy isomer does not hold for all ratios; the isomer pair HNC and HCN seems to exhibit a ratio of unity at low temperatures [72–74] despite these isomers have a ground state energy difference of approximately 7000 K [70].

Then, suitable estimation of relative abundances from the interpretation of the molecular lines is essential in order to have realistic insight in the selective cyanide and isocyanide chemistry. Radiative transfer calculations are carried out to obtain more realistic interpretation of molecular lines. Within the interstellar gas, radiative and collisional processes compete in the population of the ro-vibrational energy levels. When local thermodynamic equilibrium LTE is reached, molecules are thermalized and the populations can be obtained by the Boltzmann distribution. However, LTE is not generally a good approach, and the collisional excitation affects substantially the population of the energy levels and the emission processes. Therefore, the computation of inelastic thermal collisional rate coefficients becomes an important objective in order to improve the observation analysis.

1.4 Objective and structure of the thesis

In this context, this thesis deals with the study of the rotational excitation of cyanide/isocyanide molecules (AlCN, AlNC, MgCN, MgNC, SiCN, SiNC, HCN) due to collisions with He or H_2. The main goal is to obtain collisional inelastic rate coefficients for these collisional systems for different temperatures one can find in the cold ISM.

This work provides, for the first time, data for studying the molecular lines of metal cyanides and isocyanides species. Our results also improve the collisional data available for the HCN–H_2 collisional system. It is worth mentioning that a large number of channels have to be taken into account in the scattering calculations because these molecules have small collisional constants. For this reason, the close coupling calculations are very time consuming. In order to obtain a large amount of useful molecular data rather than a too expensive exact study we have generally used approximate quantum formulations: the Coupled States approach.

In the case of SiCN/SiNC and the interstellar metal cyanides/isocyanides (XCN/XNC with X = Al, Mg) we have obtained collisional rate coefficients with the He collisional partner as a first approach to model collisions with H_2. This approximation appears to be unsuccessful for light molecules [75, 76] but is reasonably accurate for heavier collisional systems such as SiS–H_2 [77], HC_3N [78] or CS [79,80]. Therefore, using such an approximation, we expect that the estimation of XCN–H_2 and XNC–H_2 rate coefficients will be reasonably accurate for astrophysical applications.

The structure of this manuscript is as follows: In Chapter 2, we present the general theory. We briefly explain the electronic calculations and present the time independent method for studying inelastic molecular collisions. In particular, we will present two important approximate approaches: the Coupled States (CS) and the Infinite Order Sudden methods (IOS).

In Chapter 3, we study the rotational excitation of the metal cyanides and metal isocyanides (AlCN, AlNC, MgCN, MgNC) by He using the CS approach. In this chapter, the IOS approach will be used to consider the fine structure of MgCN and MgNC.

In Chapter 4, we present the study of the rotational excitation of the SiCN($^2\Pi$) and SiNC($^2\Pi$) molecules by He also using the CS approximation.

In Chapter 5, we study the rotational excitation of HCN due to collisions with para-H_2 and ortho-H_2. The calculations were performed using the exact Close coupling (CC) approach. In the case of the HCN excitation, our calculations significantly improve the rate coefficients upon previous calculations, especially at low temperatures.

In Chapter 6, we present the results of the radiative transfer calculations of AlCN, AlNC, MgCN and MgNC species for the typical physical conditions of the circumstellar gases. Here we will see that even assuming LTE conditions the isomers present differences that can affect their relative abundance estimations.

Chapter 2

Theoretical Framework

Contents

In this chapter, we will introduce the main theoretical methods used in this thesis in order to compute the collisional rate coefficients. The computation of these rates is generally performed in two stages: first, we compute the potential energy surface (PES). The PES concept derives from the Born-Oppenheimer approximation that will be presented in section 2.1. In section 2.2.1, we will present the Hartree-Fock method for obtaining the electronic energy. The coupled clusters theory, the formalism used to generate the PESs of the collisional systems studied in this thesis, will be presented in section 2.2.2 as an example of post-Hartree-Fock treatment. The second stage of the collisional rate coefficients calculations is the study of the dynamics of the nuclei. Hence, the second part of this chapter will be devoted to the scattering theory. In order to introduce the main time-independent approaches, the most simple model will be employed: the collision of a rigid rotor with a structureless particle. Three important approaches will be developed: the close coupling and the approximate coupled states and infinite order sudden approaches.

2.1 Born−Oppenheimer Approximation

A full quantum mechanical description of the molecule is in practice too complex due the large number of particles to consider. Fortunately, using the Born-Oppenheimer (BO) approximation [81], we can study separately the electronic and nuclear motions. The physical basis of this separation rests in the differences of nuclear and electronic masses. Both electrons and nuclei experience similar electrostatic forces in a molecular system. However, the mass of the electron is about three orders of magnitude smaller ($\mathrm{m}_p/\mathrm{m}_e = 1836$) than the mass of the nuclei. Consequently, the electrons are accelerated at much greater rate and move much more rapidly than the nuclei.

Thus, in the first step of the BO approximation, we solve the electronic Schrödinger equation assuming that the nuclei are stationary. In the second step, the solutions of this electronic equation serves as a potential in a Schrödinger equation for the nuclei motion.

We will introduce the formalism of the BO approximation from the total time-independent Schrödinger equation for electronic and nuclear motion. This equation, in atomic units, can be expressed as follow:

$$\mathcal{H}(\mathbf{r},\mathbf{R})\Psi(\mathbf{r},\mathbf{R}) = E\Psi(\mathbf{r},\mathbf{R}) \tag{2.1}$$

where the total Hamiltonian of an isolated system is defined as,

$$\mathcal{H}(\mathbf{r},\mathbf{R}) = \sum_{\alpha=1}^{N} \frac{-1}{2M_\alpha}\nabla_\alpha^2 + H_e(\mathbf{r};\mathbf{R}) \tag{2.2}$$

Here, $\mathbf{R} = (\mathbf{R}_1, \mathbf{R}_2, ..., \mathbf{R}_N)$ and $\mathbf{r} = (\mathbf{r}_1, \mathbf{r}_2, ..., \mathbf{r}_M)$ denotes the $3N$ nuclear coordinates and the $3M$ electronic coordinates, respectively. $H_e(\mathbf{r};\mathbf{R})$ is the total non relativistic electronic Hamiltonian,

$$\begin{aligned} H_e(\mathbf{r};\mathbf{R}) = &-\frac{1}{2}\sum_{k=1}^{M}\nabla_k^2 - \sum_{K,k}\frac{Z_K}{|\mathbf{R}_K - \mathbf{r}_k|} \\ &+\frac{1}{2}\sum_{k\neq l}^{M}\frac{1}{|\mathbf{r}_k - \mathbf{r}_l|} + \frac{1}{2}\sum_{K\neq L}^{N}\frac{Z_K Z_L}{|\mathbf{R}_K - \mathbf{R}_L|} \end{aligned} \tag{2.3}$$

Then, the total wave function $\Psi(\mathbf{r},\mathbf{R})$ is expanded in a basis of the electronic states, $\Psi_i^e(\mathbf{r};\mathbf{R})$ as follow,

$$\Psi(\mathbf{r},\mathbf{R}) = \sum_i \Psi_i^e(\mathbf{r};\mathbf{R})\Psi_i^N(\mathbf{R}) \tag{2.4}$$

which separate the dependences on the electronic coordinates, $\mathbf{r}$, and the nucleus coordinates, $\mathbf{R}$. The adiabatic electronic eigenfunctions, $\Psi_i^e(\mathbf{r};\mathbf{R})$, in the last expansion, satisfy,

$$H_e(\mathbf{r};\mathbf{R})\Psi_i^e(\mathbf{r};\mathbf{R}) = E_i^e(\mathbf{R})\Psi_i^e(\mathbf{r};\mathbf{R}) \tag{2.5}$$

where the parametric dependence of $\Psi_i^e(\mathbf{r};\mathbf{R})$ on $\mathbf{R}$, reflects the fact that $\mathbf{R}$ is not considered as a dynamical variables in Eq. 2.3.

If we introduce 2.4 into the time-independent Schrödinger Eq. 2.1 we obtain the following system of equations for the nuclear functions $\Psi_j^N(\mathbf{R})$:

$$\begin{aligned}&\left[-\sum_{\alpha=1}^{N}\frac{1}{2M_\alpha}\nabla_\alpha^2 + E_j^e(\mathbf{R}) - E\right]\Psi_j^N(\mathbf{R})\\ &= \sum_{i\alpha}\frac{1}{2M_\alpha}\left[2\langle\Psi_j^e|\nabla_\alpha|\Psi_i^e\rangle_{\mathbf{r}}\nabla_\alpha + \langle\Psi_j^e|\nabla_\alpha^2|\Psi_i^e\rangle_{\mathbf{r}}\right]\Psi_i^N(\mathbf{R})\end{aligned} \tag{2.6}$$

where the subscript $\mathbf{r}$ on the matrix elements denotes the integration over all electronic coordinates.

Neglecting the interstate electronic couplings in the terms of Eq. 2.6 is known as the adiabatic approximation. Obviously, the effective Schrödinger equation that arises is more suitable than Eq. 2.6 for numerical purposes and can be written as,

$$\left[-\sum_{\alpha=1}^{N}\frac{1}{2M_\alpha}\nabla_\alpha^2 + V_i(\mathbf{R})\right]\Psi_i^N(\mathbf{R}) = E\Psi_i^N(\mathbf{R}) \tag{2.7}$$

where E is the total energy of the system.

Using this approach the nuclear motion is governed by the effective potential given by $V_i(\mathbf{R}) \equiv E_i^e(\mathbf{R})$ where each index i represents different electronic (excited) states. The ground electronic potential energy surface (PES) is obtained by computing the lower eigenvalue in Eq. 2.5 for a large grid of $\mathbf{R}$.

The Born-Oppenheimer approximation is valid when there are no degeneracies of two or more solutions of the electronic Schrödinger equation. It is also important that the electronic states are enough separated and that the ro-vibrational states remain moderately excited.

2.2 Ab initio quantum chemistry approaches

Ab initio calculations deal with quantum chemistry methods for solving the electronic Schrödinger Eq. 2.5. These calculations do not rely on calibration with experimental parameters and therefore are called “from first principles”. The electronic Schrödinger equation cannot be solved analytically, except for very simple systems like the hydrogen atom. Then, the theory generally transforms the Schrödinger equation into algebraic equations which can be solved using numerical methods. *Ab initio* calculations are generally used to determine molecular properties such as geometries, energies, or vibrational frequencies. In this thesis, these methods are used in order to obtain the PESs necessary to study the collisional excitation process.

The simplest method to obtain the electronic energies is based on the use of a single Slater determinant for which we optimize the orbitals variationaly. This is the Hartree-Fock (HF) self consistent field (SCF) method, and it is usually the first step of any *ab initio* calculation.

2.2.1 Hartree Fock Approximation

The Hartree-Fock approach [82,83] allows solving the electronic Schrödinger Eq. 2.5 considering a single determinant solution. The total molecular wavefunction Ψ^e is approximated by a single Slater determinant (Φ_0) which meets the requirement of the antisymmetry principle,

$$\Phi_0 = (M!)^{-1/2} \begin{vmatrix} \chi_i(\mathbf{x}_1) & \chi_j(\mathbf{x}_1) & \dots & \chi_k(\mathbf{x}_1) \\ \chi_i(\mathbf{x}_2) & \chi_j(\mathbf{x}_2) & \dots & \chi_k(\mathbf{x}_2) \\ \dots & \dots & & \dots \\ \chi_i(\mathbf{x}_N) & \chi_j(\mathbf{x}_N) & \dots & \chi_k(\mathbf{x}_N) \end{vmatrix} \tag{2.8}$$

The factor $(M!)^{-1/2}$ is a normalization factor and $\mathbf{x}$ refers to spatial and spin coordinates. In this wave function no more than one electron can occupy a spin orbital (Pauli exclusion principle). This Slater determinant has M electrons occupying M spin orbitals that can be represented like,

$$\chi_i(\mathbf{x}_1) = \psi_i \gamma \qquad \gamma = (\alpha, \beta) \tag{2.9}$$

where ψ_i and γ represent the spatial orbital and the spin function, respectively. Then, the wave function of Eq. 2.8 is the simplest antisymmetric wave function, which can be used to describe the ground state of an M-electron system. The variational principle states that the most accurate wave function of this functional form is the one which gives the lowest possible energy

$$\mathcal{E} = \langle \Phi_0 | H_e | \Phi_0 \rangle \tag{2.10}$$

where H_e is the full electronic Hamiltonian. The evaluation of the last expression leads to the following expression,

$$\mathcal{E} = \sum_{i=1}^{M} \langle i | h | i \rangle + \sum_{i=1}^{M} \sum_{j<i}^{n} \langle ij | | ij \rangle + V^N \tag{2.11}$$

where V^N represents the nuclear electrostatic energy for a specific $\mathbf{R}$. The other terms are the one-electron integral

$$\langle i|\, h\, |i\rangle = \int d\mathbf{x}_1 \chi_i^*(\mathbf{x}_1) h(\mathbf{r}_1) \chi_j^*(\mathbf{x}_1) \tag{2.12}$$

where $h(1)$ is the core Hamiltonian, and the two-electronic integral,

$$\langle ij|\, |ij\rangle = \int d\mathbf{x}_1\mathbf{x}_2 \chi_i^*(\mathbf{x}_1)\chi_j^*(\mathbf{x}_2) r_{12}^{-1}(1 - \mathcal{P}_{12})\chi_k(\mathbf{x}_1)\chi_l(\mathbf{x}_2) \tag{2.13}$$

where $\mathcal{P}_{12}$ is an operator which interchanges the coordinates of electron (1) and electron (2).

By a variational procedure we can modify the spin-orbitals constraining them to remain orthonormal. In doing so one obtains an equation that defines the "best" spin-orbitals, the ones that minimize $\mathcal{E}$,

$$\Big[h(1) + \sum_{i=1}^{M} \mathcal{J}_i(1) - \mathcal{K}_i(1)\Big]\chi_j = \sum_{i=1}^{M} \epsilon_{ij}\chi_i(1) \quad j = 1, 2, ..., \tag{2.14}$$

where the two operators

$$\begin{aligned} \mathcal{J}_i(1) &= \int d\mathbf{x}_2 |\chi_i(2)|^2 r_{12}^{-1} \\ \mathcal{K}_i(1)\chi_j(1) &= \Big[\int d\mathbf{x}_2 \chi_i^* r_{12}^{-1}\chi_i(2)\Big]\chi_j(1) \end{aligned} \tag{2.15}$$

are the Coulomb operator that represents the average local potential at $\mathbf{x}_1$ arising from an electron in χ_i and the exchange operator that modify the energy due the effects of spin correlation.

Then after considering unitary transformations of the spin-orbitals we can diagonalize the matrix of the Lagrange multipliers ϵ_{ij}.

$$f_i\, |\chi_i'\rangle = \epsilon_i'\, |\chi_i'\rangle \tag{2.16}$$

The unique set of spin-orbitals χ'_i obtained from a solution of this eigenvalue equation is called the set of canonical spin-orbitals. The Fock operator f_i depends on the spin-orbitals of all the other $M-1$ electrons. This problem is commonly solved adopting an iterative procedure and stopping when convergence is reached. For this reason the Hartree-Fock method is also known as self-consistent field (SCF).

In closed-shell calculations, the molecular states have only even numbers M, with electrons paired such $M/2$ spatial orbitals are doubly occupied. The computed wavefuntion is called restricted Hartree-Fock wavefuntion (RHF). In the unrestricted open-shell Hartree-Fock (UHF) the electron pairs are no constrained to the same spatial wavefuntion.

2.2.2 Electronic correlation

The Hartree-Fock method allows to compute the best electronic wave function that can be obtained from one electronic configuration. But even if the HF energy represents 99% of the total electronic energy, the remaining inexactitude could be important for spectroscopic and chemical calculations. The HF formalism simplifies the complicated many-electrons problem by assuming electronic interactions in an averaged way.

The accuracy depends on the size of the atomic basis set. The limit is called the Hartree-Fock limit. However, the exact wave functions, cannot generally be expressed as single determinants. Therefore, the Hartree-Fock limit is always above this exact energy. The difference is called the correlation energy. To account for electronic correlation there are many post-Hartree Fock methods such as Configuration Interaction methods [84] Multireference Perturbation Theory (CASPT2/CASPT3) [85], Møller-Plesset Perturbation theory [86], Symmetry-Adapted Perturbation Theory (SAPT) [87] or coupled clusters methods [88, 89]. There is an extensive bibliography detailing these and other methods [35, 90]. In the next section we present briefly one of the most reliable post-Hartree-Fock methods.

Coupled Clusters Method

Coupled clusters theory [88, 89] is one of the most prominent methods for constructing correlated many-particles wave functions. One of the main advantages of the coupled clusters method is its size-consistency[1]. In quantum chemistry, size-consistency is a highly desirable property due to the necessity of simulating inelastic collisions where collisional partners (at the beginning and at the end) do not interact. The employed method must not introduce any unphysical correlations in order to obtain an accurate potential energy surface (PES).

The exponential form of the correlated wave operator, called the *exponential ansatz*, is the distinguishing feature of the coupled cluster theory

$$\Psi^{CC} = e^{T}\Phi_0 \tag{2.17}$$

In the last expression Ψ^{CC} is the M-electron CC wave function, Φ_0 is the M-electron reference Slater determinant, and T is an excitation operator which generates a manifold of excited determinants by promoting electrons from occupied

---

[1] Size-consistency is a property of a calculation of a system composed of a finite amount of noninteracting subsystems, such that the computed energy of the entire system equals the sum of the energies of the subsystems calculated separately with the same method.

orbitals of the reference determinant to the excited ones. The exponential operator e^T is developed by the series expansion

$$e^T = 1 + T + \frac{1}{2!}T^2 + \frac{1}{3!}T^3 + ... = \sum_k \frac{1}{k!}T^k \tag{2.18}$$

T is the cluster operator that can be written as,

$$T = T_1 + T_2 + T_3 + ... \tag{2.19}$$

The effects of the excitation operators T_i are

$$\begin{aligned} T_1\Phi_0 &= \sum_{a,p} t_a^p \Phi_a^p \\ T_2\Phi_0 &= \sum_{a,b,p,q} t_{ab}^{pq} \Phi_{ab}^{pq} \end{aligned} \tag{2.20}$$

and likewise for T_3 to T_N. The t_a^p are called single-excitation amplitudes, t_{ab}^{pq} double-excitation amplitudes, and so on. These excitation amplitudes are determined by solving the coupled-clusters equations which are derived by substituting $e^T\Phi_0$ into the electronic Schrödinger equation and using the series expansion of e^T. Then, a finite set is used in the determination of Ψ^{CC}.

The expression for the cluster operator T is truncated to include only specific electronic excitation operators. For example, in the approach referred as " coupled cluster singles, doubles and triplets (CCSDT)", T is approximated by $T_1+T_2+T_3$. We finally note that the coupled-cluster method is based on a single-reference Hartree-Fock wavefunction, and it works only for systems that are well described by a single configuration.

The PESs computed in this thesis were calculated in the supermolecular approach based on the single and double excitation coupled-cluster method (CCSD) [91] with perturbative contributions of connected triple excitations computed as defined by Watts, Gauss & Bartlett [CCSDT(T)] [92]. The *ab initio* surfaces were calculated using MOLPRO package [23].

2.2.3 Basis functions

The inclusion of electronic correlation requires a large one-electron basis set to yield converged results. For meaningful calculations one should at least use a triple-zeta basis (TZ). In this case three basis functions are used for each valence orbital. Currently, some of the most widely used basis sets are those developed by Dunning et. al [93] (cc-pVDZ, cc-pVTZ, ...) since they are designed to converge systematically to the complete basis set limit using empirical extrapolation techniques. We can also consider the diffuse functions ($aug-$) that have been designed to improve the basis set for large internuclear separations.

Next, we can employ bond functions. Contrary to the basis functions, the bond functions are placed between atoms in the van deer Waals complexes. The idea is, instead of using a large basis, to select a smaller basis and to place bond functions in the middle of the bond length between the centers of mass of the monomers. Several works have confirmed the usefulness of these functions [94,95] These functions make the calculations less time consuming.

Theoretical predictions of molecular energies are often achieved using large orbital basis sets. However, at present, through recent advances in F12 explicitly correlated methods [96] it is possible to obtain the same high accuracy using much smaller orbitals basis sets. In particular, the CCSD(T)-(F12) [97,98] methods with augmented triple-zeta basis sets yield results as accurate as standard calculations with augmented quintuple-zeta basis sets.

2.3 Scattering theory

This section is devoted to the theory of inelastic collisions between a structureless atom A (^1S electronic state) and a diatomic molecule BC ($^1\Sigma$ electronic state) treated as a rigid rotor. The quantum theory was first developed by Arthurs and Dalgarno [17] in 1960. Following these authors we will present, first, the formulation of the scattering problem in the space-fixed frame. Then, we will give the formulation of the scattering problem in the body-fixed frame which is more appropriate to introduce the coupled states and sudden approximations.

2.3.1 Space-fixed frame

Fig 2.1 shows the coordinate system used in the space-fixed frame. We denote the internuclear vector of molecule BC by $\boldsymbol{\rho} = \overrightarrow{BC}$ and the vector that connects the center of mass H of BC to the A atom by $\mathbf{R} = \overrightarrow{HA}$. In Fig 2.1 (XYZ) is a reference frame whose axes are fixed in space. The origin O is the center of mass of the $A - BC$. In polar coordinates the A atom is described by the variables (R, Θ, Φ) while for the orientation of BC we use the angles $\hat{\boldsymbol{\rho}} = (\theta, \phi)$.

The time independent Schrödinger equation can be written (in atomic units) as,

$$\left(-\frac{{\nabla_{\mathbf{R}}}^2}{2\mu} + H_{BC}(\hat{\boldsymbol{\rho}}) + V(R, \theta') - E \right) \Psi(R, \Theta, \Phi, \theta, \phi) = 0 \tag{2.21}$$

where E is the total energy of the system. $H_{BC} = \mathbf{j}^2/2I$ is the Hamiltonian of the BC molecule; I its moment of inertia and $\mathbf{j}$ the angular momentum operator of BC; $\mu = m_{BC} m_A/(m_{BC} + m_A)$, is the reduced mass of $A - BC$ system where m_A is the mass of A and m_{BC} the mass of BC. The function, $V(R, \theta')$, is the Born-Oppenheimer intermolecular potential which depends on the variable θ'.

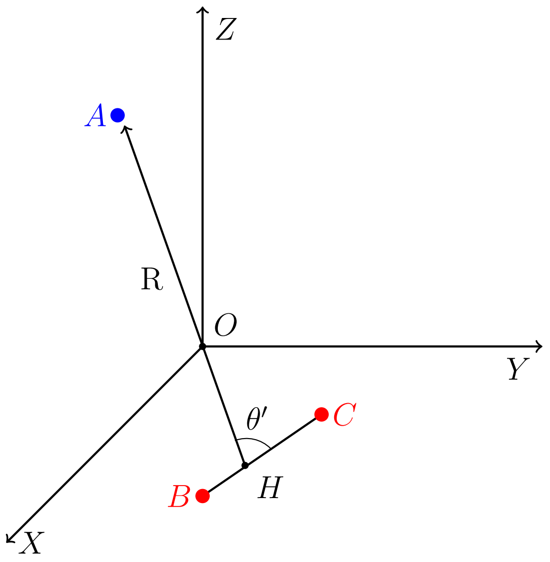

Figure 2.1: Space-fixed (XYZ) reference frame.

It is advantageous, when solving the dynamical problem, to make use of the conservation rules. In this case, the total wave function can be expressed as a sum of different components of definite total angular momentum $\mathbf{J} = \mathbf{j}+\mathbf{l}$ (where $\mathbf{l}$ is the relative angular momentum) and definite total parity ϵ (ϵ denotes the eigenvalues of Π, the inversion operator in the origin O). The Hamiltonian commutes with $\mathbf{J}^2$, J_Z and Π and therefore J, M and ϵ are conserved during the collision. For this reason, the complete solution Φ of the problem can be expanded as follow:

$$\Phi(\mathbf{R}, \hat{\boldsymbol{\rho}}) = \sum_{JM\epsilon} C_{JM\epsilon} \Psi^{JM\epsilon}(\mathbf{R}, \hat{\boldsymbol{\rho}}) \qquad (2.22)$$

where $C_{JM\epsilon}$ are the expansion coefficients that ensures the suitable boundary conditions of the scattering state; $\Psi^{JM\epsilon}$ are eigenfunctions of the total Hamiltonian with a definite total angular momentum and parity. Additionally, the wave functions $\Psi^{JM\epsilon}$ can also be developed over complete set of eigenfunctions of $\mathbf{J}^2$, J_Z, $\mathbf{j}^2$,

$\mathbf{l}^2$ and Π formed of spherical harmonics:

$$\mathcal{Y}_{jl}^{JM}(\theta,\phi;\Theta,\Phi) = \sum_{mm_l} (jmlm_l|JM) Y_{jm}(\theta,\phi) Y_{lm_l}(\Theta,\Phi) \tag{2.23}$$

where $M = m + m_l$ and $(....|..)$ is a Clebsch-Gordan coefficient.

We thus obtain the expansion employed by Arthurs and Dalgarno [17]

$$\Psi^{JMjl\epsilon}(\theta,\phi,R,\Theta,\Phi) = \sum_{j''l''} R^{-1} F_{j''l''}^{Jjl}(R) \mathcal{Y}_{j''l''}^{JM}(\theta,\phi;\Theta,\Phi) \tag{2.24}$$

where the $F(R)$ are the radial wavefunctions, the superscripts label the initial values and the sum is over (j'', l'') values such that $(-)^{j''+l''} = \epsilon$.

By substituting Eq. 2.24 into Eq. 2.21 we obtain a set of coupled equations for the radial wavefunctions

$$\begin{aligned} &\left[\frac{d^2}{dR^2} - \frac{l'(l'+1)}{R^2} + k_{j'}^2\right] F_{j'l'}^{Jjl}(R) \\ &= 2\mu \sum_{j''l''} \langle j'l'JM|V(R,\theta')|j''l''JM\rangle F_{j''l''}^{Jjl}(R) \end{aligned} \tag{2.25}$$

where the $k_{j'}^2$

$$k_{j'}^2 = 2\mu(E - E_{j'}) \tag{2.26}$$

specify the channel wavenumbers.

Solutions of Eq. 2.25 are subject to the boundary conditions

$$F_{j'l'}^{Jjl}(R) \underset{R\to 0}{\sim} 0 \tag{2.27}$$

and

$$F_{j'l'}^{Jjl}(R) \underset{R\to\infty}{\sim} \delta_{jj'}\delta_{ll'} e^{-i(k_j R - \frac{1}{2}l\pi)} - \left(\frac{k_j}{k_{j'}}\right)^{\frac{1}{2}} S^J(jl;j'l') e^{+i(k_{j'}R - \frac{1}{2}l'\pi)} \tag{2.28}$$

defines the scattering matrices S^J.

The collisions cannot induce transitions among total angular momentum states. Then, the potential matrix is diagonal in J and the coupled equations may be solved for each value of J independently.

The main advantage of the SF representation is that the centrifugal term takes a simple form in Eq. 2.25 because the SF bases are eigenfunctions of the operator $\mathbf{l}^2$. However, the evaluation of the matrix elements of the potential are more complicated because the basis functions depend on the SF coordinates, θ, whereas the potential V depends on the BF coordinate θ'.

2.3.2 Close-Coupling Approach

In order to evaluate the matrix elements of Eq. 2.25, the potential is expanded over a complete set of functions of the angular variable, θ',

$$V(R,\theta') = \sum_{\lambda} v_{\lambda}(R) P_{\lambda}(cos\theta') \tag{2.29}$$

where $P_{\lambda}(cos\theta')$ is the Legendre polynomial.

Now we can consider the matrix elements of the potential as,

$$\begin{aligned} \langle j'l'JM|V(R,\theta')|j''l''JM\rangle &= \int \mathcal{Y}_{j'l'}^{JM*}(\hat{\mathbf{r}},\hat{\mathbf{R}}) V(R,\theta') \mathcal{Y}_{j''l''}^{JM}(\hat{\mathbf{r}},\hat{\mathbf{R}}) d\hat{\mathbf{r}} d\hat{\mathbf{R}} \\ &= \sum_{\lambda} v_{\lambda}(R) \int \mathcal{Y}_{j'l'}^{JM*}(\hat{\mathbf{r}},\hat{\mathbf{R}}) P_{\lambda}(cos\theta') \mathcal{Y}_{j''l''}^{JM}(\hat{\mathbf{r}},\hat{\mathbf{R}}) d\hat{\mathbf{r}} d\hat{\mathbf{R}} \end{aligned} \tag{2.30}$$

where $\hat{\mathbf{r}} = (\theta,\phi)$ and $\hat{\mathbf{R}} = (\Theta,\Phi)$ denote polar coordinates. The last integral may be evaluated by means of the spherical harmonic addition theorem, which states that

$$P_{\lambda}(\cos\theta') = \frac{4\pi}{2\lambda+1} \sum_{\nu=-\lambda}^{\lambda} Y_{\lambda\nu}(\hat{\mathbf{r}}) Y_{\lambda\nu}^{*}(\hat{\mathbf{R}}) \tag{2.31}$$

This theorem converts the dependence of the potential on θ', which is the angle between the intramolecular vector $\mathbf{r}$ and the intermolecular vector $\mathbf{R}$, into its dependence on the SF angles $\hat{\mathbf{r}}$ and $\hat{\mathbf{R}}$ and enables the integrals to be carried out.

Then we obtain,

$$\langle j'l'JM|V(R,\theta')|j''l''JM\rangle = \sum_{\lambda} v_\lambda(R) f_\lambda(j'l', j''l''; J) \tag{2.32}$$

where $f_\lambda(j'l', j''l''; J)$ are the algebraic coefficients of Percival & Seaton [99] which are defined by the following expression,

$$\begin{aligned} f_\lambda(j'l', j''l''; J) =&(-1)^{j'+j''-J}[(2j'+1)(2l'+1)(2j''+1)(2l''+1)] \\ &\times \begin{pmatrix} j'' & j' & \lambda \\ 0 & 0 & 0 \end{pmatrix} \begin{pmatrix} l'' & l' & \lambda \\ 0 & 0 & 0 \end{pmatrix} \begin{Bmatrix} j' & l' & J \\ l'' & j'' & \lambda \end{Bmatrix} \end{aligned} \tag{2.33}$$

where $\begin{pmatrix} \cdot & \cdot & \cdot \\ \cdot & \cdot & \cdot \end{pmatrix}$ denotes the $3j$ symbol and $\begin{Bmatrix} \cdot & \cdot & \cdot \\ \cdot & \cdot & \cdot \end{Bmatrix}$ denotes a $6j$ symbol.

Then, the coupled Eq 2.25 may be written

$$\begin{aligned} &\left[\frac{d^2}{dR^2} - \frac{l'(l'+1)}{R^2} + k_{j'}^2\right] F_{j'l'}^{Jjl}(R) \\ &= 2\mu \sum_{j''l''\lambda} v_\lambda(R) f_\lambda(j'l', j''l''; J) F_{j''l''}^{Jjl}(R) \end{aligned} \tag{2.34}$$

where the index M has been dropped.

2.3.3 Inelastic cross section

We are interested in solutions that describe the diffusion of the molecule between two rotational states $|jm\rangle$ and $|j'm'\rangle$. The scattering state presents a defined structure: a plane wave representing the incoming particle from infinity without interaction plus a divergent wave which arises after the interaction. Choosing the initial relative motion to be in the Z axis, we can write the asymptotic behavior of the total wavefunction as,

$$\begin{aligned}\Phi^{jm} &\sim exp(ik_j Z)Y_{jm}(\theta,\phi)\\ &+\sum_{j'm'} f(j'm' \leftarrow jm|\Theta,\Phi)Y_{j'm'}(\theta,\phi)R^{-1}exp(ik_{j'}R)\end{aligned} \tag{2.35}$$

where the function $f(j'm' \leftarrow jm|\Theta,\Phi)$ is called the *scattering amplitude*. This is the only term that depends on the potential $V(R,\theta')$. To compute this term we can expand the wave function using the basis 2.24.

$$\Phi^{jm} = \sum_{JMl} C_{JMlj}\Psi^{JMjl} \tag{2.36}$$

By matching the known incident wave amplitudes from Eqs. 2.35 and 2.36 one can find the coefficients of the Ψ^{JMl} in the expansion of Φ^{jm}, and by matching the outgoing waves, one obtains the scattering amplitudes,

$$\begin{aligned}f(j'm' \leftarrow jm|\Theta,\Phi) = &\sum_{JMll'm'_l} \pi^{\frac{1}{2}}(2l+1)^{\frac{1}{2}} i^{l+l'+1}(k_j\ k_{j'})^{\frac{1}{2}}\\ &\times (m_j 0M;jlJ)(m'm'_l M;j'l'J)T^J(j'l';jl)Y_{l'm'_l}(\Theta,\Phi)\end{aligned} \tag{2.37}$$

where the sums are over all allowed values and T^J is the transition matrix,

$$T^J(j'l';jl) = \delta_{jj'}\delta_{ll'} - S^J(j'l';jl) \tag{2.38}$$

Then, the integral cross section can be reduced after some algebraical work [17] by the following expression:

$$\sigma(j \to j') = \frac{\pi}{(2j+1)k_{jj}^2}\sum_{J=0}^{\infty}\sum_{l=|J-j|}^{J+j}\sum_{l'=|J-j'|}^{J+j'}(2J+1)\ T^J(j'l';jl) \tag{2.39}$$

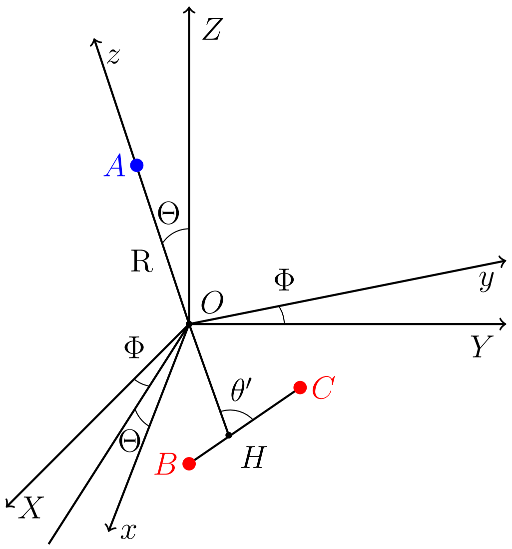

Figure 2.2: $(Oxyz)$ is the BF reference frame. $(OXYZ)$ is the SF reference frame. A rotation of Euler angles $(\Phi, \Theta, 0)$ brings the $(OXYZ)$ frame into the $(Oxyz)$ frame.

2.3.4 The body-fixed representation

Collisional systems that present strong anisotropic intermolecular potential are often studied in the body-fixed (or molecule-fixed) frame, in which the intermolecular potential is block-diagonal, and most of the couplings between channels come from the $\mathbf{l}^2$ operator.

The orientation of the body-fixed axes (xyz) relative to the space-fixed axes (XYZ) is described by the Euler angles $(\alpha, \beta, 0)$ where $(\alpha, \beta) \equiv (\Theta, \Phi)$ are the polar coordinates of the $\mathbf{R}$ vector in the space-fixed axis system (Fig 2.2). The polar and azimuthal angles of the $\boldsymbol{\rho}$ vector in the body-fixed axis system are denoted by (θ', ϕ').

In this new frame, it is convenient [100] to expand the $\Psi^{JM\epsilon}$ over a complete set of eigenfunctions of $\mathbf{J}^2$, J_Z, $\mathbf{j}^2$, $|j_z|$ and Π. First, let's consider the eigenfunctions of $\mathbf{J}^2$, J_Z, $\mathbf{j}^2$, $|j_z|$,

$$\mathcal{Z}_{j\Omega}^{JM}(\theta,\phi,\Theta,\Phi)=\left(\frac{2J+1}{4\pi}\right)^{\frac{1}{2}}D_{M\Omega}^{J*}(\Theta,\Phi,0)Y_{j\Omega}(\theta';\phi') \tag{2.40}$$

where $D_{M\Omega}^{J*}(\Theta,\Phi,0)$ are the coefficients of the irreducible representation that connect both frames. Then in order to take into account the parity conservation we must take a linear combination of the $+\Omega$ and $-\Omega$ components:

$$\mathcal{Z}_{j\bar{\Omega}}^{JM\epsilon}(\theta',\phi',\Theta,\Phi)=\frac{\mathcal{Z}_{j\bar{\Omega}}^{JM}(\theta',\phi',\Theta,\Phi)+\epsilon\mathcal{Z}_{j-\bar{\Omega}}^{JM}(\theta',\phi',\Theta,\Phi)}{[2(1+\delta_{\bar{\Omega}0})]^{\frac{1}{2}}} \tag{2.41}$$

where $\bar{\Omega}=|\Omega|$, $\epsilon=\mp1$. These functions will no longer be eigenfunctions of j_z but of $|j_z|$. Then, the total wave function of the BF frame can be expanded in the following way:

$$\Psi^{JMj\bar{\Omega}\epsilon}(R,\theta',\phi',\Theta,\Phi)=\sum_{j'\bar{\Omega}'}\frac{G_{j'\bar{\Omega}'}^{Jj\bar{\Omega}}(R)}{R}\mathcal{Z}_{j'\bar{\Omega}'}^{JM\epsilon}(\theta',\phi',\Theta,\Phi) \tag{2.42}$$

where $G_{j'\bar{\Omega}'}^{Jj\bar{\Omega}}(R)$ is the radial function.

If one introduces the last expansion in the BF representation of Eq. 2.21 we obtain a set of coupled equations:

$$\begin{aligned}&\left[\frac{d^2}{dR^2}+k_{j'}^2\right]G_{j'\bar{\Omega}'}^{Jj\bar{\Omega}}(R)\\&=2\mu\sum_{j''\bar{\Omega}''}\langle j'\bar{\Omega}'JM|V(R,\theta')+\frac{\mathbf{l}^2}{R^2}|j''\bar{\Omega}''JM\rangle G_{j''\bar{\Omega}''}^{Jj\bar{\Omega}}(R)\end{aligned} \tag{2.43}$$

with $k_{j'}^2=2\mu[E-j'(j'+1)/2I]$.

In the last equation, $\mathbf{l}^2$ couples channels $j\bar{\Omega}$ and $j'\bar{\Omega}'$ with $j'=j$, $\bar{\Omega}'=\bar{\Omega}-1,\bar{\Omega},\bar{\Omega}+1$. The matrix elements are obtained from the following expressions:

$$\langle\mathcal{Z}_{j\bar{\Omega}}^{JM\epsilon}|\mathbf{l}^2|\mathcal{Z}_{j\bar{\Omega}}^{JM\epsilon}\rangle=J(J+1)+j(j+1)-2\bar{\Omega}^2 \tag{2.44}$$

$$\begin{aligned}\langle \mathcal{Z}_{j\bar{\Omega}}^{JM\epsilon}|\mathbf{l}^2|\mathcal{Z}_{j\bar{\Omega}\pm 1}^{JM\epsilon}\rangle =& -(1+\delta_{\bar{\Omega}})^{\frac{1}{2}}[J(J+1)-\bar{\Omega}(\bar{\Omega}\pm 1)]^{\frac{1}{2}} \\ & \times [J(J+1)-\bar{\Omega}(\bar{\Omega}\pm 1)]^{\frac{1}{2}}\end{aligned} \tag{2.45}$$

If we expand the potential $V(R,\theta')$ as we did in Eqs. 2.29 we can obtain an appropriate expression to compute the potential matrix elements:

$$\begin{aligned}\langle \mathcal{Z}_{j\bar{\Omega}}^{JM\epsilon}|V(R,\theta')|\mathcal{Z}_{j'\bar{\Omega}'}^{JM\epsilon}\rangle =&\delta_{\bar{\Omega}\bar{\Omega}'}\sum_{\lambda=0}^{\lambda_{max}}(-)^{\bar{\Omega}}[(2j+1)(2j'+1)]^{\frac{1}{2}} \\ & \times \begin{pmatrix} j & j' & \lambda \\ 0 & 0 & 0 \end{pmatrix}\begin{pmatrix} j & j' & \lambda \\ \bar{\Omega} & -\bar{\Omega} & 0 \end{pmatrix} v_\lambda(r)\end{aligned} \tag{2.46}$$

The matrix elements of the interaction potential are easier to evaluate in the BF frame than in the SF frame. The conservation property $\bar{\Omega}=\bar{\Omega}'$ is incorporated in the BF representation. This latter property arises from the invariance of the potential under rotations about the BF Z-axis.

Relations between the BF and SF solutions can be obtained

$$F_{j'l'}^{Jjl\epsilon}(R)=\sum_{\bar{\Omega}'}P_{l\bar{\Omega}'}^{JM\epsilon:j}G_{j\bar{\Omega}'}^{Jj\Omega\epsilon}(R) \tag{2.47}$$

where

$$P_{l\bar{\Omega}}^{JM\epsilon:j}=(-)^{J+\Omega}2^{\frac{1}{2}}(2l+1)^{\frac{1}{2}}(1+\delta_{\bar{\Omega}0})^{\frac{1}{2}}\begin{pmatrix} j & J & l \\ \bar{\Omega} & -\bar{\Omega} & 0 \end{pmatrix} \tag{2.48}$$

This allows going from the BF radial solutions to the SF ones. This transformation is very useful because the SF frame is more suitable for evaluating the **S** matrix.

2.3.5 Coupled-States Approach

The BF could help us to introduce an important approximation. Rotationally inelastic collisions involving neutral particles tend to be induced by the interaction potential at short range. In this case the correct evaluation of the matrix elements is crucial. Then, when we deal with short-range collisions and small values of l the problem could be solved by means of the BF equations with an approximate form of the centrifugal potential.

This is the idea of the coupled states (CS), or centrifugal decoupling approximation [21]. In the BF representation the centrifugal potential matrix could be simplified in the following way:

$$\langle j'\bar{\Omega}'JM|\frac{\mathbf{l}^2}{R^2}|j''\bar{\Omega}''JM\rangle = J(J+1)\delta_{\bar{\Omega}\bar{\Omega}'} \tag{2.49}$$

Hence, the Ω coupling disappears and Eqs. 2.43 reduces to

$$\left[\frac{d^2}{dR^2} - \frac{J(J+1)}{R^2} + k_{j'}^2\right] G_{j;j'}^{J\bar{\Omega}}(R) = 2\mu \sum_{j''\lambda} v_\lambda(R) g_\lambda(j\bar{\Omega}, j''; \bar{\Omega}J) G_{j;j''}^{J\bar{\Omega}}(R) \tag{2.50}$$

where

$$g_\lambda(j\bar{\Omega}, j''; \bar{\Omega}J) = (-1)^{\bar{\Omega}} \sum_\lambda [(2j+1)(2j'+1)]^{\frac{1}{2}} \begin{pmatrix} j' & j & \lambda \\ 0 & 0 & 0 \end{pmatrix} \begin{pmatrix} j & j' & \lambda \\ \bar{\Omega} & -\bar{\Omega} & 0 \end{pmatrix} \tag{2.51}$$

We can see that no coupling arises between states of different j_z. In this representation $l_z = 0$, so that, the z components of $\mathbf{J}$ and $\mathbf{j}$ are the same. On the other hand, the usual selection rules for transitions in j will hold in this formulation due to the presence of the $3-j$ symbols which vanish unless j,j' and λ satisfy a triangle inequality.

The BF equations are now coupled only through the rotational quantum number, j. Then, the problem reduces to solving, for each value of $\bar{\Omega}$, a set of differential equations coupled in j. Therefore, the computing time is significantly reduced.

2.3.6 Infinite Order Sudden Approximation

The infinite order sudden approximation (IOS) was introduced by Pack [101]. The essence of this approximation is to neglect rotations of the frame BF and rotations of the molecule itself. Then it considers θ' as a constant. This approximation can be used for molecules with small rotational constants when collisional energies are much higher that rotational energies. In this case we can write

$$k_j^2 = 2\mu[E - Bj(j+1)] \sim 2\mu E \tag{2.52}$$

After introducing this approach the set of coupled equations in the BF frame becomes a set of uncoupled equations for each value of θ and l :

$$\left[\frac{d^2}{dR^2} - \frac{l(l+1)}{R^2} - 2\mu V(R,\theta) + k^2\right] F_l(R,\theta) = 0 \tag{2.53}$$

The equation does not depend on j and the solutions $F_l(R,\theta)$ are obtained for the parameters θ and l.

In this case the appropriate boundary conditions to this form are

$$G_l(R,\theta') \rightarrow 0 \tag{2.54}$$

as $R \rightarrow 0$, and

$$G_l(R,\theta') \sim k^{\frac{1}{2}} R[j_l(kR)A_l(\theta') - n_l(kR)B_l(\theta')] \tag{2.55}$$

as $R \rightarrow \infty$. In that expression, n_l are spherical Bessel functions of the first and second kind, respectively. The coefficients $A_l(\theta')$ and $A_l(\theta')$ are determined by solving numerically the differential Eq. 2.53 and fitting to the form of Eq. 2.55.

The relevant informations of the scattering process are contained in the scattering matrix, the elements of which can be obtained by the quantity

$$S_l(\theta') = 1 + 2iB_l(\theta')A_l^{-1}(\theta')[1 - iB_l(\theta')A_l^{-1}(\theta')]^{-1} \tag{2.56}$$

The last equation does not yield informations on rotational inelastic scattering. However, these informations can be obtained using the expression:

$$S_l(j\Omega, j'\Omega') \equiv \langle j\Omega| \, S_l(\theta') \, |j'\Omega'\rangle \tag{2.57}$$

Then partial cross sections can be derived from

$$\sigma_l(j \to j') = \frac{\pi}{k_{j'}(2j'+1)} \sum_{\Omega} (2l+1)|S_l(j\Omega, j'\Omega')| \tag{2.58}$$

and total cross section is obtained by summing over l.

$$\sigma(j \to j') = \frac{\pi}{k_{j'}} \sum_{l} \frac{2l+1}{2j'+1} \sum_{\Omega} |S_l(j\Omega, j'\Omega)|^2 \tag{2.59}$$

Obviously, the IOS approximation is less accurate than CS approximation. However, it could be useful in the cases when the conditions for its application are reached.

Chapter 3

Rotational (de-)excitation of XCN/XNC (X=Al, Mg) by He

Contents

Metal cyanides and isocyanides are the most common metal-containing molecules in the ISM. In particular, they are more abundant than their halide counterparts in the circumustellar gas. In this chapter, we study the rotational excitation of the linear molecules XCN/XNC (X = Al, Mg) due to collisions with He. First, we will present the rotational structure and spectroscopy of these molecules. Then, we will present the theory for the collisional excitation of molecules in $^2\Sigma^+$ electronic state. Finally, we report our results in the last section.

3.1 Rotational spectroscopy of XCN/XNC

Recently, Senent et. al. (2012) [71] computed structural and spectroscopic properties of XCN/XNC (X = Al, Mg) using highly correlated *ab initio* calculations. The results are in good agreement with previous experimental works [102–105].

Fig. 3.1 presents some structural and spectroscopic parameters corresponding to the AlCN and AlNC isomers in their electronic ground state. AlNC isomer is more stable than the AlCN. AlNC and its metastable isomer AlCN present linear geometric configurations. They isomerization barrier of 4216 cm^{-1} [71] restrict the intertransformation at low temperatures. We can also see that the dipole moment of AlNC is slightly larger than that of AlCN.

The fundamental frequencies of these isomers, namely, C–N stretching, the XCN(or CNX) bending and the X–C (or N–X) stretching modes are 2038 cm^{-1}, 96 cm^{-1} and 557 cm^{-1} for AlNC and 2141 cm^{-1}, 141 cm^{-1} and 475 cm^{-1} for AlCN [71], respectively. All these frequencies are above 100 K. We can then consider these molecules like rigid rotors when studying collisional excitation. Consequently, the intermolecular bond distances of the Al-CN and Al-NC were frozen at their experimental equilibrium values.

The linear AlCN($^1\Sigma^+$) and AlNC($^1\Sigma^+$) molecules are closed shell molecules. For this reason, these molecules have a simple rotational structure that is described by the Hamiltonian operator $B\mathbf{N}^2 - D\mathbf{N}^4$, as was described in chapter 2.

In Fig. 3.3, we show the first rotational energy levels of AlCN and AlNC. The rotational constant of AlNC is slightly larger than the one of AlCN. For this reason the AlCN rotational structure is more compact.

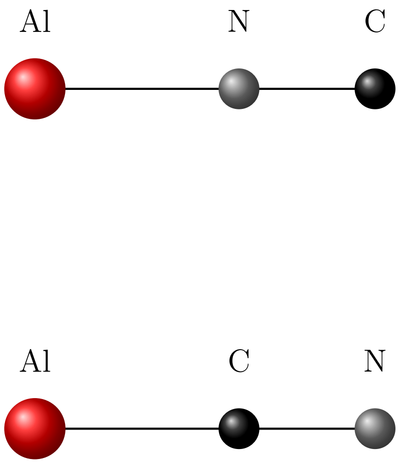

$X^1\Sigma^+$ B = 5895.85 MHz

r_{AlN}=1.86 Å μ = 3.3948 D

r_{CN}=1.18 Å E_r = 0 cm^{-1}

$X^1\Sigma^+$ B = 4966.60 MHz

r_{AlC}=2.02 Å μ = 3.7204 D

r_{CN}=1.17 Å E_r = 1980 cm^{-1}

Figure 3.1: Intermolecular bond distances, rotational constant (B), dipole moment (μ) and relative energy (E_r) of AlCN–AlNC isomers.

Similarly, we present in Fig. 3.2 some structural and spectroscopic parameters for the MgCN and MgNC isomers in their ground electronic state. We can see that MgNC isomer is more stable than the MgCN one. In this case, a barrier of 2203 cm^{-1} [71] also constrains the intertransformation at low temperatures. The fundamental frequencies of these isomers, namely, C–N stretching, the MgCN(or MgNC) bending and the Mg–C (or N–C) stretching modes are 2061 cm^{-1}, 91 cm^{-1} and 530 cm^{-1} for MgNC and 2143 cm^{-1}, 153cm^{-1} and 468 cm^{-1} for MgCN [71], respectively.

The MgCN($^2\Sigma^+$) and MgNC($^2\Sigma^+$) molecules are open shell molecules. Molecules having electronic spin, but no orbital momentum and no strong nuclear coupling, can be described in the Hund's case (b). The spin is coupled to the rotational momentum through interaction of the spin magnetic moment with the weak mag-

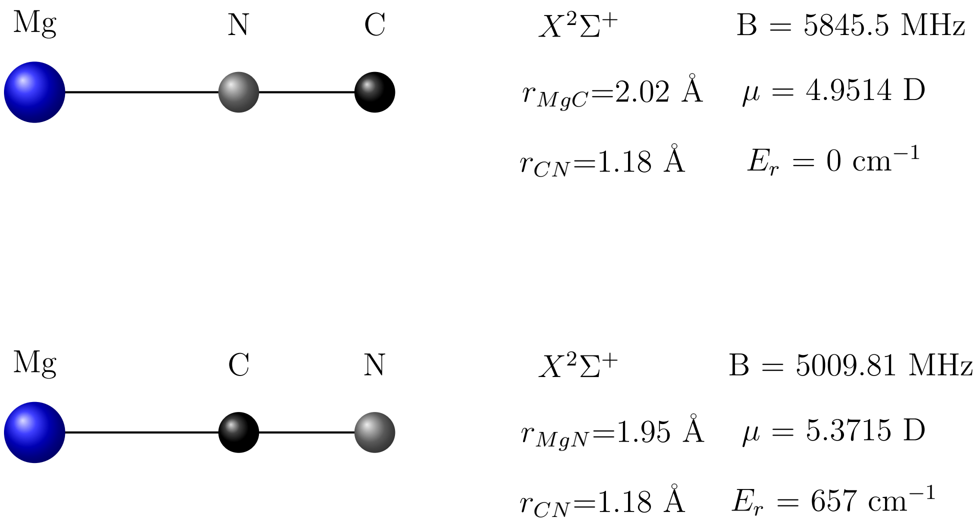

Figure 3.2: Intermolecular bond distances, rotational constant (B), dipole moment (μ) and relative energy (E_r) of MgCN–MgNC isomers.

netic field generated by the molecular rotation. The Hamiltonian operator for these molecules, including the spin-rotation interaction and the first term in the centrifugal distortion perturbation energy, may be expressed as [106]

$$H = B\mathbf{N}^2 - D\mathbf{N}^4 + \gamma\mathbf{SN} \tag{3.1}$$

Here **N** is the rotational operator, **S** is the electronic spin operator and B is the rotational constant, D is the centrifugal distortion, and γ is the spin-rotation coupling constant.

In this coupling scheme the Hamiltonian is diagonal in j, N and S and the energies,

$$E_{j,N,S} = BN(N+1) - DN^2(N+1)^2 + \frac{1}{2}\gamma[j(j+1) - N(N+1) - S(S+1)] \tag{3.2}$$

with the following quantum numbers

$$\begin{aligned} N &= 0, 1, 2, 3, 4... \\ S &= \pm\frac{1}{2} \\ j &= N \pm \frac{1}{2} \end{aligned} \tag{3.3}$$

In Fig 3.3, the blue energy levels are schematic representations of the rotational energy levels of MgCN($^2\Sigma^+$) and MgNC($^2\Sigma^+$). In the absence of spin-rotation interaction, the rotational levels are index in N, the rotational angular momentum of the nuclei. The resulting spectrum, shown on the left-hand side of the energy axes, is equivalent to the spectrum of a $^1\Sigma^+$ molecule. We can see that MgNC rotational levels are more separated than the MgCN ones because of the larger rotational constant of this isomer. The levels of the right side displays the fine structure which occurs when the spin-rotation interaction is included. For purposes of illustration the separation of fine levels have been exaggerated.

Collisional excitation among the fine structure of $^2\Sigma^+$ molecules can be considered explicitly [107]. However, often, the exact treatment is very time consuming. For this reason, different approximations are used. In the next section we discuss one of them.

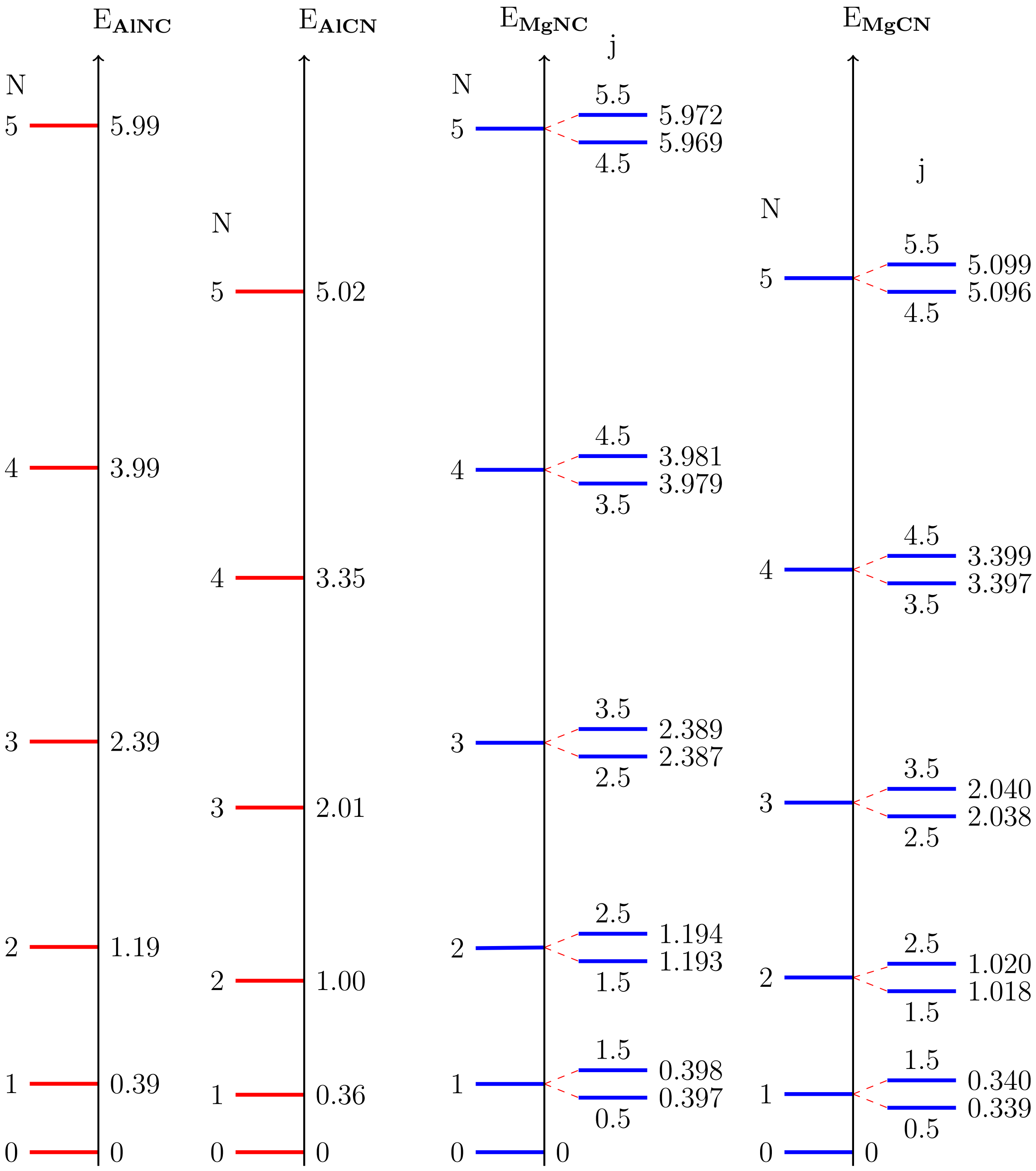

Figure 3.3: Rotational energy (cm^{-1}) levels of the AlCN/AlNC (red lines) and MgCN/MgNC (blue lines).

3.2 Collisions of $^2\Sigma$ molecules by ^1S atoms

The problem of the collision-induced transitions among fine-structure levels does not differ significantly from the problem of collisional excitation of $^1\Sigma^+$ molecules. However, for $^2\Sigma^+$ molecules a new phenomenon arises: collisions which are elastic in N but are inelastic in the parity of the molecular wave function. Then, the formulation has to consider the coupling between the rotational angular momentum and the electronic spin.

In this case, the collision does not affect the magnitude or orientation of the electronic spin [108, 109] because of the spin independence of the intermolecular potential. Then the potential matrix can be represented using a new total-J basis that takes into account the following coupling scheme,

$$\mathbf{N} + \mathbf{l} = \mathcal{J} \quad , \quad \mathcal{J} + \mathbf{S} = \mathbf{J} \tag{3.4}$$

where $\mathbf{N}$ and $\mathbf{S}$ designate, respectively, the nuclear rotational angular momentum and the electronic spin.

Following the paper of Corey and McCourt [108] the last coupling leads to a formalism that reduces the collisional excitation of $^2\Sigma^+$ molecules to the usual close-coupling equations for scattering of $^1\Sigma^+$ molecules. In particular, one can obtain the nuclear-spin-free reduced T-matrix elements.

$$\begin{aligned}(N'Sj'l'||T_K||NSJl) &= [(2j+1)(2j'+1)]^{\frac{1}{2}}(-1)^{-S-j-N'-K} \\ &\quad \times \left\{ \begin{array}{ccc} N & N' & K \\ j' & j & S \end{array} \right\} (N'l'||T_K||Nl)\end{aligned} \tag{3.5}$$

In the last expression, the values of N and N' in the right hand side are governed by the relations $N = j - 1/2$ and $N = j + 1/2$.

Then, after some development one obtains the following expression for the degeneracy-averaged cross sections [110]:

$$\sigma_{Nj\to N'j'} = \frac{\pi}{k^2}(2j'+1)\sum_K \left\{ \begin{array}{ccc} N & N' & K \\ j' & j & S \end{array} \right\}^2 P^K_{N,N'} \tag{3.6}$$

where the spin-independent tensor opacities $P^K_{N,N'}$ are defined in terms of the spin-independent reduced T–matrix elements $\langle NL|\, T^K \,|NL\rangle$.

Within the IOS approximation the nuclear-spin-free tensor opacities take a simpler form. It is proportional to cross sections out of the lowest accessible rotational level. For collisions involving molecules in $^1\Sigma^+$ electronic states we have,

$$P^K_{N,N'} = (2N+1)(2N'+1)(2K+1) \times \begin{pmatrix} N' & K & N \\ 0 & 0 & 0 \end{pmatrix}^2 \left[\frac{k^2}{\pi}\sigma_{K\to 0}\right] \tag{3.7}$$

with the constraint $|N - N'| \leq K \leq N + N'$.

Therefore, we can use IOS approximation and the cross sections out of the lowest rotational level, $N = 0$, to obtain collisional excitation among the fine structure.

The calculations can be improved using a scaling technique introduced by Neufeld & Green [111]:

$$\sigma_{jN\to j'N'} = \frac{\sigma^{IOS}_{jN\to j'N'}}{\sigma^{IOS}_{j\to j'}}\sigma_{j\to j'} \tag{3.8}$$

Within this approximation we ensure that,

$$\sum_{j'} \sigma(jN \to j'N') = \sigma(j \to j') \tag{3.9}$$

Fig. 3.4 shows a comparison between the recoupling technique employed by us (RC-IOS) and a more sophisticated approach (RC-CC) [112] that considers the exact spinless close-coupling T matrix. We can observe that there is a global

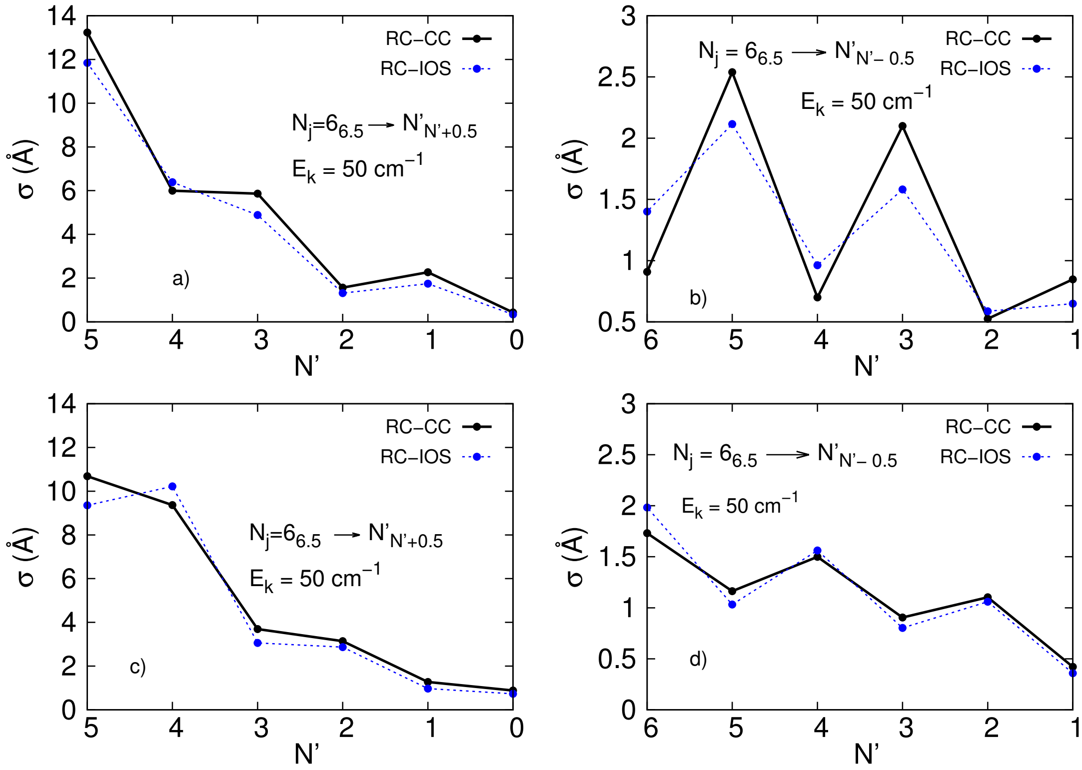

Figure 3.4: Comparison between the recoupling formulation RC-IOS (this work) and the recoupling formulation RC-CC. Figures a) and b) represent the results for MgNC molecule. Figures c) and d) represent the results for MgCN molecule.

agreement between both approximations. In particular, the RC-IOS formalism describes correctly the propensity rule in favour of the $\Delta j = \Delta N$ transitions. This propensity rule is predicted by the exact formulation [107]. For closely spaced energy levels and high collisional energies RC-IOS is a good approximation. However, as we can see in Fig. 3.3, high-lying excited rotational states become progressively significantly spaced. This effect can induce stronger deviations.

3.3 Results

Monthly Notices
of the
ROYAL ASTRONOMICAL SOCIETY

MNRAS **432,** 468–477 (2013)
Advance Access publication 2013 April 12

doi:10.1093/mnras/stt481

Cyanide/isocyanide abundances in the interstellar medium – II. Inelastic rate coefficients of Al and Mg compounds

M. Hernández Vera,[1,2]★ F. Lique,[1]★ F. Dumouchel,[1] J. Kłos,[3] J. Rubayo Soneira[2] and M.-L. Senent[4]

[1]*LOMC – UMR 6294, CNRS-Université du Havre, 25 rue Philippe Lebon, BP 540, F-76058 Le Havre, France*
[2]*Instituto Superior de Tecnologías y Ciencias Aplicadas, Quinta de Los Molinos, Plaza, La Habana 10600, Cuba*
[3]*Department of Chemistry and Biochemistry, University of Maryland, College Park, MD 20742-2021, USA*
[4]*Departamento de Química y Física Teóricas, IEM-CSIC, Serrano 121, E-28006 Madrid, Spain*

Accepted 2013 March 15. Received 2013 March 15; in original form 2013 February 28

ABSTRACT

Modelling molecular abundances in the interstellar medium (ISM) requires accurate molecular data. Then, accurate determination of collisional rate coefficients is an essential step in order to estimate the cyanide/isocyanide abundances in interstellar clouds. In addition, cyanides/isocyanides are the most common metal-containing molecules in circumstellar gas. In this work, we have carried out calculations of rate coefficients for the rotational excitation of aluminium cyanide (AlCN), aluminium isocyanide (AlNC), magnesium cyanide (MgCN) and magnesium isocyanide (MgNC) molecules in collision with He. The calculations are based on new two-dimensional potential energy surfaces obtained from highly correlated ab initio calculations. Coupled states quantum approximation was used to obtain pure rotational (de-)excitation cross-sections of AlCN, AlNC, MgCN and MgNC by He. The fine structure splitting of MgCN and MgNC was taken into account through a technique based on infinite-order sudden scaling relationship. Rate coefficients for transitions among the first 26 rotational levels of AlCN and AlNC and among the first 41 fine structure levels of MgCN and MgNC were calculated for the temperature range between 5 and 100 K. Significant differences between the rate coefficients of both isomers were observed. These differences confirm that specific calculations have to be performed for each isomer in order to obtain the necessary level of detail. The new rate coefficients should induce important consequences on the determination of metal abundance in the ISM. In particular, our work confirms that the AlCN molecule is significantly less abundant than AlNC in the ISM.

Key words: molecular data – molecular processes – scattering.

1 INTRODUCTION

Molecules containing a cyanide group are of key importance in the physical chemistry of the interstellar medium (ISM). Cyanide species are the most common metal-containing molecules in circumstellar gas (Ziurys et al. 2002; Pulliam et al. 2010) despite that the dominant role of cyanide species as metal carriers in circumstellar gas was not predicted by any chemical models. Metal cyanide compounds are present in C-rich circumstellar gas (Pulliam et al. 2010; Zack, Halfen & Ziurys 2011) and may provide a way to find other heavy metals than the one presently known. In the past, NaCN (Turner, Steimle & Meerts 1994), MgCN (Ziurys et al. 1995), SiCN (Guélin et al. 2000) or FeCN (Zack et al. 2011) have been detected in the ISM. Heavy metals in the gas phase are important in controlling the ionization of a cold dark cloud and then the chemistry and the cloud evolution (Turner et al. 2005).

Alternatively to metal cyanides, other cyanides have been observed in the ISM. The simplest cyanide HCN is a well-known interstellar molecule discovered by Snyder & Buhl (1971) and probably one of the most observed molecules. In addition, many complex organic molecules such as CH_2CN (Irvine et al. 1988), CH_3CN (Solomon et al. 1971) or CH_3CCN (Solomon et al. 1971) contain the cyanide group and play a crucial role in the chemical evolution of molecular clouds.

Usually, (metal) cyanide compounds present isomerism. Hence, for example, the AlCN/AlNC, MgCN/MgNC, SiCN/SiNC or NaCN/NaNC isomers are all stable species (Senent, Dumouchel & Lique 2012, and references therein). Assessments of cyanide/isocyanide abundances in circumstellar shells are

---

★ E-mail: mhvera28@instec.cu (MHV); francois.lique@univ-lehavre.fr (FL)

Published by Oxford University Press on behalf of the Royal Astronomical Society

readily available (Ziurys et al. 1995; Guélin et al. 2004). Commonly, large abundances correspond to the most stable isomers as they occur for MgNC. Particularly, MgCN is less stable than MgNC by about 600 cm^{-1} and the MgNC/MgCN ratio has been estimated to be $\simeq$20 by Ziurys et al. (1995). However, this is not a systematic trend. The most abundant cyanide, HCN, presents a metastable isomer HNC whose relative energy has been evaluated to be about 5000 cm^{-1}. Although HCN and HNC stabilities are quite different, the HNC/HCN astrophysical abundance ratio was estimated to be >1 (Hirota et al. 1998) in cold molecular clouds. Lique and co-workers (Dumouchel, Faure & Lique 2010; Sarrasin et al. 2010; Dumouchel, Kłos & Lique 2011) have related the unexpected large abundance of HNC to observation modelling from erroneous collisional rate coefficients. However, the abundance ratio is still high compared to the relative stability of the isomers ($\simeq$1) and the latter studies have shown the importance of having accurate collisional rate coefficients for all interstellar isomers.

Recently, Pulliam et al. (2010) suggested that the cyanide chemistry has to be reviewed. Molecular abundances in the ISM have to be understood in terms of molecular stabilities, reaction probabilities and radiative and collisional excitations. In order to understand the cyanide/isocyanide abundance in the ISM, we have initiated a series of papers in order to provide the molecular data needed for cyanide/isocyanide abundance determination. In Senent et al. (2012, hereafter Paper I), we have determined theoretical spectroscopic and structural properties of species containing third-period metals Na, Mg, Al and Si that were in very good agreement with available experimental data and that gathered complete information on these species.

In astrophysical media, collisions compete with radiative processes in altering populations in molecular ro-vibrational levels. The estimation of molecular abundances from spectral line data requires collisional rate coefficients with most abundant interstellar species such as He or H_2. He is often assumed to be a model for H_2 (Lique et al. 2008). The use of He as a substitute for H_2 could lead to significant incertitude in the case of collisions with light hydrides but is expected to be reasonable for very heavy molecules (Wernli et al. 2007) such as the metal cyanides that are presently studied. Without these rates, only approximate estimates of the molecular abundance are possible assuming local thermodynamic equilibrium, which is generally not a good approximation. Rate coefficients are also crucial to determine accurately the AlCN/AlNC, MgCN/MgNC or SiCN/SiNC abundance ratios.

In this paper, we extend the work of our previous publication (Paper I) to the calculation of inelastic rate coefficients of Al and Mg compounds. Magnesium isocyanide (MgNC) identification in the ISM was provided by Guélin, Lucas & Cernicharo (1993). MgNC is a highly reactive radical but can be easily detected due to its large dipole moment of $\simeq$5 debye (see Paper I). The magnesium cyanide (MgCN) was identified in IRC+10216 (Ziurys et al. 1995) and the aluminium isocyanide (AlNC) was also observed in the circumstellar envelope of IRC+10216 and reported by Ziurys et al. (2002). The large dipole moment of these molecules [$\simeq$5.3 and $\simeq$3.7 debye (Paper I) for MgCN and AlNC, respectively] help in the observation of radiative transitions. To the best of our knowledge, the isomer of AlNC, the AlCN molecule, has not been yet been detected in space despite that the molecule is also stable and possesses a large dipole moment of $\simeq$3.7 debye (see Paper I).

Here, we present new rotational rate coefficients for AlCN, AlNC, MgCN and MgNC based on highly accurate AlCN–He, AlNC–He, MgCN–He and MgNC–He potential energy surface (PES). The paper is organized as follows. Section 2 describes the PES used in this work. Section 3 then contains a brief description of the scattering calculations. In Section 4, we present and discuss our results.

2 POTENTIAL ENERGY SURFACE

The computation of collisional inelastic rate coefficients takes place within the Born–Oppenheimer approximation for the separation of electronic and nuclear motions. Scattering cross-sections are thus obtained by solving the equation for the motion of nuclei restricted by an electronic PES, which is independent of the masses and spins of the nuclei. Then, the first step consists in the determination of the interaction energy of the colliding systems.

To the best of our knowledge, no PES exists for the AlCN–He, AlNC–He, MgCN–He and MgNC–He van der Waals systems. The ground electronic state of the weakly bound AlCN–He and AlNC–He system is a singlet with A' reflection symmetry, whereas the ground electronic state of the weakly bound MgCN–He and MgNC–He system is a doublet with A' reflection symmetry. Within their ground electronic state, AlCN, AlNC, MgCN and MgNC molecules (denoted hereafter X-CN and X-NC) have linear geometries. Therefore, X-CN and X-NC can be considered as a linear rigid rotor.

The X-CN–He and X-NC–He ‘rigid rotor’ PESs are described by the two Jacobi coordinates R, the distance from the centre of mass of cyanide/isocyanide molecules to the He atom, and θ, the angle between $\boldsymbol{R}$ and the cyanide/isocyanide bond axis $\boldsymbol{r}$, with $\theta = 0$ corresponding to collinear He–CN/NC–X.

The intermolecular bond distances of the X-CN and X-NC were frozen at their experimental equilibrium values [$r_{\mathrm{AlC}} = 3.84$ bohr and $r_{\mathrm{CN}} = 2.21$ bohr for AlCN–He; $r_{\mathrm{AlN}} = 3.54$ bohr and $r_{\mathrm{NC}} = 2.24$ bohr for AlNC–He; $r_{\mathrm{MgC}} = 3.95$ bohr and $r_{\mathrm{CN}} = 2.21$ bohr for MgCN–He; $r_{\mathrm{MgN}} = 3.69$ bohr and $r_{\mathrm{NC}} = 2.24$ bohr for MgNC–He] (Paper I and references therein). As demonstrated by Lique & Spielfiedel (2007) for the CS–He system, for non-hydride diatomic molecules two-dimensional PESs calculated for a frozen bond distance or obtained from full three-dimensional PESs by averaging over the intermolecular ground-state vibrational wavefunction are very similar. Consequently, in the present case, we anticipate that restricting intermolecular distances to their equilibrium value will introduce little error into the calculated inelastic rate coefficients. The lowest vibrational bending frequency of AlCN, AlNC, MgCN and MgNC are $\simeq$629, 661, 633 and 629 cm^{-1} respectively (Paper I and references therein). Hence, for low-temperature collisions ($T < 100$ K), the probability of vibrational excitation is very low and can be neglected in the scattering calculations.

The AlCN–He, AlNC–He, MgCN–He and MgNC–He PESs were calculated in the supermolecular approach by means of (partially spin-restricted) coupled cluster calculations with single, double and perturbative triple excitations [(R)CCSD(T)] (Hampel, Peterson & Werner 1992; Knowles, Hampel & Werner 1993, 2000). The calculations were done with the MOLPRO 2010 package (Werner et al. 2010). For all four atoms, we used the standard correlation-consistent polarized valence quadruple-zeta basis sets of Dunning (1989) augmented with the diffuse functions of s, p, d, f and g symmetries (Kendall, Dunning & Harrison 1992). This basis set was further augmented by the [3s3p2d2f1g] bond functions optimized by Cybulski & Toczyłowski (1999) and placed at mid-distance between the He atom and the X-CN/NC centre of mass.

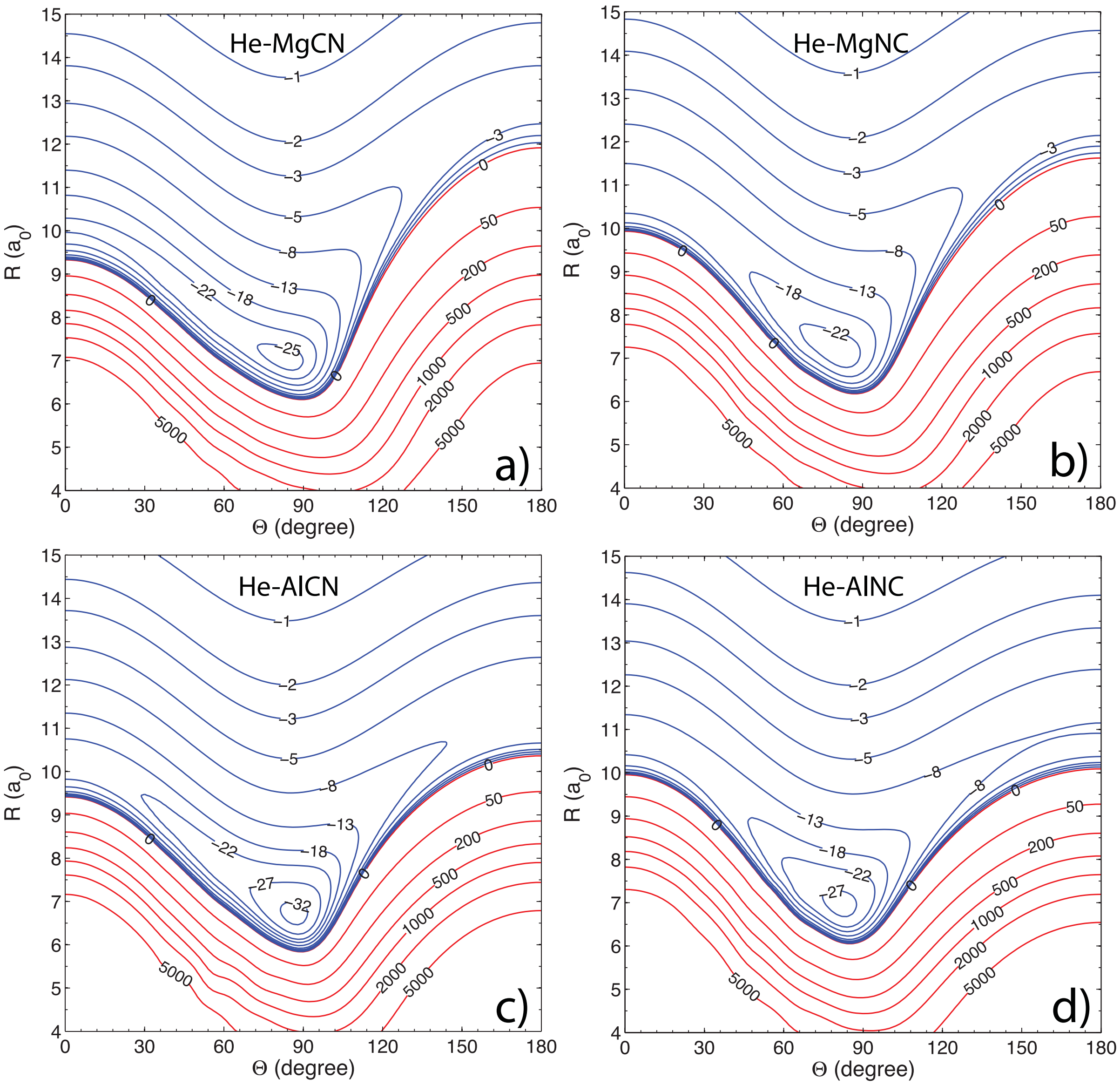

Figure 1. Contour plots of the MgCN–He (a), MgNC–He (b), AlCN–He (c) and AlNC–He (d) PES. Contour lines in units of cm^{-1}.

At all geometries, the Boys & Bernardi (1970) counterpoise procedure is used to correct for the basis set superposition error. In this procedure, the interaction energy is defined by

$$V(R,\theta) = E_{\mathrm{X-CN/NC-He}}(R,\theta) \\ -E_{\mathrm{X-CN/NC}}(R,\theta) - E_{\mathrm{He}}(R,\theta), \quad (1)$$

where the energies of the X-CN/NC and He subsystems are determined with the full (four atoms plus bond functions) basis set.

The values of the radial scattering coordinate R ranged from 4 to 30 bohr. The angular grid was uniform with a 10° spacing from 0° to 180°.

Contour plots of the four potentials are shown in Fig. 1. For these weakly bound systems, the global minima in the interaction energy were found to be -33.51 cm^{-1} ($R = 6.70$ bohr, $\theta = 86.^\circ8$) for AlCN–He, -28.47 cm^{-1} ($R = 6.94$ bohr, $\theta = 81.^\circ9$) for AlNC–He, -26.06 cm^{-1} ($R = 7.03$ bohr, $\theta = 83.^\circ6$) for MgCN–He and -23.97 cm^{-1} ($R = 7.15$ bohr, $\theta = 81.^\circ1$) for MgNC–He. We note the strong anisotropy of the four PESs. The shape of the PES is similar for all the systems, the minimal being localized for almost T-shape geometries. The anisotropy of these PESs and the location of the global minima can be qualitatively explained by inspecting the shapes of the highest occupied molecular orbitals (HOMO) of the X-CN/NC species shown in Fig. 2 using the MOLDEN orbital visualization program (Schaftenaar & Noordik 2000). One can notice that a reduction of the repulsive exchange energy in the middle of the X-CN/NC molecules approximately in the region of the centre of mass is expected. This reduction of the exchange stems from the fact that most of the electronic density is shifted towards the metal atom and distributed along the CN/NC fragment. The Mg complexes have larger orbital lobes located on the metal end which causes greater electron repulsion when He atom approaches. The repulsive wall of the PES starts at larger distances for Mg-CN/NC molecules at the $\theta = 180^\circ$ end in comparison to Al molecules. As in the middle of the Al–C bond the AlCN molecule has slightly larger electron density, one can assume a somewhat greater dispersion component attracting He atom. Therefore, the well depth is deeper

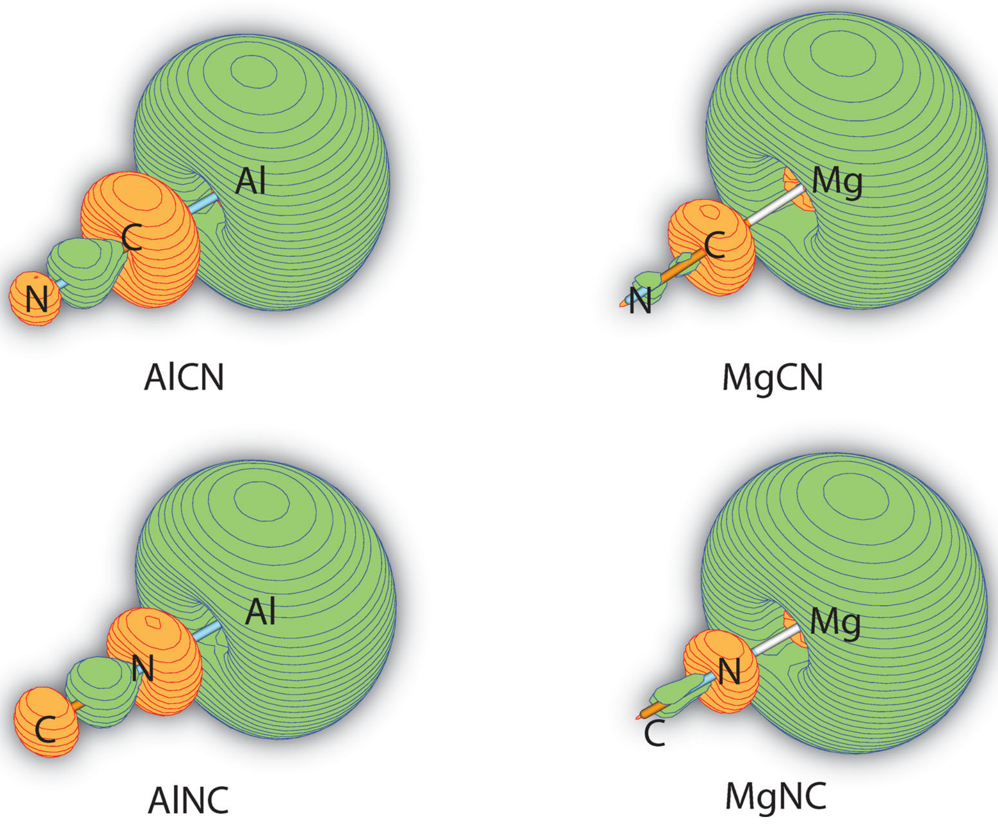

Figure 2. Representation of HOMO for MgCN/NC and AlCN/NC molecules from Hartree–Fock calculations. Colour coded lobes differ in sign.

for the He–AlCN complex in comparison to He–AlNC. The same holds for the He–MgCN/NC complexes.

The ab initio energies were fitted using a two-dimensional reproducing kernel Hilbert space method (Ho & Rabitz 1996), which interpolates through the ab initio points and extrapolates outside with R^{-6} long-range asymptotics. In the scattering MOLSCAT program (Hutson & Green 1994), the PES is expanded in Legendre polynomials:

$$V(R,\theta) = \sum_{\lambda=0}^{\lambda_{\max}} V_\lambda(R) P_\lambda(\cos\theta). \qquad (2)$$

The dependence on R of the dominant coefficients for the AlCN–He, AlNC–He, MgCN–He and MgNC–He PESs is shown in Fig. 3.

We observe that, for all the collisional systems, the largest (in magnitude) anisotropic terms ($\lambda > 0$) correspond to $\lambda = 2$. This implies that, to a first approximation, the PES is symmetric with respect to $\theta \to \pi - \theta$. For X-CN–He systems, the anisotropic terms corresponding to $\lambda = 1$, 3 are relatively large in the range of R between 7 and 10 bohr. This reflects a large (odd) anisotropy for the PES. In contrast, for X-NC–He systems, these terms are relatively small in magnitude. Consequences for the rotational excitation will be discussed in the next section.

3 SCATTERING CALCULATIONS

The main focus of this paper is the use of the fitted AlCN–He, AlNC–He, MgCN–He and MgNC–He PESs to determine rotational excitation and de-excitation cross-sections of AlCN, AlNC, MgCN and MgNC molecules by He atoms. In this work, we consider only the rotational/fine structure of cyanide/isocyanide compounds. Rate coefficients between hyperfine levels of these heavy molecules can be accurately estimated from rate coefficients between rotational/fine structure levels (see Section 5)

The AlCN($^1\Sigma^+$) and AlNC($^1\Sigma^+$) molecules have a simple rotational structure, whereas the MgCN($^2\Sigma^+$) and MgNC($^2\Sigma^+$) molecules present a fine structure due to the presence of a non-zero electronic spin. Rate coefficients between fine structure levels have to be computed if one wants to provide reliable data for astrophysical modelling.

In the following, the rotational quantum number of AlCN/AlNC will be denoted by N. For MgCN/MgNC in its ground electronic $^2\Sigma^+$ state, the molecular energy levels can be described in Hund's case (b) limit. The fine structure levels are labelled N_j, where N is the rotational angular momentum and j the total molecular angular momentum quantum number with $\boldsymbol{j} = \boldsymbol{N} + \boldsymbol{S}$, where $\boldsymbol{S}$ is the electronic spin. For molecules in a $^2\Sigma^+$ state, $S = 1/2$. Hence, for $N > 0$, two kinds of levels exist, the levels with $j = N + 1/2$ and those with $j = N - 1/2$.

We used the quantum coupled states (CS) approximation (McGuire & Kouri 1974) for the determination of cross-sections between rotational levels (i.e. neglecting fine structure levels) of all the isomers. The more accurate method is the fully quantum close-coupling (CC) approach of Arthurs & Dalgarno (1960), but this method is very computationally demanding for scattering of molecules with very small rotational constants.

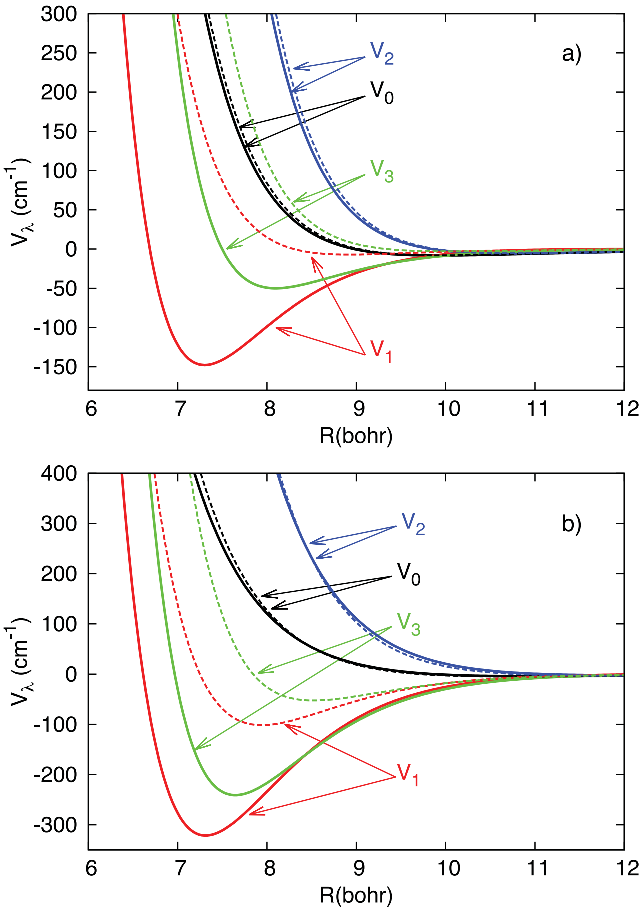

Figure 3. Plot of the first four radial Legendre expansion coefficients ($\lambda = 0, \ldots, 3$) as a function of R. (a) The solid lines denote AlCN–He while the dashed lines denote AlNC–He. (b) The solid lines denote MgCN–He while the dashed lines denote MgNC–He.

From the calculated cross-sections, one can obtain the corresponding thermal rate coefficients at temperature T by averaging over the collision energy (E_c):

$$k_{\alpha\to\beta}(T) = \left(\frac{8}{\pi\mu k_B^3 T^3}\right)^{\frac{1}{2}} \int_0^\infty \sigma_{\alpha\to\beta}\, E_c\, e^{-\frac{E_c}{k_B T}}\, dE_c, \tag{3}$$

where $\sigma_{\alpha\to\beta}$ is the cross-section from the initial level α (N) to the final level β (N'), μ is the reduced mass of the system and k_B is Boltzmann's constant.

For the MgCN and MgNC molecules, as mentioned above, the fine structure was not explicitly considered in the calculations, but taken into account using a technique based on the infinite-order sudden (IOS) approximation (Goldflam, Kouri & Green 1977) that requires determination of only rate coefficients between rotational levels. The fine structure splitting of MgCN and MgNC is at least 1/1000 of the rotational splitting and then validates the IOS approximation.

Following this technique, if one has, for a given molecule, the rate coefficients between rotational levels ($k_{N\to N'}(T)$, one can directly obtain the rate coefficients between the fine levels using the IOS approximation in which the rotational energy spacings are simply ignored compared to the collision energy.

In this approximation, inelastic rotational rate coefficients $k^{\mathrm{IOS}}_{N\to N'}(T)$ can be calculated from the 'fundamental' rates (those out of the lowest $N = 0$ level) as follows (e.g. Corey & McCourt 1983):

$$k^{\mathrm{IOS}}_{N\to N'}(T) = (2N'+1)\sum_L \begin{pmatrix} N' & N & L \\ 0 & 0 & 0 \end{pmatrix}^2 k^{\mathrm{IOS}}_{0\to L}(T). \tag{4}$$

Similarly, IOS rate coefficients among fine structure levels can be obtained from the $k^{\mathrm{IOS}}_{0\to L}(T)$ rate coefficients using the following formula (e.g. Corey & McCourt 1983):

$$k^{\mathrm{IOS}}_{N_j\to N'_{j'}}(T) = (2N+1)(2N'+1)(2j'+1) \times \sum_L \begin{pmatrix} N' & N & L \\ 0 & 0 & 0 \end{pmatrix}^2 \begin{Bmatrix} N & N' & L \\ j' & j & S \end{Bmatrix}^2 k^{\mathrm{IOS}}_{0\to L}(T), \tag{5}$$

where (: : :) and { : : : } are, respectively, the '3-j' and '6-j' symbols.

The MgCN/MgNC fine structure splittings are negligible compared with collision energies, and the above IOS prescriptions are expected to correctly predict the relative rates among fine levels. A possible improvement has been suggested (Neufeld & Green 1994). The hyperfine rates can be computed as

$$k_{N_j\to N'_{j'}}(T) = \frac{k^{\mathrm{IOS}}_{Nj\to N'j'}(T)}{k^{\mathrm{IOS}}_{N\to N'}(T)} k_{N\to N'}(T), \tag{6}$$

using the CS rate coefficients $k_{0\to L}$ for the IOS 'fundamental' rates in equations (4) and (5). This scaling procedure guarantees in particular the following equality:

$$\sum_{j'} k_{Nj\to N'j'}(T) = k^{\mathrm{CS}}_{N\to N'}(T). \tag{7}$$

In addition, we note that the fundamental excitation rates $k_{0\to L}$ were in practice replaced by the de-excitation fundamental rates using the detailed balance relation

$$k_{0\to L} = (2L+1)k_{L\to 0}. \tag{8}$$

This procedure was found to significantly improve the results at low temperature due to threshold effects.

Such an approach has been already used for open-shell molecules like SO (Lique et al. 2006) and compared with the exact CC approach. As soon as the fine structure splitting is negligible compared to rotational structure (that is presently the case), the IOS approximation leads to results in good agreement with CC results (less than 10–20 per cent of difference).

The standard time-independent coupled scattering equations were solved using the MOLSCAT code Hutson & Green (1994). The energy levels were computed with the following experimental molecular parameters (see Paper I and references therein): the rotational (B_0) and centrifugal distortion constant (D_0) of AlCN, AlNC, MgCN, MgNC were $B_0 = 0.168$ cm^{-1} and $D_0 = 9.17 \times 10^{-8}$ cm^{-1}, $B_0 = 0.200$ cm^{-1} and $D_0 = 1.30 \times 10^{-7}$ cm^{-1}, $B_0 = 0.170$ cm^{-1} and $D_0 = 9.25 \times 10^{-8}$ cm^{-1} and $B_0 = 0.199$ cm^{-1} and $D_0 = 1.41 \times 10^{-7}$ cm^{-1}, respectively. Calculations were carried out at values of the total energy ranging from 0.1 to 1000 cm^{-1} for the four collisional systems. The integration parameters were chosen to ensure convergence of the cross-sections over this range. The integral cross-sections are obtained by summing the partial cross-sections over a sufficiently large number of values of the total angular momentum J until convergence is reached. To obtain precise values for the rate constants, the energy grid was chosen to be sufficiently fine to include the numerous scattering resonances which will be described below. We extended the rotational basis sufficiently to ensure convergence of the AlCN–He and AlNC–He inelastic cross-sections for N, $N' \leq 25$. At the largest total energy

Table 1. Comparison between CC and CS AlNC–He cross-sections (in Å^2) at selected total energies (E).

Transitions	$E = 20$ cm^{-1}		$E = 50$ cm^{-1}		$E = 100$ cm^{-1}		$E = 300$ cm^{-1}	
$N \rightarrow N'$	CC	CS	CC	CS	CC	CS	CC	CS
$1 \rightarrow 0$	5.163	7.425	2.168	2.783	1.232	1.524	0.616	0.739
$2 \rightarrow 0$	5.503	6.491	3.720	4.333	2.820	3.201	1.990	2.097
$5 \rightarrow 0$	2.220	2.374	0.954	0.972	0.564	0.590	0.267	0.278
$10 \rightarrow 0$	–	–	0.003	0.002	0.003	0.003	0.001	0.001
$2 \rightarrow 1$	10.454	14.127	4.639	5.648	2.675	3.183	1.353	1.561
$3 \rightarrow 1$	9.820	10.096	6.650	7.133	5.011	5.371	3.572	3.629
$6 \rightarrow 1$	6.638	6.641	2.851	2.782	1.600	1.582	0.755	0.755
$10 \rightarrow 1$	–	–	1.897	1.868	1.389	1.210	0.588	0.540
$6 \rightarrow 5$	24.827	28.570	10.228	11.149	6.368	6.528	3.027	3.149
$7 \rightarrow 5$	21.248	19.347	9.186	8.847	6.617	6.590	4.940	4.822
$10 \rightarrow 5$	–	–	6.155	6.164	4.064	3.960	2.073	1.944
$11 \rightarrow 10$	–	–	13.367	13.934	6.628	6.997	3.684	3.651
$12 \rightarrow 10$	–	–	14.857	13.723	7.745	7.069	5.502	5.359
$15 \rightarrow 10$	–	–	30.700	31.415	4.887	4.831	2.417	2.289

considered (1000 cm^{-1}), the rotational basis extends to $N = 35$ and 32, respectively, for the AlCN–He and AlNC–He calculations. For MgCN–He and MgNC–He calculations, we extended the rotational basis sufficiently to ensure convergence of the rotational cross-sections for $N, N' \leq 40$ in order to correctly perform the summation over L in equations (4) and (5) leading to converged rate coefficients between fine structure levels with $N, N' \leq 20$. At the largest total energy considered (1000 cm^{-1}), the rotational basis extends to $N = 53$ and 51, respectively, for the MgCN–He and MgNC–He calculations.

4 RESULTS

The CS approach is expected to give accurate results at high energies and for transitions between high rotational levels for a heavy system like X-CN/NC molecules. However, errors can arise whenever weak collisions at a large impact parameter make a significant contribution, as will occur at low energies or for transitions between closely spaced levels. These errors will affect, predominately, the calculated rate coefficients only at low kinetic temperatures ($T <$ 20–30 K).

In order to check the accuracy of the CS calculations compared to the pure CC approach, we show in Table 1 the typical energy dependence of the collisional de-excitation cross-sections obtained from CS and CC calculations for the AlNC–He calculations.

It is found that the CS approach can lead to inaccuracies of 10–30 per cent for low total energy cross-sections ($<$20 cm^{-1}), but agreement improves between CC and CS cross-sections when the energy is greater than 50 cm^{-1}. Hence, the rate coefficients obtained from CS results are expected to be accurate for the temperature range considered in this work. The CS approach is also expected to be accurate for AlCN–He, MgCN–He and MgNC–He collisional systems since both the PES and rotational structure of these systems are similar to those of AlNC–He collisional systems.

4.1 AlCN/AlNC

Fig. 4 illustrates the typical energy dependence of the collisional de-excitation cross-sections obtained from the present CS calculations for a few selected rotational levels.

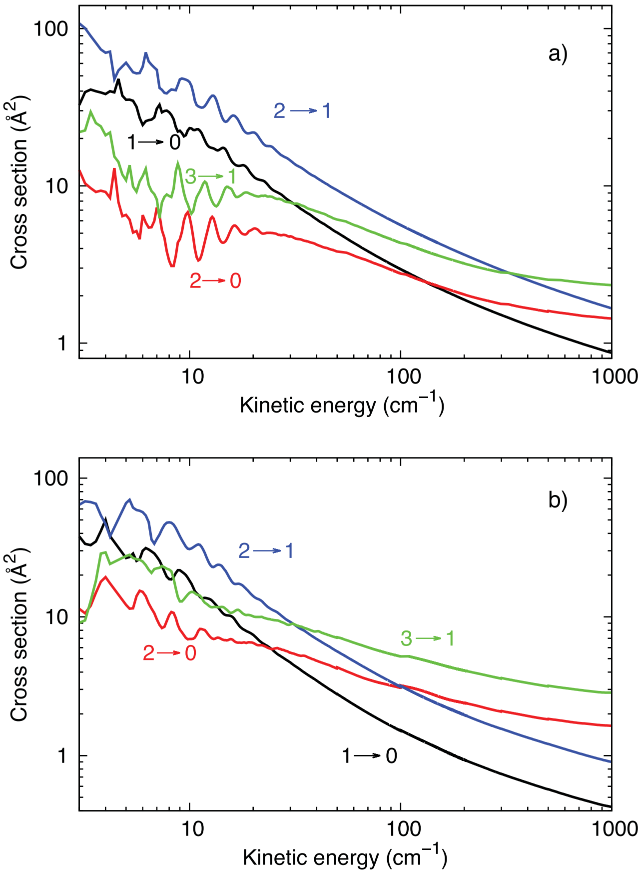

Figure 4. (a) Typical rotational de-excitation CS cross-sections for the AlCN molecules in collision with He as a function of the collision energy. (b) The same for AlNC molecules.

The de-excitation cross-sections are almost decreasing functions of the energy. For collision energies below 50 cm^{-1}, many resonances are found. These are a consequence of the quasi-bound states arising from tunnelling through the centrifugal energy barrier (shape resonances), or from the presence of an attractive potential well that allows the He atom to be temporarily trapped into the well

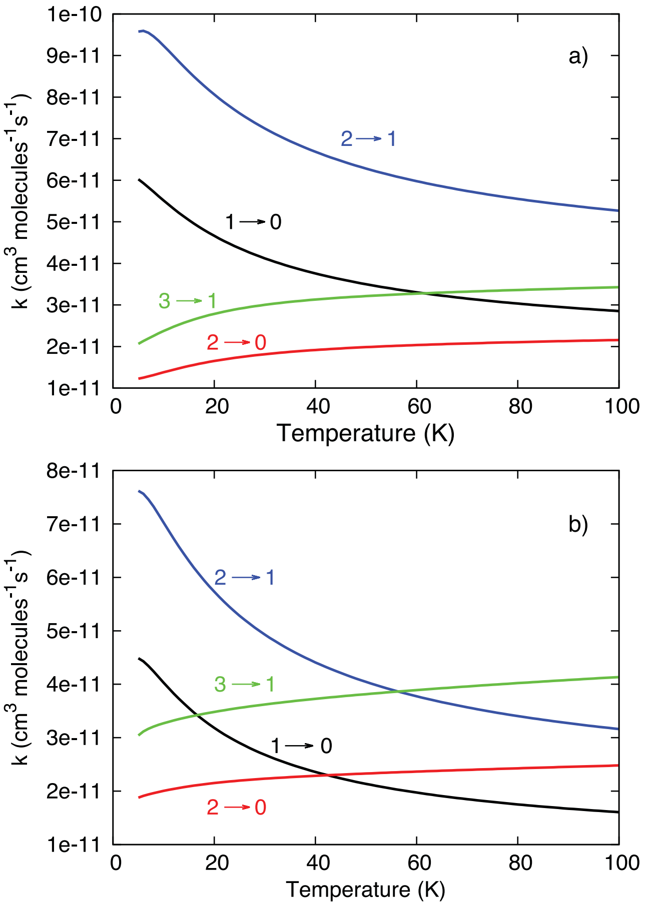

Figure 5. (a) Typical rate coefficients for the AlCN molecules in collision with He as a function of the temperature. (b) The same for AlNC molecules.

and hence quasi-bound states to be formed (Feshbach resonances) before the complex dissociates (Smith, Malik & Secrest 1979).

We obtained, by energy averaging, de-excitation rate coefficients for the first 26 ($N = 0{-}25$) rotational levels of AlCN and AlNC, from the CS cross-sections. The representative variation with temperature is illustrated in Fig. 5.

This complete set of (de)excitation rate coefficients is available online from the LAMDA [1] and BASECOL[2] websites.

Fig. 6 shows the AlCN–He and AlNC–He de-excitation rate coefficients from the $N = 10$ level at 10 and 100 K.

On the whole, the AlCN and AlNC rate coefficients are of the same order of magnitude. This is not really surprising since both the rotational structure of the two molecules and their interaction potential with He are about the same for the two colliding systems.

However, one can see that differences exist between the AlCN–He and AlNC–He rate coefficients especially at low temperature. The AlCN–He collisional systems present a stronger propensity in favour of transitions with odd ΔN than the AlNC–He systems for transitions with small ΔN.

The propensity rules seen in favour of transitions with odd ΔN are due to the shape of the PESs. Indeed, PES with large odd anisotropy, such as the AlCN–He and AlNC–He PES [see Fig. (1)], will favour transitions with odd ΔN (McCurdy & Miller 1977). However, the odd anisotropy of the AlCN–He PES is larger than that of the AlNC–He PES for a distance R between 7 and 10 bohr (where the collision takes place). That explains the stronger propensity in favour of transitions with odd ΔN in the case of AlCN–He collisions than in the case of AlNC–He collisions at low temperature.

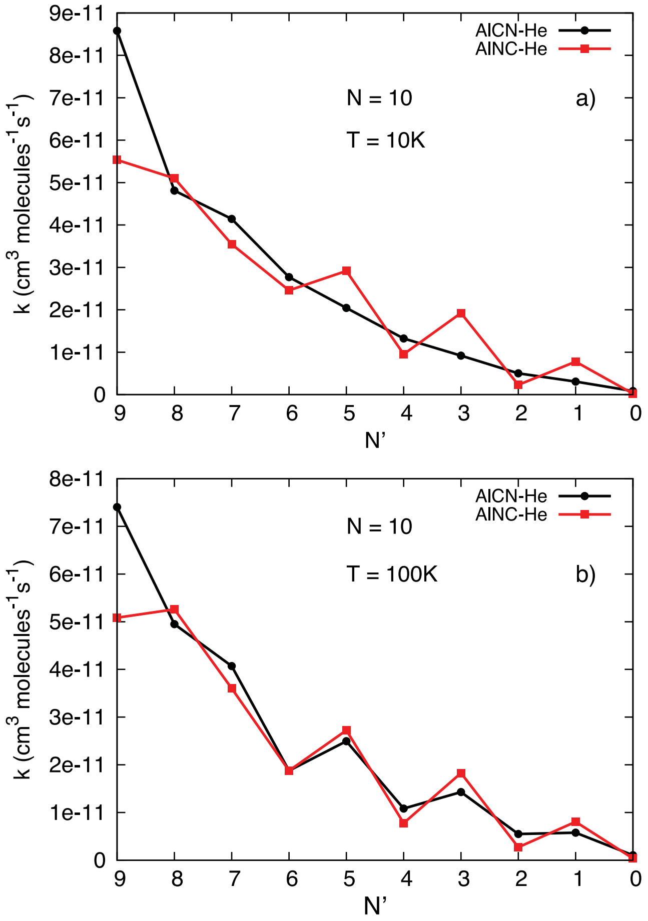

Figure 6. AlCN–He and AlNC–He de-excitation rate coefficients from the $N = 10$ at 10 K (upper panel) and 100 K (lower panel).

At higher temperatures, both systems present the same propensity rules except for the $\Delta N = 1$ transitions that are significantly larger in the case of AlCN–He collisions than in the case of AlNC–He collisions.

4.2 MgCN/MgNC

Elastic and inelastic cross-sections rate coefficients between rotational levels (i.e. without including fine structure) of MgCN/MgNC were computed using the CS approach. The shape and the energy variation of the cross-sections are similar to the one obtained for the AlCN–He and AlNC–He collisional systems. The fine structure rate coefficients were obtained from the rotational rate coefficients using the procedure described above.

The typical variation with temperature of these MgCN–He and MgNC–He state-to-state rate coefficients for $\Delta j = \Delta N$ and $\Delta j \neq \Delta N$ transitions is illustrated in Figs 7 and 8.

This complete set of (de)excitation rate coefficients is available online from the LAMDA and BASECOL websites.

We observe a propensity for $\Delta j = \Delta N$ transitions. The same propensity rule was previously obtained for CN–He (Lique et al. 2010). This behaviour, predicted theoretically (Alexander, Smedley

---

[1] http://www.strw.leidenuniv.nl/moldata/

[2] http://basecol.obspm.fr/

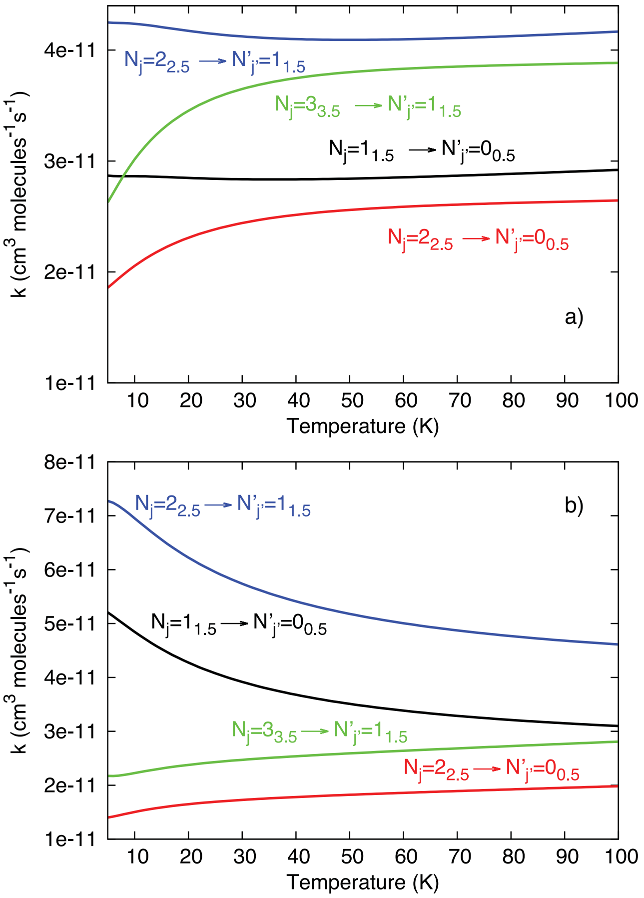

Figure 7. (a) Typical rate coefficients for the MgCN molecules in collision with He as a function of the temperature for $\Delta j = \Delta N$ transitions. (b) The same for MgNC molecules.

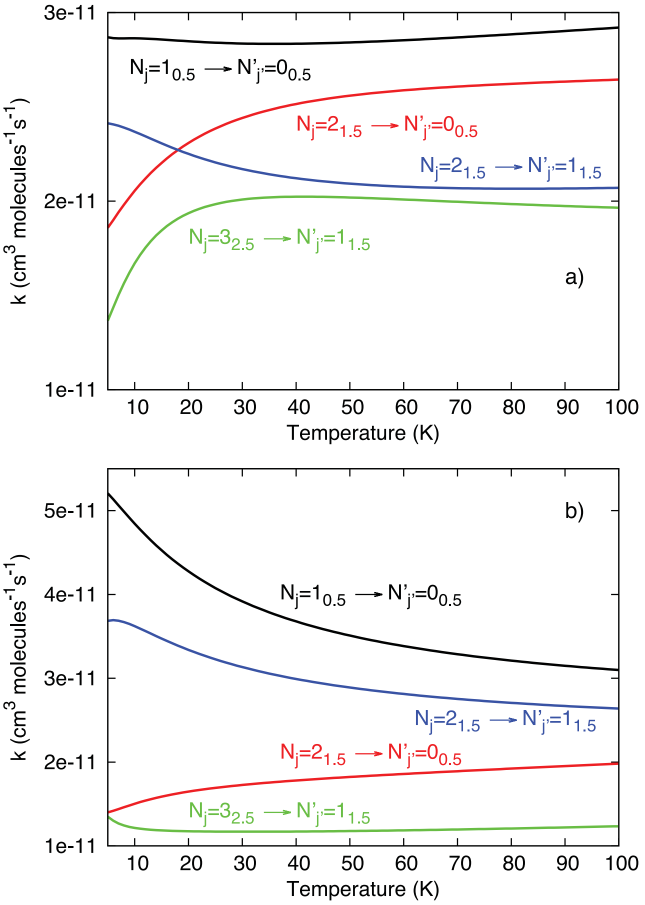

Figure 8. (a) Typical rate coefficients for the MgCN molecules in collision with He as a function of the temperature for $\Delta j \neq \Delta N$ transitions. (b) The same for MgNC molecules.

& Corey 1986), is a general feature of collisions of molecules in the $^{2S+1}\Sigma$ electronic state, as shown previously for the O_2–He collisions (Lique 2010) or SO–H_2 (Lique et al. 2007).

In order to compare MgCN–He and MgNC–He rate coefficients, we summed the fine structure resolved rate coefficients over the final state spin-projection quantum numbers. Fig. 9 shows the MgCN–He and MgNC–He de-excitation rate coefficients from the $N = 10$ level at 10 and 100 K.

As found for AlCN and AlNC rate coefficients, on the overall, the MgCN and MgNC rate coefficients seem to have the same order of magnitude. The explanation is the same as for the AlCN–He and AlNC–He collisional systems.

However, the propensity rules seen in the two sets of rate coefficients are different. The MgCN–He rate coefficients present a propensity in favour of transitions with even ΔN, whereas the MgNC–He rate coefficients present a propensity in favour of transitions with odd ΔN. The differences survive when the temperature increases.

As for the AlCN and AlNC rate coefficients, the propensity rules seen in favour of transitions with odd or even ΔN are due to the shape of the PESs. Indeed, near-homonuclear symmetry of the PES, such as the MgCN–He PES, will favour transitions with even ΔN. In contrast, the MgNC–He PES for which odd anisotropy is large will favour transitions with odd ΔN. Nevertheless, the discussion of the propensity rules coming from the shape of the PES is not as clear as for AlCN/AlNC isomers. Indeed, the V_1 and V_3 radial coefficients of the expansion of the PES are deeper in the case of MgCN than in the case of MgNC, and we could expect the opposite behaviour. However, for these complexes, the approach of the He atom to the Mg atom is highly repulsive, and at low collisional energies, the collision takes place at large distances R where the V_1 radial coefficient of the expansion of the PES is larger in magnitude than the V_2 radial coefficients for the MgNC–He complex contrary to the MgCN–He complex that shows the opposite behaviour.

5 DISCUSSION AND CONCLUSION

We have used quantum scattering calculations to investigate rotational energy transfer in collisions of AlCN, AlNC, MgCN and MgNC molecules with He atoms. The calculations are based on highly accurate 2D PESs obtained using state-of-the-art electronic structure methods. Rate coefficients for transitions involving the lowest 26 levels of the Al compounds and the lowest 41 fine structure levels of the Mg compounds were determined for temperatures ranging from 5 to 100 K.

However, in the present study, the hyperfine structure of the cyanide/isocyanide molecules has been neglected whereas it is presently observed by the actual telescope. Collisional rate coefficients when the hyperfine structure is considered can be easily obtained from the present results using the standard assumption that the rate coefficients will be proportional to the degeneracy

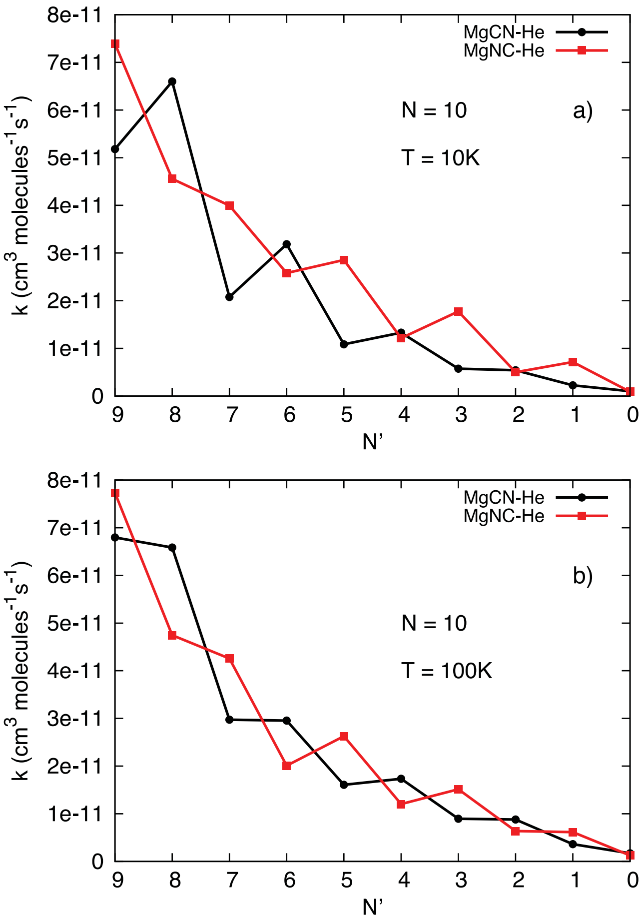

Figure 9. MgCN–He and MgNC–He de-excitation rate coefficients from the $N = 10$ at 10 K (upper panel) and 100 K (lower panel).

of the final hyperfine state, or employing the IOS scaling method (Faure & Lique 2012).

In addition, the great abundance of H_2 in the ISM makes this molecule the primary collision partner for any other species. It is generally assumed (Lique et al. 2008) that rate coefficients with He can provide a good estimate of rate coefficients for collision with para-$H_2(j = 0)$. For very heavy molecules such as the presently studied ones, the He rate coefficients scaled by a factor of 1.4 are expected to provide the correct order of magnitude of the $H_2(j = 0)$ rate coefficients. Therefore, the present results can be considered as a reasonable first estimate of collisional rate coefficients for collisions of AlCN, AlNC, MgCN and MgNC with para-$H_2(j = 0)$.

Propensity rules for odd ΔN were found for both AlCN/AlNC–He systems. In contrast, propensity rules for even ΔN were found in the case of MgCN–He system whereas propensity rules for odd ΔN were found in the case of MgNC–He system.

These different propensity rules seen for the MgCN/MgNC isomers let us predict that the excitation of these molecules in cold molecular clouds will be different and that the abundance ratio of these species cannot be simply obtained by looking at the brightness temperature ratio of the emission lines. Hence, radiative transfer calculations will have to be performed for both molecules using both sets of rate coefficients in order to accurately obtain the relative abundance of the two isomers.

For AlCN/AlNC, the present results suggest that a more intense $\Delta N = 1$ spectral line should be expected for AlCN than for AlNC molecules (considering similar abundance for both AlCN/AlNC isomers) since the magnitude of the $\Delta N = 1$ rate coefficients is larger for the AlCN–He collisional system than for AlNC–He ones and since the dipole moment of AlCN is slightly larger than the one of AlNC. Hence, the present data do not provide explanation to the absence of AlCN observations in molecular clouds and confirm that the AlCN molecule is significantly less abundant than AlNC in the ISM. However, the new rate coefficients could be introduced in radiative transfer modelling and may help to discover the AlCN molecule in molecular clouds by performing accurate excitation calculations of this molecule. Moreover, the new data could be useful for later estimations of the AlCN/AlNC abundance ratio in the ISM.

Finally, the present rate coefficients will enable more accurate estimation of the cyanide/isocyanide abundance in molecular clouds and then clarify the dominant role of cyanide species as metal carriers in circumstellar gas. Accurate determination of MgNC abundance will also be useful for the understanding of anion chemistry since dissociative attachment of MgNC has been suggested as a way to form the CN^- anion that has been recently observed in IRC+10216 (Agúndez et al. 2010).

ACKNOWLEDGEMENTS

This research was supported by the CNRS national programme ‘Physique et Chimie du Milieu Interstellaire’. MHV acknowledges the french embassy of Cuba for financial support. We thank the CPER Haute-Normandie/CNRT/Energie, Electronique, Matériaux. JK acknowledges financial support through the US National Science Foundation (Grant no. CHE-1213332 to M. H. Alexander).

REFERENCES

Agúndez M. et al., 2010, A&A, 517, 1
Alexander M., Smedley J. E., Corey G. C., 1986, J. Chem. Phys., 84, 3049
Arthurs A. M., Dalgarno A., 1960, Proc. R. Soc. Lond. Ser. A, 256, 540
Boys S. F., Bernardi F., 1970, Mol. Phys., 19, 553
Corey G. C., McCourt F. R., 1983, J. Phys. Chem., 87, 2723
Cybulski S. M., Toczyłowski R., 1999, J. Chem. Phys., 111, 10520
Dumouchel F., Faure A., Lique F., 2010, MNRAS, 406, 2488
Dumouchel F., Kłos J., Lique F., 2011, Phys. Chemistry Chemical Phys., 13, 8204
Dunning T. H., 1989, J. Chem. Phys., 90, 1007
Faure A., Lique F., 2012, MNRAS, 425, 740
Goldflam R., Kouri D. J., Green S., 1977, J. Chem. Phys., 67, 4149
Guélin M., Lucas R., Cernicharo J., 1993, A&A, 280, L19
Guélin M., Muller S., Cernicharo J., Apponi A. J., McCarthy M. C., Gottlieb C. A., Thaddeus P., 2000, A&A, 363, L9
Guélin M., Muller S., Cernicharo J., McCarthy M. C., Thaddeus P., 2004, A&A, 426, L49
Hampel C., Peterson K. A., Werner H.-J., 1992, Chem. Phys. Lett., 190, 1
Hirota T., Yamamoto S., Mikami H., Ohishi M., 1998, ApJ, 503, 717
Ho T.-S., Rabitz H., 1996, J. Chem. Phys., 104, 2584
Hutson J. M., Green S., 1994, MOLSCAT computer code, version 14, Collaborative Computational Project No. 6, Engineering and Physical Sciences Research Council, UK
Irvine W. M. et al., 1988, ApJ, 334, L107
Kendall R. A., Dunning T. H., Harrison R. J., 1992, J. Chem. Phys., 96, 6796
Knowles P. J., Hampel C., Werner H.-J., 1993, J. Chem. Phys., 99, 5219
Knowles P. J., Hampel C., Werner H.-J., 2000, J. Chem. Phys., 112, 3106
Lique F., 2010, J. Chem. Phys., 132, 044311
Lique F., Spielfiedel A., 2007, A&A, 462, 1179
Lique F., Dubernet M.-L., Spielfiedel A., Feautrier N., 2006, A&A, 450, 399

Lique F., Senent M.-L., Spielfiedel A., Feautrier N., 2007, J. Chem. Phys., 126, 164312

Lique F., Toboła R., Kłos J., Feautrier N., Spielfiedel A., Vincent L. F. M., Chałasiński G., Alexander M. H., 2008, A&A, 478, 567

Lique F., Spielfiedel A., Feautrier N., Schneider I. F., Kłos J., Alexander M. H., 2010, J. Chem. Phys., 132, 024303

McCurdy C. W., Miller W. H., 1977, J. Chem. Phys., 67, 2488

McGuire P., Kouri D. J., 1974, J. Chem. Phys., 60, 463

Neufeld D. A., Green S., 1994, ApJ, 432, 158

Pulliam R. L., Savage C., Agúndez M., Cernicharo J., Guélin M., Ziurys L. M., 2010, ApJ, 725, L181

Sarrasin E., Abdallah D. B., Wernli M., Faure A., Cernicharo J., Lique F., 2010, MNRAS, 404, 518

Schaftenaar G., Noordik J. H., 2000, J. Comput. Aided Mol. Des., 14, 123

Senent M. L., Dumouchel F., Lique F., 2012, MNRAS, 420, 1188 (Paper I)

Smith L. N., Malik D. J., Secrest D., 1979, J. Chem. Phys., 71, 4502

Snyder L. E., Buhl D., 1971, ApJ, 163, L47

Solomon P. M., Jefferts K. B., Penzias A. A., Wilson R. W., 1971, ApJ, 168, L107

Turner B. E., Steimle T. C., Meerts L., 1994, ApJ, 426, L97

Turner B. E., Petrie S., Dunbar R. C., Langston G., 2005, ApJ, 621, 817

Werner H.-J. et al., 2010, MOLPRO, version 2010.1 – a package of ab initio programs

Wernli M., Wiesenfeld L., Faure A., Valiron P., 2007, A&A, 464, 1147

Zack L. N., Halfen D. T., Ziurys L. M., 2011, ApJ, 733, L36

Ziurys L. M., Apponi A. J., Guélin M., Cernicharo J., 1995, ApJ, 445, L47

Ziurys L. M., Savage C., Highberger J. L., Apponi A. J., Guélin M., Cernicharo J., 2002, ApJ, 564, L45

This paper has been typeset from a TEX/LATEX file prepared by the author.

Chapter 4

Rotational (de-)excitation of SiCN/SiNC in collisions with He

Contents

The astrophysical observations suggest that the SiCN and SiNC radicals have similar abundances in the ISM. However, the abundance estimations have not been determined through detailed radiative transfer calculations due to the absence of molecular data. In this chapter, we compute the rate coefficients for the SiCN-He and SiNC-He collisional systems. We present the coupled states approach for collisions of $^2\Pi$ molecules and a structureless particle. Finaly, we will present and discuss the results of the CS calculations in the last section.

4.1 Rotational spectroscopy of SiCN and SiNC

In Fig. 4.1, we show structural and spectroscopic parameters corresponding to the SiCN and SiNC isomers in their electronic ground state. The parameters have been taken from the paper of Senent et. al. (2012) [71]. SiCN and its metastable isomer SiNC have linear geometry configurations. We can see that the dipole moments of both molecules are almost the same. Using highly correlated *ab initio* calculations Richardson et al. [113] have computed an isomerization barrier of 7340 cm^{-1} for these isomers. This barrier restricts the intertransformation at low temperatures.

The fundamental frequencies, namely, the C–N stretching, the SiCN(or SiNC) bending and the Si–C (or N–Si) stretching modes are 2116 cm^{-1}, 283 cm^{-1} and 569 cm^{-1} for SiCN and 1992 cm^{-1}, 234 cm^{-1} and 645 cm^{-1} for SiNC [113]. All these frequencies are above 100 K. We can then consider these molecules like rigid rotors when studying the collisional excitation. Therefore, the intermolecular bond distances of the Si-CN and Si-NC were frozen at their experimental equilibrium values.

In a Hund's case (a) representation, the wave functions for a diatomic molecule in a $^2\Pi$ electronic state can be written as a product of a wave function describing the electronic motion of the rotationaless diatomic multiplied by a wave function describing the rotational motion,

$$|jm\Omega\Lambda S\Sigma\rangle = |jm\Omega\rangle|\Lambda S\Sigma\rangle \tag{4.1}$$

where j represents the total angular momentum; m and Ω denote the projection of j along the space- and molecule-fixed axes, respectively; S denotes the spin angular momentum with projection Σ along molecular axis and Λ is the projection of the electronic orbital angular momentum along the molecular axis. For molecules in a

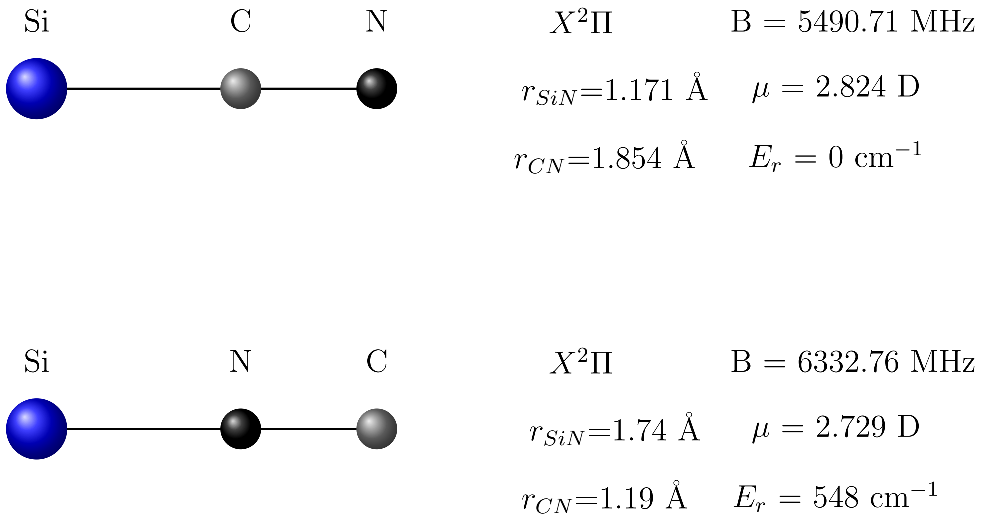

Figure 4.1: Intermolecular bond distances, rotational constant (B), dipole moment (μ) and relative energy (E_r) of SiCN–SiNC isomers.

$^2\Pi$ electronic state, $\Lambda = \pm 1$ and $\Sigma = \pm 1/2$. The molecule splits into two spin-orbit manifolds, one with $|\Omega| = 1/2$ and the other one with $|\Omega| = 3/2$.

It will be convenient to use the definite parity states defined by

$$\begin{aligned} |jm\bar{\Omega}\epsilon\rangle \equiv |\Lambda\epsilon\rangle =& 2^{-\frac{1}{2}}(|jm\bar{\Omega}\rangle|\Lambda = 1, \Sigma = \bar{\Omega} - 1\rangle \\ &+ \epsilon jm, -\bar{\Omega}\rangle|\Lambda = -1, \Sigma = -\bar{\Omega} + 1\rangle) \end{aligned} \tag{4.2}$$

where $\bar{\Omega} \equiv |\Omega|$, and where $\epsilon \pm 1$ refers to the parity of the wave function with respect to inversion of the space-fixed axis system, so that

$$i_{sf}\,|jm\bar{\Omega}\epsilon\rangle = \epsilon(-1)^{j+S}\,|jm\bar{\Omega}\epsilon\rangle \tag{4.3}$$

where i_{sf} is the inversion operator. In the spectroscopic nomenclature, the $\epsilon = +1$ levels are designated as **f** and the $\epsilon = -1$ levels as **e**. The rotational wave function

$|jm\Omega\rangle$ can be written as rotational matrix elements,

$$|jm\Omega\rangle = [(2j+1)/8\pi^2]^{1/2} D^{j*}_{m\Omega}(\alpha\beta\gamma) \tag{4.4}$$

where $(\alpha\beta\gamma)$ are the Euler angles that describe the orientation of the molecule in the fixed space.

The rotational energies can be written as

$$\begin{aligned} E_{j,\bar{\Omega}=3/2,\epsilon} = &\frac{1}{2}A + B[j(j+1) - \frac{7}{4}] + \\ &\frac{1}{2}\epsilon(B/A)(2q + pB/A)(j-1/2)(j+1/2)(j+3/2) \end{aligned} \tag{4.5}$$

and

$$E_{j,\bar{\Omega}=1/2,\epsilon} = -\frac{1}{2}A + B[j(j+1) + \frac{1}{4}] + \frac{1}{2}\epsilon p(j+\frac{1}{2}) \tag{4.6}$$

In the last equations A is the spin-orbital constant, and B the rotational constant. The last terms on the right hand side of these equations describe the splitting between the parity levels, which is designated as Λ doubling. This splitting is characterized by the parameters p and q.

The parameters A, p and q are 2121930 MHz, 2068 MHz and 0.869 MHz for SiNC and 1760530 MHz, 7.03 MHz and 0.869 MHz for SiNC [104]. The first rotational energy levels of these molecules can be found in the last section of this chapter.

4.2 Collisional excitation of $^2\Pi$ molecules

The orbital motion of the atom about the center of mass of the molecule is described by the spherical harmonics $|lm_l\rangle$. The complete wavefunction for the atom-molecule system can be expressed as a linear combination of products of $|lm_l\rangle$ functions and the $|jm\bar{\Omega}\epsilon\rangle$ functions.

$$\begin{aligned} |jm\bar{\Omega}\epsilon lm_l\rangle =& 2^{-\frac{1}{2}}\ |lm_l\rangle(|jm\bar{\Omega}\rangle|\Lambda=1,\Sigma=\bar{\Omega}-1\rangle \\ &+\epsilon|jm,-\bar{\Omega}\rangle|\Lambda=-1,\Sigma=-\bar{\Omega}+1\rangle) \end{aligned} \tag{4.7}$$

As explained in Chapter 2, it will be convenient to expand the eigenfunctions of the total Hamiltonian in terms of eigenfunctions of the total angular momentum J and its projection M defined by

$$|jl\bar{\Omega}\epsilon JM\rangle = \sum_{mm_l}(jmlm_l|jlJM)|jm\bar{\Omega}\epsilon lm_l\rangle \tag{4.8}$$

where $(...|...)$ is a Clebsch-Gordan coefficient. In a total-J representation built from the definite-Ω molecular basis, wave functions for the atom-molecule collision system can be written as

$$|jl\bar{\Omega}\Lambda\Sigma JM\rangle = |jl\bar{\Omega}\epsilon JM\rangle\,|\Lambda\Sigma\rangle \tag{4.9}$$

As in the initial formulation of Arthurs and Dalgarno [17], we can expand the wave function for the atom-molecule in terms of the $|jl\bar{\Omega}\epsilon\Lambda\Sigma JM\rangle$. The radial functions are solutions of a set of coupled differential equations

$$\left[\frac{d^2}{dR^2}-\frac{l'(l'+1)}{R^2}+k^2_{J\bar{\Omega}\epsilon}\right]U^J_{\gamma'}(R) = 2\mu\sum_{\gamma''}\langle\gamma''JM|V|\gamma'JM\rangle U^J_{\gamma''}(R) \tag{4.10}$$

where $\gamma = (jl\bar{\Omega}\epsilon\Lambda\Sigma)$ and $k^2_{j\bar{\Omega}\epsilon} = E - E_{j\bar{\Omega}}\epsilon$. In Eq. 4.10 the potential matrix elements are given by

$$\langle\gamma'JM|\,V_{el}\,|\gamma JM\rangle = \langle j'l'\Omega'JM|\,V_{\Lambda'\Lambda}(R,\theta)\,|jl\Omega JM\rangle \tag{4.11}$$

In the last expression, the terms $V_{\Lambda',\Lambda}$ denote the diabatic matrix elements

$$V_{\Lambda',\Lambda}(R,\theta) = \delta_{\Sigma'\Sigma}\,\langle\Lambda'\Sigma'|\,V\,|\Lambda\Sigma\rangle = \sum_{\mathcal{L}}V_{\mathcal{L},\Lambda'-\Lambda}(R)d^{\mathcal{L}}_{\Lambda'-\Lambda}(\theta) \tag{4.12}$$

where the electronic basis $|\Lambda\Sigma\rangle$ are components of the Π state with the projection of the electronic orbital angular momentum $\Lambda = \pm 1$.

Now, it is convenient to introduce the definite symmetry molecular electronic wavefunctions in order to show the connection between the *adiabatic* potentials of A' and A'' symmetry and the $V_{\Lambda',\Lambda}$ terms.

$$|\Lambda\eta\rangle = 2^{-1/2}[|\Lambda\rangle + \eta\,|-\Lambda\rangle] \tag{4.13}$$

where $\eta = \pm 1$. Since the Euler angle γ is chosen to be zero in Eq. 4.4, under reflection in the molecular frame xz plane these wave functions behave as

$$\sigma(xz)\,|\Lambda\eta\rangle = (-1)^{\Lambda}\eta\,|\Lambda\eta\rangle \tag{4.14}$$

For a Π state the $\eta = +1$ wave function is antisymmetric with respect to reflection in the triatomic plane (A'' symmetry in the reducded C_s symmetry group) while the $\eta = -1$ wave function is symmetric (A' symmetric). Since the radial expansion coefficients in Eq. 4.12 satisfy the symmetry relation

$$V_{\mathcal{L},\Lambda'-\Lambda}(R) = V_{\mathcal{L},-\Lambda'+\Lambda}(R) \tag{4.15}$$

the electronic potential matrix elements are diagonal in the adiabatic $|\Lambda\eta\rangle$ electronic basis. The connection between the *adiabatic* potentials of A' and A'' symmetry and the *diabatic* potentials is

$$\begin{aligned} V_{A'} &= \langle\Lambda\eta|\,V\,|\Lambda\eta\rangle_{\eta=1} = V_{1,1}(R,\theta) - V_{1,-1}(R,\theta) \\ V_{A''} &= \langle\Lambda\eta|\,V\,|\Lambda\eta\rangle_{\eta=-1} = V_{1,1}(R,\theta) + V_{1,-1}(R,\theta) \end{aligned} \tag{4.16}$$

A general expression for the coupling potential have been derived by Alexander [114]. Expanding the Eq. 4.11 one can arrive to the following expression:

$$\begin{aligned}
&\langle J'l'\bar{\Omega}'\epsilon' JM|\, V\, |Jl\bar{\Omega}\epsilon JM\rangle = \sum_{MM_LM'M_L'} \frac{1}{2}(jmlm_l|jlJM)(j'm'l'm_l'|j'l'JM) \\
&\times[\delta_{\bar{\Omega}\bar{\Omega}'}(\langle l'm_l'j'm'\bar{\Omega}|\, V_{1,1}\, |lm_ljm\bar{\Omega}\rangle + \epsilon\epsilon' \langle l'm_l'j'm',-\bar{\Omega}|\, V_{-1,-1}\, |lm_ljm,-\bar{\Omega}\rangle) \\
&+(1-\delta_{\bar{\Omega}\bar{\Omega}'})(\epsilon \langle l'm_l'j'm',\bar{\Omega}'|\, V_{1,-1}\, |lm_ljm,-\bar{\Omega}\rangle + \\
&\epsilon' \langle l'm_l'j'm',-\bar{\Omega}'|\, V_{-1,1}\, |lm_ljm,\bar{\Omega}\rangle)]
\end{aligned} \tag{4.17}$$

Eq.4.17 can be further simplified after some angular momentum algebra. In practice, the potential matrix elements are computed using the following expression:

$$\begin{aligned}
&\langle J'l'\bar{\Omega}'\epsilon' JM|\, V\, |Jl\bar{\Omega}\epsilon JM\rangle = (-1)^{J+j'+j-\bar{\Omega}}[(2j+1)(2j'+1)(2l+1)(2l'+1)]^{\frac{1}{2}} \\
&\times \sum_{\mathcal{L}} \frac{1}{2}[1-\epsilon\epsilon'(-1)^{j+j'+\mathcal{L}}] \begin{pmatrix} l' & \mathcal{L} & l \\ 0 & 0 & 0 \end{pmatrix}^2 \begin{Bmatrix} j' & l' & J \\ l & j & \mathcal{L} \end{Bmatrix} \\
&\times \left[\delta_{\bar{\Omega}\bar{\Omega}'} V_{\mathcal{L},0}(R) \begin{pmatrix} j' & \mathcal{L} & j \\ -\bar{\Omega} & 0 & \bar{\Omega} \end{pmatrix} + \epsilon(1-\delta_{\Omega\Omega'})V_{\mathcal{L},2}(R) \begin{pmatrix} j' & \mathcal{L} & j \\ -\bar{\Omega}' & 2 & -\bar{\Omega} \end{pmatrix}\right]
\end{aligned} \tag{4.18}$$

where $V_{\mathcal{L},0}(R)$ are equivalent to terms which would arise if the average of the A' and A'' atom-molecule potential surfaces were fit to an expansion in Legendre polynomials. Similarly the $V_{\mathcal{L},2}(R)$ terms would arise if one-half the difference between the the A' and A'' surfaces were fit to an expansion in associated Legendre polynomials. Therefore, in the scattering calculations it is more appropriate to use the average

$$V_{sum} = \frac{1}{2}(V_{A''} + V_{A'}) \tag{4.19}$$

and half-difference

$$V_{diff} = \frac{1}{2}(V_{A''} - V_{A'}) \tag{4.20}$$

of the two potential energy surfaces. It is the V_{sum} which is responsible for inducing inelastic collisions within a given spin-orbital manifold, and V_{dif} which induce inelastic collisions between the two spin-orbital manifold.

The solutions of Eq. 4.10 are subject to the boundary conditions,

$$\begin{aligned}&\underset{R\to 0}{lim}\, U_{\gamma'}^{JM\gamma}(R) = \delta_{\gamma,\gamma'} exp[-i(k_{j\bar{\Omega}\epsilon}R - l\pi/2)]\\&-(k_{j'\bar{\Omega}'\epsilon'}/k_{j\bar{\Omega}\epsilon})^{\frac{1}{2}} \times S^J(\gamma;\gamma')exp[i(k_{j'\bar{\Omega}'\epsilon'} - l'\pi/2)]\end{aligned} \tag{4.21}$$

The scattering amplitude can be constructed as in the Arthurs-Dalgarno [17] formulation for collisions involving $^1\Sigma$ diatomics. Then, the integral cross section for the $j\bar{\Omega}\epsilon \to j'\bar{\Omega}'\epsilon'$ transition, is given by the expression:

$$\sigma(j\bar{\Omega}\epsilon \to j'\bar{\Omega}'\epsilon') = \frac{\pi}{(2j+1)\; k^2_{j\bar{\Omega}\epsilon}} \sum_J (2J+1) \sum_{ll'} |T^J(jl\bar{\Omega}\epsilon\;; j'l'\bar{\Omega}'\epsilon')|^2 \tag{4.22}$$

The main difficuly of solving CC calculations is related to the large number of coupled equations which must be considered. The problem is further complicated owing to the presence of the spin-orbit components.

In order to simplify the computations of the cross sections, we will use in this chapter the coupled states approximation. This approximation replaces the centrifugal terms in Eq. 4.10 by an average value $\bar{L}(\bar{L}+1)/R^2$. The potential matrix can be block diagonalized by a transformation to a new basis defined by

$$|j\bar{\Omega}\epsilon JM\rangle = \sum_L B_L^{jJ}\, |jL\bar{\Omega}\epsilon JM\rangle \tag{4.23}$$

The potential matrix in this new basis becomes,

$$\langle j'\bar{\Omega}'\epsilon' JM|\, V\, |j\bar{\Omega}\epsilon JM\rangle = \sum_{LL'} B_{L'}^{j'J} B_L^{jJ}\, \langle j'L'\bar{\Omega}\epsilon' JM|\, V\, |jL\bar{\Omega}\epsilon JM\rangle \tag{4.24}$$

After some angular momentum algebra, the last expression takes the following form [107],

$$\begin{aligned}
&\langle j'\bar{\Omega}\epsilon' JM|\, V\, |J\bar{\Omega}\epsilon JM\rangle = (-1)^{1-\bar{\Omega}}[(2j+1)(2j'+1)]^{1/2} \times \\
&\sum_{\mathcal{L}} \frac{1}{2}[1-\epsilon\epsilon'(-1)^{j+j'+\mathcal{L}}] \begin{pmatrix} j' & \mathcal{L} & j \\ 0 & 0 & 0 \end{pmatrix} \times \\
&\left[\delta_{\bar{\Omega}\bar{\Omega}'} V_{\mathcal{L},0}(R) \begin{pmatrix} j' & \mathcal{L} & j \\ -\bar{\Omega} & 0 & \bar{\Omega} \end{pmatrix} - \epsilon(1-\delta_{\bar{\Omega}\bar{\Omega}'}) V_{\mathcal{L},2}(R) \begin{pmatrix} j' & \mathcal{L} & j \\ -\bar{\Omega} & 2 & \bar{\Omega} \end{pmatrix}\right]
\end{aligned} \tag{4.25}$$

where the indices, J and M have been dropped. Using this approximation, Eq. 4.10 takes the form,

$$\left[\frac{d^2}{dR^2} - \frac{\bar{L}(\bar{L}+1)}{R^2} + k^2_{j\bar{\Omega}\epsilon}\right] U^{\bar{L}\nu j\bar{\Omega}\epsilon}_{j'\bar{\Omega}'\epsilon'}(R) = 2\mu \sum_{j''\epsilon''\bar{\Omega}''} \langle j'\nu\bar{\Omega}'\epsilon'|V|j''\nu\bar{\Omega}''\epsilon''\rangle U^{\bar{L}\nu j\bar{\Omega}\epsilon}_{j''\bar{\Omega}''\epsilon''}(R) \tag{4.26}$$

In the last expression, the radial functions are subject to boundary conditions:

$$\begin{aligned}
&\lim_{R\to\infty} U^{\bar{L}\nu j\bar{\Omega}\epsilon}_{j'\bar{\Omega}'\epsilon'} = \delta_{jj'}\delta_{\bar{\Omega}\bar{\Omega}'}\delta_{\epsilon\epsilon'} exp[-i(k_{j\bar{\Omega}\epsilon}R - \bar{L}\pi/2)] \\
&-(k_{j'\bar{\Omega}'\epsilon'}/k_{j\bar{\Omega}}\epsilon)^{1/2} S^{\bar{L}}(j\bar{\Omega}\epsilon; j'\bar{\Omega}'\epsilon') exp[i(k_{j'\bar{\Omega}'\epsilon'}R - \bar{L}\pi/2)]
\end{aligned} \tag{4.27}$$

that defines the S and T matrices. Finally, the expression of the integral cross section is given in terms of the T matrix elements by the expression,

$$\sigma(j\bar{\Omega}\epsilon \to j'\bar{\Omega}'\epsilon') = \frac{\pi}{(2j+1)k^2_{j\bar{\Omega}\epsilon}} \sum_{\bar{L}} (2\bar{L}+1) \sum_{\nu} |T^{\bar{L}\nu}(j\bar{\Omega}\epsilon; j'\bar{\Omega}\epsilon')|^2 \tag{4.28}$$

4.3 Results

Mon. Not. R. Astron. Soc. **000**, 1–10 (2015) Printed 16 February 2015 (MN LaTeX style file v2.2)

Cyanides/isocyanides abundances in the interstellar medium - IV. Temperature dependance of SiCN / SiNC rate coefficients

M. Hernández Vera[1,2], F. Lique[1⋆], J. Kłos[3], F. Dumouchel[1] and J. Rubayo Soneira[2]
[1] *LOMC - UMR 6294, CNRS-Université du Havre, 25 rue Philippe Lebon, BP 540, 76058, Le Havre, France*
[2] *Instituto Superior de Tecnologías y Ciencias Aplicadas, Quinta de Los Molinos, Plaza, La Habana 10600, Cuba*
[3] *Department of Chemistry and Biochemistry, University of Maryland, College Park, MD 20742-2021, USA*

16 February 2015

ABSTRACT

Modeling molecular abundances in the interstellar medium requires accurate molecular data. Then, accurate determination of collisional rate coefficients is an essential step in order to estimate the cyanides/isocyanides abundances in interstellar clouds. In this work, we have carried out calculations of rate coefficients for the rotational excitation of SiCN and SiNC molecules in collision with He. The calculations are based on new two-dimensional potential energy surfaces obtained from highly-correlated *ab initio* calculations. Coupled-States quantum approximation was used to obtain pure rotational (de-)excitation cross-sections of SiCN and SiNC by He. The fine structure and lambda doublet splitting of SiCN and SiNC levels was taken into account explicitly. Rate coefficients for transitions among the first 92 rotational levels of SiCN and SiNC were calculated for the temperature range between 5 and 100 K. Moderate differences between the rate coefficients of both isomers were observed. These differences confirm that specific calculations have to be performed for each isomer in order to obtain the necessary level of detail. The new rate coefficients should induce important consequences on the determination of SiCN and SiNC abundance in the interstellar medium. In particular, we anticipate the abundance of SiCN and SiNC will no longer be the same.

Key words: Molecular data, Molecular processes, scattering.

1 INTRODUCTION

Cyanides molecules are ubiquitous in the interstellar medium (ISM) (Snyder & Buhl 1971; Guelin et al. 1986; Ziurys et al. 1995, 2002; Guélin et al. 2000, 2004; Pulliam et al. 2010; Zack et al. 2011). Cyanide species are the most common metal-containing molecules in circumstellar gas Dunbar & Petrie (2002) and the hydrogen cyanide (HCN) is one of the most abundant interstellar molecules that is frequently used as tracer of interstellar regions such as dark cold clouds (e.g. Irvine & Schloerb 1984), circumstellar envelopes, (e.g. Cernicharo et al. 1996), cool carbon stars (Harris et al. 2003) or comets (e.g. Lis et al. 1997).

Usually, cyanide compounds present isomerism. Frequently, large abundances correspond to the most stable isomers as it occurs for MgNC. MgCN is less stable than MgNC by about 650 cm^{-1} and the MgNC/MgCN abundance ratio has been estimated to be $\simeq 20$ by Ziurys et al. (1995). Nevertheless, the ratio is not systematically governed by the relative stabilities of the two isomers. Thus, in contrast to purely thermochemical considerations (HNC is less stable than HCN by about 0.6 eV Bowman et al. (1993)), the abundance of HNC in space is large: the HNC/HCN abundance ratio is estimated to be around unity in dark cold clouds Sarrasin et al. (2010). Another pair of isomers that escape to this trend are the SiCN and SiNC molecules that seems to be in similar abundance (Guélin et al. 2004) whereas SiNC is less stable than SiCN by about 550 cm^{-1} ((Senent et al. 2012), hereafter Paper I).

Molecular abundances in the ISM have to be understood in terms of molecular stabilities, reaction probabilities and radiative and collisional excitations. In order to have a new insight in the cyanides/isocyanides abundance in the ISM, we have initiated a series of papers in order to provide the molecular data needed for cyanides/isocyanides abundance determination. In Paper I, we have determined theoretical

---

⋆ E-mail: francois.lique@univ-lehavre.fr spectroscopic and structural properties of species containing third-period metals Na, Mg, Al and Si that were in very good agreement with available experimental data and that gathered complete information on these species.

In Hernández Vera et al. (2013) (hereafter Paper II), we have presented the calculation of collisional excitation rate coefficients of AlCN, AlNC, MgCN and MgNC molecules by He (as a model of H_2) for temperatures ranging from 5 to 100 K. In Hernández Vera & Lique (2014) (hereafter Paper III), we have used these new data to simulate the excitation of these species by performing radiative transfer calculations for typical physical conditions encountered in the circumstellar gas. The calculations have shown that the estimation of the cyanides/isocyanides abundance ratio deduced from lines intensity ratio leads to large differences compared to exact radiative transfer calculations. We have also confirmed that AlCN and MgCN are significantly less abundant than AlNC and MgNC, respectively. It confirms the evidence of selective cyanides chemistry.

In this fourth paper, we focus on the excitation of the SiCN and SiNC isomers. SiCN and SiNC were observed for the first time in the ISM more than 10 years ago. SiCN was detected in the expanding shell of the evolved carbon star IRC+10216 by (Guélin et al. 2000). SiNC was discovered 4 years later in the same source Guélin et al. (2004). SiNC and SiCN have been found to have similar abundance in IRC+10216 ($\sim 4 \times 10^{-9}$ with respect to H_2, (Guélin et al. 2004)). Such findings could be surprising because of the different stabilities of the two isomers but SiCN and SiNC molecule have been latter observed in spectral survey of IRC+10216 (Cernicharo et al. 2011) and of Orion-KL (Tercero et al. 2011). The new observations confirms that SiCN and SiNC may be in similar abundances. Note that the observations interpretations were performed assuming local thermodynamic equilibrium (LTE) conditions that are not necessary fulfilled in these media.

In circumstellar gas, in addition of these two species, a surprisingly rich silicon chemistry has been discovered, even in regions where the temperature is fairly low Takano et al. (1992). Silicon is known to be depleted from the gas phase due to its incorporation into silicate grains. However, it is unclear what fraction of silicon remains in the gas phase. Accurate abundance determination of silicon bearing molecules (including SiCN and SiNC) in the ISM will enable a better understanding of the interstellar Silicon chemistry.

In astrophysical media, collisions compete with radiative processes in altering populations in molecular rovibrational levels. The estimation of molecular abundances from spectral line data requires collisional rate coefficients with most abundant interstellar species such as He or H_2. He is often assumed to be a model for H_2 (Lique et al. 2008; Roueff & Lique 2013). The use of He as a substitute for H_2 could lead to significant incertitude in case of collisions with light hydrides but is expected to be reasonable for heavy molecules (Roueff & Lique 2013) such as SiCN and SiNC that are presently studied. Without these rates, only approximate estimates of the molecular abundance are possible assuming LTE, which is generally not a good approximation even for these cyanide/isocyanide species (Paper III). Rate coefficients are also crucial to determine accurately the SiCN/SiNC abundance ratios.

In the present paper, we extend the work of our previous publications (paper I, II and III) to the excitation of the SiCN and SiNC molecules. Here, we present new rotational rate coefficients for SiCN and SiNC based on highly accurate SiCN–He and SiNC–He potentiel energy surfaces (PES). The paper is organized as follows. Section 2 describes the PES used in this work. Section 3 then contains a brief description of the scattering calculations. In Section 4, we present and discuss our results.

2 POTENTIAL ENERGY SURFACES

2.1 ab initio calculations

When the SiCN($X^2\Pi$) and SiNC($X^2\Pi$) radicals interact with a spherical structureless target, the doubly-degenerate Π electronic state is split into two states, one of A' symmetry and one of A'' symmetry. These two states correspond to the singly occupied π orbital lying in, or perpendicular to, the triatomic plane, respectively.

Within their ground electronic state, SiCN and SiNC molecules have linear geometries. Therefore, SiCN and SiNC can be considered as a linear rigid rotor. The SiCN–He and SiNC–He "rigid rotor" PES are described by the two Jacobi coordinates R, the distance from the centre of mass of cyanide/isocyanide molecules to the He atom, and θ, the angle between $\vec{R}$ and the cyanides/isocyanides bond axis $\vec{r}$, with $\theta = 0$ degree corresponding to colinear He–CN/NC–Si.

The intermolecular bond distances of the SiCN and SiNC were frozen at their experimental equilibrium values [$r_{SiC} = 3.50$ bohr and $r_{CN} = 2.21$ bohr for SiCN–He; $r_{SiN} = 3.28$ bohr and $r_{NC} = 2.25$ bohr for SiNC–He] (Paper I and references therein). As demonstrated by Lique & Spielfiedel (2007) for the CS-He system and by Denis-Alpizar et al. (2013) for the HCN–He system, for non-hydride molecules two-dimensional PESs calculated for a frozen bond distance or obtained from full dimensional PESs by averaging over the intermolecular ground state vibrational wavefunction are very similar. Consequently, in the present case, we anticipate that restricting intermolecular distances to their equilibrium value will introduce little error into the calculated inelastic rate coefficients.

Ab initio calculations of the PESs of SiCN($X^2\Pi$)/SiNC($X^2\Pi$)–He van der Waals complexes being in A' and A'' electronic states were carried out at the partially spin-restricted coupled cluster with single, double and perturbative triple excitations [RCCSD(T)] (Hampel et al. 1992; Watts et al. 1993) level of theory using MOLPRO package (Werner et al. 2012). In order to determine the interaction potential, $V(R,\theta)$, the basis set superposition error (BSSE) was corrected at all geometries using the Boys and Bernardi counterpoise scheme Boys & Bernardi (1970):

$$\begin{aligned} V(R,\theta,r) &= E_{\mathrm{SiCN/SiNC-He}}(R,\theta,r) \\ &\quad - E_{\mathrm{SiCN/SiNC}}(R,\theta,r) - E_{\mathrm{He}}(R,\theta,r) \end{aligned} \qquad (1)$$

where the energies of the SiCN/SiNC and He monomers are computed in a full basis set of the complex.

For all four atoms, we used the standard correlation-consistent polarized valence-quadruple-zeta basis sets of Dunning (Dunning 1989) (cc-pVTZ) augmented with the diffuse functions of s, p, d, f and g symmetries (aug-cc-pVTZ) (Kendall et al. 1992). This basis set was further augmented by the $[3s3p2d2f1g]$ bond functions optimized by Cybulski & Toczyłowski (1999) and placed at mid-distance between the He atom and the SiCN/SiNC centre of mass.

The calculations were carried out for θ angle values from 0° to 180° in steps of 10°. R-distances were varied from 4.0 to 20.0 a_0, yielding 31 points for each angular orientation.

2.2 analytical representations

To perform the scattering calculations we need to represent the He-SiCN and He-SiNC potentials in form of analytical expressions. For this purpose we expand the so-called half-sum (V_{sum}) and half-difference (V_{diff}) diabatic potentials, as previously defined by Alexander (1985), in a series of reduced Wigner functions:

$$\begin{aligned} V_{sum}(R,\theta) &= \frac{1}{2}\left[V_{A''}(R,\theta)+V_{A'}(R,\theta)\right] = \qquad (2)\\ &= \sum_{l=0}^{l_{max}} V_{l0}(R)d_{l0}(\cos\theta) \\ V_{diff}(R,\theta) &= \frac{1}{2}\left[V_{A''}(R,\theta)-V_{A'}(R,\theta)\right] = \qquad (3)\\ &= \sum_{l=2}^{l_{max}} V_{l2}(R)d_{l2}(\cos\theta)\,. \end{aligned}$$

For all the potentials in this work we set $l_{max} = 16$. This ensures that the relatively high anisotropy of these potentials is well represented. We determine the $V_{l\mu}(R)$ $(\mu = 0, 2)$ radial coefficients by linear list square fitting of the angular expansion at each discrete radial point to a set of angular *ab initio* points. The highly repulsive energies were weighted in the fit with a weight of $1/E^6$ to influence better description of the potential in the energies that will be sampled during the scattering process. The worst relative errors of the analytical representations are around 9 to 30% for the distance R=4 a_0 for the collinear geometries where the energies are already very repulsive, on the order of 10^6 cm^{-1}. For the remaining angles the relative error is around 1% for this distance. The relative errors of the fits for larger distances are very small for both complexes, from 0.1 to 10^{-3} %. The absolute error in the region of the attractive long range interaction is usually on the order of 10^{-1} to 10^{-3} cm^{-1} or better. The radial expansion coefficients $V_{l\mu}(R)$ obtained in this way are then represented by the one-dimensional Reproducing Kernel Hilbert Space (RKHS) interpolation fits Ho & Rabitz (1996) with the smoothness parameter $m = 2$ and with the fixed long range R^{-6} radial kernel for the extrapolation beyond the last *ab initio* radial point at 20 a_0. The Fortran routines for the PES are available from the authors.

We will describe now features of the He-SiCN and He-SiNC PES's. Both systems reveal qualitatively similar shape, with the T-shape minima located around 3-4 a_0 closer than minima for the collinear approaches, due to the length of the SiCN or SiNC molecule. Also for both complexes, the global minimum is located on the A'' adiabatic potential.

The global minimum for the He-SiCN interaction is located on the A'' adiabatic potential, shown in the bottom panel of Figure 1, for the T-shape geometry. The global minimum of -52.85 cm^{-1} is located at $R_e = 6.1$ a_0 and $\theta_e = 98°$. The He-SiCN A' adiabatic potential shown in the upper panel of Figure 1 is characterized by a skewed minimum of -30.8 cm^{-1} located at $R = 7.1$ a_0 and $\theta = 68°$. There is another local minimum of -14.06 cm^{-1} located at $R = 10.0$ a_0 and $\theta = 180°$, which corresponds to the He–Si-C-N arrangement. The He–N-C-Si collinear arrangement ($\theta = 0°$) has a saddle of -20.14 cm^{-1} at $R = 10.0$ a_0. The V_{sum} diabatic potential shown in top panel of Figure 3 has a minimum of -29.61 cm^{-1} for $\theta = 72°$ at R=7.1 a_0.

Similarly, the He-SiNC interaction has a global minimum of -41.83 cm^{-1} on the A'' adiabatic potential shown in bottom panel of Figure 2 at $R_e = 6.5$ a_0 at $\theta_e = 96°$. The He-SiNC A' potential has a skewed minimum of -33.80 cm^{-1} at $R = 7.0$ a_0 and $\theta = 71°$. The V_{sum} diabatic potential shown in top panel of Figure 4 has a minimum of -31.65 cm^{-1} for $\theta = 74°$ at R=6.9 a_0. The local collinear minimum at $\theta = 180°$ corresponding to the He–Si-N-C arrangement is -15.76 cm^{-1} at $R = 9.7$ a_0. The other collinear minimum, for the He–C-N-Si arrangement, is -14.41 cm^{-1} at $R = 10.7$ a_0. One can notice in this case, that the collinear minima are much similar in energy than for the He-SiCN case, which are around 6 cm^{-1} apart. Also the difference in minima between the A'' and A' potentials in the T-shape geometry is much smaller than for He-SiCN complex.

3 SCATTERING CALCULATIONS

The open-shell SiCN and SiNC molecules have $^2\Pi$ electronic ground states. For both molecules, the electronic orbital angular momentum and the electron spin have well-defined projections of $\Lambda = \pm 1$ and $\Sigma = \pm 1/2$, onto the internuclear axis. Because of this, there are two spin-orbit manifolds; the lower-energy $^2\Pi_{1/2}$ with $|\Omega| = |\Lambda + \Sigma| = 1/2$ (labelled F_1), and the higher-energy $^2\Pi_{3/2}$ with $|\Omega| = 3/2$ (labelled F_2). Each rotational level j is split into two close lying Λ-doublet levels labelled e (total parity $+(-1)^{j-1/2}$) and f (total parity $-(-1)^{j-1/2}$) Brown et al. (1975).

The energies of the rotational levels, including the spin-orbit and Λ-doubling fine structure is given by

$$\begin{aligned} E_{j,\Omega=3/2,\varepsilon} &= \frac{1}{2}A_{so} + B_0\left[j(j+1) - 7/4\right] \qquad (4)\\ &\quad + \frac{\varepsilon}{2}(B_0/A_{so})(2q + pB_0/A_{so}) \\ &\quad \times (j-1/2)(j+1/2)(j+3/2) \\ E_{j,\Omega=1/2,\varepsilon} &= -\frac{1}{2}A_{so} + B_0\left[j(j+1) + 1/4\right] + \frac{\varepsilon}{2}p(j+1/2) \end{aligned}$$

where ε=+1 for the e-labelled and –1 for the f-labelled levels. Here B_0 is the rotational constant in the lowest vibrational manifold of SiCN/SiNC, A_{so} is the spin-orbit constant of SiCN/SiNC and the two Λ doubling parameters of SiCN/SiNC are p and q. In the scattering calculations reported here we assume that the value of the spin orbit constant is not altered by approach of He atom. This is certainly a valid approximation at the moderate-to-large SiCN/SiNC–He distances of importance in low energy collisions.

Table 1 gives the energy of the first rotational levels of both SiCN and SiNC molecules computed from molecular constant taken from Paper I and references therein.

The rotational constant of SiCN is slightly lower than the one of SiNC. This leads to a more compact structure for the SiCN isomer. Nevertheless, we did not expect significant

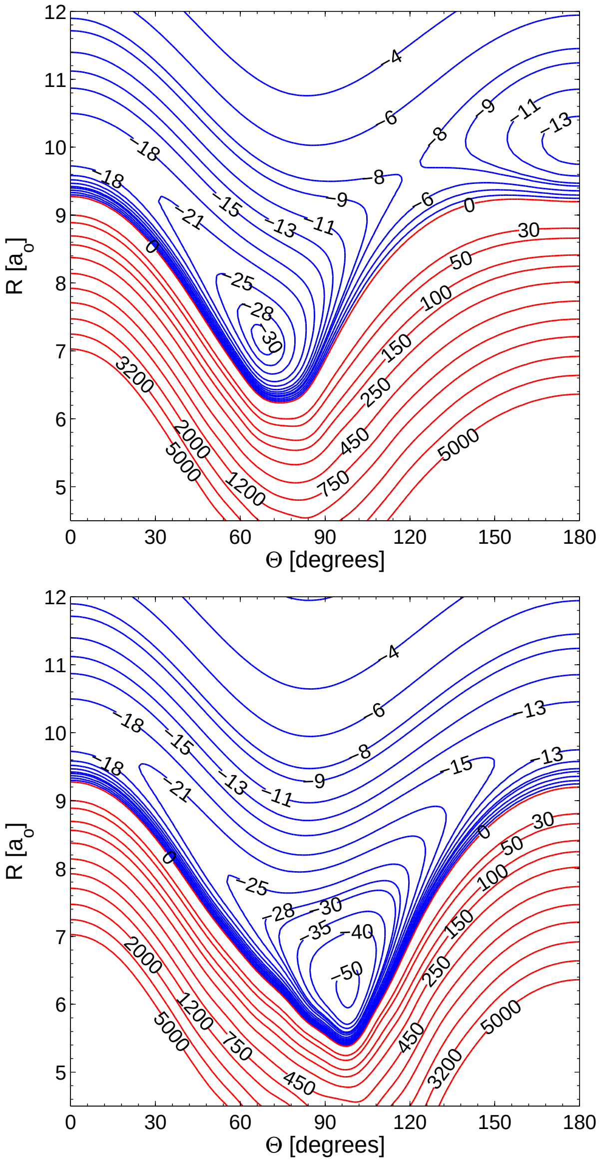

Figure 1. Contour plots of the SiCN–He A' (upper panel) and A'' (lower panel) PES. Energy is in cm^{-1}. Red contour lines represent repulsive interaction energies.

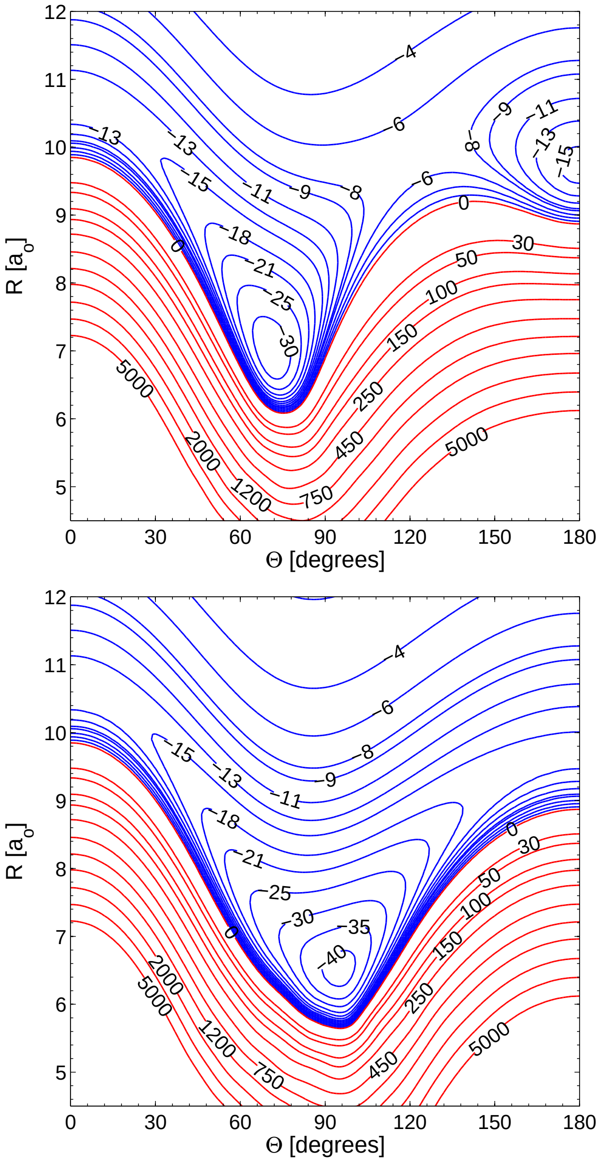

Figure 2. Contour plots of the SiNC–He A' (upper panel) and A'' (lower panel) PES. Energy is in cm^{-1}. Red contour lines represent repulsive interaction energies.

differences in the collisional excitation cross sections arising from the different energetic structures.

In the pure Hund's case (a) limit, it is V_{sum} potential which is responsible for inducing inelastic collisions within a given spin-orbit manifold, and V_{diff} which inducing inelastic collisions between the two ($\Omega = 1/2$) and ($\Omega = 3/2$) spin-orbit manifold Alexander (1985).

For both the SiCN/SiNC–He systems, as the A' and A'' PES's are quite similar so that we do not anticipate any sizeable cross sections / rate coefficients for spin orbit changing transitions. We then expect that most of the transitions occur within a spin orbit manifold.

We used the quantum Coupled-States approximation (CS) (McGuire & Kouri 1974) determine inelastic cross sections for the scattering of SiCN/SiNC by collision with He. The hyperfine structure of both SiCN and SiNC molecules was ignored in the calculations. However, cross sections between hyperfine levels can be estimated from cross section between rotational levels using simple treatments Lique et al. (2009); Faure & Lique (2012). Cross sections were calculated by means of the HIBRIDON package[1]. Calculations for collision of SiCN/SiNC with He were carried out for a total energy grid ranging from 0.2 to 1000 cm^{-1}. The integration parameters were chosen to meet convergence criteria

---

[1] The HIBRIDON package was written by M. H. Alexander, D. E. Manolopoulos, H.-J. Werner, and B. Follmeg, with contributions by P. F. Vohralik, D. Lemoine, G. Corey, R. Gordon, B. Johnson, T. Orlikowski, A. Berning, A. Degli-Esposti, C. Rist, P. Dagdigian, B. Pouilly, G. van der Sanden, M. Yang, F. de Weerd, S. Gregurick, J. Kłos and F. Lique, http://www2.chem.umd.edu/groups/alexander/

Table 1. Energy levels of SiCN and SiNC molecules in their $^2\Pi$ electronic state.

j	ϵ	Ω	E_{SiNC}	E_{SiCN}
0.5	e	0.5	0.000	0.000
0.5	f	0.5	0.000	0.001
1.5	e	0.5	0.638	0.553
1.5	f	0.5	0.638	0.555
2.5	e	0.5	1.700	1.475
2.5	f	0.5	1.702	1.477
3.5	e	0.5	3.189	2.765
3.5	f	0.5	3.190	2.769
4.5	e	0.5	5.102	4.425
4.5	f	0.5	5.104	4.429
5.5	e	0.5	7.440	6.453
5.5	f	0.5	7.443	6.458
6.5	e	0.5	10.204	8.850
6.5	f	0.5	10.207	8.857
7.5	e	0.5	13.393	11.616
7.5	f	0.5	13.396	11.624
8.5	e	0.5	17.008	14.751
8.5	f	0.5	17.011	14.760
...	...	...	...	...
1.5	e	1.5	59.023	71.036
1.5	f	1.5	59.023	71.036
2.5	e	1.5	60.094	71.963
2.5	f	1.5	60.094	71.963
3.5	e	1.5	61.593	73.261
3.5	f	1.5	61.593	73.261
4.5	e	1.5	63.521	74.929
4.5	f	1.5	63.521	74.929
5.5	e	1.5	65.877	76.969
5.5	f	1.5	65.877	76.969
6.5	e	1.5	68.661	79.379
6.5	f	1.5	68.661	79.379
7.5	e	1.5	71.873	82.160
7.5	f	1.5	71.874	82.160
8.5	e	1.5	75.514	85.312
8.5	f	1.5	75.515	85.312

of 0.2 % for the cross sections. The integration range was set from 4.5 a_0 to 80 a_0. At the largest total energy (1000 cm^{-1}) the SiCN and SiNC rotational basis was extended to $j = 40.5$ to ensure convergence of the rotational levels of SiCN and SiNC up to $j = 25.5$ for the F_1 manifold and up to $j = 20.5$ for the F_2 manifold . Inelastic cross sections were determined over a large grid of collision energies. Subsequent averaging over a Boltzmann distribution of collision energies yielded room temperature rate constants, as follows:

$$k_{jF_i\epsilon\to j'F_i'\epsilon'}(T) = \left(\frac{8}{\pi\mu k_B^3 T^3}\right)^{\frac{1}{2}} \times \int_0^\infty \sigma_{jF_i\epsilon\to j'F_i'\epsilon'}\, E_c\, e^{-\frac{E_c}{k_B T}}\, dE_c \quad (5)$$

where the SiCN/SiNC rotational levels are labeled by the rotational quantum number j, the spin-orbit manifold label F_i, and the parity index ϵ. Here k_B is Boltzmann's constant, μ is the collision reduced mass and E_c is the collision energy.

The accuracy of the CS approximation compared to the full close coupling (CC) approach has been evaluated for a small number of energies. Tables 2 and 3 present the comparison.

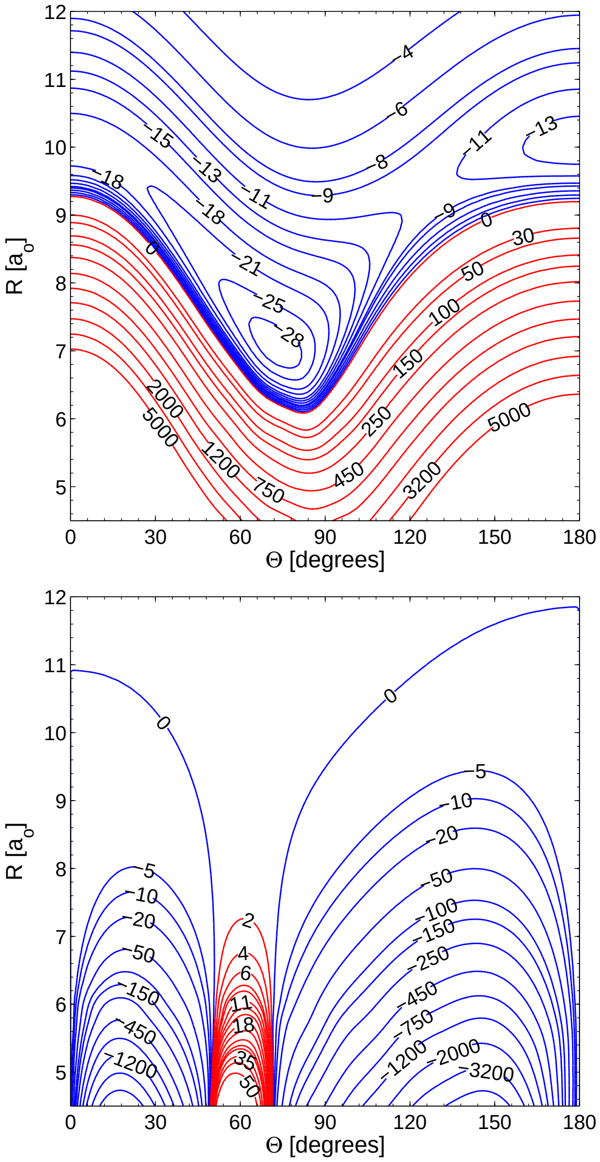

Figure 3. Contour plots of SiCN–He V_{sum} (upper panel), and V_{diff} (lower panel) potentials from this work. Energy is in cm^{-1}. Red contour lines represent repulsive interaction energies.

It is found that the CS approach can lead to inaccuracies of 20-50% for very low total energy cross sections (< 50 cm^{-1}) but agreement improves between CC and CS cross sections when the total energy is greater than 50 cm^{-1} and we expect that the corresponding rate coefficients will be accurate since they are not as sensitive to the accuracy of description of the resonances. The relative accuracy of the CS approximation compared to full CC approach can be explained by the relatively small energy spacing between SiCN and SiNC rotational levels.

4 RESULTS

Using the new *ab initio* PESs and the computational scheme described above, we have obtained the energy dependance

Table 2. Comparison between CC and CS SiCN–He cross sections (in Å^2) at selected total energies (E). Transitions were chosen among levels in the F$_1$ spin-orbit manifold.

	$E = 20$ cm^{-1}		$E = 50$ cm^{-1}		$E = 100$ cm^{-1}		$E = 300$ cm^{-1}	
Transitions	CC	CS	CC	CS	CC	CS	CC	CS
$j = 1.5, f \to j = 0.5, f$	6.607	9.068	2.762	3.523	1.482	1.854	0.617	0.765
$j = 2.5, f \to j = 0.5, f$	6.262	7.517	4.490	5.421	3.021	3.663	1.440	2.082
$j = 2.5, f \to j = 1.5, f$	10.70	13.33	4.279	5.259	2.321	2.807	0.959	1.158
$j = 3.5, f \to j = 1.5, f$	1.051	1.123	6.527	7.618	4.463	5.246	2.170	3.015
$j = 5.5, f \to j = 0.5, f$	1.731	1.812	0.843	0.837	0.409	0.410	0.166	0.167
$j = 6.5, f \to j = 1.5, f$	3.318	3.542	1.559	1.522	0.753	0.741	0.290	0.279
$j = 6.5, f \to j = 5.5, f$	20.87	30.01	7.744	8.990	4.033	4.629	1.498	1.806
$j = 7.5, f \to j = 5.5, f$	19.00	16.30	10.56	10.56	6.819	7.373	3.345	4.305
$j = 10.5, f \to j = 0.5, f$	...	...	0.126	0.125	0.204	0.146	0.141	0.115
$j = 10.5, f \to j = 1.5, f$	...	...	0.126	0.125	0.406	0.403	0.138	0.129
$j = 10.5, f \to j = 5.5, f$	...	...	3.385	3.665	1.747	1.785	0.602	0.619
$j = 11.5, f \to j = 10.5, f$	...	...	13.13	14.29	5.391	6.067	1.722	2.227
$j = 12.5, f \to j = 10.5, f$	...	...	15.15	11.23	8.351	8.167	3.608	4.883
$j = 15.5, f \to j = 10.5, f$	...	...	...	...	2.721	2.928	0.843	0.925

Table 3. Comparison between CC and CS SiNC–He cross sections (in Å^2) at selected total energies (E). Transitions were chosen among levels in the F$_1$ spin-orbit manifold.

	$E = 20$ cm^{-1}		$E = 50$ cm^{-1}		$E = 100$ cm^{-1}		$E = 300$ cm^{-1}	
Transitions	CC	CS	CC	CS	CC	CS	CC	CS
$j = 1.5, f \to j = 0.5, f$	3.080	4.342	1.753	2.282	1.041	1.400	0.427	0.544
$j = 2.5, f \to j = 0.5, f$	6.704	7.533	4.207	4.777	2.785	3.241	1.415	1.961
$j = 2.5, f \to j = 1.5, f$	4.992	7.569	2.837	3.670	1.718	2.295	0.715	0.875
$j = 3.5, f \to j = 1.5, f$	1.051	1.123	6.272	6.768	4.166	4.658	2.106	2.829
$j = 5.5, f \to j = 0.5, f$	1.533	2.001	5.673	7.210	3.213	4.115	0.135	0.141
$j = 6.5, f \to j = 1.5, f$	3.226	4.026	1.005	1.297	0.577	0.727	0.239	0.239
$j = 6.5, f \to j = 5.5, f$	16.44	17.29	5.209	6.490	2.977	3.870	1.175	1.439
$j = 7.5, f \to j = 5.5, f$	28.66	28.32	10.68	9.901	6.727	6.783	3.242	4.071
$j = 10.5, f \to j = 0.5, f$	...	...	0.537	0.608	0.185	0.237	0.112	0.105
$j = 10.5, f \to j = 1.5, f$	...	...	0.336	0.273	0.311	0.238	0.165	0.139
$j = 10.5, f \to j = 5.5, f$	...	...	2.594	3.326	1.214	1.554	0.475	0.521
$j = 11.5, f \to j = 10.5, f$	...	...	10.58	10.92	4.054	5.107	1.365	1.807
$j = 12.5, f \to j = 10.5, f$	...	...	19.54	17.97	8.820	7.834	3.609	4.646
$j = 15.5, f \to j = 10.5, f$	...	...	...	...	1.967	2.569	0.659	0.767

of the SiCN–He and SiNC–He cross sections and the corresponding temperature dependance of the rate coefficients. The complete set of (de-)excitation rate coefficients will be made available through the LAMDA (Schöier et al. 2005) and BASECOL (Dubernet et al. 2013) databases.

Figure 5 shows the temperature dependence of the SiCN–He collisional de-excitation rate coefficients for transitions out of the $j = 8.5$, e/f levels in both the ground (F_1) and excited (F_2) spin-orbit manifolds.

First of all, for spin-orbit conserving transitions, one can see a strong propensity in favor of Λ-doublet labels conversing transitions ($e \to e$ or $f \to f$). The propensity is slightly more pronounced for high rotational states than for low ones and for transitions within the F_1 spin orbit manifold.

As expected, the spin orbit changing transitions are lower than the spin orbit conserving transitions. For spin orbit changing transitions, the rate coefficients show a propensity to populate e final levels when starting from initial f levels or to populate f final levels when starting from initial e levels. Such behavior has been already observed for NO–He collisions Kłos et al. (2008). The magnitude of the spin orbit changing transition increase with increasing temperature and one could anticipate that at higher temperatures, there may be a clear competition between spin orbit changing and spin orbit conserving transitions.

Figure 6 shows the temperature dependence of the SiCN–He collisional de-excitation rate coefficients for transitions out of the $j = 8.5$, e/f levels in both the ground (F_1) and excited (F_2) spin-orbit manifolds.

The propensity rules are exactly the same than for the SiCN–He collisional system. Such similarity could have been anticipated when looking at the PES and at the rotational structure.

Then, it is interesting to compare SiCN–He and SiNC–He rate coefficients. Fig. 7 shows the SiCN–He and SiNC–He de-excitation rate coefficients from the $j = 8.5$, f, F_1/F_2 level at 25 K.

We first note that a global agreement between both sets of data exist. However, interesting differences that could have a significant impact on the radiative transfer calculations exist. Indeed, for some transitions, the propensity rules seen in the two sets of rate coefficients are different. For both spin-orbit-conserving $F_1 \to F_1$ and $F_2 \to F_2$, t the SiCN-He rate coefficients present a propensity in favour of

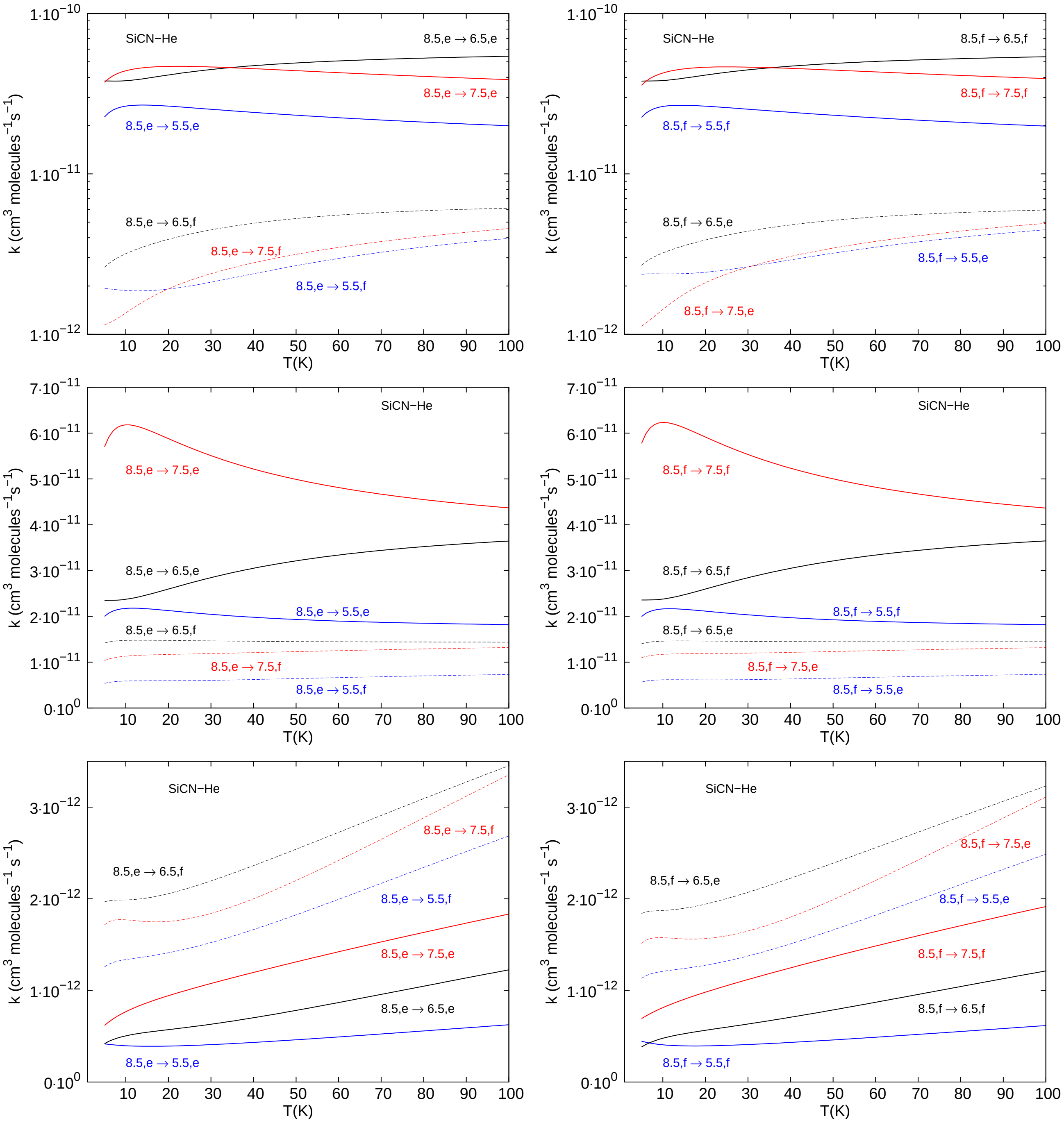

Figure 5. Temperature dependence of temperature dependence of the SiCN–He collisional de-excitation rate coefficients for transitions out of the $j = 8.5$, e/f, F_1/F_2. The upper panels correspond to transitions within the F_1 spin orbit manifold. The middle panels correspond to transitions within the F_2 spin orbit manifold. The lower panels correspond to spin orbit changing ($F_2 \rightarrow F_1$) transitions.

transitions with $\Delta j = 1$ whereas the SiNC-He rate coefficients present a strong propensity in favour of transitions with $\Delta j = 2$. The differences are more pronounced for transitions within the F_2 spin orbit manifold than for transitions within the F_1 spin orbit manifold. These propensity are due to the shape of the different PESs. Even if they seems to be similar, the anisotropy of the SiCN PES is larger than the one of the SiNC so that the propensity rules with respect to odd or even Δj transitions are not the same (McCurdy & Miller 1977). Such effect has been already observed by Sarrasin et al. (2010) and Dumouchel et al. (2010) for the HCN/HNC isomers and in paper II for the MgCN/MgNC isomers.

From this comparison, one can anticipate that the excitation of SiCN and SiNC will be different and that specific radiative transfer calculations will have to be performed in order to accurately determine SiCN and SiNC abundances in the ISM.

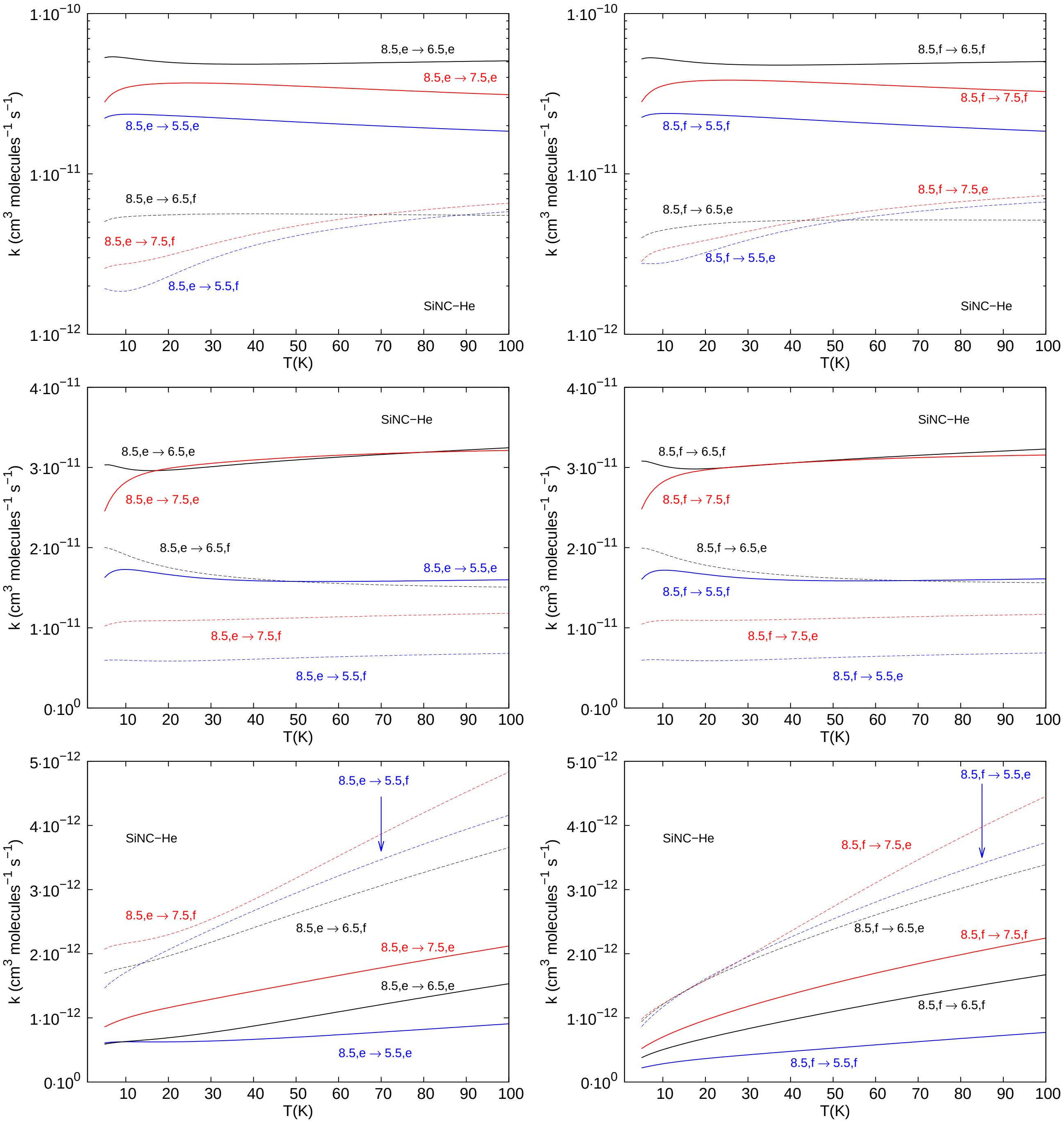

Figure 6. Temperature dependence of temperature dependence of the SiCN–He collisional de-excitation rate coefficients for transitions out of the $j = 8.5$, e/f, F_1/F_2. The upper panels correspond to transitions within the F_1 spin orbit manifold. The middle panels correspond to transitions within the F_2 spin orbit manifold. The lower panels correspond to spin orbit manifold changing ($F_2 \to F_1$) transitions.

5 DISCUSSION AND CONCLUSION

We have used quantum scattering calculations to investigate rotational energy transfer in collisions of SiCN and SiNC molecules with He atoms. The calculations are based on highly accurate 2-D potential energy surfaces obtained using state-of-the-art electronic structure methods. Rate coefficients for transitions involving the lowest 92 levels of both SiCN and SiNC were determined for temperatures ranging from 5 to 100 K.

The rate coefficients for spin orbit conserving transitions were found to be significantly larger than the one corresponding to spin orbit changing transitions. For these transitions, a clear propensity was found for λ-doubling conserving transitions.

In addition, for these dominant transitions, a propensity for $\Delta j = 1$ transitions was found for the SiCN–He system

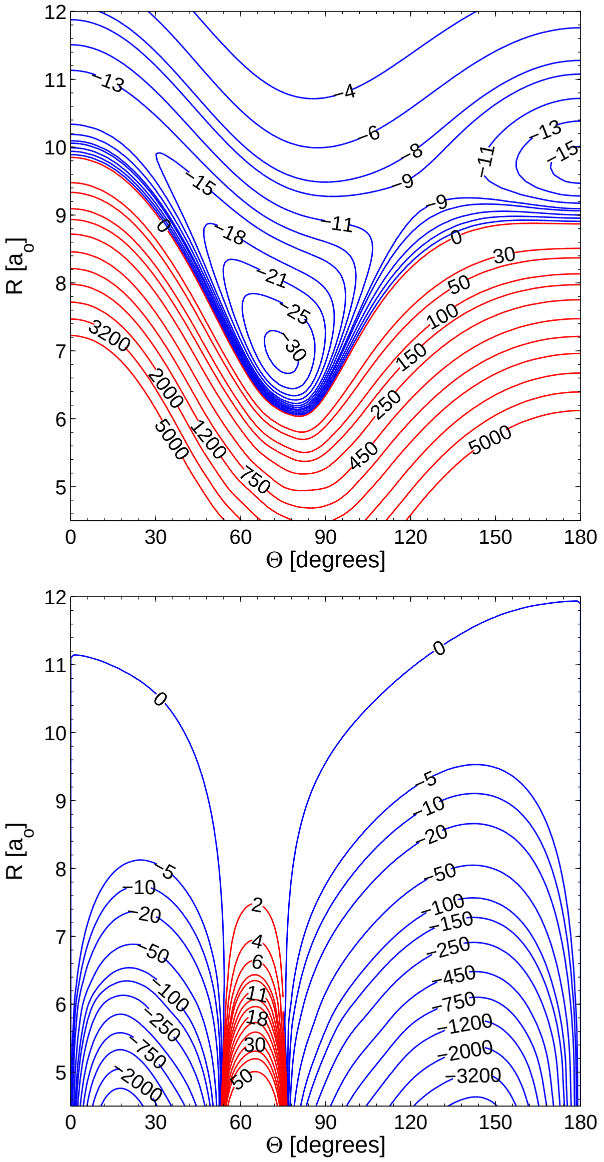

Figure 4. Contour plots of SiNC–He V_{sum} (upper panel), and V_{diff} (lower panel) potentials from this work. Energy is in cm^{-1}. Red contour lines represent repulsive interaction energies.

whereas a propensity for $\Delta j = 2$ transitions was found for SiNC–He system. These different propensity rules seen for the SiCN/SiNC isomers let us predict that the excitation of these molecules in molecular clouds will be different and that the abundance ratio of these species cannot be simply obtained by looking at the brightness temperature ratio of the emission lines (even correcting from the different dipole moment). Hence, radiative transfer calculations will have to be performed for both molecules using both sets of rate coefficients in order to accurately obtained the relative abundance of the two isomers.

We anticipate that the present results suggest that more intense $\Delta j = 1$ spectral lines will be expected for SiCN than for SiNC molecules (considering similar abundance for both SiCN/SiNC isomers) since the magnitude of the $\Delta j = 1$ rate coefficients is larger for SiCN–He collisional system than for SiNC–He ones and since the dipole moment of SiCN is slightly larger than the one of SiNC (2.8 D vs. 2.7 D; Paper I) Previous observations have effectively shown that SiCN emission lines were larger the SiNC ones. However, as LTE conditions were assumed, it is not yet possible to confirm that SiCN/SiNC molecules are about the same abundance in the ISM. Further investigations have to be lead to accurately estimate SICN and SiNC abundances.

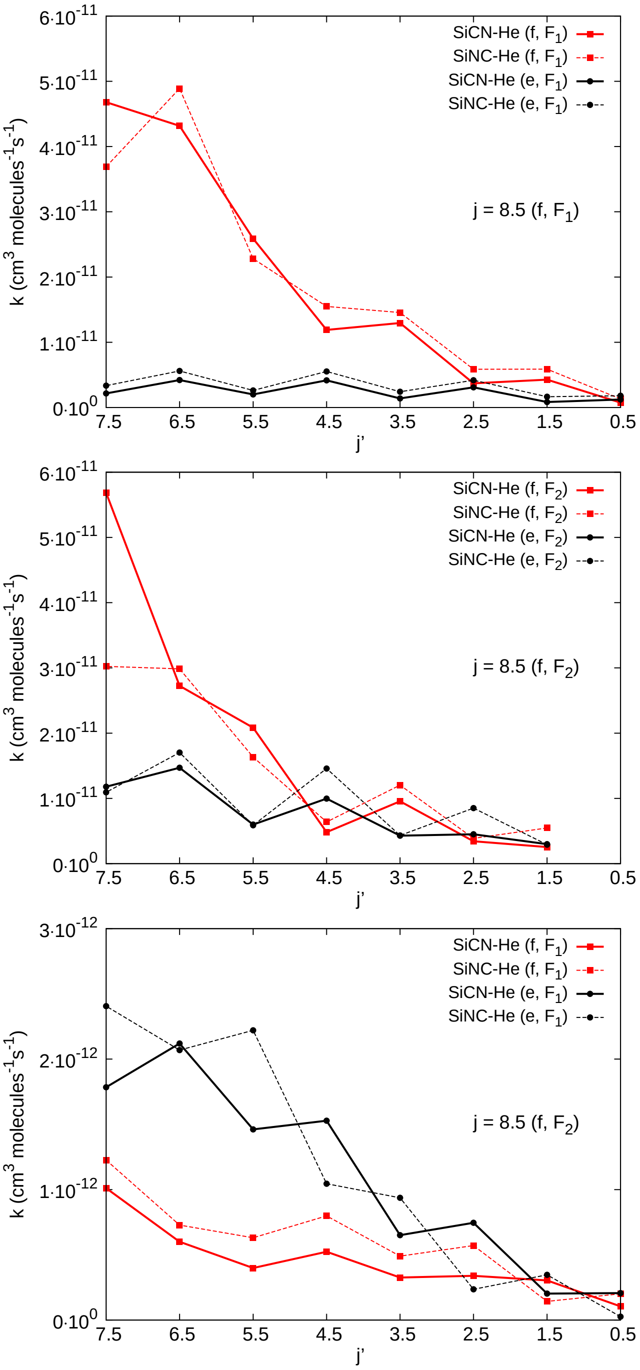

Figure 7. Comparison between the SiCN-He and SiNC-He rate coefficients at 25 K for spin-orbit-conserving $F_1 \rightarrow F_1$ (upper panel), $F_2 \rightarrow F_2$ (middle panel) and spin-orbit-changing $F_2 \rightarrow F_1$ transitions out of the $j = 8.5$, f, F_1/F_2 level.

6 ACKNOWLEDGMENTS

This research was supported by the CNRS national program "Physique et Chimie du Milieu Interstellaire". MHV and FL acknowledge the french embassy of Cuba and Campus France for financial support. We also thank the CPER Haute-Normandie/CNRT/Energie, Electronique, Matériaux.

REFERENCES

Alexander M. H., 1985, Chem. Phys., 92, 337

Bowman J. M., Gazdy B., Bentley J. A., Lee T. J., Dateo C. E., 1993, J. Chem. Phys., 99, 308

Boys S. F., Bernardi F., 1970, Mol. Phys., 19, 553

Brown J. M. et al., 1975, J. Molec. Spectrosc., 55, 500

Cernicharo J., Agúndez M., Guélin M., 2011, in IAU Symposium, Vol. 280, IAU Symposium, Cernicharo J., Bachiller R., eds., pp. 237–248

Cernicharo J., Barlow M. J., Gonzalez-Alfonso E., Cox P., Clegg P. E., Nguyen-Q-Rieu A., et al., 1996, A&A, 315, L201

Cybulski S. M., Toczyłowski R., 1999, J. Chem. Phys., 111, 10520

Denis-Alpizar O., Kalugina Y., Stoecklin T., Vera M. H., Lique F., 2013, J. Chem. Phys., 139, 224301

Dubernet M.-L. et al., 2013, A&A, 553, A50

Dumouchel F., Faure A., Lique F., 2010, MNRAS, 406, 2488

Dunbar R. C., Petrie S., 2002, ApJ., 564, 792

Dunning T. H., 1989, J. Chem. Phys., 90, 1007

Faure A., Lique F., 2012, MNRAS, 425, 740

Guelin M., Gomez-Gonzalez J., Cernicharo J., Kahane C., 1986, A&A, 157, L17

Guélin M., Muller S., Cernicharo J., Apponi A. J., McCarthy M. C., Gottlieb C. A., Thaddeus P., 2000, A&A, 363, L9

Guélin M., Muller S., Cernicharo J., McCarthy M. C., Thaddeus P., 2004, A&A, 426, L49

Hampel C., Peterson K. A., Werner H.-J., 1992, Chem. Phys. Lett., 190, 1

Harris G. J., Pavlenko Y. V., Jones H. R. A., Tennyson J., 2003, MNRAS, 344, 1107

Hernández Vera M., Lique F., 2014, MNRAS

Hernández Vera M., Lique F., Dumouchel F., Kłos J., Rubayo Soneira J., Senent M.-L., 2013, MNRAS, 432, 468

Ho T.-S., Rabitz H., 1996, J. Chem. Phys., 104, 2584

Irvine W. M., Schloerb F. P., 1984, ApJ., 282, 516

Kendall R. A., Dunning T. H., Harrison R. J., 1992, J. Chem. Phys., 96, 6796

Kłos J., Lique F., Alexander M. H., 2008, Chem. Phys. Lett., 455, 1

Largo-Cabrerizo A., 1988, Chemical Physics Letters, 147, 95

Lique F., Spielfiedel A., 2007, A&A, 462, 1179

Lique F., Toboła R., Kłos J., Feautrier N., Spielfiedel A., Vincent L. F. M., Chałasiński G., Alexander M. H., 2008, A&A, 478, 567

Lique F., van der Tak F. F. S., Kłos J., Bulthuis J., Alexander M. H., 2009, Astron. Astrophys., 493, 557

Lis D. C. et al., 1997, Icarus, 130, 355

McCurdy C. W., Miller W. H., 1977, J. Chem. Phys., 67, 2488

McGuire P., Kouri D. J., 1974, J. Chem. Phys., 60, 463

Pulliam R. L., Savage C., Agúndez M., Cernicharo J., Guélin M., Ziurys L. M., 2010, ApJL, 725, L181

Roueff E., Lique F., 2013, Chem. Rev., 113, 8906

Sarrasin E., Abdallah D. B., Wernli M., Faure A., Cernicharo J., Lique F., 2010, MNRAS, 404, 518

Schöier F. L., van der Tak F. F. S., van Dishoeck E. F., Black J. H., 2005, A&A, 432, 369

Senent M. L., Dumouchel F., Lique F., 2012, MNRAS, 420, 1188

Snyder L. E., Buhl D., 1971, ApJL, 163, L47

Takano S., Saito S., Tsuji T., 1992, PASJ, 44, 469

Tercero B., Vincent L., Cernicharo J., Viti S., Marcelino N., 2011, A&A, 528, A26

Watts J. D., Gauss J., Bartlett R. J., 1993, J. Chem. Phys., 98, 8718

Werner H.-J., Knowles P. J., Knizia G., Manby F. R., Schütz M., 2012, WIREs Comput Mol Sci, 2, 242

Zack L. N., Halfen D. T., Ziurys L. M., 2011, ApJL, 733, L36

Ziurys L. M., Apponi A. J., Guelin M., Cernicharo J., 1995, ApJL, 445, L47

Ziurys L. M., Savage C., Highberger J. L., Apponi A. J., Guélin M., Cernicharo J., 2002, ApJL, 564, L45

Chapter 5

Rotational (de-)excitation of HCN with H_2

Contents

HCN is one of the most abundant interstellar molecules. This molecule is considered as an excellent tracer of dense interstellar gases. For key interstellar molecules like HCN, the most accurate calculations should be performed. In this chapter, we have used new highly correlated 4-dimensional PES to perform CC calculations of the rotational excitation of HCN by para-H_2 and ortho-H_2. The PES was obtained from a collaborative work (Appendix B). In this chapter, we will present the rotational spectroscopy of the colliding partners (HCN and H_2), the formalism for collisions between two diatomic molecules and the results.

5.1 Spectroscopy of HCN and H_2

Many theoretical and experimental works have been devoted to the spectroscopy of hydrogen [115–117] and hydrogen cyanide [118–120] molecules. In Fig. 5.1, we present some structural and spectroscopic parameters of HCN and H_2 molecules in their electronic ground states. The large dipole moment of HCN is one of the reasons of its traceability in the ISM. In contrast, H_2 is a homonuclear diatomic and therefore does not have a permanent electric dipole moment so that there is no emission coming from pure rotational transitions.

The experimental fundamental frequencies of HCN, namely, H–C stretching, the HCN bending and the C–N stretching modes are 3315 cm^{-1}, 716 cm^{-1} and 2080 cm^{-1} respectively [70]. In the case of molecular hydrogen, the lowest vibrational frequency is 4162 cm^{-1} [121]. Thus, the vibrational excitation of both molecules requires temperatures above 1000 K. In addition, a recent study dedicated to the ro-vibrational excitation of HCN by He [122] showed that neglecting the bending of HCN is a very reasonable approximation for treating the pure rotational excitation at low and moderate temperatures. For this reason, we will assume both molecules as rigid rotors in our dynamical calculations.

Owing to its identical hydrogen nuclei (with nuclear spin 1/2), H_2 exists in ortho (o-H_2) and para (p-H_2) forms, also called nuclear-spin isomers. In the electronic ground state, the rotational levels of o-H_2 have odd values of the rotational momentum j, while the levels of p-H_2 have even j values. Ortho-to-para conversion is forbidden in non-reactive inelastic collisions. Then, we have to consider separately the collisional process for both species. On the other hand, both nuclear spin isomers are considered important collisional partners even at moderated temper-

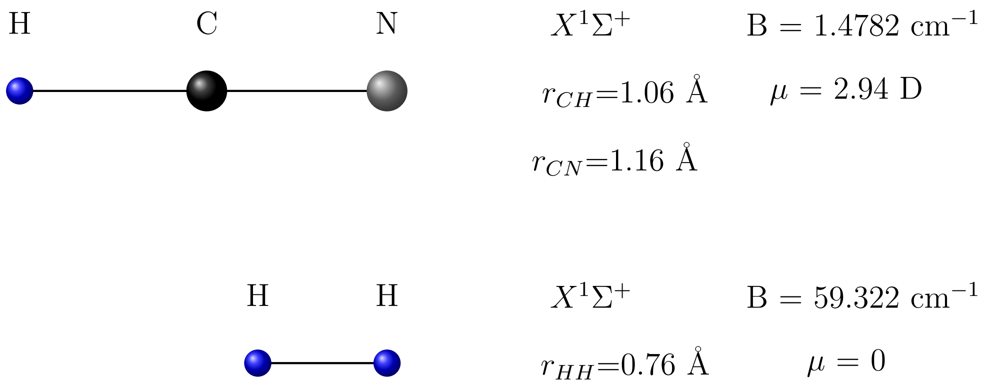

Figure 5.1: Intermolecular bond distances, rotational constant (B) and dipole moment (μ) of HCN and H_2 molecules.

atures because ortho-to-para ratio of H_2 is not necessarily at thermal equilibrium in the ISM [123, 124].

Fig. 5.1 gives also the rotational constants of both molecules. The rotational constant of HCN is 50 times lower than the one of the hydrogen molecule. Hence, the HCN rotational levels will be considerably more compact than the rotational levels of p-H_2 or o-H_2. This effect is shown in Fig. 5.2. We can see that the first excited rotational levels of p-H_2 and o-H_2 are above 100 cm^{-1}. Consequently, for temperatures lower than 100 K, the excitation of higher rotational levels ($j > 2$) of H_2 is unlikely to proceed.

Finally, we note that HCN has an hyperfine structure due to the nuclear quadrupole moment of ^{14}N. The hyperfine structure of HCN has shown dramatic non-LTE behaviour [125]. Then, the collisional excitation of these lines should be considered. In this thesis we do not consider this hyperfine structure. However, using a procedure similar to the one discussed by Lanza et al. [126], our collisional rate coeffi-

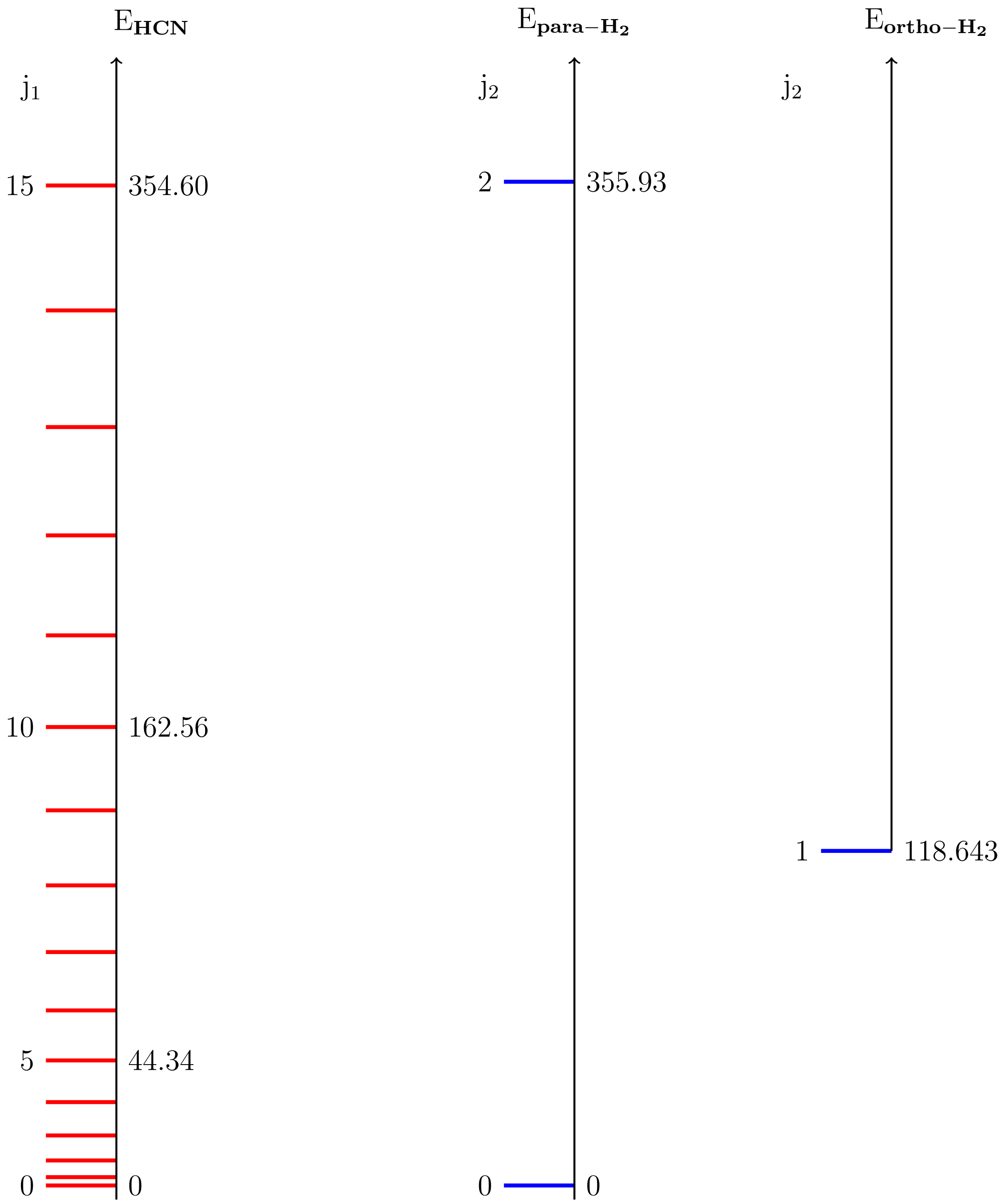

Figure 5.2: First rotational energy (cm^{-1}) levels of the HCN molecules and the p-H_2 and o-H_2 nuclear spin isomers.

cients could be employed to model the collisional excitation among the hyperfine structure of HCN.

5.2 Rotor ($^1\Sigma$) - rotor($^1\Sigma$) collision

The time-independent Schrödinger equation for the scattering of two rigid rotors is given by,

$$H\Psi(\hat{\boldsymbol{\rho}}_1, \hat{\boldsymbol{\rho}}_2, \mathbf{R}) = E\Psi(\hat{\boldsymbol{\rho}}_1, \hat{\boldsymbol{\rho}}_2, \mathbf{R}) \tag{5.1}$$

where $\hat{\boldsymbol{\rho}}_1$ and $\hat{\boldsymbol{\rho}}_2$ are the angles which describe the orientations of rotors 1 and 2, respectively, and $\mathbf{R}$ is the collision coordinate, defined with respect to space fixed axes.

The total Hamiltonian defined in the center-of-mass coordinate system may be written as,

$$H = -\frac{1}{2\mu}\nabla_R^2 + H_1(\hat{\boldsymbol{\rho}}_1) + H_2(\hat{\boldsymbol{\rho}}_2) + V(\mathbf{R}, \boldsymbol{\rho}_1, \boldsymbol{\rho}_2) \tag{5.2}$$

The first term represents the relative kinetic energy of the target and projectile, H_1 and H_2 are the Hamiltonians of the two rigid rotors.

Following the methodology discussed in sections 2.3, we coupled the angular momentum of the two rotors, $\mathbf{j}_1$ and $\mathbf{j}_2$, to form $\mathbf{j}_{12}$, the total internal angular momentum. Then $\mathbf{j}_{12}$ is coupled to the orbital angular momentum $\mathbf{l}$ to form the total angular momentum $\mathbf{J}$. This leads to the total angular momentum representation. Next, the angular wavefuntion can be represented as follow:

$$\begin{aligned}\varphi^{JM}_{j_1 j_2 j_{12} l}(\hat{\boldsymbol{\rho}}_1, \hat{\boldsymbol{\rho}}_2, \hat{\mathbf{R}}) = \sum_{m_{j_1} m_{j_2} m_{j_{12}} m_l} & (j_1 m_1 j_2 m_2 | j_{12} m_{12})(j_{12} m_{12} l m_l | JM) \\ & \times Y_{j_1 m_{j1}}(\hat{\boldsymbol{\rho}}_1) Y_{j_2 m_{j2}}(\hat{\boldsymbol{\rho}}_2) Y_{l m_l}(\hat{\mathbf{R}})\end{aligned} \tag{5.3}$$

Thus $\mathbf{j}_1 + \mathbf{j}_2 = \mathbf{j}_{12}$ and $\mathbf{j}_{12} + \mathbf{l} = \mathbf{J}$.

Another conservation law is associated with the parity of the total Hamiltonian eigenfunctions.

$$P|j_1 j_2 j_{12} l J M\rangle = (-1)^{j_1+j_2+l} |j_1 j_2 j_{12} l J M\rangle \tag{5.4}$$

The eigenfunctions of the total Hamiltonian present a definite total angular momentum and parity. They can be written as follow,

$$\Psi^{JM}(\mathbf{R}, \hat{\boldsymbol{\rho}}_1, \hat{\boldsymbol{\rho}}_2) = \sum_{j_1 j_2 j_{12} l} R^{-1} U^{JM}_{j_1 j_2 j_{12} l}(R) \varphi^{JM}_{j_1 j_2 j_{12} l}(\hat{\boldsymbol{\rho}}_1, \hat{\boldsymbol{\rho}}_2, \hat{\mathbf{R}}) \tag{5.5}$$

where we have expanded over the angular basis 5.3.

Using the expansion 5.5, the total Schrödinger equation is transformed into the usual CC equations:

$$\begin{aligned} \left[\frac{d^2}{dR^2} - \frac{l(l+1)}{R^2} + k^2_{j_1 j_2} \right] U^{J\gamma}_{\gamma'}(R) = \\ 2\mu \sum_{\gamma''} V^J_{\gamma',\gamma''}(R) U^{J\gamma}_{\gamma''} \end{aligned} \tag{5.6}$$

where $\gamma = (j_1, j_2, j_{12}, l)$ and μ is the reduced mass of the system and $k_{j_1 j_2}$ can be written as,

$$k_{j_1 j_2} = [2\mu(E - E_{j_1} - E_{j_2})]^{\frac{1}{2}} \ . \tag{5.7}$$

In the last expression, E and E_{j_i} refer to the total energy and to the internal energy of the molecule i. In order to compute the potential matrix, it is convenient to expand the interaction potential in a triple series of spherical harmonics

$$V(\hat{\boldsymbol{\rho}}_1, \hat{\boldsymbol{\rho}}_2, \mathbf{R}) = \sum_{L_1 L_2 L} A_{L_1 L_2 L}(R) \sum_{M_1 M_2 M} Y_{L_1 M_1}(\hat{\boldsymbol{\rho}}_1) Y_{L_2 M_2}(\hat{\boldsymbol{\rho}}_2) Y_{LM}(\hat{\mathbf{R}}) \tag{5.8}$$

Using this expansion the coupling matrix elements are obtained by integrating the interaction potential over all coordinates except R:

$$V^J_{\gamma,\gamma'}(R) = \sum_{L_1 L_2 L} A_{L_1,L_2,L}(-1)^{J+j_1+j_2+j'_{12}}(4\pi)^{-\frac{3}{2}}$$
$$\times[L][L_1 L_2 j_1 j_2 j_{12} l j'_1 j'_2 j'_{12} l']^{\frac{1}{2}} \begin{pmatrix} L & l' & l \\ 0 & 0 & 0 \end{pmatrix} \begin{pmatrix} L_1 & j'_1 & j_1 \\ 0 & 0 & 0 \end{pmatrix} \begin{pmatrix} L_2 & j'_2 & j_2 \\ 0 & 0 & 0 \end{pmatrix}$$
$$\times \begin{Bmatrix} l' & l & L \\ j_{12} & j'_{12} & J \end{Bmatrix} \begin{Bmatrix} j'_{12} & j'_2 & j'_1 \\ j_{12} & j_2 & j_1 \\ L & L_2 & L_1 \end{Bmatrix} \tag{5.9}$$

where $[a, b, ..] = (2a + 1)(2b + 1)...$ and the last term in the right side of equation is a $9 - j$ symbol. Besides being diagonal in J and independent of M, there is no coupling between channels of different parity. Solutions of Eq. 5.6, subject to the boundary conditions

$$U^{J\gamma}_{\gamma'}(R) \underset{R\to 0}{\sim} 0$$
$$U^{J\gamma}_{\gamma'}(R) \underset{R\to\infty}{\sim} \delta_{\gamma,\gamma'} e^{-i(k_{j_1 j_2} R - \frac{1}{2} l\pi)} - \left(\frac{k_{j_1 j_2}}{k_{j'_1 j'_2}}\right)^{\frac{1}{2}} S^J_{\gamma,\gamma'} e^{+i(k_{j'_1 j'_2} R - \frac{1}{2} l'\pi)} \tag{5.10}$$

define the scattering matrix S^J.

Cross sections for the rotational excitation and relaxation phenomena can be obtained directly from the S matrices. Cross sections for the $j_1 j_2 \to j'_1 j'_2$ transition is obtained as follow:

$$\sigma(j_1 j_2 \to j'_1 j'_2) = \frac{\pi}{(2j_1 + 1)(2j_2 + 1)k_{j_1 j_2}} \sum_{J j_{12} j'_{12} l l'} (2J + 1)|T^J_{\gamma,\gamma'}(E)|^2 \tag{5.11}$$

5.3 Results

THE JOURNAL OF CHEMICAL PHYSICS **140**, 224302 (2014)

Rotational excitation of HCN by para- and ortho-H_2

Mario Hernández Vera,[1,2,a)] Yulia Kalugina,[1,3] Otoniel Denis-Alpizar,[4,5] Thierry Stoecklin,[4] and François Lique[1,b)]
[1] *LOMC - UMR 6294, CNRS-Université du Havre, 25 rue Philippe Lebon, BP 1123, 76 063 Le Havre cedex, France*
[2] *InSTEC, Quinta de Los Molinos, Plaza, La Habana 10600, Cuba*
[3] *Tomsk State University, 36 Lenin av., Tomsk 634050, Russia*
[4] *Université de Bordeaux, ISM, CNRS UMR 5255, 33405 Talence Cedex, France*
[5] *Departamento de Física, Universidad de Matanzas, Matanzas 40100, Cuba*

(Received 8 April 2014; accepted 19 May 2014; published online 9 June 2014)

Rotational excitation of the hydrogen cyanide (HCN) molecule by collisions with para-$H_2(j = 0, 2)$ and ortho-$H_2(j = 1)$ is investigated at low temperatures using a quantum time independent approach. Both molecules are treated as rigid rotors. The scattering calculations are based on a highly correlated *ab initio* 4-dimensional (4D) potential energy surface recently published. Rotationally inelastic cross sections among the 13 first rotational levels of HCN were obtained using a pure quantum close coupling approach for total energies up to 1200 cm^{-1}. The corresponding thermal rate coefficients were computed for temperatures ranging from 5 to 100 K. The HCN rate coefficients are strongly dependent on the rotational level of the H_2 molecule. In particular, the rate coefficients for collisions with para-$H_2(j = 0)$ are significantly lower than those for collisions with ortho-$H_2(j = 1)$ and para-$H_2(j = 2)$. Propensity rules in favor of even Δj transitions were found for HCN in collisions with para-$H_2(j = 0)$ whereas propensity rules in favor of odd Δj transitions were found for HCN in collisions with $H_2(j \geq 1)$. The new rate coefficients were compared with previously published HCN-para-$H_2(j = 0)$ rate coefficients. Significant differences were found due the inclusion of the H_2 rotational structure in the scattering calculations. These new rate coefficients will be crucial to improve the estimation of the HCN abundance in the interstellar medium. © *2014 AIP Publishing LLC*. [http://dx.doi.org/10.1063/1.4880499]

I. INTRODUCTION

Excitation of rotational and vibrational degrees of freedom during molecular collisions lead to changes in translational kinetic energy in many media. During the last decade, many studies were focused on considering the inclusion of accurate collisional cross sections in the kinetic equations of the gas.[1–3] The inclusion of the energy dependent cross sections, neglected in previous simplest kinetic models, is essential to understand energy relaxation process as it is clearly illustrated for atmospherical applications by Huestis *et al.*[4] Then, to understand this process, the knowledge of accurate rate coefficients for ion-neutral and neutral-neutral collisions is becoming increasingly important, as there is evidence of more internal excitation of molecular species than had previously been thought.

In this work, we investigate the rotational (de-)excitation processes during collisions between hydrogen cyanide (HCN) and H_2 (both para- and ortho-H_2) molecules. Both, the H_2 and HCN molecules are important in many applications. In particular, in combustion applications, HCN is an important intermediate in the reactions of hydrocarbon flames containing a nitrogen source (NO_x).[5,6] HCN is also considered as a key molecule in prebiotic chemistry and a potential source of fixed nitrogen in the early biosphere.[7] Additionally, HCNs have been widely observed in extraterrestrial sources, such as comets,[8] cold molecular clouds,[9,10] circumstellar envelopes,[11] and active galaxies.[12] It is also among the few molecules detected in high-redshifted galaxies, along with CO, CN, and HCO^+ molecules.[13] HCN can be used as a tracer of the dense interior of molecular clouds where key dynamical processes take place. Very recently, the Atacama Large Millimeter/submillimeter Array (ALMA) interferometer and the Herschel Space Observatory have collected new HCN emission spectra from molecular clouds like Sgr A*,[14] from circumstellar envelope like IRC+10216,[15] but also from more distant objects like external galaxies.[16,17]

Modeling of molecular emission spectra from interstellar medium (ISM) requires the use of inelastic rate coefficients for collisional (de-)excitation by collisions with H_2, the most abundant interstellar collisional partner.[18] Without these rate coefficients, estimation of the physical and chemical conditions of molecular clouds can be done only assuming local thermodynamic equilibrium (LTE), which is generally not a good approximation.

The first study of collisional excitation of HCN by He [as a model for H_2] was performed in the 1970s by Green and Thaddeus.[19] Then, Monteiro and Stutzki[20] obtained collisional excitation cross sections among the hyperfine structure of the HCN molecule using the limited uniformed electron gas model[21] for describing the HCN–He interaction.

Recently, Sarrasin *et al.*[22] and Dumouchel *et al.*[23] published new accurate HCN–He rate coefficients between the

---

a)marhvera@gmail.com
b)francois.lique@univ-lehavre.fr

first 26 rotational states and for temperatures ranging from 5 to 500 K. These data cover most of physical conditions where the HCN molecule can be observed. Data for collisions involving para-$H_2(j = 0)$ instead of He have been extrapolated by using the ratio of the reduced mass.[24] However, the accuracy of this widely used approximation is known to be unpredictable as has been previously found for the rotational excitation of CO,[25] SO,[26] or CN[27] molecules. Besides, the ortho-H_2 isomer, which is also present in the ISM, cannot be modeled from He data. Taking into account the importance of the HCN molecule for interstellar chemistry, it seems very important to compute accurate HCN–H_2 rate coefficients.

Hence, Ben Abdallah *et al.*[28] have recently computed new rate coefficients for the rotational and hyperfine (de-)excitation of HCN by para-$H_2(j = 0)$ using a potential energy surface (PES) averaged over the H_2 orientations. Although this work improved the accuracy of thermal rates in comparison with the results obtained from collisions with He, the calculations considered H_2 as a structureless collisional partner. The results of this approximation can differ from those obtained using a most rigorous treatment, as we will demonstrate in the present work. In addition, ortho-H_2 rate coefficients are still not available. Accurate calculations with para- and ortho-H_2 requires the use of a new PES taking fully into account the orientation of the H_2 molecule, and then, scattering calculations which consider the rotational structure of both species.

While being computationally expensive, the determination of rate coefficients for collisions of rigid polyatomic molecules with diatomic molecules can be now performed using a close coupling (CC) approach as it has been recently done, for example, for the HNC–H_2 collisional system.[29] In this work, we use a new four dimensional PES for the ground electronic state of the HCN–H_2 collisional system to investigate the rotational excitation of HCN with both para-H_2 and ortho-H_2. Collisional cross sections for the first 13 rotational levels of HCN in collision with $H_2(j = 0 - 2)$ are reported for total energies up to 1200 cm^{-1}, yielding to rate coefficients up to 100 K.

The paper is organized as follows: Section II details the scattering calculations and Sec. III presents and discusses our results. Conclusions are given in Sec. IV.

II. SCATTERING CALCULATIONS

A. Potential energy surface

In our scattering calculations, we employed the recently computed HCN–H_2 PES of Denis-Alpizar *et al.*[30] The accuracy of the new PES was estimated by comparing theoretical HCN–H_2 transition frequencies with the experimental ones of Ishiguro *et al.*[31,32] The agreement between the theoretical and experimental results was found to be better than 0.5% showing that the PES can be used with confidence for the scattering calculations.

We will briefly remind the features of the HCN-H_2 PES and we refer the reader to Ref. 30 for more details. The *ab initio* calculations were performed using the Jacobi coordinate system. In such coordinate system, the vector **R** connects the centers of mass of HCN and H_2 while the rotation of HCN and H_2 molecules is defined by θ and θ' angles, respectively, and ϕ is the dihedral angle (see Fig. 1 of Ref. 30).

The *ab initio* PES has been calculated using the explicitly correlated coupled cluster with single, double, and perturbative triple excitations [CCSD(T)-F12a] method with an augmented correlation-consistent triple zeta (aVTZ) basis set. The use of explicitly correlated coupled clusters methods for generating van der Waals complex PES has been investigated in detail by Lique *et al.*[33] and Ajili *et al.*[34] The theoretical approach used in Ref. 30 is an extension to the case of two rigid rotors of the methodology used by Ajili *et al.*[34] Then, it is expected that the present PES calculated at the CCSD(T)-F12a level together with diffuse basis set of aVTZ quality fully reaches the CCSD(T)/CBS accuracy. Both molecules were treated as rigid rotors fixing the internuclear distances of H_2 and HCN at its averaged and experimental equilibrium values, respectively: $r_{HH} = 1.448\ a_0$ for H_2 and $r_{CN} = 2.179\ a_0$ and $r_{CH} = 2.013\ a_0$ for HCN. The equilibrium structure is linear with the nitrogen of HCN pointing towards H_2 at an intermolecular separation of 7.20 a_0. The corresponding well depth is $-195.20\ \text{cm}^{-1}$. A secondary minimum of $-183.59\ \text{cm}^{-1}$ was found for a T-shape configuration with the H of HCN pointing towards the center of mass of H_2. Such conclusions are in good agreement with the experimental findings of Moore *et al.*[35] that conclude that linear HCN–H_2 is the most stable geometry of the complex.

Then, in order to solve the close-coupling equations for scattering, the PES $V(R, \theta, \theta', \phi)$ was expanded over angular functions for all R-distance using the following expression:[36]

$$V(R, \theta, \theta', \phi) = \sum_{l_1,l_2,l} v_{l_1,l_2,l}(R) A_{l_1,l_2,l}(\theta, \theta', \phi), \qquad (1)$$

where $A_{l_1,l_2,l}(\theta, \theta', \phi)$ is formed from coupled spherical functions associated with the rotational angular momenta of HCN and H_2. In Eq. (1), the index l_2 is even because H_2 is homonuclear. To construct the above expansion, at each point of the radial grid R we have fitted the *ab initio* points using a linear least squares method using $l_1^{max} = 17$ and $l_2^{max} = 4$.

The quality of the fitted procedure was checked by evaluating the root-mean-square (RMS) of the differences between the *ab initio* and the fitted energies. For negative energies, the RMS was of the order of $10^{-4}\ \text{cm}^{-1}$ while for energies in the range $0 \leq E \leq 1000\ \text{cm}^{-1}$, it is about 0.008 cm^{-1}.

B. Collision dynamics

In this paper, we investigate the following inelastic collision process:

$$\text{HCN}(j_1) + \text{o;p}-\text{H}_2(j_2) \rightarrow \text{HCN}(j_1') + \text{o;p}-\text{H}_2(j_2'), \qquad (2)$$

where j_1 and j_2 represent the rotational energy levels of HCN and H_2, respectively. p-H_2 and o-H_2 designate para-H_2 and ortho-H_2. Note that the para–ortho-H_2 conversion is forbidden during the collisions.

The rotational levels of HCN and H_2 were obtained using the experimental spectroscopic constants from Huber and Herzberg.[37]

TABLE I. Influence of the para-H_2 rotational basis on the convergence of the cross sections (Å^2) for selected transitions and for 3 total energies. The numbers in parentheses indicate the H_2 rotational basis.

Transition	E = 100 cm^{-1}			E = 500 cm^{-1}			E = 1000 cm^{-1}		
j_2,j_1 → j_2',j_1'	(0)	(0–2)	(0–4)	(0)	(0–2)	(0–4)	(0)	(0–2)	(0–4)
0,1 → 0,0	1.793	2.081	2.081	0.588	0.689	0.690	0.365	0.414	0.414
0,2 → 0,0	5.712	5.508	5.501	2.769	2.924	2.925	2.002	2.036	2.033
0,3 → 0,0	1.236	1.409	1.409	0.261	0.265	0.265	0.174	0.171	0.171
0,3 → 0,1	0.214	0.244	0.244	4.781	4.963	4.965	3.612	3.632	3.626
0,3 → 0,2	2.931	3.394	3.396	1.601	1.664	1.663	1.041	1.073	1.070
0,5 → 0,3	13.359	12.107	12.844	5.841	6.073	6.074	4.528	4.506	4.494
0,10 → 0,8	...	...	...	7.131	7.467	7.471	5.065	5.106	5.096
0,10 → 0,9	...	...	...	1.909	1.933	1.929	1.496	1.459	1.449
2,1 → 0,2	...	...	...	...	0.023	0.026	...	0.085	0.095
2,2 → 0,0	...	...	...	...	0.020	0.023	...	0.007	0.007
2,2 → 0,1	...	...	...	...	0.014	0.015	...	0.047	0.052
2,2 → 2,1	...	...	...	...	18.355	18.493	...	6.177	6.205
2,3 → 2,1	...	...	...	...	4.976	4.981	...	3.340	3.366
2,5 → 0,4	...	...	...	...	0.014	0.016	...	0.047	0.053
2,5 → 2,3	...	...	...	...	6.999	7.016	...	4.186	4.204
2,5 → 2,4	...	...	...	...	24.625	24.761	...	7.759	7.782
2,10 → 0,8	...	...	...	...	...	...	...	0.023	0.026
2,10 → 0,9	...	...	...	...	...	...	...	0.036	0.041
2,10 → 2,8	...	...	...	...	...	...	...	4.805	4.756
2,10 → 2,9	...	...	...	...	...	...	...	9.699	9.703

We used the quantum CC approach to obtain the inelastic cross sections. The standard time-independent coupled scattering equations were solved using the MOLSCAT code developed by Hutson and Green.[38] The calculations were performed employing the propagator of Manolopoulos.[39] The reduced mass of the system is 1.876 amu. The collisions were studied at values of the total energy ranging from 3 to 1200 cm^{-1} for collision of HCN with para-H_2 and from 121.6 to 1200 cm^{-1} for collision of HCN with ortho-H_2. The integration parameters were chosen to ensure convergence of the cross sections over this range. In most of the calculations, the integration range extended from 4 to 40 bohrs. At the lowest energies, the integration range was extended to 50 bohrs in order to fully converge the cross sections. The rotational basis was increased up to $j_1 = 18$ at the largest total energy in order to ensure the convergence of the 13 first (up to $j_1 = 12$) rotational levels of HCN. Additionally, the maximum value of the total angular momentum J was set large enough to converge the inelastic cross sections to within 0.02 Å^2.

From the rotationally inelastic cross sections $\sigma_{j_1 j_2 \to j_1' j_2'}$ one can compute the corresponding thermal rate coefficients at a temperature T by a Maxwellian average over the collision energy (E$_K$),

$$k_{j_1 j_2 \to j_1' j_2'}(T) = \left(\frac{8}{\pi \mu k_B^3 T^3}\right)^{\frac{1}{2}} \times \int_0^\infty \sigma_{j_1 j_2 \to j_1' j_2'}(E_K) E_K e^{(-E_K/k_B T)} dE_K, \tag{3}$$

where k_B is the Boltzmann constant and μ is the reduced mass. To obtain precise values for the rate constants, the energy grid was chosen to be sufficiently fine to include the numerous scattering resonances which will be described below. Calculations with the range of total energies mentioned above allow us to determine rate coefficients up to 100 K.

III. RESULTS

A large number of channels have to be taken into account in the scattering calculations because of the coupling between the angular momenta of both molecules. Therefore, it is crucial to optimize the rotational basis of H_2 in order to keep calculations feasible. Tests of the para-H_2 and ortho-H_2 basis were performed at different values of total energy. The convergence tests are presented in Tables I and II for para- and ortho-H_2, respectively. For collisions with para-$H_2(j_2 = 2)$, it is found that inclusion of the $H_2(j_2 = 4)$ channel is not needed to obtain convergence at more than 5%–10%. Hence, we have retained, for the determination of rotational excitation cross section of HCN in collision with para-H_2, only the $H_2(j_2 = 0, 2)$ rotational basis. For ortho-$H_2(j_2 = 1)$, it was found that inclusion of the $H_2(j_2 = 3)$ channels affect cross sections by less than 5%. Thus, for the determination of rotational excitation cross section of HCN in collision with ortho-H_2, only the $H_2(j_2 = 1)$ basis was retained.

Figure 1 shows the collisional energy dependence of the de-excitation integral cross sections of HCN in collision with para-$H_2(j_2 = 0, 2)$ and ortho-$H_2(j_2 = 1)$. The resonances that appear for energies lower than 100 cm^{-1} are related to the presence of the attractive potential wells at the T-shape and linear geometry configurations, which allows quasi-bound states to be formed before the complex dissociates. Quasi-bound states may arise from tunneling through the centrifugal energy barrier (shape resonances) or from excitation

TABLE II. Influence of the ortho-H_2 rotational basis on the convergence of the cross sections (Å^2) for selected transitions and for 3 total energies. The numbers in parentheses indicate the H_2 rotational basis.

Transition	E = 200 cm^{-1}		E = 500 cm^{-1}		E = 1000 cm^{-1}	
$j_2,j_1 \rightarrow j_2',j_1'$	(1)	(1–3)	(1)	(1–3)	(1)	(1–3)
1,1 → 1,0	16.931	16.870	7.545	7.609	4.112	4.107
1,2 → 1,0	4.821	4.900	2.415	2.481	1.684	1.721
1,2 → 1,1	24.942	24.922	10.795	10.882	5.954	5.954
1,3 → 1,0	1.888	1.828	0.926	0.933	0.554	0.558
1,5 → 1,2	5.186	5.058	1.953	1.958	1.457	1.447
1,5 → 1,3	14.240	14.192	5.362	5.409	3.895	3.949
1,5 → 1,4	41.785	42.004	13.072	13.142	7.299	7.270
1,7 → 1,6	...	...	14.629	14.690	7.746	7.698
1,10 → 1,8	...	...	6.776	6.835	4.469	4.519
1,10 → 1,9	...	...	18.422	18.485	8.580	8.523

of the HCN–H_2 complex to a bend-stretch level that is energetically accessible but is asymptotically closed (Feschbach resonances). At first, it seems that the resonances are more pronounced for cross sections with para-$H_2(j_2 = 0)$ than the collisions with $H_2(j_2 \geq 1)$. Nonetheless, Denis-Alpizar *et al.*[30] reported that the total number of bound states for HCN–para-$H_2(j_2 = 0)$ is 101 whereas for the HCN–ortho-$H_2(j_2 = 1)$ 330 bound states were founded. There are around three times more states for the ortho form than for the para form of the complex. This generates more and hence overlapping resonances for the case of collisions with ortho-H_2, leading to the effect of continuous behavior in the integral cross-sections for collisions with ortho-$H_2(j_2 = 1)$.

We also found important differences between collisions with the two H_2 species. The cross sections for collisions with $H_2(j_2 > 0)$ are up to 3 times larger than those with $H_2(j_2 = 0)$. Additionally, the cross sections for collisions with $H_2(j_2 = 1)$ and $H_2(j_2 = 2)$ are quite similar. The origin of this behavior can be explained by the magnitude of the radial coefficients $v_{l_1 l_2 l}(R)$ of Eq. (1). The radial coefficients that mainly contribute to cross sections with $j_2 \rightarrow j_2'$ transitions are those with l_2 in the $|j_2 - j_2'| < l_2 < |j_2 + j_2'|$ range. Hence, for collisions with ortho-H_2 ($j_2 = 1$), only the $l_2 = 0$, 2 terms contribute whereas for collisions with para-$H_2(j_2 = 2)$, the $l_2 = 0$, 2, 4 terms contribute. The fact that the radial expansion terms with $l_2 = 4$ are significantly lower than the one with $l_2 = 0,2$ leads to similar behavior in the excitation process with $H_2(j_2 = 1)$ and $H_2(j_2 = 2)$. The radial coefficients with $l_2 = 2$ are not negligible compared to the one with $l_2 = 0$ which also explain the difference for collisions with $H_2(j_2 = 0)$ and $H_2(j_2 = 1)$. This trend was already observed for the isomer HNC[29] and for several interstellar species like SiS,[40] CO,[41] or HCl.[42] The significant j_2 dependence of the cross sections is due to the large anisotropy of the PES with respect to H_2 rotations (see Ref. 30).

Moreover, cross sections for j_2 changing transitions are up to three orders of magnitude smaller than cross sections for j_2 conserving transitions. This is expected if we remind that the rotational constant of H_2 is an order of magnitude larger than the one of HCN. Therefore, the energy gap between H_2 rotational levels is much more important than for HCN so that

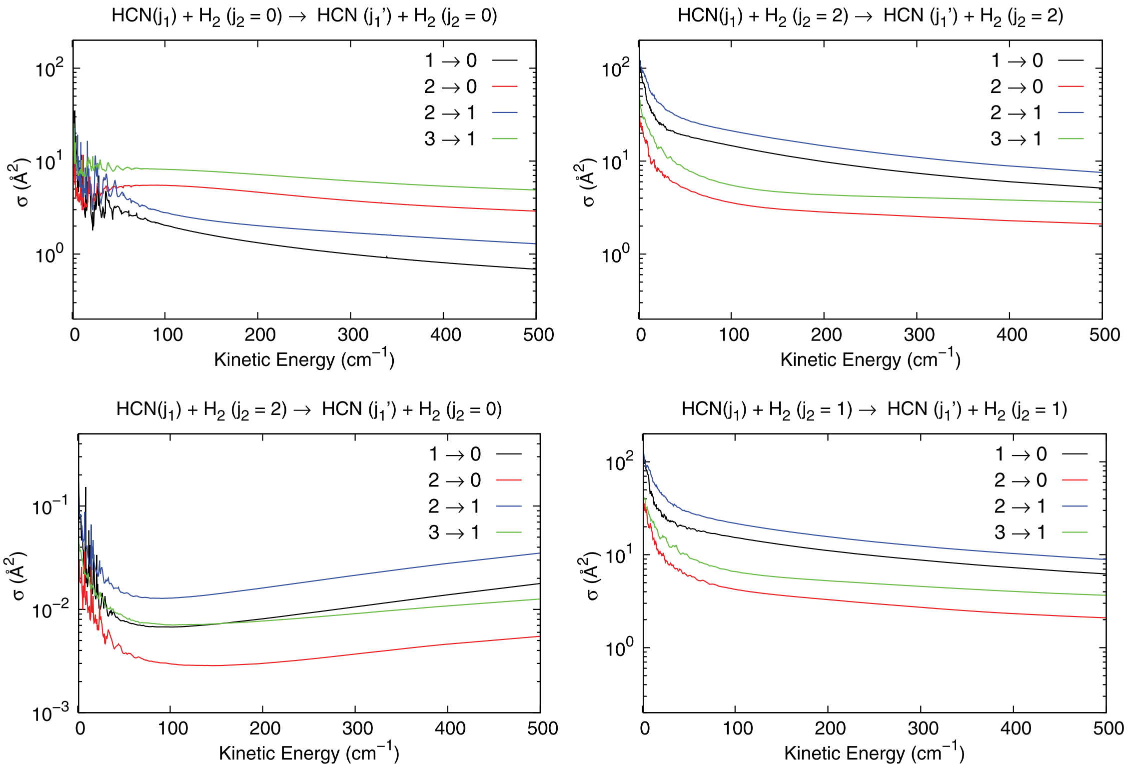

FIG. 1. Kinetic energy dependence of the cross section for collisions of HCN with para- and ortho-$H_2(j_2 = 0$–$2)$.

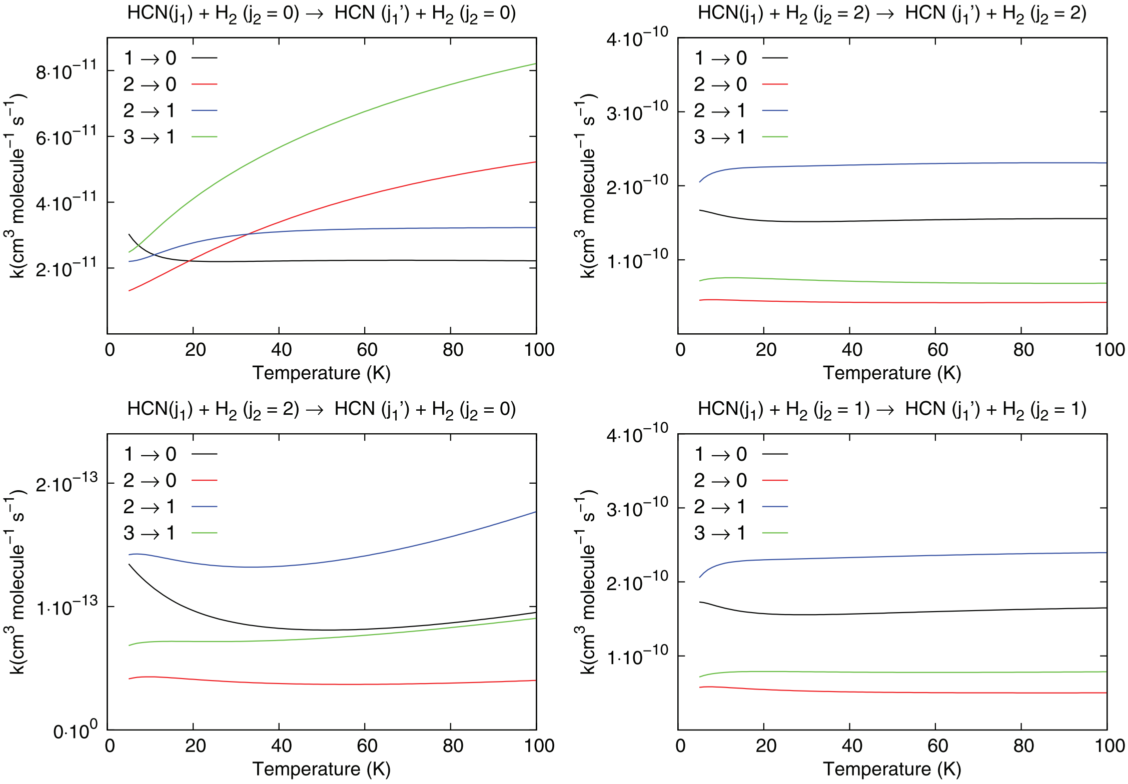

FIG. 2. De-excitation rate coefficients as a function of temperature for collisions of HCN with para- and ortho-$H_2(j_2 = 0–2)$.

the probability of rotational transitions in this molecule is very low.

The calculated inelastic cross sections were used to obtain excitation and de-excitation rate coefficients between the 13 first ($j_1 = 0–12$) rotational levels of HCN due to collisions with $H_2(j_2 = 0–2)$. Figure 2 shows the rate coefficients as a function of temperature in the 5–100 K temperature range. The rate coefficients obviously display the same behavior as the integral cross sections. In particular, the rate coefficients for collisions with $H_2(j_2 = 0)$ and $H_2(j_2 > 0)$ differ significantly.

Then, we were interested in illustrating the propensity rules of pure HCN rotational transitions. Figure 3 shows (de-)excitation rotational rate coefficients out of HCN(j_1 = 10) level at 10 and 100 K due to collisions with both para- and ortho-H_2. The propensity depends on the quantum state of the H_2 molecule. The highlight is the difference that exists between collisions with $H_2(j_2 = 0)$ and $H_2(j_2 = 1, 2)$. Collisions with $H_2(j_2 = 0)$ show a remarkable propensity rules in favor of even Δj_1 transitions while for collisions with $H_2(j_2 = 1)$ and $H_2(j_2 = 2)$, a strong propensity in favor of $\Delta j_1 = 1$ transition is observed. Rate coefficients for collisions with $H_2(j_2 = 0)$ and $H_2(j_2 = 1, 2)$ differ up to one order of magnitude for transitions with $\Delta j_1 = 1$. The explanation of such behavior could be found in the features of the PES. As already shown by Denis-Alpizar *et al.*,[30] the averaged potential over the rotational wave function of $H_2(j_2 = 0)$ shows a larger near-homonuclear symmetry in comparison with the potential obtained by averaging over the rotational wave function of ortho-$H_2(j_2 = 1)$. Indeed, this feature in the PES will

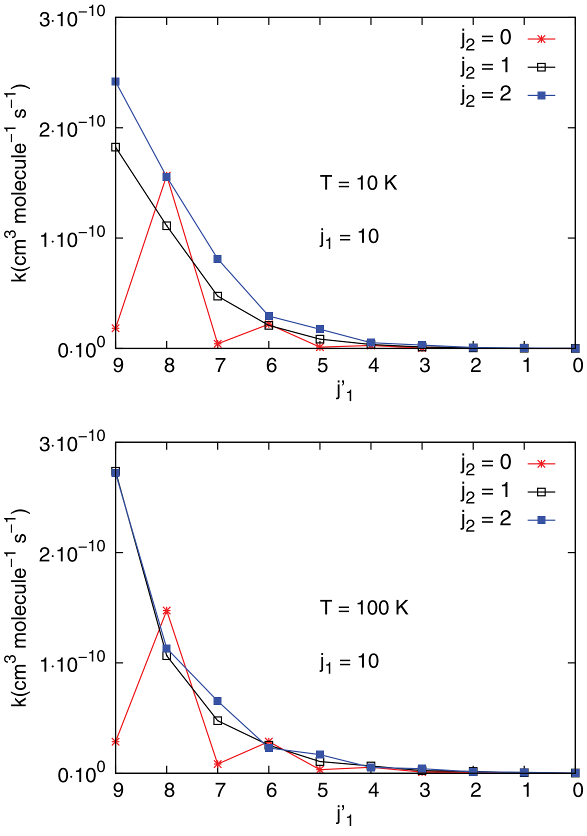

FIG. 3. Propensity rules for transitions out of the initial j_1=10 state of the HCN molecule in collisions para- and ortho-H_2 collisions for T = 10 and 100 K.

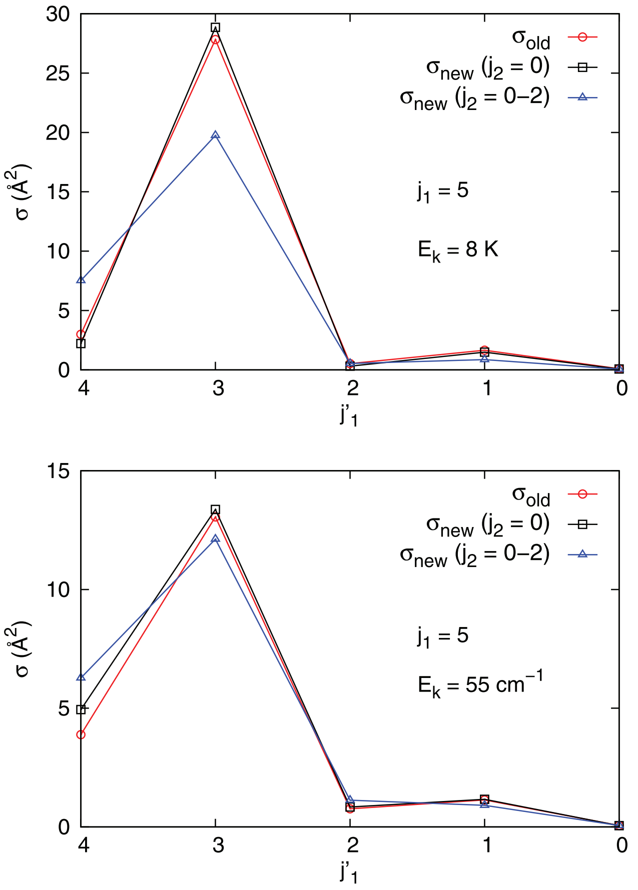

FIG. 4. Comparisons between de-excitation cross sections obtained from the present calculations (σ_{new}) including $j_2 = 0$ and $j_2 = 0$–2 basis, and the results from Ben Abdallah *et al.*[28] (σ_{old}).

favor transitions with even Δj_1 for collisions with $H_2(j_2 = 0)$ and transitions with $\Delta j_1 = 1$ for collisions with $H_2(j_2 > 1)$ as expected from theoretical considerations.[43]

Finally, we compare in Fig. 4 our present de-excitation cross sections (including only $j_2 = 0$ and $j_2 = 0$–2 basis) with those obtained by Abdallah *et al.*[28] using a PES averaged over H_2 rotations and carrying out scattering calculations that did not include coupling with $j_2 = 2$ levels of H_2. The agreement between present calculations (including only $j_2 = 0$) and those of Ben Abdallah *et al.*[28] is extremely good for all the collisional energy range explored in this work. Such agreement can be explained by the similar shape of the average PESs used in both cases. Indeed, despite Ben Abdallah *et al.*[28] used "only" a CCSD(T) method and aVTZ basis set augmented by bond functions, the average PES employed in this work, with a minimum of 79.23 cm^{-1}, is only about 8 cm^{-1} deeper than the one presented by Ben Abdallah *et al.*[28] The secondary minimum obtained in both cases for a value of θ close to 60°, differ by only about 1 cm^{-1}. Then, the agreement shows that the cross sections are not extremely sensitive to the PES accuracy in the intermediate collisional energy range considered in this work.

However, the inclusion of $H_2(j_2 = 2)$ in the H_2 rotational basis significantly impacts the magnitude of the cross sections so that old and new results diverge by a factor up to 2. Hence, in this case, it is necessary to retain the $H_2(j_2 = 2)$ rotational state in the rotational basis in order to get full convergence of the scattering calculations. When the collision energy increases, so that the kinetic energy is comparable or greater than the well depth of the potential, the coupling between H_2 rotational channels become less important. For this reason we can see in Fig. 4 that at moderate collisional energies the difference is less pronounced that at low energies.

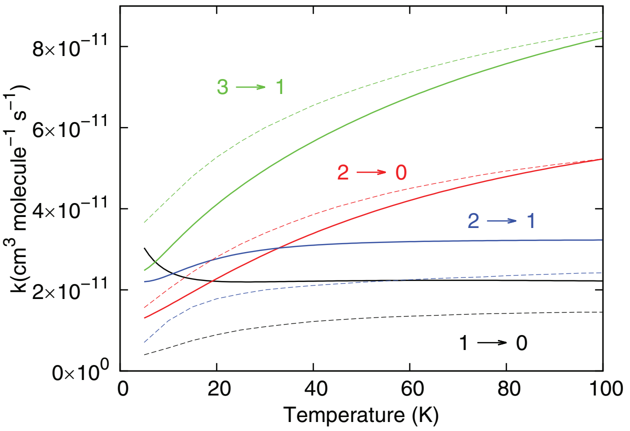

FIG. 5. Comparisons between de-excitation rate coefficients obtained from present calculation (continuous line) and results from Ben Abdallah *et al.*[28] (dashed line).

The inclusion of $j_2 = 2$ channel leads to rate coefficients that differ up to 50% from those of Ben Abdallah *et al.*[28] as one can see in Fig. 5. In particular, odd and even Δj_1 transitions are not affected by the same effect. Rate coefficients for $\Delta j_1 = 1$ transitions increase due to the use of full H_2 basis whereas rate coefficients for $\Delta j_1 = 2$ transitions decrease due to the use of full H_2 basis. This suggests that an accurate description of the inelastic collision of HCN by para-$H_2(j_2 = 0)$ should consider the rotational structure of H_2 especially at low temperatures.

IV. SUMMARY AND CONCLUSIONS

In this work, we have investigated rotational energy transfer in collisions of the HCN molecule with para-$H_2(j_2 = 0, 2)$ and ortho-$H_2(j_2 = 1)$ molecules. We have carried out 4-dimensional quantum close coupling scattering calculations based on a new reliable 4-dimensional *ab initio* potential energy surface for the HCN–H_2 complex. Integral cross sections for transitions involving the 13 lowest levels of the HCN molecule and $H_2(j_2 = 0$–$2)$ molecules were determined for total energies up to 1200 cm^{-1}. Corresponding rate coefficients were given for temperatures ranging from 5 to 100 K.

The results show that the cross sections and rate coefficients are dependent on the rotational level of H_2. The cross sections and rate coefficients for collisions with $H_2(j_2 = 0)$ are lower than the ones for collisions with $H_2(j_2 = 1, 2)$. We have also found that calculations with the PES averaged over H_2 rotations can induce important deviations in the cross sections and then in the rate coefficients. This suggests that the rotational structure of H_2 should not be neglected when studying the rotational excitation of the HCN molecule by H_2.

Finally, for collisions with $H_2(j_2 = 0)$, we found propensity rules in favor of even Δj_1 for HCN transitions whereas the propensity rules of the isomer HNC in collisions with $H_2(j_2 = 0)$ are in favor of transitions with $\Delta j_1 = 1$ as reported in Ref. 29. Hence, it confirms that the collisional excitation of the two isomers is very different in cold ISM where para-$H_2(j_2 = 0)$ is the most abundant collisional partner. In cold dark clouds, the modeling of the HCN and HNC line intensities from radiative transfer calculations will require to take into account different rate coefficients of the two isomers. The present data will help in this project. Indeed, we expect that these results can be used to improve the HNC/HCN abundance ratio estimation.

Finally, the present calculations will be extended to higher rotational levels and temperature to cover the astrophysical needs, especially for the interpretation of the observations of warm ISM.

ACKNOWLEDGMENTS

This research was supported by the CNRS national program "Physique et Chimie du Milieu Interstellaire." M.H.V. acknowledges the French Embassy in Cuba for financial support. M.H.V., Y.K., and F.L. thank the CPER Haute-Normandie/CNRT/Energie, Electronique, Matériaux. Y.K. acknowledges Tomsk State University Competitiveness Improvement Program.

[1] A. Sizhuk and S. Yezhov, J. Mol. Liq. **127**, 84 (2006).
[2] I. Shishkova and S. Sazhin, Int. J. Heat Mass Transfer **71**, 26 (2014).
[3] G. M. Kremer, A. W. Silva, and G. M. Alves, Physica A **389**, 2708 (2010).
[4] D. L. Huestis, S. W. Bougher, J. L. Fox, M. Galand, R. E. Johnson, J. I. Moses, and J. C. Pickering, "Cross sections and reaction rates for comparative planetary aeronomy," in *Comparative Aeronomy*, edited by A. F. Nagy, A. Balogh, T. E. Cravens, M. Mendillo, and I. Mueller-Wodarg (Springer, New York, 2009), p. 63.
[5] L. D. Smoot, S. C. Hill, and H. Xu, Prog. Energy Combust. Sci. **24**, 385–408 (1998).
[6] B. Shen, Q. Yao, and X. Xu, Fuel Process. Technol. **85**, 1301 (2004).
[7] F. Tian, J. Kasting, and K. Zahnle, Earth Planet. Sci. Lett. **308**, 417 (2011).
[8] D. C. Lis, J. Keene, K. Young, T. G. Phillips, D. Bockelee-Morvan, J. Crovisier, P. Schilke, P. F. Goldsmith, and E. A. Bergin, Icarus **130**, 355 (1997).
[9] B. E. Turner, L. Pirogov, and Y. C. Minh, Astrophys. J. **483**, 235 (1997).
[10] J. Hatchell, T. J. Millar, and S. D. Rodgers, Astron. Astrophys. **332**, 695 (1998).
[11] J. Cernicharo, M. J. Barlow, E. Gonzalez-Alfonso, P. Cox, P. E. Clegg, Nguyen-Q-Rieu, A. Omont, M. Guelin, X.-W. Liu, R. J. Sylvester, T. Lim, M. J. Griffin, B. M. Swinyard, S. J. Unger, P. A. R. Ade, J.-P. Baluteau, E. Caux, M. Cohen, R. J. Emery, J. Fischer, I. Furniss, W. M. Glencross, M. A. Greenhouse, C. Gry, M. Joubert, D. Lorenzetti, B. Nisini, R. Orfei, D. Pequignot, P. Saraceno, G. Serra, C. J. Skinner, H. A. Smith, W. A. Towlson, H. J. Walker, C. Armand, M. Burgdorf, D. Ewart, A. di Giorgio, S. Molinari, M. Price, S. Sidher, D. Texier, and N. Trams, Astron. Astrophys. **315**, L201 (1996).
[12] J. P. Pérez-Beaupuits, S. Aalto, and H. Gerebro, Astron. Astrophys. **476**, 177 (2007).
[13] M. Guélin, P. Salomé, R. Neri, S. García-Burillo, J. Graciá-Carpio, J. Cernicharo, P. Cox, P. Planesas, P. M. Solomon, L. J. Tacconi, and P. vanden Bout, Astron. Astrophys. **462**, L45 (2007).
[14] J. R. Goicoechea, M. Etxaluze, J. Cernicharo, M. Gerin, D. A. Neufeld, A. Contursi, T. A. Bell, M. De Luca, P. Encrenaz, N. Indriolo, D. C. Lis, E. T. Polehampton, and P. Sonnentrucker, Astrophys. J. **769**, L13 (2013).
[15] J. Cernicharo, F. Daniel, A. Castro-Carrizo, M. Agundez, N. Marcelino, C. Joblin, J. R. Goicoechea, and M. Guélin, Astrophys. J. **778**, L25 (2013).
[16] F. Combes, S. García-Burillo, V. Casasola, L. Hunt, M. Krips, A. J. Baker, F. Boone, A. Eckart, I. Marquez, R. Neri, E. Schinnerer, and L. J. Tacconi, Astron. Astrophys. **558**, A124 (2013).
[17] T. Izumi, K. Kohno, S. Martín, D. Espada, N. Harada, S. Matsushita, P.-Y. Hsieh, J. L. Turner, D. S. Meier, E. Schinnerer, M. Imanishi, Y. Tamura, M. T. Curran, A. Doi, K. Fathi, M. Krips, A. A. Lundgren, N. Nakai, T. Nakajima, M. W. Regan, K. Sheth, S. Takano, A. Taniguchi, Y. Terashima, T. Tosaki, and T. Wiklind, Publ. Astron. Soc. Jpn. **65**, 100 (2013).
[18] E. Roueff and F. Lique, Chem. Rev. **113**, 8906 (2013).
[19] S. Green and P. Thaddeus, Astrophys. J. **191**, 653 (1974).
[20] T. S. Monteiro and J. Stutzki, Mon. Not. R. Astron. Soc. **221**, 33P (1986).
[21] R. G. Gordon and Y. S. Kim, J. Chem. Phys. **56**, 3122 (1972).
[22] E. Sarrasin, D. B. Abdallah, M. Wernli, A. Faure, J. Cernicharo, and F. Lique, Mon. Not. R. Astron. Soc. **404**, 518 (2010).
[23] F. Dumouchel, A. Faure, and F. Lique, Mon. Not. R. Astron. Soc. **406**, 2488 (2010).
[24] F. Lique, R. Toboła, J. Kłos, N. Feautrier, A. Spielfiedel, L. F. M. Vincent, G. Chałasiński, and M. H. Alexander, Astron. Astrophys. **478**, 567 (2008).
[25] M. Wernli, P. Valiron, A. Faure, L. Wiesenfeld, P. Jankowski, and K. Szalewicz, Astron. Astrophys. **446**, 367 (2006).
[26] F. Lique, M.-L. Senent, A. Spielfiedel, and N. Feautrier, J. Chem. Phys. **126**, 164312 (2007).
[27] Y. Kalugina, F. Lique, and J. Kłos, Mon. Not. R. Astron. Soc. **422**, 812 (2012).
[28] D. Ben Abdallah, F. Najar, N. Jaidane, F. Dumouchel, and F. Lique, Mon. Not. R. Astron. Soc. **419**, 2441 (2012).
[29] F. Dumouchel, J. Kłos, and F. Lique, Phys. Chem. Chem. Phys. **13**, 8204 (2011).
[30] O. Denis-Alpizar, Y. Kalugina, T. Stoecklin, M. H. Vera, and F. Lique, J. Chem. Phys. **139**, 224301 (2013).
[31] M. Ishiguro, T. Tanaka, K. Harada, C. J. Whitham, and K. Tanaka, J. Chem. Phys. **115**, 5155 (2001).
[32] M. Ishiguro, K. Harada, K. Tanaka, T. Tanaka, Y. Sumiyoshi, and Y. Endo, Chem. Phys. Lett. **554**, 33 (2012).
[33] F. Lique, J. Kłos, and M. Hochlaf, Phys. Chem. Chem. Phys. **12**, 15672 (2010).
[34] Y. Ajili, K. Hammami, N. E. Jaidane, M. Lanza, Y. N. Kalugina, F. Lique, and M. Hochlaf, Phys. Chem. Chem. Phys. **15**, 10062 (2013).
[35] D. T. Moore, M. Ishiguro, L. Oudejans, and R. E. Miller, J. Chem. Phys. **115**, 5137 (2001).
[36] S. Green, J. Chem. Phys. **62**, 2271 (1975).
[37] K. P. Huber and G. Herzberg, *Molecular Spectra and Molecular Structure. IV. Constants of Diatomic Molecules* (Van Nostrand Reinhold, New York, 1979).
[38] J. M. Hutson and S. Green, molscat computer code, version 14 (1994), distributed by Collaborative Computational Project No. 6 of the Engineering and Physical Sciences Research Council (UK).
[39] D. E. Manolopoulos, J. Chem. Phys. **85**, 6425 (1986).
[40] J. Kłos and F. Lique, Mon. Not. R. Astron. Soc. **390**, 239 (2008).
[41] D. R. Flower, J. Phys. B **34**, 2731 (2001).
[42] M. Lanza, Y. Kalugina, L. Wiesenfeld, and F. Lique, J. Chem. Phys. **140**, 064316 (2014).
[43] C. W. McCurdy and W. H. Miller, J. Chem. Phys. **67**, 463 (1977).

Chapter 6

Radiative transfer calculations

Contents

The high quality of modern radio and infrared wavelength observations requires efficient modeling techniques to infer physical and chemical parameters such as temperatures, densities, and molecular abundances. In this chapter, we present a set of radiative transfer calculations for metal cyanides and isocyanides based on the large velocity gradient (LGV) approximation. We will simulate the excitation of these molecules in the circumstellar gas, the media where metal-containing molecules are frequently observed. The theory is based on statistical equilibrium calculations, involving collisional and radiative processes and including radiation from background sources.

6.1 Radiative transfer calculations

The modelling of molecular spectra observations is usually performed through radiative transfer calculations. Different codes have been developed in order to perform these calculations [127]. In this chapter we use the `RADEX` code [128]. Here, we expose briefly its main principles.

In homogeneous molecular clouds, the emitted light arises from the spontaneous decay of excited rotational levels. The population of each rotational level is determined by radiative and collisional processes.

In order to present the main aspects of the formalism, let's start considering the general transfer equation for radiation propagating a distance ds,

$$dI_\nu ds = j_\nu - \alpha_\nu I_\nu \tag{6.1}$$

where j_ν and α_ν are the local emission and extinction coefficients, respectively. The variable ν is the frequency associated to the transition from the upper level u to the lower level l. Next, the source function is defined as,

$$S_\nu \equiv \frac{j_\nu}{\alpha_\nu} \tag{6.2}$$

and the optical depth measured along a light path of infinitesimally small length is,

$$d\tau_\nu \equiv \alpha_\nu ds \tag{6.3}$$

Using these definitions, Eq. 6.1 can be expressed in the integral form,

$$I_\nu = I_\nu(0)e^{-\tau} + \int_0^{\tau_\nu} S_\nu(\tau'_\nu)e^{-(\tau_\nu - \tau'_\nu)}d\tau'_\nu \tag{6.4}$$

where I_ν is the radiation emerging from the medium and $I_\nu(0)$ is the background radiation entering the medium. The emission due to the transition $u \rightarrow l$ with laboratory frequency ν_{ul}, reads

$$j_\nu = \frac{h\nu_{ul}}{4\pi} n_u A_{ul} \gamma_\nu \tag{6.5}$$

where A_{ul} is the spontaneous downward rate, n_u is the density of molecules in level u and γ_ν is the frequency-dependent line emission profile. On the other hand, the absorption coefficient can be obtained from the following expression,

$$\alpha_\nu = \frac{h\nu_{ul}}{4\pi}(n_l B_{lu}\phi_\nu - n_\nu B_{ul}\chi_\nu) \tag{6.6}$$

where B_{ul} and B_{lu} are the Einstein coefficients for stimulated transitions; ϕ_ν and χ_ν are the line profiles for absorption and stimulated emission, respectively. If we consider complete angular and frequency redistribution of the emitted photons, so that $\gamma_\nu = \phi_\nu = \chi_\nu$ then the source function takes the form

$$S_{\nu_{ul}} = \frac{n_u A_{ul}}{n_l B_{lu} - n_u B_{ul}} \tag{6.7}$$

For many interstellar and circumstellar media, the density is too low to reach local thermodynamic equilibrium (LTE), but statistical equilibrium (SE) can often be assumed.

$$\begin{aligned} &\sum_{j>l}\left[n_j A_{jl} + (n_j B_{jl} - n_l B_{lj})\bar{J}_{jl}\right] + \sum_j n_j C_{jl} \\ &= \sum_{j<l}\left[n_l A_{lj} + (n_l B_{lj} - n_j B_{jl})\bar{J}_{lj}\right] + \sum_j n_l C_{lj} \end{aligned} \tag{6.8}$$

In the last expression, the $C_{il} = n_{col} k_{ij}$ with k_{ij} the collisional rates coefficients in $\mathrm{cm}^3\ \mathrm{s}^{-1}$ and n_{col} the density of collisional partners. $\bar{J}_{jl}$ is the integrated mean intensity over the line profile. Expression 6.8 indicates that the number of quenching transitions from the l level equals the number of (de-)excitations towards this level.

Escape probability

The interdependence of molecular level populations and of the local radiation field makes difficult to solve the radiative transfer equations. The problem can be simplified by decoupling the equations for the level populations and the radiative transfer. The key of this approximation is to substitute J in Eq. 6.8 by a term that is independent of the radiation field. For that purpose, one needs to consider the so-called "escape probability" first introduced by Sobolev [129].

The escape probability, β, represents the fraction of the photons that manage to escape from the cloud. If β is the chance that a newly created photon can escape from the cloud, we can infer that $J_\nu = S_\nu(1-\beta)$. Now the statistical equilibrium equations take a very easy form:

$$n_u \sum_{l=1}^{N_{lev}} (C_{ul} - \beta A_{ul}) = \sum_{l=1}^{N_{lev}} n_l C_{lu} \tag{6.9}$$

which is an expression that is independent of the radiation field. The escape probability is derived from the large velocity gradient (LVG) approximation [129],

$$\beta_{LVG} = \frac{1}{\tau} \int_0^\tau e^{-\tau} d\tau = \frac{1 - e^{-\tau}}{\tau} \tag{6.10}$$

`RADEX` uses this approximation to estimate the excitation and radiation field. As a first guess the populations are calculated in the optically thin case ($\tau << 1$) or for LTE conditions; this then gives the optical depth and hence the escape probability, from which the new level populations can be calculated. The program iterates this procedure until convergence is reached and then computes all line intensities.

6.2 Results

Monthly Notices
of the
ROYAL ASTRONOMICAL SOCIETY

MNRAS **448,** 2438–2447 (2015) doi:10.1093/mnras/stv140

Cyanide/isocyanide abundances in the interstellar medium – III. The excitation of Al and Mg compounds

Mario Hernández Vera[1,2]★ and François Lique[1]

[1]*LOMC - UMR 6294, CNRS-Université du Havre, 25 rue Philippe Lebon, BP 1123, Le Havre F-76063, France*
[2]*Instituto Superior de Tecnologías y Ciencias Aplicadas, Quinta de Los Molinos, Plaza, La Habana 10600, Cuba*

Accepted 2015 January 19. Received 2015 January 16; in original form 2014 October 6

ABSTRACT

Cyanide species are the most common metal-containing molecules in the circumstellar gas. The exact determination of their abundances requires accurate molecular data. For this purpose, collisional excitation rate coefficients are essential in order to simulate the excitation processes and hence to model the emission lines. In this paper, we use the aluminium cyanide (AlCN), aluminium isocyanide (AlNC), magnesium cyanide (MgCN) and magnesium isocyanide (MgNC) collisional data recently computed to simulate the excitation of these molecules in the circumstellar gas. We perform radiative transfer calculations for typical physical conditions encountered in the circumstellar gas. We obtain the brightness and excitation temperatures of selected lines frequently observed towards the circumstellar envelopes. In circumstellar gas, we have found that local thermodynamic equilibrium conditions are not fulfilled for these species and that radiative transfer calculations are needed in order to accurately determine their abundances. The calculations also show that the estimations of the cyanides/isocyanides abundance ratios deduced from line intensities ratios lead to large differences compared to exact radiative transfer calculations. Finally, the results confirm that AlCN and MgCN are significantly less abundant than AlNC and MgNC, respectively. This shows again the evidence of selective cyanide chemistry.

Key words: line: profiles – molecular processes – radiative transfer – circumstellar matter – stars: individual: IRC+10216.

1 INTRODUCTION

Observations towards the carbon-rich star IRC+10216 have shown the presence of different metal cyanides and isocyanides, such as aluminium cyanide (AlCN; Ziurys et al. 2002), magnesium cyanide (MgCN; Ziurys et al. 1995), magnesium isocyanide (MgNC; Guélin et al. 1986), iron monocyanide (FeCN; Zack, Halfen & Ziurys 2011) or potassium cyanide (KCN; Pulliam et al. 2010) in the circumstellar gas. Likely, the envelopes of the asymptotic giant branch stars present the best conditions for the formation of these molecules. Indeed, MgNC was also detected in the circumstellar gas of the protoplanetary nebulae CRL 2688 (Highberger et al. 2001) and CRL 618 (Highberger & Ziurys 2003).

Other metal-containing species, such as metal halides (NaCl, AlCl, KCl, AlF; Cernicharo & Guélin 1987) or metal monoxides (AlO, FeO; Walmsley et al. 2002; Tenenbaum & Ziurys 2009), have also been observed in the circumstellar gas. However, their abundances are much lower than those of metal cyanides and isocyanides, which remain the most common metal-containing molecules in the circumstellar gas.

Several studies have attempted to understand the synthesis of metal cyanides and isocyanides and their important role in the chemistry of circumstellar gas. Hence, several processes have been suggested for their formation. Guélin, Lucas & Cernicharo (1993) have studied a mechanism involving photodesorption of MgNC from dust-grain mantles. Later, Kawaguchi et al. (1993), considering that metals are generally ionized, suggested that ion/molecule reactions could be responsible for the formation of the MgNC molecule. More recently, Petrie (1996) and Dunbar & Petrie (2002) discussed a similar formation pathway and generalized it to the formation of metal cyanides and isocyanides. They supported a gas phase formation route driven by the radiative association of ionized metals M^+ and cyanopolyynes,

$$M^+ + HC_{2n+1}N \rightarrow MN(C_{2n+1})H^+ + h\nu, \quad (1)$$

followed by the dissociative recombination of the cation newly formed

$$\begin{aligned} & \rightarrow M(C_{2n+1}N) + H \\ MN(C_{2n+1})H^+ + e & \rightarrow M(CN) + C_{2n}H \\ & \rightarrow M + HC_{2n+1}N. \quad (2) \end{aligned}$$

★ E-mail: mhvera28@instec.cu

Published by Oxford University Press on behalf of the Royal Astronomical Society

The large abundance of cyanopolyynes, such as HC_3N (Turner 1971) and HC_5N (Avery et al. 1976) in the outer envelope of IRC+10216, supports the latter hypothesis. Cabezas et al. (2013) have introduced the above gas phase formation pathways in astrochemical models to quantify the formation of MgCN, MgNC and HMgNC. The abundance ratios for these three molecules obtained from the astrochemical models are in good agreement with the observations.

However, despite this progress, the abundance and chemical evolution of metal-bearing molecules in the circumstellar gas are still not completely understood. First, the dominant role of cyanide species as metal carriers in circumstellar gas is not predicted by any chemical models. Secondly, chemical models show that metal-bearing molecules should be formed in the inner circumstellar envelope, and then disappear from the gas phase at the onset of dust formation. However, most of the metal cyanides and isocyanides have been observed in the outer envelope of IRC+10216 (Guélin et al. 1993), well beyond the dust formation zone. Thirdly, there is also little evidence of metal-bearing molecules in dense interstellar clouds (Turner et al. 2005). This absence is currently related to metal accretion on grains (Draine 2009). However, the extent to which metals contribute to dust formation and their diffusion in the stellar outflows remains unclear.

Pulliam et al. (2010) have recently suggested that the chemistry of cyanides (and not only metal cyanides) has to be reviewed. For this purpose, we have initiated a series of papers to provide accurate molecular data for interstellar and circumstellar cyanides and isocyanides. Cyanide molecules present isomers (HCN/HNC, AlCN/AlNC, MgCN/MgNC, SiCN/SiNC, etc.) that are, most of the time, stable species (Senent, Dumouchel & Lique 2012, hereafter Paper I). In Paper I, we have determined the theoretical spectroscopic and structural properties of SiCN/SiNC and of some of the metal cyanides (X-CN/X-NC with X = Al, Mg and Na) that were in very good agreement with the available experimental data. In Hernández Vera et al. (2013, hereafter Paper II), we have computed the excitation rate coefficients for the AlCN, AlNC, MgCN and MgNC molecules due to collisions with He (as a model of H_2) for temperatures ranging from 5 to 100 K. The importance of having accurate rate coefficients for both isomers has been demonstrated recently by Lique and co-workers (Dumouchel, Faure & Lique 2010; Dumouchel, Kłos & Lique 2011; Sarrasin et al. 2010), who have related the unexpected large abundance of HNC (compared to HCN) to models using erroneous collisional rate coefficients.

Assessments of cyanide/isocyanide abundances in circumstellar gas are readily available (Ziurys et al. 1995; Guélin et al. 2004). Commonly, large abundances correspond to the most stable isomers as occurs for MgNC. Indeed, MgCN is less stable than MgNC by about 650 cm^{-1} (Paper I) and the MgNC/MgCN ratio has been estimated to be $\simeq$22 by Ziurys et al. (1995). Nevertheless, the ratio is not systematically governed by the relative stabilities of the two isomers. SiCN and SiNC molecules seem to be in similar abundance (Guélin et al. 2004) whereas SiNC is less stable than SiCN by about 550 cm^{-1} (Paper I). Note that in all these studies, the estimation of the cyanide/isocyanide abundance ratios was deduced from line intensity ratios, assuming that the excitation of both isomers is similar. Such an assumption is in contradiction with the results of Paper II. Indeed, we have found that the collisional excitation of the isomers is significantly different, questioning the approaches previously used to determine cyanides/isocyanides abundance ratios.

In this work, we employ the new thermal rate coefficients recently published in Paper II to simulate the excitation of X-CN and X-NC (X = Al, Mg) molecules for typical densities and temperatures of the circumstellar gas. This study will allow us to understand and accurately analyse the emission of these molecules from the circumstellar gas. All these species have been observed in the circumstellar gas, with the exception of AlCN. The paper is organized as follows. In Section 2, we present the molecular data used in the radiative transfer calculations. In Section 3, we discuss the physical parameters that were used for simulating the excitation of X-CN and X-NC (X = Al, Mg) molecules. Finally, in Section 4, we present the results. We provide a discussion and our conclusions in Section 5.

2 MOLECULAR DATA

In radiative transfer calculations, presented in Section 3, both the collisional and radiative (de-)excitation processes are taken into account. In this section, we present a summary of the molecular data used in these calculations.

AlCN and AlNC molecules are $^1\Sigma^+$ electronic ground-state molecules. The rotational quantum number of AlCN and AlNC is denoted by N. In contrast, MgCN and MgNC molecules are $^2\Sigma^+$ electronic ground-state molecules. Because of the presence of a non-zero electronic spin, the rotational states splits into two fine structure levels. For MgCN and MgNC in their ground electronic $^2\Sigma^+$ state, the molecular energy levels are then described in the Hund's case (b) limit. The fine structure levels are labelled by N_j. Here, N is the rotational angular momentum and j is the total molecular angular momentum quantum number with $\vec{j} = \vec{N} + \vec{S}$, where $\vec{S}$ is the electronic spin. For the molecules in a $^2\Sigma^+$ state, $S = 1/2$. Hence, for $N > 0$, two kinds of levels exist, the levels with $j = N + 1/2$ and those with $j = N - 1/2$.

In Tables 1 and 2, we show the frequencies and the Einstein coefficients (A_{ul}) for a small selection of radiative transitions frequently observed for AlCN (Walker & Gerry 1999), AlNC (Robinson, Apponi & Ziurys 1997), MgCN (Anderson, Steimle & Ziurys 1994) and MgNC (Kawaguchi et al. 1993) isomers. Einstein coefficients and frequencies were obtained from the Cologne Data base for Molecular Spectroscopy (CDMS; Müller et al. 2005). The computed dipole moments of AlCN, AlNC, MgCN and MgNC molecules are 3.72, 3.34, 5.37 and 4.95 D, respectively (Paper I).

Differences between AlCN and AlNC Einstein coefficients (A_{ul}) can be related to differences in both the rotational structure and the dipole moments of the isomers. The same is observed for MgCN

Table 1. Einstein A_{ul} (in s^{-1}) coefficients and transition frequencies ν (in GHz) of AlCN/AlNC molecules.

N	N'	ν(AlCN)	ν(AlNC)	A_{ul}(AlCN)	A_{ul}(AlNC)
1	0	10.05	11.97	4.80(−8)	6.56(−8)
2	1	20.10	23.94	4.61(−7)	6.30(−7)
3	2	30.15	35.91	1.61(−6)	2.28(−6)
⋮	⋮	⋮	⋮	⋮	⋮
8	7	80.40	95.74	3.47(−5)	4.74(−5)
9	8	90.45	107.71	4.97(−5)	6.79(−5)
10	9	100.49	119.68	6.85(−5)	9.37(−5)
11	10	110.54	131.64	9.16(−5)	1.25(−4)
12	11	120.59	143.61	1.12(−4)	1.63(−4)
⋮	⋮	⋮	⋮	⋮	⋮
18	17	180.85	215.36	4.08(−4)	5.58(−4)
19	18	190.89	227.31	4.80(−3)	6.57(−4)
20	19	200.93	239.26	5.61(−4)	7.67(−4)

Table 2. Einstein A_{ul} (in s^{-1}) coefficients and transition frequencies ν (in GHz) of MgCN/MgNC molecules.

N_j	$N'_{j'}$	ν(MgCN)	ν(MgNC)	A_{ul}(MgCN)	A_{ul}(MgNC)
$1_{0.5}$	$0_{0.5}$	10.17	11.92	8.13(−8)	1.34(−7)
$1_{1.5}$	$0_{0.5}$	10.19	11.94	1.23(−7)	2.03(−7)
$2_{1.5}$	$1_{0.5}$	20.37	23.86	9.79(−7)	1.61(−6)
$2_{2.5}$	$1_{1.5}$	20.39	23.87	1.09(−6)	1.80(−6)
$3_{2.5}$	$2_{1.5}$	30.56	35.79	3.67(−6)	6.06(−6)
$3_{3.5}$	$2_{2.5}$	30.57	35.81	3.86(−6)	6.37(−6)
⋮	⋮	⋮	⋮	⋮	⋮
$8_{7.5}$	$7_{6.5}$	81.50	95.45	7.83(−5)	1.29(−4)
$8_{8.5}$	$7_{7.5}$	81.52	95.47	7.90(−5)	1.30(−4)
$9_{8.5}$	$8_{7.5}$	91.69	107.38	1.12(−4)	1.86(−4)
$9_{9.5}$	$8_{8.5}$	91.70	107.39	1.13(−4)	1.97(−4)
$10_{9.5}$	$9_{8.5}$	101.88	119.31	1.55(−4)	2.56(−4)
$10_{10.5}$	$9_{9.5}$	101.89	119.33	1.56(−4)	2.57(−4)
$11_{10.5}$	$10_{9.5}$	112.06	131.24	2.17(−4)	3.42(−4)
$11_{11.5}$	$10_{10.5}$	112.08	131.26	2.18(−4)	3.44(−4)
$12_{11.5}$	$11_{10.5}$	122.25	143.17	2.70(−4)	4.46(−4)
$12_{12.5}$	$11_{11.5}$	122.26	143.18	2.71(−4)	4.48(−4)

and MgNC isomers. Nevertheless, the differences are moderate, so we do not anticipate any major differences in the excitation of the isomers due to the differences in the radiative rates.

We also note that AlCN, AlNC, MgCN and MgNC rate coefficients have been computed recently. The details of the calculations can be found in Paper II and we only summarize the results here. We have studied the following inelastic collisions:

$$\begin{aligned} \mathrm{AlCN}(N) + \mathrm{He} &\rightarrow \mathrm{AlCN}(N') + \mathrm{He};\\ \mathrm{AlNC}(N) + \mathrm{He} &\rightarrow \mathrm{AlNC}(N') + \mathrm{He};\\ \mathrm{MgNC}(N_j) + \mathrm{He} &\rightarrow \mathrm{MgNC}(N'_{j'}) + \mathrm{He};\\ \mathrm{MgNC}(N_j) + \mathrm{He} &\rightarrow \mathrm{MgNC}(N'_{j'}) + \mathrm{He}. \end{aligned} \tag{3}$$

Four new potential energy surfaces (PESs) were computed for the AlCN($^1\Sigma^+$)–He, AlNC($^1\Sigma^+$)–He, MgCN($^2\Sigma^+$)–He and MgNC($^2\Sigma^+$)–He van der Waals systems. The PESs were calculated in the supermolecular approach by means of (partially spin-restricted) coupled cluster calculations with single, double and perturbative triple [(R)CCSD(T)] excitations (Hampel, Peterson & Werner 1992; Knowles, Hampel & Werner 1993, 2000).

We used the quantum coupled-states (CS) approach (McGuire & Kouri 1974) to obtain the excitation cross-sections among the rotational energy levels of all isomers. The standard time-independent coupled scattering equations were solved using the MOLSCAT code (Hutson & Green 1994). The fine structure of the MgCN and MgNC molecules was not explicitly taken into account in the calculations, but considered using a technique based on the infinite-order sudden (IOS) approximation (Faure & Lique 2012). State-to-state rate coefficients were obtained for temperatures ranging from 5 to 100 K. Transitions between the first 26 ($N \le 25$) rotational levels of AlCN and AlNC and the first 41 ($N \le 20$) fine structure levels of MgCN and MgNC were considered.

Fig. 1 presents AlCN–He and AlNC–He de-excitation rate coefficients from the $N = 12$ rotational state at a temperature of 50 K. As already discussed in Paper II, the AlCN and AlNC rate coefficients are, on average, of the same order of magnitude. They both show a propensity rule in favour of odd ΔN transitions. However, the rate coefficients corresponding to $\Delta N = 1$ transitions are significantly different. AlCN rate coefficients are up to 50 per cent larger than AlNC ones. As we will see, this implies important consequences in the radiative transfer calculations.

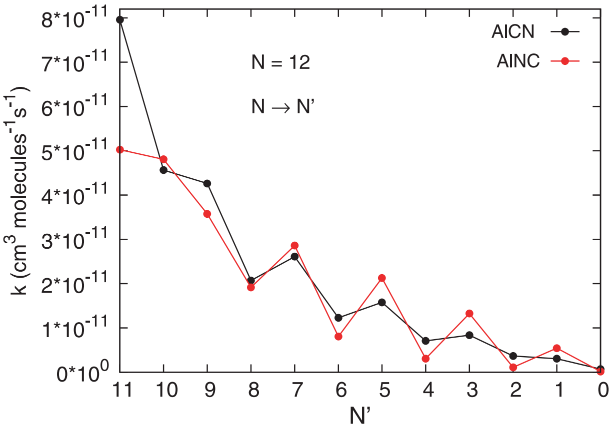

Figure 1. State-to-state AlCN/AlNC rate coefficients out of the $N = 12$ level at 50 K.

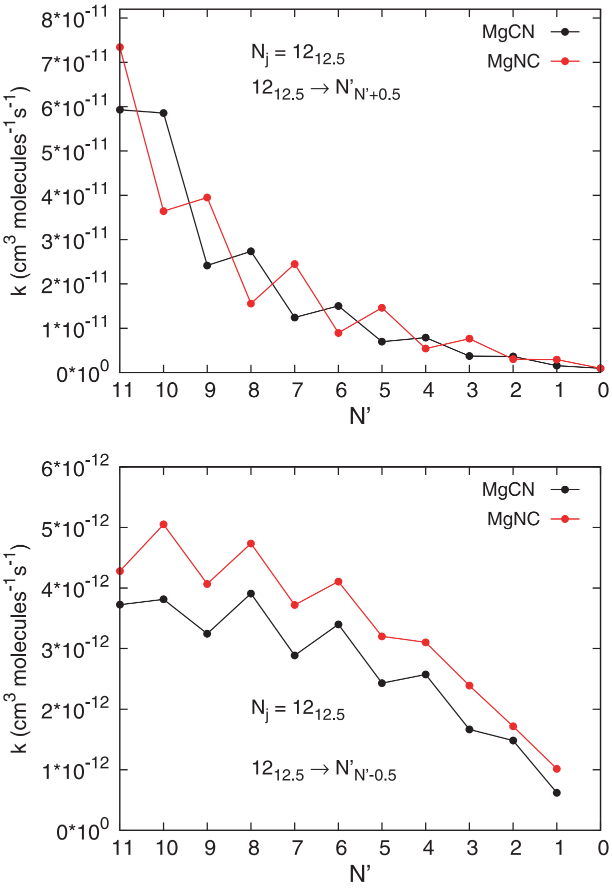

Figure 2. State-to-state MgCN/MgNC rate coefficients out of the $N = 12$, $j = 12.5$ level at 50 K.

Fig. 2 presents MgCN–He and MgNC–He de-excitation rate coefficients from the $N_j = 12_{12.5}$ fine structure level at a temperature of 50 K. Both $\Delta N = \Delta j$ and $\Delta N \neq \Delta j$ transitions are presented. First, the rate coefficients among the fine structure levels show, as expected, propensity rules in favour of $\Delta N = \Delta j$. Then, for $\Delta N = \Delta j$ transitions, the MgCN–He rate coefficients present a propensity in favour of transitions with even ΔN, whereas the MgNC–He rate coefficients present a propensity in favour of transitions with odd

Table 3. Critical densities n^* for AlCN/AlNC collisions (in cm^{-3}) at 20, 50 and 100 K.

	20 K		50 K		100 K	
N	n^*(AlCN)	n^*(AlNC)	n^*(AlCN)	n^*(AlNC)	n^*(AlCN)	n^*(AlNC)
1	7.35(2)	1.14(3)	9.80(2)	2.19(3)	1.20(3)	2.91(3)
2	3.38(3)	5.71(3)	3.98(3)	7.06(3)	4.43(3)	7.97(3)
3	8.67(3)	1.44(4)	9.97(3)	1.68(4)	1.09(4)	1.83(4)
⋮	⋮	⋮	⋮	⋮	⋮	⋮
8	1.04(5)	1.70(5)	1.11(5)	1.74(5)	1.13(5)	1.72(5)
9	1.43(5)	2.31(5)	1.51(5)	2.36(5)	1.52(5)	2.31(5)
10	1.91(5)	3.02(5)	1.99(5)	3.10(5)	1.99(5)	3.01(5)
11	2.44(5)	3.85(5)	2.55(5)	3.96(5)	2.54(5)	3.82(5)
12	3.06(5)	4.82(5)	3.20(5)	4.97(5)	3.18(5)	4.77(5)
⋮	⋮	⋮	⋮	⋮	⋮	⋮
18	8.89(5)	1.40(6)	9.24(5)	1.43(6)	9.16(5)	1.37(6)
19	1.03(6)	1.62(6)	1.06(6)	1.65(6)	1.06(6)	1.57(6)
20	1.15(6)	1.86(6)	1.19(6)	1.89(6)	1.18(6)	1.78(6)

ΔN. As for AlCN and AlNC, we will see that these differences imply important consequences in the radiative transfer calculations.

In order to estimate H_2 rate coefficients, the main collisional partner in the circumstellar gas, we apply a scaling factor of 1.38 to the He rate coefficients (Lique et al. 2008). This approach appears to be unsuccessful for light molecules (Roueff & Lique 2013; Lanza et al. 2014) but is reasonably accurate for heavier collisional systems, such as SiS–H_2 (Lique et al. 2008), HC_3N (Wernli et al. 2007) or CS (Lique, Spielfiedel & Cernicharo 2006; Stoecklin et al. 2013). Hence, using such an approximation, we can expect that the estimation of X-CN–H_2 and X-NC–H_2 rate coefficients will be accurate within a factor of 2.

From knowledge of both collisional rate coefficients and Einstein coefficients, it is possible to compute critical densities for collisions with molecular hydrogen, defined as

$$n_i^*(T) = \frac{A_{i\rightarrow f}}{\sum_{f<i} k_{i\rightarrow f'}}, \qquad (4)$$

where i and f refer to initial and final states of the molecules. The n_N^* density is the H_2 density at which photon de-excitation and collisional de-excitation are equal.

Tables 3 and 4 present the critical densities at 20, 50 and 100 K, for Al and Mg compounds, respectively.

The critical densities of the first radiative transitions are of the order of 10^3–10^4 cm^{-3}, whatever the temperature is. The values are weakly dependent on the temperature because the temperature dependence of the cyanides/isocyanides rate coefficients is also weak. For all the isomers, the computed critical densities increase with the excitation rotational/fine structure levels. This can be explained by the fact that the Einstein emission coefficients vary approximately as N^3 whereas the collisional rate coefficients stay within the same order of magnitude. In the circumstellar gas, the observed lines of the metal cyanides and isocyanides are generally those from initial energy levels with N between 8 and 21. For these lines, the typical critical densities are of the order of 10^5–10^6 cm^3.

Hence, from these tables, it can be seen that for many common interstellar media (especially circumstellar gas), the local

Table 4. Critical densities n^* for MgCN/MgNC collisions (in cm^{-3}) at 20, 50 and 100 K.

	20 K		50 K		100 K	
N_j	n^*(MgCN)	n^*(MgNC)	n^*(MgCN)	n^*(MgNC)	n^*(MgCN)	n^*(MgNC)
$1_{0.5}$	2.04(3)	2.23(3)	2.04(3)	2.73(3)	1.99(3)	3.09(3)
$1_{1.5}$	1.13(3)	1.62(3)	1.08(3)	1.79(3)	1.04(3)	1.88(3)
$2_{1.5}$	3.53(4)	4.68(4)	3.49(4)	5.27(4)	3.43(4)	5.61(4)
$2_{2.5}$	2.79(4)	4.14(4)	2.74(4)	4.59(4)	2.72(4)	4.83(4)
$3_{2.5}$	5.89(4)	8.29(4)	5.88(4)	9.15(4)	5.85(4)	9.62(4)
$3_{3.5}$	5.18(4)	7.74(4)	5.11(4)	8.48(4)	5.08(4)	8.85(4)
⋮	⋮	⋮	⋮	⋮	⋮	⋮
$8_{7.5}$	4.01(5)	5.94(5)	3.78(5)	6.02(5)	3.59(5)	5.92(5)
$8_{8.5}$	3.88(5)	5.78(5)	3.65(5)	5.82(5)	3.46(5)	5.69(5)
$9_{8.5}$	5.30(5)	7.73(5)	4.96(5)	7.80(5)	4.67(5)	7.60(5)
$9_{9.5}$	5.16(5)	7.54(5)	4.82(5)	7.57(5)	4.53(5)	7.34(5)
$10_{9.5}$	6.79(5)	9.82(5)	6.34(5)	9.90(5)	5.92(5)	9.59(5)
$10_{10.5}$	6.63(5)	9.62(5)	6.18(5)	9.64(5)	5.77(5)	9.28(5)
$11_{10.5}$	8.51(5)	1.23(6)	7.95(5)	1.23(6)	7.38(5)	1.19(6)
$11_{11.5}$	8.33(5)	1.20(6)	7.78(5)	1.21(6)	7.23(5)	1.15(6)
$12_{11.5}$	1.05(6)	1.50(6)	9.80(5)	1.82(6)	9.07(5)	1.45(6)
$12_{12.5}$	1.03(6)	1.48(6)	9.63(5)	1.80(6)	8.90(5)	1.72(6)

thermodynamic equilibrium (LTE) conditions are not fully met and that rate coefficients are needed to model cyanides/isocyanides emissions.

3 RADIATIVE TRANSFER CALCULATIONS

We have performed radiative transfer calculations for typical physical conditions from where AlNC/AlCN and MgNC/MgCN emissions are detected (i.e. from circumstellar gas).

Non-LTE calculations were performed with the RADEX code (van der Tak et al. 2007) using the large velocity gradient (LVG) approximation for an expanding sphere. The LVG approach, first proposed by Sobolev (1960), provides a local expression for the angle-averaged mean intensity that thoroughly simplifies the resolution of the statistical equilibrium equations. This approximation implies that the velocity gradient is large enough to decouple radiatively the different points of the cloud. For each point of the cloud, the excitation conditions depend only on the local density, the kinetic temperature and the escape probability. Rotational excitation of cyanides and isocyanides can be induced by collisions with H_2 as well as by absorption of photons. We also include the cosmic microwave background radiation at 2.73 K. In all the calculations, a linewidth of 30 km s^{-1} was taken into account (e.g. Ziurys et al. 1995). Such a broad linewidth corresponds to the typical width of the emission lines coming from the outer envelope of the IRC+10216 envelope (i.e. from where the metal cyanides and isocyanides have been detected). The IRC+10216 outer envelope is usually assumed to be the region located between $\simeq 10^{16}$ and $\simeq 10^{17}$ cm from the star (Cordiner & Millar 2009).

As mentioned in the introduction, metal cyanides/isocyanides have been mainly observed in circumstellar gas. Indeed, Ziurys et al. (2002) reported the first detection of AlNC in IRC+10216 circumstellar gas using the Institut de Radioastronomie Millimétrique (IRAM) 30-m telescope. They observed the $N = 11 \rightarrow 10$, $N = 12 \rightarrow 11$ and $N = 13 \rightarrow 12$ transitions at 2 mm and the $N = 18 \rightarrow 17$ and $N = 21 \rightarrow 20$ transitions at 1.2 mm. The rotational temperature ($T_{\rm rot}$) was estimated to be around 60 K, suggesting that AlNC emission comes from the outer envelope. The column density of AlNC was estimated to be $N_{\rm AlNC} \sim 9 \times 10^{11}$ cm^{-2}.

The MgNC and MgCN isomers have been also observed towards the same source. The $N = 19 \rightarrow 18$, $N = 14 \rightarrow 13$, $N = 13 \rightarrow 12$, $N = 12 \rightarrow 11$, $N = 9 \rightarrow 8$, $N = 8 \rightarrow 7$ and $N = 7 \rightarrow 6$ transitions of MgNC were reported by Guélin et al. (1993). The fine structure of the MgNC molecule was not resolved in these first observations. The rotational temperature was estimated to be around ∼15 K for this isomer. Meanwhile, the observation of the $N = 11 \rightarrow 10$, $N = 10 \rightarrow 9$ and $N = 9 \rightarrow 8$ transitions of MgCN were reported by Ziurys et al. (1995). In this case, the two spin-rotation components were resolved for the $N = 11 \rightarrow 10$ transition. This later work suggested that the [MgNC]/[MgCN] abundance ratio is ∼ 22 and that the column densities of $N_{\rm MgNC}$ and $N_{\rm MgCN}$ are around $\sim 5 \times 10^{13}$ cm^{-2} and $\sim 2 \times 10^{12}$ cm^{-2}, respectively.

MgNC has also been observed in the circumstellar gas of the protoplanetary nebulae CRL 2688 (Highberger et al. 2001) and CRL 618 (Highberger & Ziurys 2003). Again, the observations also seem to indicate an outer shell distribution for this molecule in these regions.

Metal cyanides seem then to be mainly distributed in the external shell of the circumstellar gas and particularly in the external shell of carbon-rich stars, such as IRC+10216. Modelling of this region (Crosas & Menten 1997) indicates that kinetic temperature varies approximately from 10 to 100 K while molecular hydrogen densities could be constrained in the interval $n(H_2) = 10^4$–10^6 cm^{-3}. As a consequence, we have chosen three different kinetic temperatures (20, 50 and 100 K) for the radiative transfer calculations. The column densities were set at three different values: 10^{11}, 10^{12} and 10^{13} cm^{-2}. We consider molecular hydrogen densities in a range from 10^2 to 10^8 cm^{-3}.

In the radiative transfer calculations, we include all the energy levels for which both radiative and collisional data are available. By testing the sensitivity of the radiative transfer calculations to the number of rotational levels considered, we have found that the calculations are fully converged for temperatures up to 50 K. At temperatures around 100 K, uncertainties of the order of ≃20 per cent exist, particularly for the MgCN/MgNC isomers where collisional data up to only $N = 20$ are available. Indeed, at 100 K, the population of rotational levels with $N = 25$ is around 2 per cent and that of rotational levels with $N = 30$ is around 1 per cent.

4 RESULTS

In this section, we only show results for the observed $N = 18 \rightarrow 17$ and $N = 11 \rightarrow 10$ transitions of AlNC/AlCN and for the observed $N_j = 11_{11.5} \rightarrow 10_{10.5}$ and $N_j = 9_{9.5} \rightarrow 8_{8.5}$ transitions of MgNC/MgCN. However, the behaviour observed for these lines gives a representation of the general behaviour.

Figs 3–5 show the excitation temperature ($T_{\rm Ex}$) of the AlCN and AlNC lines as a function of molecular hydrogen density for temperatures of 20, 50 and 100 K. We varied the column density of AlCN/AlNC from 10^{11} to 10^{13} cm^{-2} but we have found that the column density has almost no impact on the magnitude of the excitation temperature. Actually, the three curves cannot be distinguished in the plots. This can be explained by the fact that AlCN/AlNC lines are optically thin for the physical conditions considered in this work.

At very low volume densities of molecular hydrogen, the excitation temperatures, for both isomers, tend to be equal to the adopted value of the background radiation field (2.7 K). The excitation temperatures rise to higher values as collisional excitation becomes more important. At volume densities above a critical value, the excitation temperature approaches the kinetic temperature, at which point the LTE approximation can be used.

At low temperatures (≃20 K), the critical density lies at $\approx 10^5$–10^6 cm^{-3}, while for higher temperatures, the critical density is slightly larger (up to a factor of 2–3), especially for transitions between highly excited states. The temperature dependence of the critical density is then relatively weak.

By matching the critical densities presented in Table 1 and the information of Figs 3–5, we can conclude that at typical physical conditions of the outer shell of the circumstellar gas [10^4 cm^{-3} < $n(H_2)$ < 10^6 cm^{-3}], AlCN and AlNC lines are not thermalized and non-LTE analysis is required.

Figs 3–5 also show the brightness temperatures of the AlCN and AlNC lines as a function of molecular hydrogen density. As the optical depth is small for these lines ($\tau \ll 1$), $T_{\rm B}$ is proportional to the column densities. $T_{\rm B}$ increases gradually with the density before being constant at around $n(H_2) = 10^6$–10^7 cm^{-3} when LTE conditions are reached.

To compare AlCN and AlNC emissions, we show in Figs 3–5 the brightness temperature ratios $T_{\rm B}[{\rm AlCN}]/T_{\rm B}[{\rm AlNC}]$. From this plot, we can clearly see that the AlCN isomer presents a stronger emission than the AlNC isomer for low densities of molecular hydrogen. For the $N = 18 \rightarrow 17$ transition, the line of AlCN can be up to three to four times larger than that of AlNC, especially at low temperatures and densities [$n(H_2) \leq 10^5$ cm^{-3}].

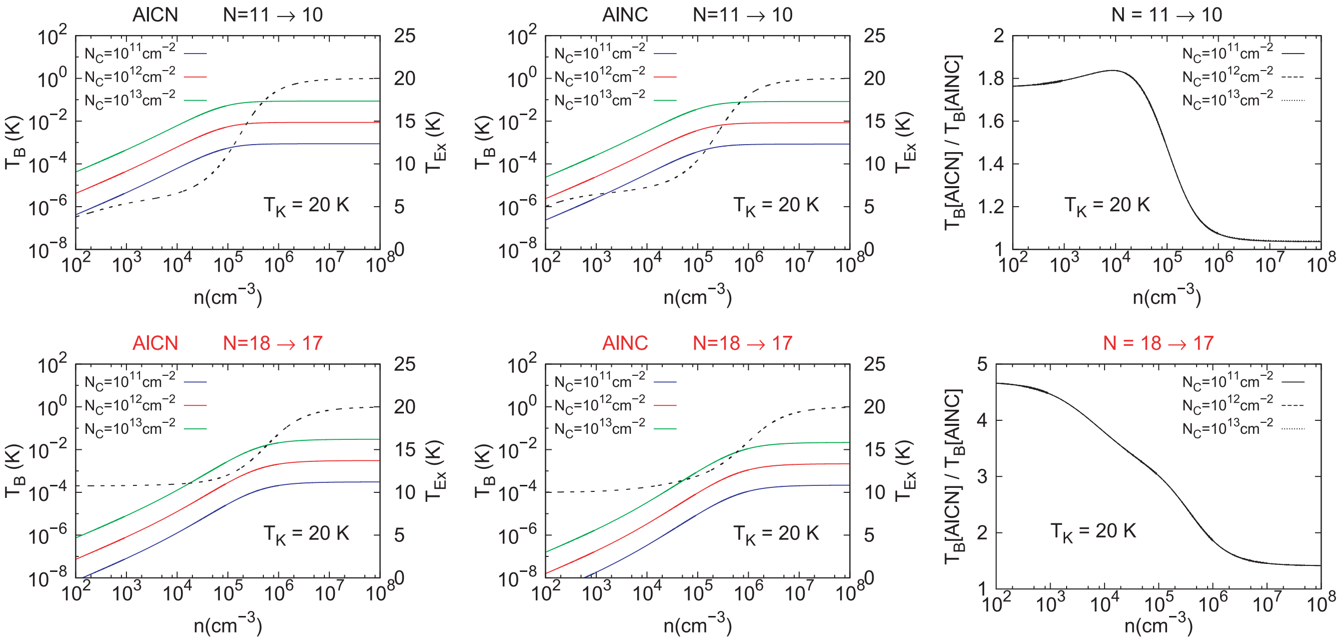

Figure 3. Excitation temperature (T_{Ex}, dashed lines), brightness temperature (T_{B}, solid lines) and brightness temperature ratios (T_{B}[AlCN]/T_{B}[AlNC], right panels) for the $N = 18 \rightarrow 17$ and $N = 11 \rightarrow 10$ lines of AlCN and AlNC. The H_2 volume density varies between 100 and 10^8 cm^{-3} and the AlCN and AlNC column density from 10^{11} to 10^{13} cm^{-2} by a step factor of 10. The kinetic temperature is 20 K. The linewidth is 30 km s^{-1}

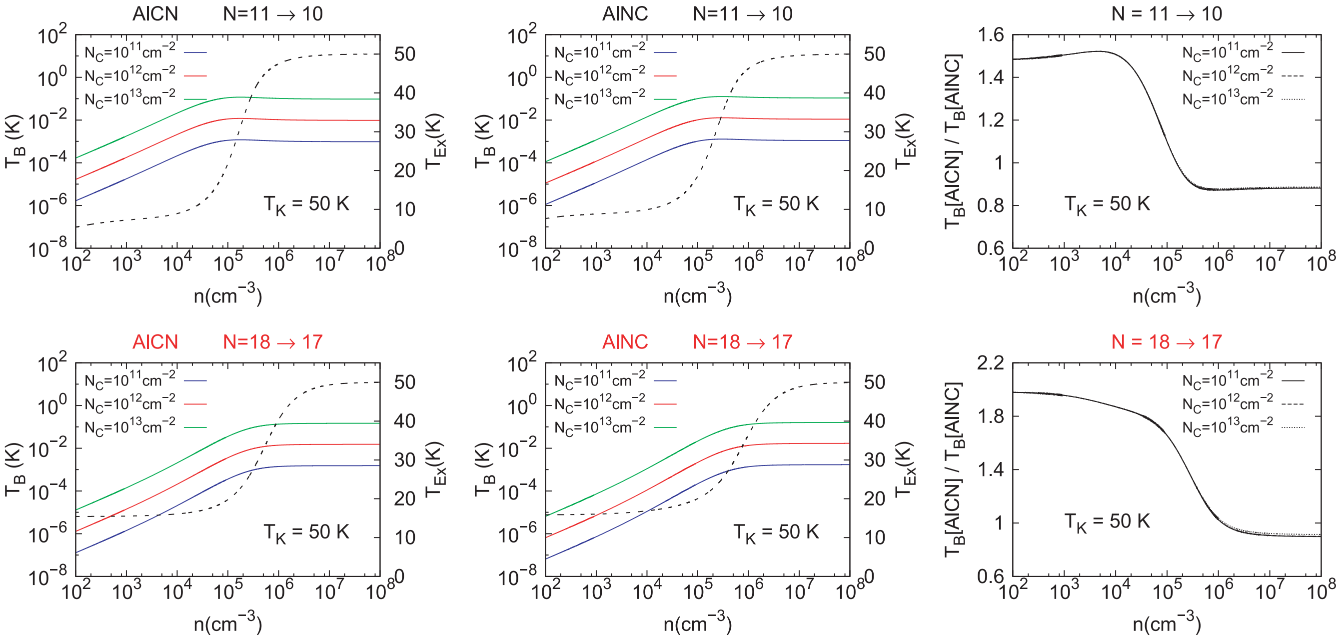

Figure 4. Same as Fig. 3 but at a kinetic temperature of 50 K.

In contrast, it can be seen that AlNC emission is stronger at large molecular hydrogen densities but the differences are not as large as at low densities. However, the differences are more pronounced at high temperatures than at low temperatures. When LTE conditions are reached, populations of the energy levels are determined by a Boltzmann distribution. The fact that AlCN lines are weaker than AlNC lines can be explained by (i) a lower rotational constant for AlCN than for AlNC, leading to a lower population of the high-energy levels at high temperature for this isomer and (ii) weaker Einstein coefficients of the AlCN lines than the AlNC lines.

Figs 6–8 show similar plots for the MgCN/MgNC molecules. The MgCN and MgNC lines are also optically thin so that, as in the case of AlCN and AlNC lines, the column density does not affect the magnitude of the excitation temperatures.

The behaviour of the excitation temperatures is very similar to that of AlCN and AlNC. The critical density lies also at $\approx 10^5$–10^6 cm^{-3} at low temperatures and slightly increases with increasing temperatures.

The effect of suprathermal excitation seen at 100 K is essentially the same for both isomers, even though it is more

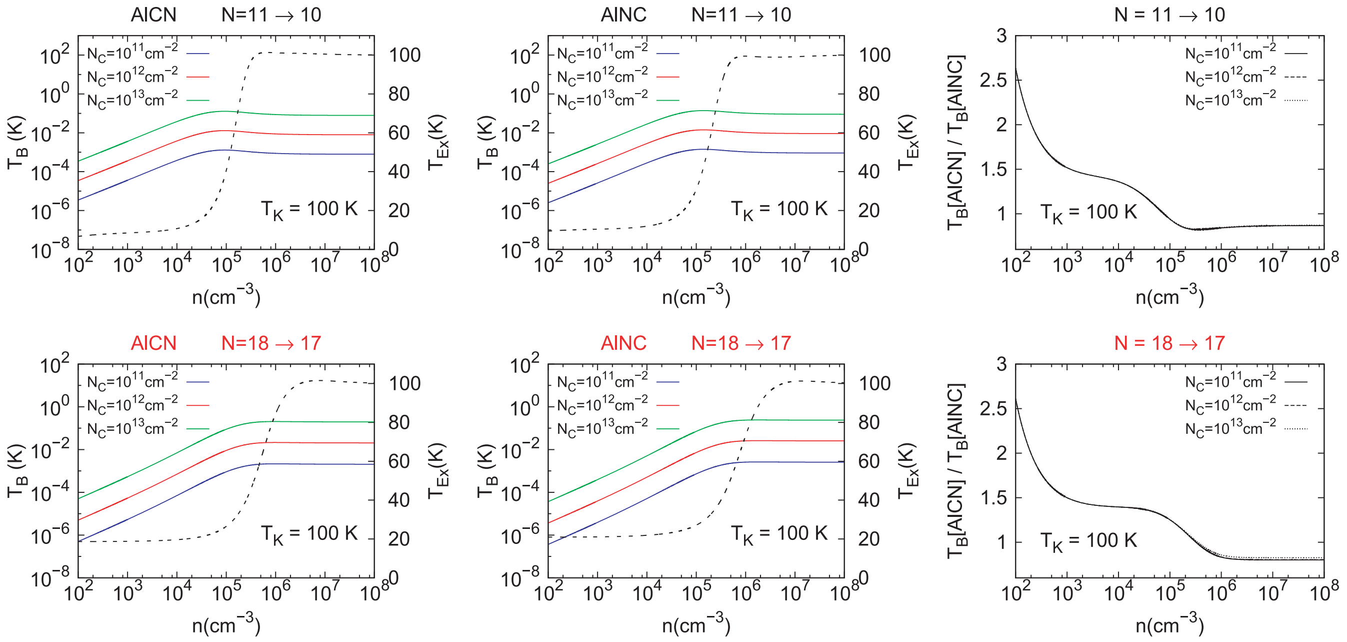

Figure 5. Same as Fig. 3 but at a kinetic temperature of 100 K.

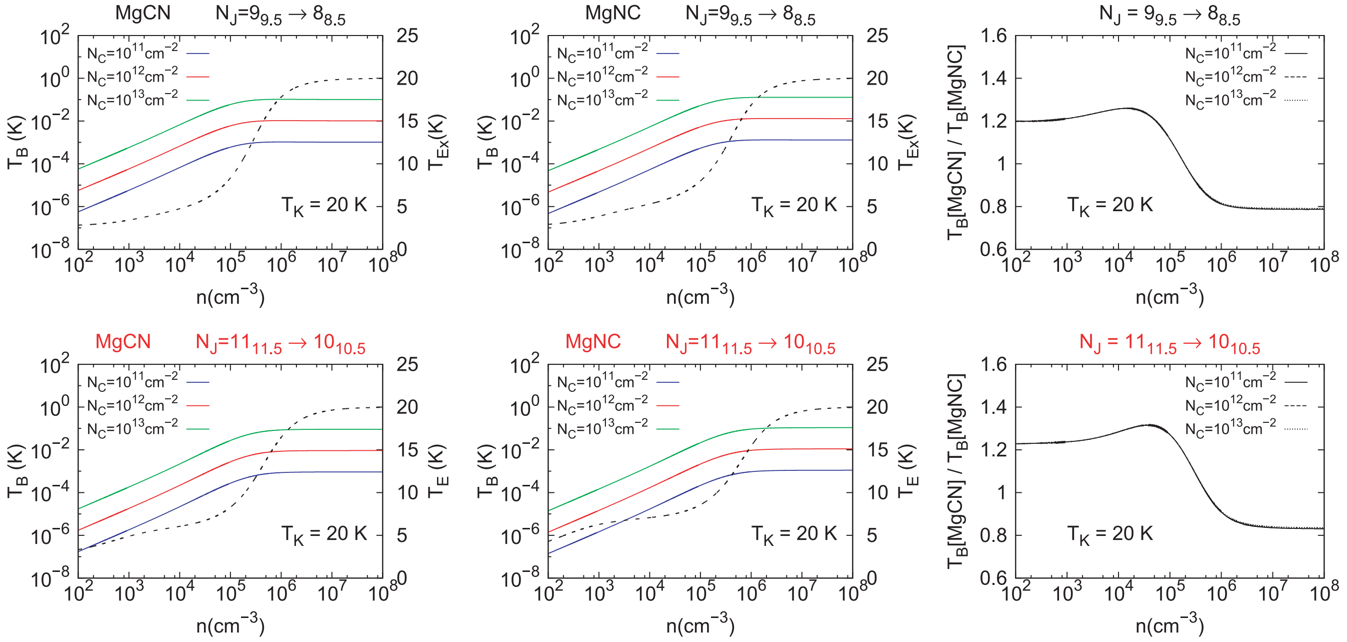

Figure 6. Excitation temperature ($T_{\rm Ex}$, dashed lines), brightness temperature ($T_{\rm B}$, solid lines) and brightness temperature ratios ($T_{\rm B}$[MgCN]/$T_{\rm B}$[MgNC], right panels) for the $N = 11 \rightarrow 10$ and $N = 9 \rightarrow 8$ lines of MgCN and MgNC. The H_2 volume density varies between 100 and 10^8 cm^{-3} and the MgCN and MgNC column density from 10^{11} to 10^{13} cm^{-2} by a step factor of 10. The kinetic temperature is 20 K. The linewidth is 30 km s^{-1}.

pronounced for MgCN than for MgNC. The differences seen in both sets of rate coefficients certainly explain these slight differences.

The behaviour of the brightness temperatures is also very similar to that of AlCN and AlNC. Indeed, brightness temperatures are also proportional to the column densities. However, the brightness temperature ratio $T_{\rm B}$[MgCN]/$T_{\rm B}$[MgNC] does not vary with density as much as in the case of AlCN/AlNC isomers. The deviations between the brightness temperatures of both isomers are usually less than 30–50 per cent in the interval of $n(\rm H_2) = 10^4$–10^6 cm^{-3} for all temperatures. Below the critical density, we can observe that MgCN lines are stronger than those of MgNC whatever the temperature is. As for AlCN/AlNC, the differences can be explained by the differences in the rate coefficients. Then, we have a significant impact of the collisional rate coefficients, showing that the MgCN/MgNC abundance ratio has to be determined through radiative transfer calculations.

For densities above the critical density, MgNC lines are stronger than the MgCN ones. This can be explained by the MgNC transition probabilities for spontaneous decay, which are larger than those of MgCN. The differences are more pronounced than for Al compounds. Hence, even assuming LTE conditions, the MgCN/MgNC

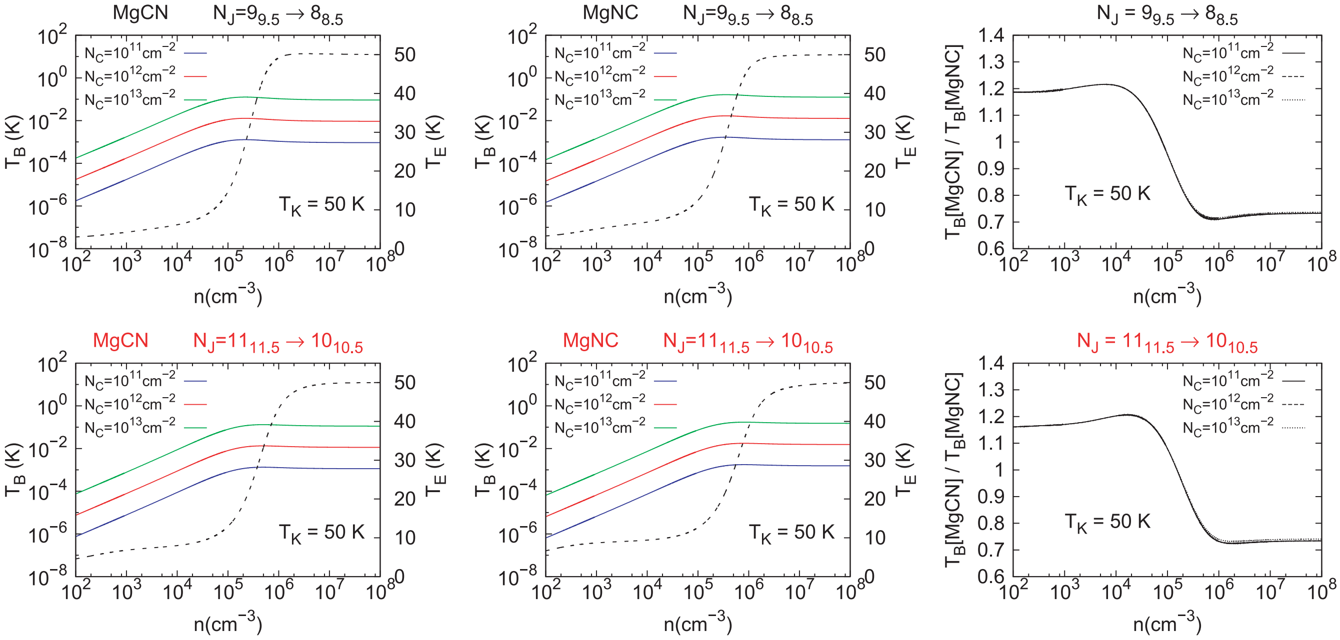

Figure 7. Same as Fig. 6 but at a kinetic temperature of 50 K.

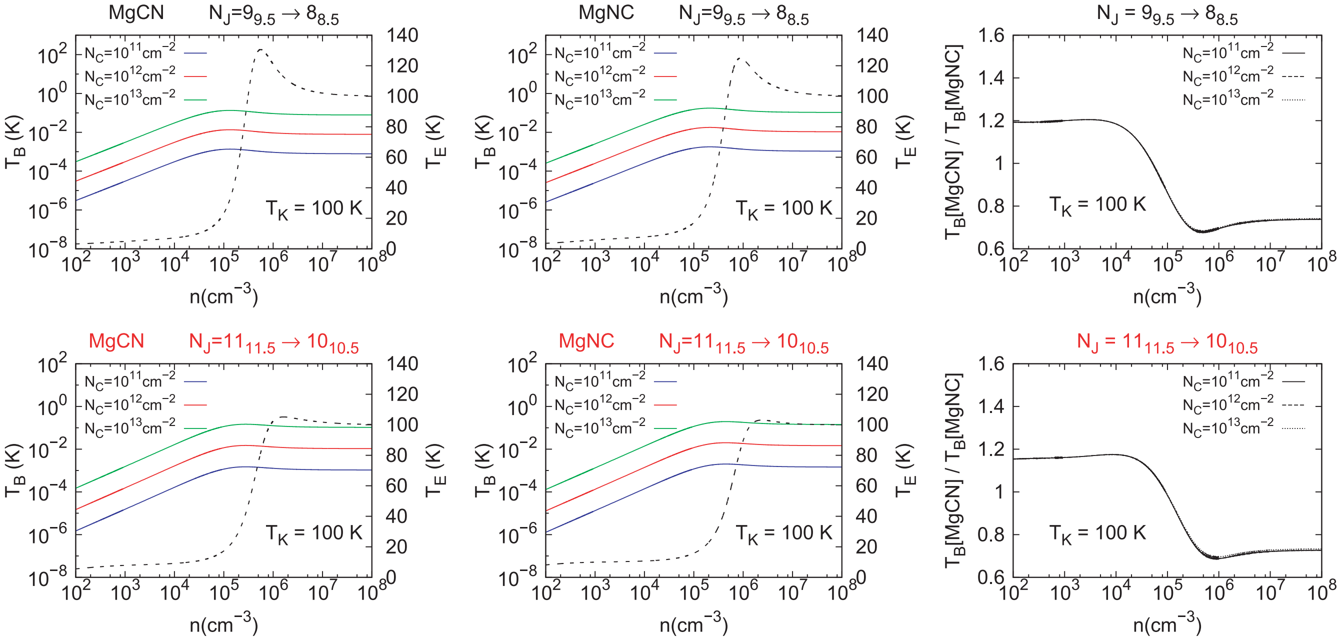

Figure 8. Same as Fig. 6 but at a kinetic temperature of 100 K.

abundance ratio determined from a simple line intensity ratio will lead to erroneous values.

Finally, Fig. 9 shows, at 20 K, the dependence of the MgCN/MgNC brightness temperatures on the column density, for the $N_j = 9_{9.5} \rightarrow 8_{8.5}$ and $N_j = 11_{11.5} \rightarrow 10_{10.5}$ transitions. In these calculations, the hydrogen density $n(\mathrm{H_2})$ was fixed at 3×10^4 cm^{-3}.

For these physical conditions, the MgCN/MgNC lines are optically thin, so we can observe a linear dependence of the brightness temperatures with the column densities. This linear dependence allows us to determine the abundance ratio of these isomers simply from the ratio of the molecular line intensities using the following relation:

$$\frac{T_\mathrm{B}(\mathrm{MgCN})}{T_\mathrm{B}(\mathrm{MgNC})} = \frac{\alpha_\mathrm{MgCN}}{\alpha_\mathrm{MgNC}} \times \frac{N_\mathrm{MgCN}}{N_\mathrm{MgNC}}. \tag{5}$$

Here, α_MgCN and α_MgNC are the slopes of the function

$$T_\mathrm{B} = \alpha_\mathrm{MgCN/MgNC} N_\mathrm{MgCN/MgNC}$$

for the MgCN and MgNC isomers, respectively.

In the absence of radiative transfer calculations, the estimation of the abundance ratio was generally obtained using the assumption

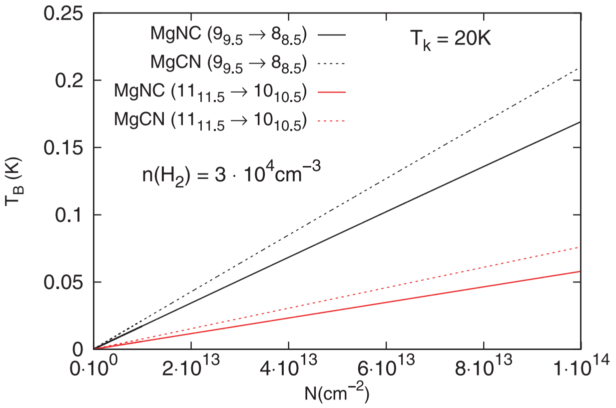

Figure 9. Column density dependence of the brightness temperature for the $N_j = 9_{8.5} \rightarrow 8_{7.5}$ transition of MgCN and MgNC at 20 K. The linewidth is 30 km s^{-1}.

that the excitation of both isomers was the same ($\alpha_{\rm MgCN} = \alpha_{\rm MgNC} = 1$; Ziurys et al. 1995).

Obviously, such an analysis is erroneous, and an accurate analysis of both MgCN and MgNC emissions will lead to a different estimate of the abundance ratio.

As an example, we have determined the [MgNC]/[MgCN] abundance ratio in IRC+10216 from the observations of Ziurys et al. (1995). Using the same physical parameters [$n(\rm H_2 = 3 \times 10^4$ cm^{-3}, T = 15–20 K] as Ziurys et al. (1995), we have obtained a new [MgNC]/[MgCN] abundance ratio of ∼30. Such a value is ∼50 per cent higher than the value previously obtained from simple line intensities analysis (Ziurys et al. 1995). It clearly shows the need for accurate molecular excitation simulations in order to precisely determine molecular abundance in astrophysical media.

5 DISCUSSION AND CONCLUSIONS

In this work, we have studied the excitation of AlCN, AlNC, MgCN and MgNC molecules in the circumstellar gas. We have employed new collisional rate coefficients to determine the excitation of these cyanide and isocyanide molecules.

We have found that, at typical physical conditions of the outer shells of the circumstellar gas, the observed lines of cyanides and isocyanides are not thermalized and non-LTE analysis is required. The AlCN and MgCN isomers present stronger line intensities at low $n(\rm H_2)$ than their isomers, principally due to larger collisional rate coefficients. In contrast, for $n(\rm H_2)$ above critical densities, the MgNC and AlNC lines are more intense than those of MgCN and AlCN, respectively, mainly because of their larger Einstein A_{ul} coefficients.

The calculations have also shown that the estimations of the abundance ratios of the isomers, from a simple analysis of the line intensities ratios, lead to inaccuracies for both Al and Mg compounds.

Radiative transfer calculations can also be useful to quantify the upper limit of the abundance of AlCN, which, despite being stable, has not yet been detected. The comparison between AlCN and AlNC modelled brightness temperatures indicates that the AlCN lines are expected to be stronger than those of AlNC for the typical physical conditions encountered in the outer shell of the IRC+10216 circumstellar envelope, for a similar abundance. Hence, the non-detection of the rotational lines of AlCN implies that its column density is significantly lower than that of AlNC.

For a molecular abundance of AlCN, a factor of 2 lower than that of AlNC, the intensity of the AlCN lines is expected to be similar to that of the AlNC lines, implying that the AlCN lines would be observable. The non-detection of AlCN lines probably means that their intensities are much lower than those of AlNC. Using the present radiative transfer calculations, we can then estimate that, in the IRC+10216 circumstellar gas, the upper limit of its column density is $N_{\rm AlCN} = N_{\rm AlNC}/2$ (i.e. $\sim 4 \times 10^{11}$ cm^{-2}).

The low abundance and non-detection of AlCN could have many causes. First, the isomerization barrier (Paper I) of AlCN and AlNC is of the order of 3000 K so that interconversion is almost impossible in circumstellar gas. If the production of AlNC is significantly favoured, there is very little chance to obtain AlCN through isomerization. By comparison, the isomerization barrier of MgCN and MgNC isomers is three times lower. Secondly, the presence of $\rm Al^+$ or $\rm Mg^+$ in the outer shell is critical to produce X-CN and X-NC isomers. The relative abundances of $\rm Al^+/Mg^+$ in the gas phase is not clear (Mauron & Huggins 2010) but the Mg condensation temperature is significantly less than that of Al, so that Mg is likely to be less depleted in the outer envelope. This hypothesis is reinforced by the fact that the abundance of the Mg element is larger than that of Al in the Universe (Lodders 2003). We can also note that, although the general level of incorporation of the metals into molecules is small, Al is integrated to several molecules in the inner shells (Cernicharo & Guélin 1987; Ziurys, Apponi & Phillips 1994). In contrast, Mg has been detected exclusively in the outer shells, forming just three cyanide compounds (MgCN, MgNC and HMgCN).

Finally, we expect that new observations of metal cyanides and isocyanides will be performed using the Atacama Large Millimeter/submillimeter Array (ALMA) interferometer. Such observations, combined with the theoretical tools provided in this paper, will allow us to gain new insight into the cyanides and isocyanides abundances in the circumstellar gas.

ACKNOWLEDGEMENTS

We thank Jose Cernicharo for kindly providing us with radiative molecular data of AlCN, AlNC, MgCN and MgNC molecules. This research was supported by the CNRS national programme 'Physique et Chimie du Milieu Interstellaire'. MHV acknowledge the French embassy of Cuba and Campus France for financial support. We also thank the CPER Haute-Normandie/CNRT/Energie, Electronique, Matériaux.

REFERENCES

Anderson M. A., Steimle T. C., Ziurys L. M., 1994, ApJ, 429, L41
Avery L. W., Broten N. W., MacLeod J. M., Oka T., Kroto H. W., 1976, ApJ, 205, L173
Cabezas C., Cernicharo J., Alonso J. L., Agúndez M., Mata S., Guélin M., Peña I., 2013, ApJ, 775, 133
Cernicharo J., Guélin M., 1987, A&A, 183, L10
Cordiner M. A., Millar T. J., 2009, ApJ, 697, 68
Crosas M., Menten K. M., 1997, ApJ, 483, 913
Draine B. T., 2009, in Henning T., Grün E., Steinacker J., eds, ASP Conf. Ser. Vol. 414, Cosmic Dust – Near and Far. Astron. Soc. Pac., San Francisco, p. 453
Dumouchel F., Faure A., Lique F., 2010, MNRAS, 406, 2488
Dumouchel F., Kłos J., Lique F., 2011, Phys. Chem. Chem. Phys. (Inc. Faraday Trans.), 13, 8204
Dunbar R. C., Petrie S., 2002, ApJ, 564, 792
Faure A., Lique F., 2012, MNRAS, 425, 740

Guélin M., Gomez-Gonzalez J., Cernicharo J., Kahane C., 1986, A&A, 157, L17

Guélin M., Lucas R., Cernicharo J., 1993, A&A, 280, L19

Guélin M., Muller S., Cernicharo J., McCarthy M. C., Thaddeus P., 2004, A&A, 426, L49

Hampel C., Peterson K. A., Werner H.-J., 1992, Chem. Phys. Lett., 190, 1

Hernández Vera M., Lique F., Dumouchel F., Kłos J., Rubayo Soneira J., Senent M.-L., 2013, MNRAS, 432, 468 (Paper II)

Highberger J. L., Ziurys L. M., 2003, ApJ, 597, 1065

Highberger J. L., Savage C., Bieging J. H., Ziurys L. M., 2001, ApJ, 562, 790

Hutson J. M., Green S., 1994, molscat computer code, version 14 (1994), distributed by Collaborative Computational Project No. 6 of the Engineering and Physical Sciences Research Council (UK)

Kawaguchi K., Kagi E., Hirano T., Takano S., Saito S., 1993, ApJ, 406, L39

Knowles P. J., Hampel C., Werner H., 1993, J. Chem. Phys., 99, 5219

Knowles P. J., Hampel C., Werner H.-J., 2000, J. Chem. Phys., 112, 3106

Lanza M., Kalugina Y., Wiesenfeld L., Faure A., Lique F., 2014, MNRAS, 443, 3351

Lique F., Spielfiedel A., Cernicharo J., 2006, A&A, 451, 1125

Lique F., Toboła R., Kłos J., Feautrier N., Spielfiedel A., Vincent L. F. M., Chałasiński G., Alexander M. H., 2008, A&A, 478, 567

Lodders K., 2003, ApJ, 591, 1220

McGuire P., Kouri D. J., 1974, J. Chem. Phys., 60, 2488

Mauron N., Huggins P. J., 2010, A&A, 513, A31

Müller H. S. P., Schlöder F., Stutzki J., Winnewisser G., 2005, J. Mol. Struct., 742, 215

Petrie S., 1996, MNRAS, 282, 807

Pulliam R. L., Savage C., Agúndez M., Cernicharo J., Guélin M., Ziurys L. M., 2010, ApJ, 725, L181

Robinson J. S., Apponi A. J., Ziurys L. M., 1997, Chem. Phys. Lett., 278, 1

Roueff E., Lique F., 2013, Chem. Rev., 113, 8906

Sarrasin E., Abdallah D. B., Wernli M., Faure A., Cernicharo J., Lique F., 2010, MNRAS, 404, 518

Senent M. L., Dumouchel F., Lique F., 2012, MNRAS, 420, 1188 (Paper I)

Sobolev V., 1960, Moving Envelopes of Stars. Harvard books on astronomy. Harvard University Press, Cambridge, MA

Stoecklin T., Denis-Alpizar O., Halvick P., Dubernet M.-L., 2013, J. Chem. Phys., 139, 124317

Tenenbaum E. D., Ziurys L. M., 2009, ApJ, 694, L59

Turner B. E., 1971, ApJ, 163, L35

Turner B. E., Petrie S., Dunbar R. C., Langston G., 2005, ApJ, 621, 817

van der Tak F. F. S., Black J. H., Schöier F. L., Jansen D. J., van Dishoeck E. F., 2007, A&A, 468, 627

Walker K. A., Gerry M. C. L., 1999, Chem. Phys. Lett., 301, 200

Walmsley C. M., Bachiller R., Pineau des Forêts G., Schilke P., 2002, ApJ, 566, L109

Wernli M., Wiesenfeld L., Faure A., Valiron P., 2007, A&A, 475, 391

Zack L. N., Halfen D. T., Ziurys L. M., 2011, ApJ, 733, L36

Ziurys L. M., Apponi A. J., Phillips T. G., 1994, ApJ, 433, 729

Ziurys L. M., Apponi A. J., Guélin M., Cernicharo J., 1995, ApJ, 445, L47

Ziurys L. M., Savage C., Highberger J. L., Apponi A. J., Guélin M., Cernicharo J., 2002, ApJ, 564, L45

This paper has been typeset from a TEX/LATEX file prepared by the author.

Chapter 7

Conclusions

In the first part of this thesis, we have studied the rotational excitation of interstellar metal cyanides and isocyanides (AlCN, AlNC, MgCN, MgNC) in collisions with He. To the best of our knowledge, it is the first time that the rotational excitation of these compounds is studied using quantum approaches and highly correlated PES. The collisional rate coefficients of Al and Mg isomers do not present the same propensity rules. We have assess the impact of these differences in the molecular emission simulations using radiative transfer calculations.

In the calculations we have taken into account that molecular hydrogen is the main collisional partner in the ISM. We have also assumed that the rate coefficients with He can provide a good estimate of rate coefficients for collision with H_2 (j = 0). In agreement with the astrophysical observations, we have confirmed that metal isocyanides are more abundant than metal cyanides. However, we have shown that the estimation of the relative abundances from the simple line intensity ratios lead to significant deviations compared to more exact calculations performed using radiative transfer calculations.

These calculations rise also the question of whether collisional rates involving helium can be used to model those for $H_2(j = 0)$. This approximation is not always advisable at low collisional energies when the scattering is "sensitive" to the particular features of the different PESs. However, such discrepancies are thought to decrease with increasing temperatures. On the other hand, there are still some important reasons to keep He as a collisional partner. First, He represents around 10-20% of the gas constituents in the ISM and should be, in principle, considered in the collisional excitation process. Second, as we mention before, some studies suggest that for heavy molecules like metal cyanides/isocyananides, He could be used as a model for $H_2(j = 0)$. Third, the collisions with He allow performing faster calculations and a simpler computation of the PESs.

We have also used quantum scattering calculations to investigate rotational energy transfer in collisions of SiCN and SiNC molecules with He atoms. For the dominant spin-orbit conserving transitions, a propensity for $\Delta j = 1$ transitions was found for the SiCN-He system whereas a propensity for $\Delta j = 2$ transitions was found for SiNC-He system. These different propensity rules seen for the SiCN/SiNC isomers let us predict that the excitation of these molecules in molecular clouds will be different and that the abundance ratio of these species cannot be simply obtained by looking at the brightness temperature ratio of the emission lines. Hence, radiative transfer calculations will have to be performed for both molecules using both sets of rate coefficients in order to accurately obtain the relative abundances of the two isomers.

Finaly, we have also performed closed-coupling calculations for the rotational excitation of HCN in collisions with H_2. The inclusion of the H_2 rotational structure

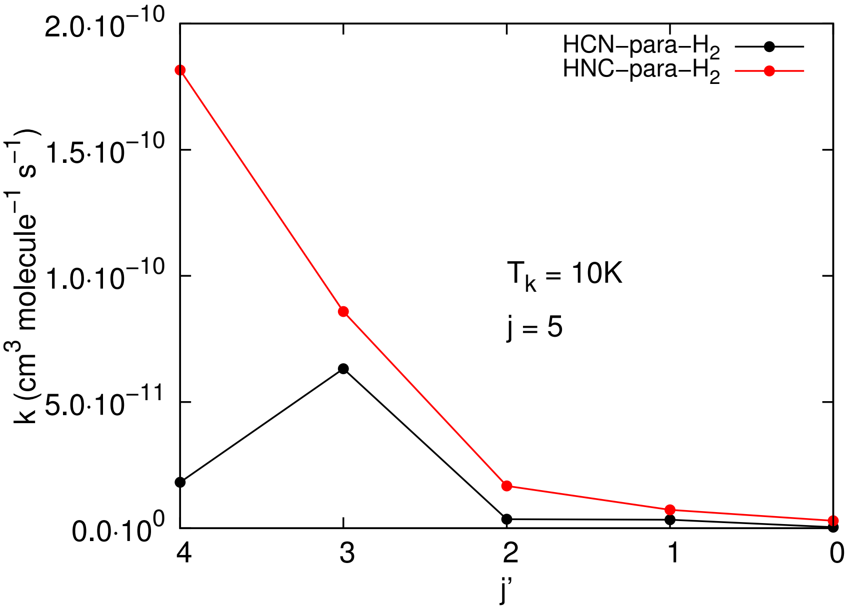

Figure 7.1: HCN–p-H_2 and HNC–p-H_2 de-excitation rate coefficients from the initial level j = 5 at 10 K .

in our calculations allows improving previous results of Ben Abdallah et al. [130] based on PES averaged over the H_2 rotations.

We have complemented the work of Dumouchel et al. [131] who performed a similar study for the HNC isomer. Fig. 7.1 shows a comparison of p-H_2 collisional rate coefficients of HNC (Dumouchel et al.) and HCN (this work). We note that the rate coefficients of HCN and HNC present different propensity rules. These differences confirm that specific calculations have to be performed for each isomer.

In the future we will evaluate the impact of our collisional rates coefficients in the HCN and HNC emissions for different physical conditions of the ISM. In fact, some preliminary radiative transfer calculations have been already performed at low temperatures. In Fig. 7.2, we have estimated the line intensities of HCN using our rate coefficients and we have compared the line intensities of HNC obtained using the rate coefficients of Dumouchel et al. [131]. The differences between the two isomers are significant. For $n(H_2 < 10^5)$ we have found $T_B[HNC]/T_B[HCN]$ can reach values larger than 4 for the observed $1 \rightarrow 0$ transition while for $2 \rightarrow 1$ the brightness temperature ratio can be as large as 5!

Fig. 7.2 also shows the results obtained using the He scaled rate coefficients from Sarrasin et al. [132]. The He scaled rate coefficients yield a good qualitative description of the intensity lines, especially for HCN molecule. This shows that for heavy molecules, He scaled rates may be very useful to explore the excitation of interstellar molecules when there is a lack of H_2 molecular data. This is a good example of the accuracy we can expect for metal cyanides and isocyanides.

Anyway, we point out that for important interstellar tracers like HCN and HNC, the most accurate calculations have to be performed considering the very high spatial and spectral resolution of the last generation of telescopes.

Outlook

This thesis brings new perspectives for future directions of investigation. For example, collisional cross sections of some observed metal cyanides/isocyanides are still unknown. In the near future, we hope to study the collisional excitation of the asymmetric top NaCN [133]. This metal cyanide is the only one thought to be in the inner shell of the circumstellar gas [63] and is the most abundant metal cyanide. On the other hand, it presents several metastable isomers that could be also detected in the future. Other interesting metal cyanide species like the observed T-shaped asymmetric top KCN [62] or the linear FeCN [61] are also

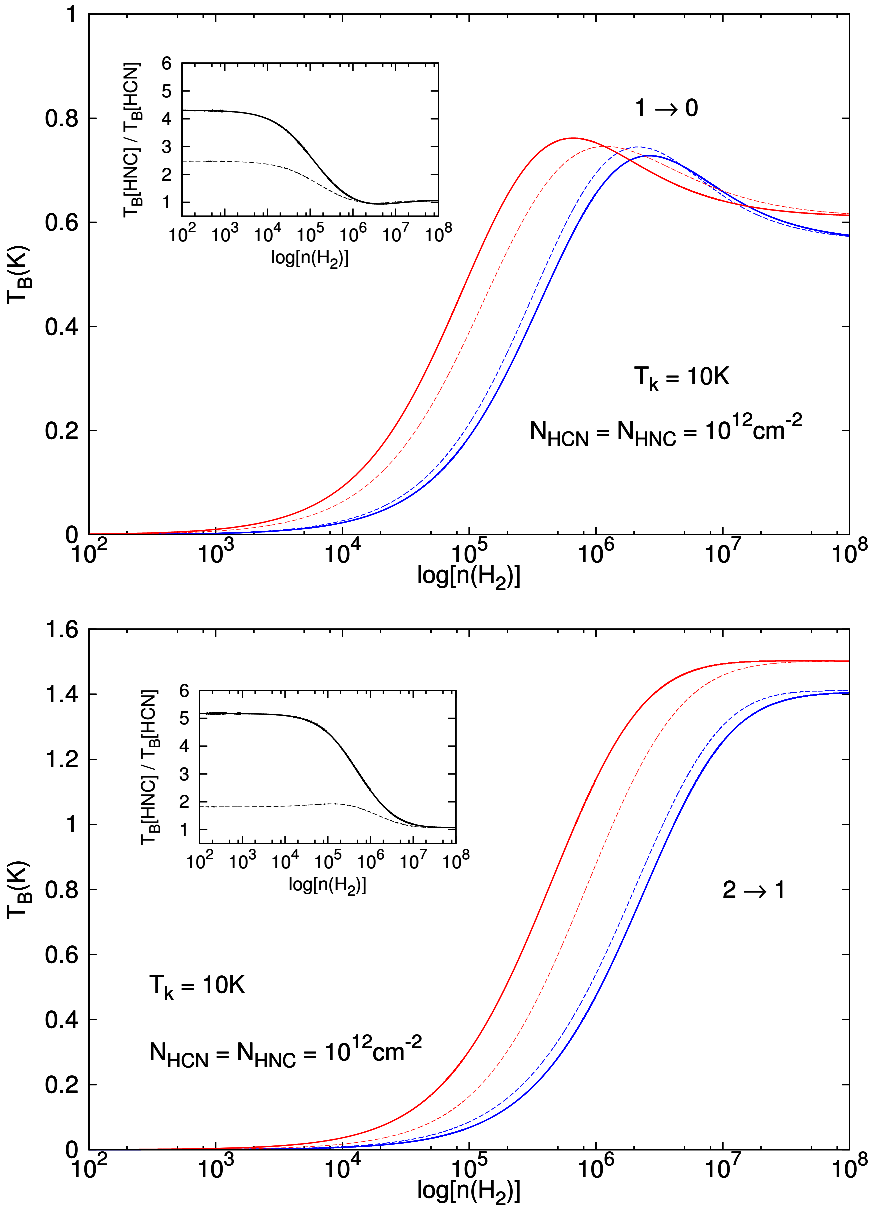

Figure 7.2: Solid lines: brightness temperature obtained with p-H_2 in collisions with HCN (blue lines) and in collisions with HNC (red lines). Dashed lines: brightness temperature obtained with He scaled rate coefficients. All calculations were performed with `RADEX` code.

candidates for future investigations.

Another important group of metal-bearing molecules are the metal halides which are confined to the inner shell of the circumstellar gas. In most cases, the cyanides appear more abundant than their halide counterparts. In IRC+10216, for example, the [KCN]/[KCl] ratio is ~ 1.5, while [NaCN]/[NaCl] ~ 5 [64,134]. However, this is not a general rule; aluminum clearly favors the halides, with [AlNC]/[AlCl] ~ 0.003 and [AlNC]/[AlF] ~ 0.002 [64]. In addition, some halide counterparts of metal cyanides, such as MgCl or MgF have yet to be detected. The computation of new collisional rate coefficients for metal halides will be useful for further interpretations of these observations.

Additionally, some organic species like the important symmetric-top molecule methyl cyanide (CH_3CN) are still waiting for accurate calculations of collisional excitations. We note that for symmetric top molecules radiative transitions can occur only within a K-ladder [1]. However, collisional transitions are permitted across this quantum number. Therefore, the population of one K-ladder is largely determined by collisions and, hence, is closely related to the kinetic temperature and density of the region. This property makes CH_3CN an ideal probes of hot molecular cores. Because of the large number of atoms, molecules like CH_3CN or CH_2CN are challenging for theoreticians. Nonetheless, at present, these calculations may be feasible due the computational advances.

In order to cover all physical conditions, it is also desirable to extend calculations of the collisional rate coefficients to higher temperatures and to a larger number of rotational levels. The extension of the studies will be especially useful for HCN and HNC isomers that have been detected in hot environments. Extrapolation to

---

[1] K is the quantum number for the projection of angular momentum along the symmetry axis

higher temperatures could be a first solution. However, the risk of extrapolation have been emphasized by some authors [135]. For this reason, we believe that quantum calculations have to be performed even if some approximations have to be employed.

The determination of new chemical rate constants will be also essential in order to understand the selective cyanides chemistry. Emphasis is placed on key reactions that have been identified as crucial in determining the predicted abundances of the species observed in the interstellar medium. Finally, from the fundamental molecular physics point of view, the balance and/or competition between reactive and nonreactive channels will be a theoretical motivation for future investigations.

Appendix A

Numerical calculations

The log derivative method

Both `Hibridon` and `MOLSCAT` scattering codes have different algorithms to solve the coupled equations which occur in the quantum treatment of inelastic collisions. In this thesis, all the calculations have been performed using the log derivative method of Manolopoulos [136] based on the log derivative algorithm of Johnson [137].

The coupled equations can be written in matrix notation as,

$$\mathbf{\Psi}''(R) = \mathbf{W}(R)\mathbf{\Psi}(R) \tag{A.1}$$

where

$$\mathbf{W}(R) = 2\mu\mathbf{V}(R) - \mathbf{k}^2 \tag{A.2}$$

The wave function $\mathbf{\Psi}$ is a square matrix, each column being a linearly independent solution of the Schrödinger equation; $\mathbf{V}$ is the potential matrix that include the centrifugal term; μ is the reduced mass, and $\mathbf{k}$ is a matrix of asymptotic channel wave vectors. In principle the number of coupled equations is infinite, but in practice the expansion is truncated at some finite value.

The log derivative matrix is defined by

$$\mathbf{Y}(R) = \mathbf{\Psi}'(R)\mathbf{\Psi}^{-1}(R) \tag{A.3}$$

The log derivative methods propagates directly this matrix rather than the wave function and its derivative. This eliminates the stability problems which can arise when integration is started deep inside the classically forbidden region.

We can obtain from Eq. A.3 and Eq. A.1 the Ricatti matrix equation

$$\mathbf{Y}'(R) = \mathbf{W}(R) - \mathbf{Y}^2(R) \tag{A.4}$$

The log derivative matrix may be propagated using the $\mathcal{Y}$ propagator in an interval $[R', R'']$. The propagator $\mathcal{Y}$ is defined as,

$$\begin{bmatrix} \mathbf{\Psi}'(R') \\ \mathbf{\Psi}'(R'') \end{bmatrix} = \begin{bmatrix} \mathcal{Y}_1(R', R'') & \mathcal{Y}_2(R', R'') \\ \mathcal{Y}_3(R', R'') & \mathcal{Y}_4(R', R'') \end{bmatrix} \begin{bmatrix} -\mathbf{\Psi}'(R') \\ \mathbf{\Psi}'(R'') \end{bmatrix} \tag{A.5}$$

The stability of the matrix $\mathcal{Y}$ is independent of whether or not the log derivative matrix has a singularity at some point within the interval.

We can also obtain a recursion relation for the log derivative matrix:

$$\mathbf{Y}(R'') = \mathcal{Y}_4(R', R'') - \mathcal{Y}_3(R', R'')[\mathbf{Y}(R') + \mathcal{Y}_1(R', R'')]^{-1}\mathcal{Y}_2(R', R'') \tag{A.6}$$

This recursion relation is used to propagate $\mathbf{Y}$ on a series of small intervals.

The improved log derivative method implemented in `MOLSCAT` and `Hibridon`

The method of Manolopoulos [136] differ from the original method of Johnson [136] in the use of a piecewise constant diagonal reference potential for the homogeneous problem.

The homogeneous equation has the form,

$$\mathbf{\Phi}''(R) = \mathbf{W}_{ref}(R)\mathbf{\Phi}(R) \tag{A.7}$$

where $\mathbf{W}_{ref}$ is continuous throughout the interval $[a, b]$. From now on $[R', R'']$ will denote both half sectors $[a, c]$ and $[c, b]$ where $c = (b - a)/2$. $\mathbf{W}_{ref}$ can be defined as,

$$W_{ref}(R)_{ij} = \delta_{ij} p_j^2 \tag{A.8}$$

Then, the Eq. A.7 can be solved analytically. The propagator matrix y corresponding to the homogeneous solution $\mathbf{\Phi}$ have been defined by Manolopoulos [136],

$$\begin{aligned} y_1(R', R'')_{ij} = y_4(R', R'')_{ij} &= \delta_{ij} \begin{cases} |p_j| coth |p_j| h, & p_j^2 \geq 0, \\ |p_j| cot |p_j| h, & p_j^2 \leq 0, \end{cases} \\ y_1(R', R'')_{ij} = y_4(R', R'')_{ij} &= \delta_{ij} \begin{cases} |p_j| coth |p_j| h, & p_j^2 \geq 0, \\ |p_j| cot |p_j| h, & p_j^2 \leq 0, \end{cases} \end{aligned} \tag{A.9}$$

where $h = (b - a)/2$. The effective half-sector propagators for the solutions of the

Eq. A.1 are also defined like fallows,

$$\begin{aligned}
\hat{\mathcal{Y}}_1(R', R'') &= y_1(R', R'') + Q(R'), \\
\hat{\mathcal{Y}}_2(R', R'') &= y_2(R', R''), \\
\hat{\mathcal{Y}}_3(R', R'') &= y_3(R', R''), \\
\hat{\mathcal{Y}}_4(R', R'') &= y_4(R', R'') + Q(R'')
\end{aligned} \tag{A.10}$$

where the $Q = W - W_{ref}$.

The log derivative matrix is then propagated across the sector from a to b using the following recurrence relation,

$$\hat{\mathbf{Y}}(R'') = \hat{\mathcal{Y}}(R', R'') - \hat{\mathcal{Y}}(R', R'')[\hat{\mathbf{Y}}(R') + \hat{\mathcal{Y}}(R', R'')]^{-1}\hat{\mathcal{Y}}(R', R'') \tag{A.11}$$

This algorithm is a kind of “potential following” because the potential change from one sector to the next. This version of log derivative method reduce the matrix operations at subsequent energies and improve the convergence of the solution with respect to the number of grid points.

The parameters of `MOLSCAT`

In order to make more efficient the computation with `MOLSCAT` we have split the calculations in segments of total energies. For each segment we have optimized the input parameters of `MOLSCAT` in order to converge cross sections among the levels of our interest. Below we present the main parameters that have been used:

`STEPS` is the step size of the propagator.

`RMIN` is the starting point of the integration.

`RMAX` is the range of the integration.

`JMAX` define the rotational basis set.

`LMAX` specifies the highest Legendre term to include in the expansion of the potential.

Tables A.1 and A.2 show the parameters the parameters corresponding to the Al compounds. For AlCN-He and AlNC-He collisional systems we have extended the rotational basis sufficiently to ensure convergence of the AlCN-He and AlNC-He inelastic cross-sections for N,$N' \leq 25$. At the largest total energy considered (1000 cm^{-1}), the rotational basis extends to N=35 and 32, respectively, for the AlCN-He and AlNC-He calculations

Tables A.3 and A.4 show the parameters of Mg compounds. For MgCN-He and MgNC-He collisional systems, we have converged the first 40 rotational levels in order to correctly perform the summation over L in Eq. 3.7. This lead to converged rate coefficients between fine structure levels with N,$N' \leq 20$. At the largest total energy considered (1000 cm^{-1}), the rotational basis extends to $N = 53$ and 51, respectively, for the MgCN-He and MgNC-He calculations.

In the case of HCN, the rotational basis was increased up to $j_1 = 18$ at the largest total energy in order to ensure the convergence of the 13 first (up to $\text{j}_1 =$ 12) rotational levels of HCN.

In all cases, the maximum value of the total angular momentum J was set large enough to converge the inelastic cross sections to within $0.02 \mathring{A}^2$.

Table A.1: The MOLSCAT parameters for the CS calculations of the AlCN-He collisional system.

Energy total (cm^{-1})	Steps	JMAX	LMAX	RMAX
0 → 5	80	16	30	50
5 → 10	70	20	30	50
10 → 30	60	20	30	50
30 → 50	40	22	30	50
50 → 100	20	26	30	50
100 → 300	16	28	30	50
300 → 500	12	30	30	50
500 → 1000	8	35	30	50

Table A.2: The MOLSCAT parameters for the CS calculations of the AlNC-He collisional system.

Energy total (cm^{-1})	Steps	JMAX	LMAX	RMAX
0 → 5	80	20	30	50
5 → 10	70	22	30	50
10 → 30	60	22	30	50
30 → 50	30	26	30	50
50 → 100	20	27	30	50
100 → 300	10	29	30	50
300 → 500	9	30	30	50
500 → 1000	8	32	30	50

Table A.3: The MOLSCAT parameters for the CS calculations of the MgCN-He collisional system.

Energy total (cm^{-1})	Steps	JMAX	LMAX	RMAX
0 → 5	80	20	30	50
5 → 10	70	20	30	50
10 → 30	60	22	30	50
30 → 50	40	24	30	50
50 → 100	25	28	30	50
100 → 300	22	34	30	50
300 → 500	15	40	30	50
500 → 1000	13	53	30	50

Table A.4: The MOLSCAT parameters for the CS calculations of the MgNC-He collisional system.

Energy total (cm^{-1})	Steps	JMAX	LMAX	RMAX
0 → 5	80	20	30	50
5 → 10	70	20	30	50
10 → 30	60	22	30	50
30 → 50	40	22	30	50
50 → 100	30	28	30	50
100 → 300	22	34	30	50
300 → 500	15	40	30	50
500 → 1000	13	51	30	50

Table A.5: The MOLSCAT parameters for the CC calculations of the HCN–para-H_2 collisional system.

Energy total (cm^{-1})	Steps	J2MAX	J1MAX	RMAX
0 → 30	50	10	2	70
30 → 50	20	12	2	70
50 → 100	10	12	2	70
100 → 300	6	17	2	50
300 → 1000	5	18	2	50

Table A.6: The MOLSCAT parameters for the CC calculations of the HCN–ortho-H_2 collisional system.

Energy total (cm^{-1})	Steps	J2MAX	J1MAX	RMAX
130 → 300	15	12	1	50
300 → 1000	5	18	1	50

The parameters of `Hibridon`

The `Hibridon` program package was employed to study the SiCN-He and SiNC-He collisional systems. In this case we have also specified the following parameters for different segments of energies.

`SPAC` is the interval (sector) width in the log-derivative integration.

`RENDAI` is the end point for the integration, the point at which the S matrix is determined.

`JTOT2` is the final value of the total angular momentum.

`NUMAX` is the maximum value of the projection index ν in the CS calculations (Eq. 4.28)

`JMAX` define the rotational basis set.

In table A.7 and A.8 we present the paremeters employed in the calculations for each interval of energies. These parameters have ensured the convergence among the rotational levels of SiCN and SiNC up to j= 25.5 for the F_1 manifold and up to j= 20.5 for the F_2 manifold.

Table A.7: The Hibridon parameters for the CS calculations of the SiCN–He collisional system.

Energy total (cm^{-1})	SPAC	JTOT2	NUMAX	JMAX	RENDAI
0 → 5	0.05	10	0	15	80
5 → 10	0.05	15	3	15	80
10 → 20	0.05	25	5	15	80
20 → 35	0.05	25	8	25	80
35 → 50	0.05	28	10	28	80
50 → 75	0.05	28	14	28	100
75 → 100	0.05	40	18	35	100
100 → 150	0.1	40	20	35	100
150 → 250	0.1	45	25	40	100
250 → 500	0.1	65	33	50	100
500 → 1000	0.1	75	40	70	100

Table A.8: The Hibridon parameters for the CS calculations of the SiNC–He collisional system.

Energy total (cm^{-1})	SPAC	JTOT2	NUMAX	JMAX	RENDAI
0 → 5	0.05	12	0	15	80
5 → 10	0.05	15	3	15	80
10 → 20	0.05	25	5	15	80
20 → 35	0.05	26	8	25	80
35 → 50	0.05	27	10	28	80
50 → 75	0.05	28	14	28	100
75 → 100	0.05	35	18	35	100
100 → 150	0.1	35	20	35	100
150 → 250	0.1	45	25	40	100
250 → 500	0.1	65	33	50	100
500 → 1000	0.1	75	40	70	100

Appendix B

The PES of HCN-H_2

In this paper, we report a new PES for the HCN-H_2 collisional system. The PES have been used to compute the HCN-H_2 bound states. The very good agreement between theory and experiments shows the accuracy of the *ab initio* calculations.

THE JOURNAL OF CHEMICAL PHYSICS **139**, 224301 (2013)

A new *ab initio* potential energy surface for the collisional excitation of HCN by para- and ortho-H_2

Otoniel Denis-Alpizar,[1,2,a)] Yulia Kalugina,[3,4] Thierry Stoecklin,[1] Mario Hernández Vera,[3,5] and François Lique[2,b)]
[1] *Université de Bordeaux, ISM, CNRS UMR 5255, 33405 Talence Cedex, France*
[2] *Departamento de Física, Universidad de Matanzas, Matanzas 40100, Cuba*
[3] *LOMC - UMR 6294, CNRS-Université du Havre, 25 rue Philippe Lebon, BP 540, 76058, Le Havre, France*
[4] *Department of Optics and Spectroscopy, Tomsk State University, 36 Lenin av., Tomsk 634050, Russia*
[5] *Instituto Superior de Tecnologías y Ciencias Aplicadas, Quinta de Los Molinos, Plaza, La Habana 10600, Cuba*

(Received 4 October 2013; accepted 12 November 2013; published online 9 December 2013)

We present a new four-dimensional potential energy surface for the collisional excitation of HCN by H_2. *Ab initio* calculations of the HCN–H_2 van der Waals complex, considering both molecules as rigid rotors, were carried out at the explicitly correlated coupled cluster with single, double, and perturbative triple excitations [CCSD(T)-F12a] level of theory using an augmented correlation-consistent triple zeta (aVTZ) basis set. The equilibrium structure is linear HCN–H_2 with the nitrogen pointing towards H_2 at an intermolecular separation of 7.20 a_0. The corresponding well depth is -195.20 cm^{-1}. A secondary minimum of -183.59 cm^{-1} was found for a T-shape configuration with the H of HCN pointing to the center of mass of H_2. We also determine the rovibrational energy levels of the HCN–para-H_2 and HCN–ortho-H_2 complexes. The calculated dissociation energies for the para and ortho complexes are 37.79 cm^{-1} and 60.26 cm^{-1}, respectively. The calculated ro-vibrational transitions in the HCN–H_2 complex are found to agree by more than 0.5% with the available experimental data, confirming the accuracy of the potential energy surface. © *2013 AIP Publishing LLC*. [http://dx.doi.org/10.1063/1.4833676]

I. INTRODUCTION

Hydrogen cyanide (HCN) is a central molecule in the physical-chemistry of many media. For example, HCN is an important intermediate in the combustion reactions of hydrocarbon flames containing a nitrogen source.[1] HCN is also an important constituent of earth and planetary atmospheres[2] and plays a major role in the physical chemistry of these atmospheres. For example, in Titan atmosphere, HCN rotational emission is the dominant cooling process and is therefore responsible for the thermal structure of the thermosphere.[3]

From the astrophysical point of view, HCN is ubiquitous. Hydrogen cyanide is one of the most observed molecule in the interstellar medium (ISM). Owing to its large dipole moment, this molecule and its closely related molecule HNC are frequently used by astronomers to determine the physical and chemical conditions in many regions of the ISM.[4–9] They are also powerful probes of high density gas, as at the opposite of molecules like CO or CS, they do not seem to deplete on grain surfaces in the denser cold part of prestellar cores.[10]

The analysis of the astronomical HCN emission spectra requires the knowledge of accurate spectroscopical data, as well as collisional rate coefficients with the most abundant interstellar species. Indeed, collisional processes contribute, in competition with the radiative processes, to populate the rovibrational levels of the molecules. Consequently, the calculation of rate coefficients for the rotational excitation of HCN by H_2 (H_2 being the most abundant collisional partner is the ISM) has been a major goal for astrochemistry.

The first work dedicated to the rotational excitation of HCN by collisions with He atoms (as a model for H_2) was performed by Green and Thaddeus[11] in 1974. Then, many collisional studies of astrophysical interest have been devoted to the HCN–He collisional system and we just mention here the most recent ones.[12–14] However, in all these studies, He was used as a model for H_2 and recent results on rotational excitation of SO,[15] SiS,[16,17] or HNC[18] have pointed out that rate coefficients for collisions with H_2 are generally different from those for collisions with He, particularly for the case of collision with ortho-H_2.

Recently, Ben Abdallah *et al.*[19] have studied the rotational excitation of HCN by collisions with H_2 and provided rate coefficients for the rotational and hyperfine (de-)excitation of the HCN by para-H_2 at low temperature. However, these authors computed and used a potential energy surface (PES) averaged over the H_2 rotation, resulting in simplified dynamical calculations only valid for the collisional excitation by $H_2(j = 0)$ at low temperatures. Then, the validity of the approximation used by Ben Abdallah *et al.*[19] needs to be checked by comparing with calculations involving a global PES. Moreover, as HCN is also observed in high temperatures astrophysical environments, it seems also important to compute a new global HCN–H_2 PES in order to provide new rate coefficients for the rotational excitation of HCN by H_2 (para- and ortho-H_2) at high temperatures. These new data

---

[a)] otonieldenisalpizar@gmail.com
[b)] francois.lique@univ-lehavre.fr

0021-9606/2013/139(22)/224301/8/$30.00

will provide the astronomical community with the necessary tools to interpret HCN emission that will be observed with high spatial and spectral resolutions from the Atacama Large Millimeter/sub-millimeter Array (ALMA) interferometer.

From the experimental point of view, to the best of our knowledge, collisional excitation studies of HCN by H_2 are not available. However, several studies dedicated to the measurement of the HCN–H_2 van der Waals spectrum were performed during the last decade.[20–23] High resolution infrared[21,22] and millimeter-wave spectroscopy combined with a pulsed supersonic jet technique[20] have been used to study the van der Waals complex structure in great detail. Very recently, Fourier-transform microwave spectroscopy was applied to observe rotational transitions in the HCN–H_2 complex (both para- and ortho-H_2 species) in order to improve hyperfine molecular constants of the complex.[23] From these studies, Ishiguro *et al.*[20] and Moore *et al.*[21] were able to show that ortho-H_2 and para-H_2 bind at opposite ends of HCN. Moore *et al.*[22] used an average one-dimensional *ab initio* model of the PES to justify this analysis.

In this paper, we present a new four-dimensional (4D) potential energy surface for the HCN–H_2 system obtained from first principle calculations. As a first application and in order to check the accuracy of the new PES, we compute the bound energy levels of HCN–para-H_2 and HCN–ortho-H_2 complexes and compare the calculated HCN–H_2 frequencies with the experimental ones.[20,23] This paper is organized as follows. The *ab initio* calculations and the analytical representation of the PES are described in Sec. II. Features of the PES are discussed in Sec. III. The bound levels of the complexes and the comparison of calculated and experimental transitions frequencies are presented in Sec. IV.

II. *Ab initio* CALCULATIONS AND ANALYTICAL REPRESENTATION

A. *Ab initio* calculations

In the present work, we use the Jacobi coordinate system presented in Fig. 1. The origin of coordinates is placed at the center of mass of the HCN molecule and the vector **R** connecting HCN and the center of the H_2 bond is directed along the *z*-axis. The rotation of HCN and H_2 molecules is defined by θ and θ' angles, respectively. φ is the dihedral angle.

A very recent study dedicated to the ro-vibrational excitation of HCN by He[14] showed that neglecting the bending of HCN is a very reasonable approximation for treating the pure rotational rotational excitation at low and moderate temperatures. Indeed, some of us computed a 4D PES taking in account the bending angle of the HCN molecule and found that the results for the pure rotational excitation were in good agreement with those considering the collisional partner as rigid. Consequently and as we are mainly interested in the pure rotational excitation of the title system, the collision partners are then considered as rigid (i.e., we neglect effects of the normal mode vibrations of the HCN and H_2).

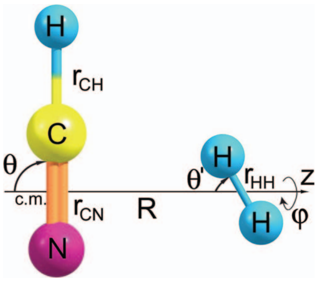

FIG. 1. Jacobi coordinate system of the HCN–H_2 system.

As shown before,[24] a better description of the intermolecular potential is obtained by fixing the molecular distance at its averaged value in the ground vibrational level rather than at the equilibrium distance. Accordingly, we used a H_2 bond distance $r_{\text{H-H}} = 1.448736$ a$_0$.[25] For HCN, we used the following interatomic distances $r_{CN} = 2.17923\ a_0$, $r_{CH} = 2.01350\ a_0$ (corresponding to the linear equilibrium geometry of HCN[26]).

Ab initio calculations of the PES of the HCN–H_2 van der Waals complex being in its ground electronic state were carried out at the explicitly correlated coupled cluster with single, double, and perturbative triple excitations [CCSD(T)-F12a][27] level of theory using an augmented correlation-consistent triple zeta (aVTZ) basis set.[28] The calculations were performed using Molpro 2010 package.[29] Additionally to the aVTZ basis set, density fitting and resolution of the identity techniques (needed for F12 calculations) require auxiliary basis sets. In the present study, we used the default corresponding auxiliary basis sets[30] from Molpro basis set library.

In all calculations, the interaction potential $V(R, \theta, \theta', \varphi)$ was corrected by the basis set superposition error (BSSE) with the Boys and Bernardi counterpoise scheme[31]

$$V(R,\theta,\theta',\varphi) = E_{\text{HCN}-\text{H}_2}(R,\theta,\theta',\varphi) - E_{\text{HCN}}(R,\theta,\theta',\varphi) - E_{\text{H}_2}(R,\theta,\theta',\varphi), \tag{1}$$

where the energies of HCN and H_2 are computed in the full basis set of the complex.

In order to evaluate the accuracy of CCSD(T)-F12a method in comparison with the standard CCSD(T) method using the aug-cc-pVXZ (X = D, T, Q) basis sets (hereafter aVDZ, aVTZ, aVQZ) and including results extrapolated to the Complete Basis Set (CBS) limit,[32] we have carried out additional calculations for selected angular orientations of the HCN–H_2 complex. The results are reported in Fig. 2.

As can be seen, the CCSD(T)-F12a together with diffuse basis set of aVTZ quality fully reaches the CCSD(T)/CBS accuracy as previously found for other van der Waals systems such as HCl–He[33] or O_2–He.[34] This comparison shows again that the CCSD(T)-F12a leads to an excellent description of the interaction energies using a relatively limited atomic basis set.

In order to accurately describe the anisotropy of the potential energy surface, the calculations were carried out for a large grid of angular orientations: we vary the θ angle from 0° to 180° with a step of 10°, the θ' angle from 0° to 180° with a step of 15°, and the φ angle from 0° to 90° with a step of 15°. *R*-distances vary from 3.5 to 30 bohrs in order to get 39 radial grid points for each angular orientation.

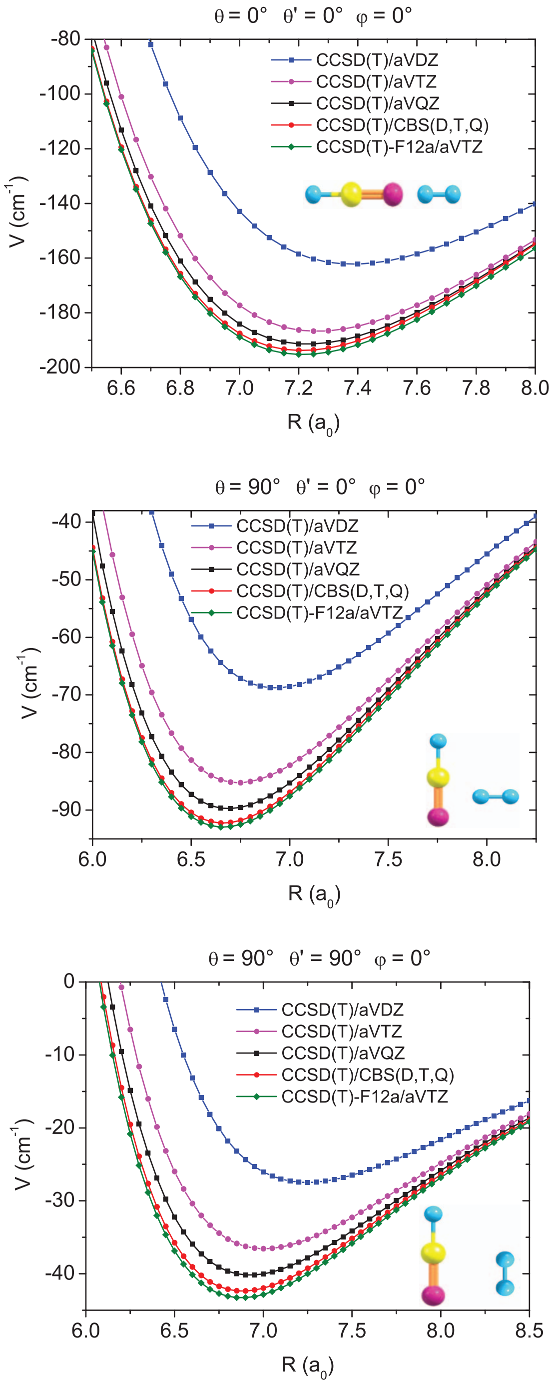

FIG. 2. Potential energy cuts of 4D PES for several angular orientations. Energy is in cm^{-1}.

B. Analytical representation

The angular part of the analytical representation of the PES is represented by a product of normalized associated Legendre functions and a cosine function. Hence, the potential is expressed such as

$$V(R,\theta',\theta,\varphi)=\sum_{l_1=0}^{4}\sum_{l_2=0}^{17}\sum_{m=0}^{min(l_1,l_2,3)} v^{m}_{l_1,l_2}(R) \times\bar{P}^{m}_{l_1}(\cos\theta')\,\bar{P}^{m}_{l_2}(\cos\theta)\cos(m\varphi), \qquad (2)$$

where $v^{m}_{l_1,l_2}(R)$ are the radial functions. Only even values of l_1 are included in this expansion because of the H exchange symmetry of H$_2$. For each value of the radial grid, we fitted the *ab initio* points using a least squares method. We used a weight function for energies higher than 5000 cm^{-1} as

$$w(E(\theta',\theta,\varphi))=\frac{V_0}{E(\theta',\theta,\varphi)}. \qquad (3)$$

By trial and error, the values of the weight function parameter were found to be V$_0$ = 5000 cm^{-1}. In total, we get 135 angular coefficients for each radial point.

The analytical representation of the radial coefficients $v^{m}_{l_1,l_2}(R)$ was divided in three parts, corresponding to the short-range, the intermediate, and the long-range regions as detailed in the three following expressions:

$$F_{sr}(R)=\sum_{n=0}^{10} e^{-\alpha R}R^{n}C^{m,n}_{l_1,l_2} R\leq 6a_0, \qquad (4)$$

$$F_{ir}(R)=\sum_{k=4}^{11}\frac{C^{m,k}_{l_1,l_2}}{R^{k}} 6<R<11a_0, \qquad (5)$$

$$F_{lr}(R)=\sum_{k=4}^{8}\frac{t_k(\beta R)}{R^{k}}C^{m,k}_{l_1,l_2} R\geq 11a_0, \qquad (6)$$

where the $t_k(x)$ is the Tang-Toennies damping function

$$t_k(x)=1-e^{-x}\sum_{i=0}^{k}\frac{x^{i}}{i!} \qquad (7)$$

and α = 1.8 a$_0^{-1}$, β = 4.0 a$_0^{-1}$. These analytical functions allowed us to get an accurate representation of the PES using a least-square procedure to compute the final coefficients. The quality of the fitted surface was checked by evaluating the root-mean-square (RMS) of the differences between the *ab initio* energies and the fitted energies. For negative energies, the RMS was on the order of 10^{-4} cm^{-1}. For energies in the range $0 \leq E \leq 1000$ cm^{-1}, the RMS was 0.008 cm^{-1} while for $1000 < E \leq 10\,000$ cm^{-1} we found the RMS = 3.656 cm^{-1}. The analytical representation of the PES is available from the authors upon request.

III. FEATURES OF THE POTENTIAL ENERGY SURFACE

The global minimum ($D_e = -195.20$ cm^{-1}) of the 4D PES corresponds to a linear geometry of the HCN–H$_2$ complex with $\theta = 0°$, $\theta' = 0°$ or 180°, and $R = 7.20$ a$_0$. A secondary minimum of −183.59 cm^{-1} is found for the T-shape configuration associated with $\theta' = 90°$, $\theta = 180°$, and $R = 7.75$ a$_0$. This finding is in good agreement with the experimental one of Moore *et al.*[22] which concludes that linear HCN–H$_2$ is the most stable geometry of the complex.

The contour plots in Figs. 3 and 4 show the anisotropy of the interaction with respect to the HCN and H$_2$ rotation. In Fig. 3, we present the anisotropy of the potential as a function

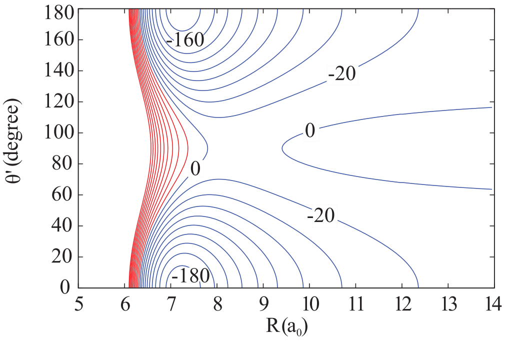

FIG. 3. Contour plot of the PES for $\theta = 0°$. Contour lines are equally spaced by 20 cm^{-1}. Red contour lines represent the repulsive interaction energies.

of θ' for fixed values of θ and φ. As one can see, there is relatively strong anisotropy of the PES with respect to the θ' Jacobi angle. Figure 4 shows the interaction energies for $\varphi = 0°$ with R relaxing in the range [7.0, 8.0] a_0. Here again, we found a relatively strong anisotropy of the PES with respect to these two Jacobi angles. Therefore, we can anticipate that rotational state of H_2 will significantly influence the magnitude of the HCN excitation cross sections.

In Fig. 4, we can see the secondary minimum associated with the T-shape configuration (with the H of HCN pointing to the center of mass of H_2) which is only 11.61 cm^{-1} above the global minimum. Then, we expect this configuration of the HCN–H_2 complex to be almost equally important for the dynamics of the system.

The analysis of the PES features may be supplemented by taking advantage of the H exchange symmetry of the H_2 molecule and averaging our PES over the para and ortho rotational wave function of H_2 such as

$$V_{av} = \langle Y^*_{j_1,k}(\theta', \varphi)|V(R, \theta', \theta, \varphi)|Y_{j_1,k}(\theta', \varphi)\rangle, \qquad (8)$$

where j_1 denotes the rotational angular momentum of H_2. The projection of j_1 on the intermolecular axis is k. This integral was evaluated numerically, using a Gauss-Chebyshev quadrature of 20 points for the integration over φ and a Gauss-Legendre quadrature with 10 points over θ'.

Figure 5(a) shows the contour plot for the averaged potential over para-H_2($j_1 = 0$). The most stable configuration of the complex is obtained for the linear configuration of HCN–H_2 and for an intermolecular separation of 8.14 a$_0$. This surface can be compared with the approximate PES of Ben Abdallah *et al.*[19] Our averaged surface, with a minimum of −79.23 cm^{-1}, is 8.46 cm^{-1} deeper than the one presented by Abdallah *et al.*[19] while the secondary minimums obtained in both cases for a value of θ close to 60°, differ only by 1.1 cm^{-1}. But the most interesting result is that they found the most stable configuration for $\theta = 164°$ while we obtained it for a linear configuration of HCN in agreement with the conclusions of the experiments of Ishiguro *et al.*[20] These differences result from the fact that they averaged over φ and θ' using only three different angular configurations of the complex.

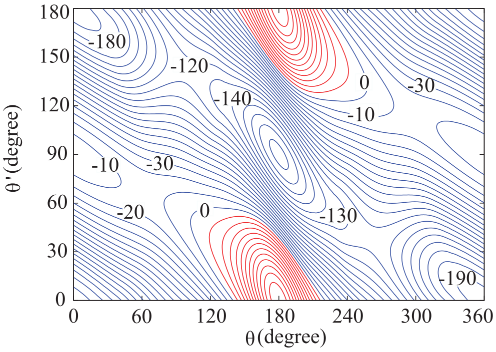

FIG. 4. Contour plot of the PES for $\varphi = 0°$ and R relax in the range [7.0, 8.0] a_0. Contour lines are equally spaced by 10 cm^{-1}. Red contour lines represent the repulsive interaction energies.

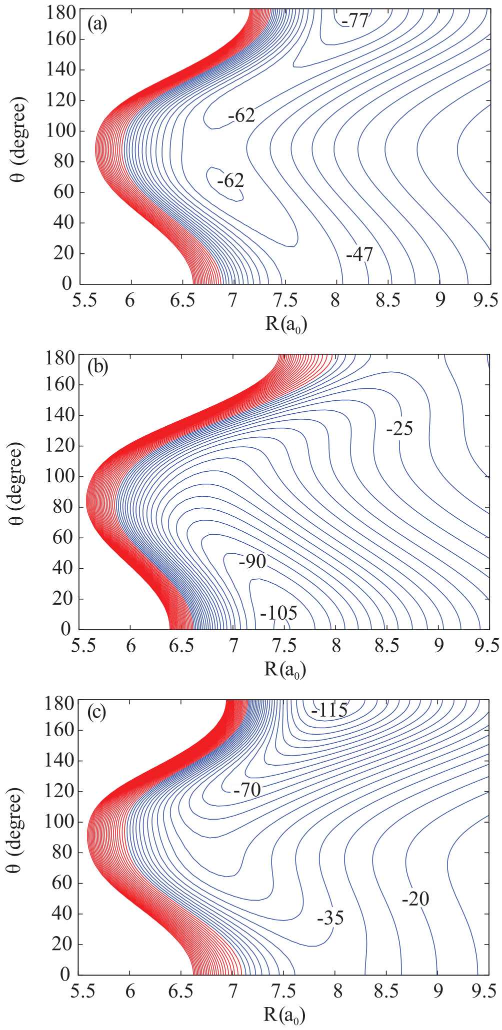

FIG. 5. Contour plot of the average PES over the rotational wave function of H_2. (a) corresponds to the average over ($j_1 = 0, k = 0$); (b) corresponds to the average over ($j_1 = 1, k = 0$); (c) corresponds to the average over ($j_1 = 1, k = \pm 1$). Contour lines are equally spaced by 5 cm^{-1}. Red contour lines represent the repulsive interaction energies.

In the ortho-H_2($j_1 = 1$) case, the wave function can be ($j_1 = 1, k = 0$) or ($j_1 = 1, k = \pm 1$). We plotted the two corresponding averaged potentials in Figs. 5(b) and 5(c). These averaged potential are deeper than the one obtained for para-H_2. In both cases, the minimum corresponds to a linear configuration of the complex, but with $\theta = 0^\circ$ or 180°. These two configurations of the HCN–ortho-H_2 complex are corresponding to the H atom and to the N atom of HCN pointing towards H_2, respectively, while experimental observations of Moore *et al.*[21,22] lead to a linear configuration of the complex with the H atom of HCN pointing towards H_2.

Then, in order to understand the nature of interactions in HCN–H_2 system, we have performed analytical calculations of interaction energy based on multipolar expansion. In the framework of the long-range approximation,[35] the potential energy of two interacting systems can be written as

$$V = E_{elec} + E_{ind} + E_{disp}, \tag{9}$$

where E_{elec}, E_{ind}, and E_{disp} are the electrostatic, induction, and dispersion contributions to the total interaction energy of the complex. For interacting HCN and H_2 molecules, the electrostatic, induction, and dispersion terms from R^{-4} through the order of R^{-8} are

$$\begin{aligned} E_{elec} = & -\frac{1}{3}T_{\alpha\beta\gamma}\mu^A_\alpha\Theta^B_{\beta\gamma} + \frac{1}{9}T_{\alpha\beta\gamma\delta}\Theta^A_{\alpha\beta}\Theta^B_{\gamma\delta} \\ & - \frac{1}{105}T_{\alpha\beta\gamma\delta\epsilon}\mu^A_\alpha\Phi^B_{\beta\gamma\delta\epsilon} - \frac{1}{45}T_{\alpha\beta\gamma\delta\epsilon}\Omega^A_{\alpha\beta\gamma}\Theta^B_{\delta\epsilon} \\ & + \frac{1}{315}T_{\alpha\beta\gamma\delta\epsilon\varphi}\left(\Theta^A_{\alpha\beta}\Phi^B_{\gamma\delta\epsilon\varphi} + \Theta^B_{\alpha\beta}\Phi^A_{\gamma\delta\epsilon\varphi}\right) \\ & - \frac{1}{945}T_{\alpha\beta\gamma\delta\epsilon\varphi\nu}\mu^A_\alpha\Gamma^B_{\beta\gamma\delta\epsilon\varphi\nu} \\ & - \frac{1}{1575}T_{\alpha\beta\gamma\delta\epsilon\varphi\nu}\Omega^A_{\alpha\beta\gamma}\Phi^B_{\delta\epsilon\varphi\nu} \\ & - \frac{1}{2835}T_{\alpha\beta\gamma\delta\epsilon\varphi\nu}\Sigma^A_{\alpha\beta\gamma\delta\epsilon}\Theta^B_{\varphi\nu}, \end{aligned} \tag{10}$$

$$\begin{aligned} E_{ind} = & -\frac{1}{2}T_{\alpha\beta}T_{\gamma\delta}\alpha^B_{\alpha\beta}\mu^A_\beta\mu^A_\gamma \\ & + \frac{1}{3}T_{\alpha\gamma}T_{\beta\delta\phi}\alpha^B_{\alpha\beta}\mu^A_\gamma\Theta^A_{\delta\phi} \\ & - \frac{1}{18}T_{\alpha\gamma\delta}T_{\beta\phi\epsilon}\left(\alpha^B_{\alpha\beta}\Theta^A_{\gamma\delta}\Theta^A_{\phi\epsilon} + \alpha^A_{\alpha\beta}\Theta^B_{\gamma\delta}\Theta^B_{\phi\epsilon}\right) \\ & - \frac{1}{15}T_{\alpha\gamma}T_{\beta\delta\phi\epsilon}\alpha^B_{\alpha\beta}\mu^A_\gamma\Omega^A_{\delta\phi\epsilon} \\ & - \frac{1}{15}T_{\alpha\varphi}T_{\beta\gamma\delta\epsilon}E^B_{\alpha,\beta\gamma\delta}\mu^A_\varphi\mu^A_\epsilon \\ & - \frac{1}{6}T_{\alpha\beta\varphi}T_{\gamma\delta\epsilon}C^B_{\alpha\beta,\gamma\delta}\mu^A_\varphi\mu^A_\epsilon, \end{aligned} \tag{11}$$

$$\begin{aligned} E_{disp} = & -\frac{C^0_6}{6\alpha^A\alpha^B}\Big[T_{\alpha\beta}T_{\gamma\delta}\alpha^A_{\alpha\gamma}\alpha^B_{\beta\delta} \\ & - \frac{2}{3}T_{\alpha\beta}T_{\gamma\delta\phi}\alpha^B_{\alpha\gamma}A^A_{\beta,\delta\phi} + \frac{1}{3}T_{\alpha\beta\gamma}T_{\delta\phi\epsilon}\big(\alpha^A_{\alpha\delta}C^B_{\beta\gamma,\phi\epsilon} \\ & + \alpha^B_{\alpha\delta}C^A_{\beta\gamma,\phi\epsilon}\big) + \frac{2}{15}T_{\alpha\beta}T_{\gamma\delta\phi\epsilon}\big(\alpha^A_{\alpha\gamma}E^B_{\beta,\delta\phi\epsilon} \\ & + \alpha^B_{\alpha\gamma}E^A_{\beta,\delta\phi\epsilon}\big)\Big], \end{aligned} \tag{12}$$

where $\alpha = (\alpha_{xx} + \alpha_{yy} + \alpha_{zz})/3$ is a mean polarizability. Superscripts A and B denote molecules HCN and H_2, respectively. In the present work, we adopted the tensor notations of Buckingham.[35] Definition of multipole moments and polarizabilities is presented in Table I. Tensor $T_{\alpha\beta\gamma\ldots\nu} = \nabla_\alpha\nabla_\beta\nabla_\gamma\ldots\nabla_\nu R^{-1}$ is the symmetric tensor relative to the permutation of any pair of subscripts. The tensor T of rank n, $T^{(n)}$, is proportional to $R^{-(n+1)}$. There is a summation over repeated indexes. Expression (12) was obtained in "constant-ratio" approximation,[36] which allows to evaluate dispersion contribution through static properties of subsystems and isotropic C^0_6 dispersion coefficient. One should note, that all properties in Eqs. (10)–(12) are represented in the coordinate system of the complex.

TABLE I. Molecular properties of monomers HCN and H_2 calculated at CCSD(T)/aV5Z level of theory using finite-field method. Literature values are in parenthesis. All values are in a.u.

Param.	Definition	HCN[a]	H_2
μ_z	Dipole moment	− 1.188 (−1.180[b])	0
Θ_{zz}	Quadrupole moment	1.703 (1.646[b])	0.4823
Ω_{zzz}	Octupole moment	− 9.822 (−9.762[b])	0
Φ_{zzzz}	Hexadecapole moment	23.274 (22.45[b])	0.3177
Σ_{zzzzz}	5th-order multipole moment	− 110.120	0
Γ_{zzzzzz}	6th-order multipole moment	352.377	0.1702
α_{xx}	Dipole polarizability	13.933	4.7284
α_{zz}		22.248	6.7168
$A_{z,zz}$	Dipole-quadrupole polarizability	− 11.714	0
$A_{x,zx}$		− 1.489	0
$E_{x,xxx}$	Dipole-octupole polarizability	− 34.229	− 1.7800
$E_{z,zzz}$		100.156	4.4462
$C_{xx,xx}$	Quadrupole polarizability	33.996	4.8331
$C_{xz,xz}$		39.886	4.4469
$C_{zz,zz}$		67.184	6.3610

[a] Properties were calculated with respect to the origin at the center of mass with N atom along the positive direction of z axis.

[b] Theoretical values by Maroulis and Pouchan.[40]

The values of multipole moments and polarizabilities used in analytical calculations are presented in Table I. These values were calculated in the coordinate system of monomers at the CCSD(T)/aV5Z level of theory using finite-field method of Cohen and Roothaan[37] since it was not possible to compute them at the CCSD(T)-F12 level. The isotropic dispersion coefficient $C^0_6 = 34.148\ E_h a^6_0$ was calculated at the CCSD PROPAGATOR method[38] using the Molpro routine.[39]

In Fig. 6, we present the major contributions to the interaction energy in long-range approximation for the equilibrium configuration of HCN–H_2 complex. One can see that the electrostatic interactions are dominant for this complex. The leading electrostatic term is the H_2 quadrupole–HCN dipole interaction proportional to $\Theta\mu R^{-4}$; the H_2 quadrupole–HCN quadrupole and H_2 quadrupole–HCN octupole interactions proportional to $\Theta\Theta R^{-5}$ and $\Theta\Omega R^{-6}$, compensate each other. The other contributions are relatively small and do not contribute much to the behavior of the long range PES.

Figure 7 shows the curves of the interaction energy for different orientations of monomers at long-range separations. There is a good agreement between the CCSD(T)-F12a results and analytical calculations for $R > 13\ a_0$, which confirms

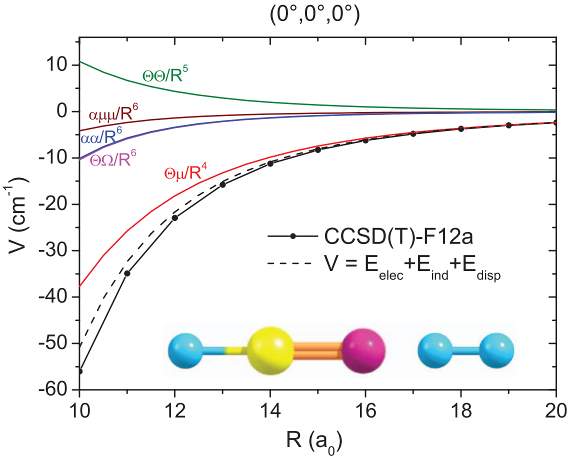

FIG. 6. Different contributions to the interaction energy of HCN–H_2 system for equilibrium configuration with $\theta = 0°$ and $\theta' = 0°$. Energy is in cm^{-1}. Solid black line – CCSD(T)-F12a calculations; dashed black line – total interaction energy in long-range approximation; solid color lines – major contributions to interaction energy from Eqs. (10) to (12).

that both analytical and *ab initio* calculations have a correct physical behavior. This also means that the present PES can be used with confidence to describe cold molecular collisions.

IV. BOUND STATES CALCULATIONS

We used a close coupling approach to compute the rovibrational energy levels of the HCN–H_2 complex. As described in a previous study,[41,42] we implemented the bound state calculations in our diatom-diatom Close Coupling scattering code according to the approach proposed by Danby[43] and Hutson[44] for the R-matrix and log-derivative propagators, respectively. Recently, we used the same approach to calculate the bound states of several diatom-diatom complexes.[45,46]

Briefly, our code solves the rovibrationally inelastic Close Coupling equations in the space fixed frame using the Jacobi coordinates. The vibrational levels of the van der Waals complex are calculated by performing calculations for all the values of the total angular momentum J and parity leading to bound states.

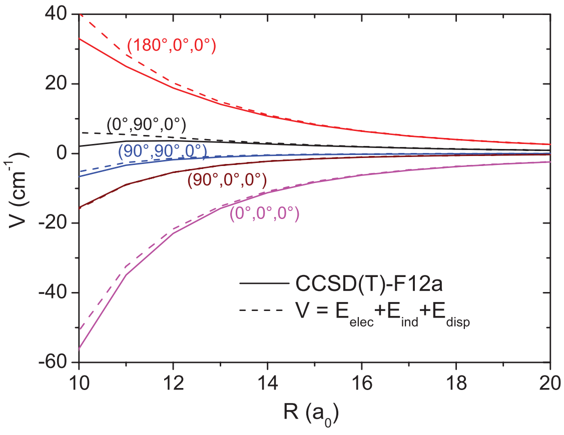

FIG. 7. Comparison of *ab initio* and analytical calculations of the PES for fixed angular arrangements. Energy is in cm^{-1}. Solid lines – CCSD(T)-F12a calculations; dashed lines – analytical calculations.

In the present study, we performed the diatom-linear molecule calculations using for both HCN and H_2, a rigid rotor description. The calculations were done separately for ortho- and para-H_2. We used the vibrationally averaged rotational constants for both molecules (B = 59.322 cm^{-1} for H_2[47] and B = 1.47822 cm^{-1} for the HCN[48]).

The convergence of the bound levels of HCN–H_2 complex with respect to the HCN and H_2 rotational basis was tested. Twelve rotational states were included in the basis set describing the HCN molecule while for para-H_2 we included two rotational states. In the case of HCN–ortho-H_2, we also included two rotational states for ortho-H_2 and 13 for HCN. The maximum propagation distance was 50 a_0.

The calculations were performed for two values of the propagator step size (0.1 and 0.05 a_0) and the values of the bound state energies were obtained from a Richardson extrapolation as suggested by Hutson.[44]

The results of the lower bound states calculations are presented in Tables II and III. The other energy levels are available in the supplementary material.[49] The rovibrational energies are given relative to the ground state energy of infinitely separated HCN and para-H_2. The spacing between the levels $j_1 = 0$ and $j_1 = 2$ in the para form and between the $j_1 = 1$ and $j_1 = 3$ levels in the ortho form are larger than the well depth of the potential. Consequently, all the HCN–para-H_2 bound states are associated with $j_1 = 0$ while those of HCN–ortho-H_2 involve only $j_1 = 1$. For ortho-H_2, the quantum number associated with the angular momentum $j_{12} = j_1 + j_2$, where j_2 designates the HCN rotational state and is also necessary to classify the levels as j_1 is non-zero.

In Table II, we report, for the HCN–para-H_2 complex, the energy, the total angular momentum J, and the parity ε (where $\varepsilon = (-1)^{j_1+j_2+L}$) of the lower bound levels (E < 20 cm^{-1}). We also assign the approximate quantum number j_2 and the orbital quantum number L. In Table III, we report the same

TABLE II. Lower bound levels (E < 20 cm^{-1}) of the HCN–para-H_2 van der Waals complex. The approximate quantum numbers j_2 and L are also given.

State			Energy	State			Energy
J	ε	(j_2, L)	(cm^{-1})	J	ε	(j_2, L)	(cm^{-1})
0	+	(0,0)	−37.79	2	−	(1,0)	−27.89
0	+	(1,1)	−31.46	2	−	(2,1)	−24.03
0	+	(2,2)	−23.87	3	−	(0,3)	−33.16
1	−	(0,1)	−37.00	3	−	(1,2)	−26.90
1	−	(1,0)	−31.27	3	−	(1,4)	−24.63
1	−	(1,2)	−29.09	3	−	(2,1)	−21.92
1	−	(2,1)	−25.39	3	+	(1,3)	−24.69
1	−	(2,3)	−20.68	3	+	(2,2)	−21.81
1	+	(1,1)	−30.08	4	+	(0,4)	−30.14
1	+	(2,2)	−23.28	4	+	(1,3)	−22.95
2	+	(0,2)	−35.45	4	+	(1,5)	−22.19
2	+	(1,1)	−29.69	4	−	(1,4)	−20.63
2	+	(1,3)	−26.30	5	+	(0,5)	−26.40
2	+	(2,0)	−25.51	6	+	(0,6)	−21.97
2	+	(2,2)	−22.08				

TABLE III. Lower bound levels (E < 77 cm^{-1}) of the HCN–ortho-H_2 van der Waals complex. The approximate quantum numbers j_2, j_{12} and L are also given.

State			Energy	State			Energy
J	ε	(j_2, j_{12}, L)	(cm^{-1})	J	ε	(j_2, j_{12}, L)	(cm^{-1})
0	+	(0,1,1)	58.38	2	−	(2,2,2)	72.97
0	+	(1,2,2)	68.60	3	−	(0,1,2)	63.48
0	+	(2,3,3)	75.26	3	−	(1,2,1)	67.74
1	−	(0,1,2)	59.24	3	−	(1,2,5)	69.42
1	−	(1,1,1)	63.95	3	−	(2,1,2)	74.41
1	−	(1,2,1)	65.30	3	−	(2,3,4)	76.65
1	−	(2,2,2)	70.11	3	+	(1,1,2)	67.91
1	−	(2,3,2)	74.00	3	+	(1,1,4)	70.33
1	+	(1,1,0)	63.93	3	+	(2,2,1)	75.85
1	+	(1,1,2)	65.63	4	+	(0,1,3)	66.83
1	+	(2,3,3)	76.52	4	+	(1,2,2)	70.61
2	+	(0,1,1)	60.94	4	+	(1,2,6)	73.03
2	+	(1,2,0)	65.56	4	−	(1,2,3)	70.94
2	+	(1,1,2)	66.76	4	−	(2,2,2)	74.22
2	+	(2,2,1)	72.46	5	−	(0,1,4)	70.97
2	+	(3,4,2)	73.03	5	−	(1,2,3)	74.25
2	+	(3,4,4)	74.93	5	+	(1,1,4)	74.69
2	−	(1,1,1)	65.58	6	+	(0,1,5)	75.88
2	−	(1,1,3)	67.45				

TABLE IV. Comparison of observed and calculated transition frequencies in MHz.

	Transition	Frequencies		
	J′–J″	Calculated	Observed	% difference
HCN–para-H_2				
	1–0	23 649	23 665[a]	0.07
	3–2	68 823	69 155[b]	0.48
	4–3	90 616	90 933[b]	0.35
	5–4	112 040	112 149[b]	0.10
	6–5	133 024	133 575[b]	0.41
HCN–ortho-H_2				
	1–0	25 723	25 768[a]	0.18
	3–2	76 103	76 209[b]	0.14
	4–3	100 446	100 590[b]	0.14
	5–4	124 179	124 370[b]	0.15
	6–5	147 368	147 614[b]	0.17

[a] Average of hyperfine components from Ref. 23.

[b] Average of hyperfine components from Ref. 20.

information for the lower bound levels (E < 77 cm^{-1}) of the the HCN–ortho-H_2 complex. In addition, we also assign the approximate quantum number j_{12}. This attribution allowed us to determine the transitions of the system in the ground state of HCN and to compare them with the experimental results.

The maximum value of the total angular momentum J leading to bound states is 9 for HCN–para-H_2 and 11 for HCN–ortho-H_2. The total number of bound states supported by our PES is 101 for HCN–para-H_2 and 330 for HCN–ortho-H_2. There are around three times more states for the ortho form than for the para form. This is related to the fact that with $j_1 = 0$, a single value of j_{12} is possible for any given value of j_2 , while with $j_1 = 1$, three values of j_{12} are obtained. A similar ratio between the number of ortho and para states was observed previously for the H_2–O_2 complex.[45] The dissociation energies of the ground states of the para and ortho species are 37.79 cm^{-1} and 60.26 cm^{-1}, respectively. These values are at least more than 4 times the dissociation energy found for the HCN–He complex (8.986 cm^{-1})[14] confirming that van der Waals complexes are generally more bonded with H_2 than with He. A comparison with the result of the bound levels calculations for the isoelectronic CO–H_2 complex,[47] also shows a smaller dissociation energy for the para-H_2 complex than for the ortho-H_2 complex. However, the HCN–H_2 complexes have a larger dissociation energy than the complex CO–H_2 (23.7 cm^{-1} for CO–para-H_2 and 30.8 cm^{-1} for CO–ortho-H_2), as we expected given the difference between the wells depths of these two surfaces.

The bound state energies were used to determine the transitions frequencies in the HCN–H_2 van der Waals complex. In the frequencies calculations, we considered HCN in its ground rotational state. These transitions are compared in Table IV with the spectroscopic data available published by Ishiguro *et al.*[20,23] These authors reported several lines including the splitting into several hyperfine components due to the spin angular momentum of the nitrogen nucleus (I = 1). As our calculations do not include the hyperfine structure and because the spin splitting is very small in comparison with the spacings of the rotational lines, we compare our results with those of Ishiguro *et al.*[20,23] averaged over the hyperfine components. The agreement between our results and experimental ones is better than 0.5% in all cases. It confirms the accuracy of the new HCN–H_2 PES.

V. CONCLUSION

We have developed a new 4D analytical PES for the HCN–H_2 van der Waals complex based on a large grid of *ab initio* points obtained at CCSD(T)-F12a level and using an aVTZ basis set. The equilibrium structure of the HCN–H_2 complex was found to be linear with the nitrogen pointing towards H_2. The corresponding well depth is 195.20 cm^{-1}. We found a secondary minimum only 11.61 cm^{-1} above the global minimum in which the H atom of HCN is pointing towards the center of mass of H_2.

As a first application, the rovibrational bound states were computed within the rigid-rotor approximation. The total number of bound states supported by our PES is 101 for HCN–para-H_2 and 330 for HCN–ortho-H_2. The dissociation energies of the ground states of the para and ortho species are 37.79 cm^{-1} and 60.26 cm^{-1}, respectively. The calculated transitions frequencies are found to be in very good agreement with the experimental available data. This level of agreement suggests that our PES is accurate enough for computing accurate inelastic cross sections.

Finally, the present PES was also compared with the previous existing models. The differences which were found and taking into account the astrophysical importance of this molecule give a supplementary interest to new Close Coupling calculations of the inelastic cross sections which will be performed using this new surface. In particular, inelastic cross sections and rate coefficients will be provided for the first time for the ortho-H_2 collisional partner. These results will be very valuable for the astrophysical modeling of "hot environment" where ortho-H_2 is abundant.

ACKNOWLEDGMENTS

We acknowledge Jose Cernicharo for stimulating this studies and for fruitful discussions. This work has been supported by the Agence Nationale de la Recherche (ANR-HYDRIDES), contract ANR-12-BS05-0011-01 and by the CNRS national program "Physique et Chimie du Milieu Interstellaire." M.H.V. acknowledge the french embassy of Cuba for financial support. F.L. thank the CPER Haute-Normandie/CNRT/Energie, Electronique, Matériaux. *Ab initio* calculations were performed using High Performance Computing resources of SKIF-Cyberia (Tomsk State University).

[1] J. A. Miller and C. T. Bowman, Prog. Energy Combust. Sci. **15**, 287 (1989).
[2] Q. Li, D. J. Jacob, I. Bey, R. M. Yantosca, Y. Zhao, Y. Kondo, and J. Notholt, Geophys. Res. Lett. **27**, 357, doi:10.1029/1999GL010935 (2000).
[3] R. V. Yelle, Astrophys. J. **383**, 380 (1991).
[4] G. J. Harris, Y. V. Pavlenko, H. R. A. Jones, and J. Tennyson, Mon. Not. R. Astron. Soc. **344**, 1107 (2003); e-print arXiv:astro-ph/0306141.
[5] Y. Gao and P. M. Solomon, Astrophys. J. **606**, 271 (2004).
[6] Y. Gao, C. L. Carilli, P. M. Solomon, and P. A. V. Bout, Astrophys. J. Lett. **660**, L93 (2007).
[7] J. Graciá-Carpio, S. García-Burillo, P. Planesas, A. Fuente, and A. Usero, Astron. Astrophys. **479**, 703 (2008).
[8] W. A. Baan, C. Henkel, A. F. Loenen, A. Baudry, and T. Wiklind, Astron. Astrophys. **477**, 747 (2008).
[9] F. Daniel, M. Gerin, E. Roueff, J. Cernicharo, N. Marcelino, F. Lique, D. C. Lis, D. Teyssier, N. Biver, and D. Bockelee-Morvan, "Nitrogen isotopic ratios in Barnard 1: A consistent study of the N_2H^+, NH_3, CN, HCN and HNC isotopologues," Astron. Astrophys. (in press), e-print arXiv:1309.5782 [astro-ph.GA].
[10] P. Hily-Blant, M. Walmsley, G. Pineau Des Forêts, and D. Flower, Astron. Astrophys. **480**, L5 (2008); e-print arXiv:0801.2876.
[11] S. Green and P. Thaddeus, Astrophys. J. **191**, 653 (1974).
[12] E. Sarrasin, D. B. Abdallah, M. Wernli, A. Faure, J. Cernicharo, and F. Lique, Mon. Not. R. Astron. Soc. **404**, 518 (2010).
[13] F. Dumouchel, A. Faure, and F. Lique, Mon. Not. R. Astron. Soc. **406**, 2488 (2010).
[14] O. Denis-Alpizar, T. Stoecklin, P. Halvick, and M.-L. Dubernet, J. Chem. Phys. **139**, 034304 (2013).
[15] F. Lique and A. Spielfiedel, Astron. Astrophys. **462**, 1179 (2007).
[16] F. Lique and J. Kłos, J. Chem. Phys. **128**, 034306 (2008).
[17] J. Kłos and F. Lique, Mon. Not. R. Astron. Soc. **390**, 239 (2008).
[18] F. Dumouchel, J. Kłos, and F. Lique, Phys. Chem. Chem. Phys. **13**, 8204 (2011).
[19] D. B. Abdallah, F. Najar, N. Jaidane, F. Dumouchel, and F. Lique, Mon. Not. R. Astron. Soc. **419**, 2441 (2012).
[20] M. Ishiguro, T. Tanaka, K. Harada, C. J. Whitham, and K. Tanaka, J. Chem. Phys. **115**, 5155 (2001).
[21] D. T. Moore, M. Ishiguro, L. Oudejans, and R. E. Miller, J. Chem. Phys. **115**, 5137 (2001).
[22] D. T. Moore, M. Ishiguro, and R. E. Miller, J. Chem. Phys. **115**, 5144 (2001).
[23] M. Ishiguro, K. Harada, K. Tanaka, T. Tanaka, Y. Sumiyoshi, and Y. Endo, Chem. Phys. Lett. **554**, 33 (2012).
[24] P. Jankowski and K. Szalewicz, J. Chem. Phys. **123**, 104301 (2005).
[25] K. P. Huber and G. Herzberg, *Molecular Spectra and Molecular Structure. IV. Constants of Diatomic Molecules* (Van Nostrand Reinhold, New York, 1979).
[26] G. Strey and I. M. Mills, Mol. Phys. **26**, 129 (1973).
[27] G. Knizia, T. B. Adler, and H. Werner, J. Chem. Phys. **130**, 054104 (2009).
[28] T. H. Dunning, J. Chem. Phys. **90**, 1007 (1989).
[29] H.-J. Werner, P. J. Knowles, G. Knizia, F. R. Manby, M. Schütz *et al.*, Molpro, version 2010.1, a package of *ab initio* programs, 2010, see http://www.molpro.net.
[30] K. Yousaf and K. Peterson, Chem. Phys. Lett. **476**, 303 (2009).
[31] S. F. Boys and F. Bernardi, Mol. Phys. **19**, 553 (1970).
[32] K. A. Peterson, D. E. Woon, and T. H. Dunning, Jr., J. Chem. Phys. **100**, 7410 (1994).
[33] Y. Ajili, K. Hammami, N. E. Jaidane, M. Lanza, Y. N. Kalugina, F. Lique, and M. Hochlaf, Phys. Chem. Chem. Phys. **15**, 10062 (2013).
[34] F. Lique, J. Kłos, and M. Hochlaf, Phys. Chem. Chem. Phys. **12**, 15672 (2010).
[35] A. D. Buckingham, *Intermolecular Interactions: From Diatomics to Biopolymers* (Wiley, New York, 1978).
[36] X. Li, K. L. C. Hunt, J. Pipin, and D. Bishop, J. Chem. Phys. **105**, 10954 (1996).
[37] H. D. Cohen and C. C. J. Roothaan, J. Chem. Phys. **43**, S34 (1965).
[38] R. Moszynski, P. S. Zuchowski, and B. Jeziorski, Collect. Czech. Chem. Commun. **70**, 1109 (2005).
[39] T. Korona, M. Przybytek, and B. Jeziorski, Mol. Phys. **104**, 2303 (2006).
[40] C. P. G. Maroulis, Theor. Chim. Acta **93**, 131 (1996).
[41] F. Turpin, P. Halvick, and T. Stoecklin, J. Chem. Phys. **132**, 214305 (2010).
[42] P. Halvick, T. Stoecklin, F. Lique, and M. Hochlaf, J. Chem. Phys. **135**, 044312 (2011).
[43] G. Danby, J. Phys. B **16**, 3393 (1983).
[44] J. M. Hutson, Comput. Phys. Commun. **84**, 1 (1994).
[45] Y. Kalugina, O. Denis-Alpizar, T. Stoecklin, and F. Lique, Phys. Chem. Chem. Phys. **14**, 16458 (2012).
[46] O. Denis-Alpizar, T. Stoecklin, P. Halvick, M. Dubernet, and S. Marinakis, J. Chem. Phys. **137**, 234301 (2012).
[47] P. Jankowski and K. Szalewicz, J. Chem. Phys. **108**, 3554 (1998).
[48] G. Herzberg, *Molecular Spectra and Molecular Structure, Vol. 3: Electronic Spectra and Electronic Structure of Polyatomic Molecules* (Van Nostrand, New York, 1950), p. 757.
[49] See supplementary material at http://dx.doi.org/10.1063/1.4833676 for the tables which report the higher energy levels of the bound states of the HCN–para-H_2 and HCN–ortho-H_2 complexes.

Bibliography

[1] K. M. Ferrière. The interstellar environment of our galaxy. *Reviews of Modern Physics*, 73:1031–1066, October 2001.

[2] Pablo Fosalba, Alex Lazarian, Simon Prunet, and Jan A. Tauber. Dust polarization from starlight data. *AIP Conference Proceedings*, 609(1):44–50, 2002.

[3] O. E. H. Rydbeck, J. Ellder, A. Sume, A. Hjalmarson, and W. M. Irvine. Radio astronomical determination of ground state transition frequencies of CH. *A&A*, 34:479–482, September 1974.

[4] K. B. Jefferts, A. A. Penzias, and R. W. Wilson. Observation of the CN Radical in the Orion Nebula and W51. *ApJL*, 161:L87, August 1970.

[5] A. E. Douglas and G. Herzberg. Note on CH^+ in Interstellar Space and in the Laboratory. *ApJ.*, 94:381, September 1941.

[6] H. I. Ewen and E. M. Purcell. Observation of a Line in the Galactic Radio Spectrum: Radiation from Galactic Hydrogen at 1,420 Mc./sec. *Nature*, 168:356, September 1951.

[7] G. R. Carruthers. Rocket Observation of Interstellar Molecular Hydrogen. *ApJL*, 161:L81, August 1970.

[8] R. W. Wilson, K. B. Jefferts, and A. A. Penzias. Carbon Monoxide in the Orion Nebula. *ApJL*, 161:L43, July 1970.

[9] H. C. Kim, R. J. Chastain, and L. Magnani. E(B-V), CO, and CH as Molecular Gas Tracers in a Translucent Cloud. In *American Astronomical Society Meeting Abstracts #200*, volume 34 of *Bulletin of the American Astronomical Society*, page 766, May 2002.

[10] R. Shetty, S. C. Glover, C. P. Dullemond, and R. S. Klessen. Modelling CO emission - I. CO as a column density tracer and the X factor in molecular clouds. *MNRAS*, 412:1686–1700, April 2011.

[11] T. Liu, Y. Wu, and H. Zhang. Gaseous CO Abundance. An Evolutionary Tracer for Molecular Clouds. *ApJL*, 775:L2, September 2013.

[12] D. A. Williams and S. Viti. *Observational Molecular Astronomy*. January 2014.

[13] S. Leurini, C. Codella, A. Gusdorf, L. Zapata, A. Gómez-Ruiz, L. Testi, and T. Pillai. Evidence of a SiO collimated outflow from a massive YSO in IRAS 17233-3606. *A&A*, 554:A35, June 2013.

[14] V. Wakelam, I. W. M. Smith, E. Herbst, J. Troe, W. Geppert, H. Linnartz, K. Öberg, E. Roueff, M. Agúndez, P. Pernot, H. M. Cuppen, J. C. Loison, and D. Talbi. Reaction Networks for Interstellar Chemical Modelling: Improvements and Challenges. *SSRv*.

[15] Piergiorgio Casavecchia and Millard H. Alexander. Uncloaking the quantum nature of inelastic molecular collisions. *Science*, 341(6150):1076–1077, 2013.

[16] Simon Chefdeville, Yulia Kalugina, Sebastiaan Y. T. van de Meerakker, Christian Naulin, Franois Lique, and Michel Costes. Observation of partial wave resonances in low-energy o2h2 inelastic collisions. *Science*, 341(6150):1094–1096, 2013.

[17] A. M. Arthurs and A. Dalgarno. The theory of scattering by a rigid rotator. *Proceedings of the Royal Society of London. Series A. Mathematical and Physical Sciences*, 256(1287):540–551, 1960.

[18] U. Fano and G. Racah. *Irreducible tensorial sets.* Academic Press, New York, 1959.

[19] C. F. Curtiss. The quantum mechanics of collisions between diatomic molecules. *J. Chem. Phys.*, 21(11):2045–2050, 1953.

[20] K. Takayanagi. The theory of collisions between two diatomic molecules. *Prog. Theor. Phys*, 11(6):557–594, 1954.

[21] Paul McGuire and Donald J. Kouri. Quantum mechanical close coupling approach to molecular collisions. jz conserving coupled states approximation. *J. Chem. Phys.*, 60(6):2488–2499, 1974.

[22] Thomas P. Tsien, Gregory A. Parker, and Russell T Pack. Rotationally inelastic molecular scattering. computational tests of some simple solutions of the strong coupling problem. *J. Chem. Phys.*, 59(10):5373–5381, 1973.

[23] Hans-Joachim Werner, Peter J. Knowles, Gerald Knizia, Frederick R. Manby, and Martin Schtz. Molpro: a general-purpose quantum chemistry program

package. *Wiley Interdisciplinary Reviews: Computational Molecular Science*, 2(2):242–253, 2012.

[24] M. J. Frisch, G. W. Trucks, H. B. Schlegel, G. E. Scuseria, M. A. Robb, J. R. Cheeseman, G. Scalmani, V. Barone, B. Mennucci, G. A. Petersson, H. Nakatsuji, M. Caricato, X. Li, H. P. Hratchian, A. F. Izmaylov, J. Bloino, G. Zheng, J. L. Sonnenberg, M. Hada, M. Ehara, K. Toyota, R. Fukuda, J. Hasegawa, M. Ishida, T. Nakajima, Y. Honda, O. Kitao, H. Nakai, T. Vreven, J. A. Montgomery, Jr., J. E. Peralta, F. Ogliaro, M. Bearpark, J. J. Heyd, E. Brothers, K. N. Kudin, V. N. Staroverov, R. Kobayashi, J. Normand, K. Raghavachari, A. Rendell, J. C. Burant, S. S. Iyengar, J. Tomasi, M. Cossi, N. Rega, J. M. Millam, M. Klene, J. E. Knox, J. B. Cross, V. Bakken, C. Adamo, J. Jaramillo, R. Gomperts, R. E. Stratmann, O. Yazyev, A. J. Austin, R. Cammi, C. Pomelli, J. W. Ochterski, R. L. Martin, K. Morokuma, V. G. Zakrzewski, G. A. Voth, P. Salvador, J. J. Dannenberg, S. Dapprich, A. D. Daniels, . Farkas, J. B. Foresman, J. V. Ortiz, J. Cioslowski, and D. J. Fox. Gaussian09 Revision D.01. Gaussian Inc. Wallingford CT 2009.

[25] J. M. Hutson and S. Green, 1994. MOLSCAT computer code, version 14 (1994), distributed by Collaborative Computational Project No. 6 of the Engineering and Physical Sciences Research Council (UK).

[26] The Hibridon package was written by M. H. Alexander, D. E. Manolopoulos, H.-J. Werner, B. Follmeg and P. J. Dagdigian, with contributions by P. F. Vohralik, D. Lemoine, G. Corey, R. Gordon, B. Johnson, T. Orlikowski, A. Berning, A. Degli-Esposti, C. Rist, B. Pouilly, G. van der Sanden, M. Yang, F. de Weerd, S. Gregurick, J. Klos and F. Lique. Support for its

development was provided by grants (to MHA) from the U. S. National Science Foundation, the U. S. Army Research Office, the Office of Scientific Research of the U. S. Air Force, and (to HJW) from the German Fonds der Chemische Industrie. Copyright (c) 1987, 1991, 1993, 1996, 2000, 2001, 2003, 2004, 2007, 2008, 2009, 2010, 2011 University of Maryland at College Park. All rights reserved. .

[27] A. Spielfiedel, N. Feautrier, F. Najar, D. Ben Abdallah, F. Dayou, M. L. Senent, and F. Lique. Fine and hyperfine excitation of C_2H by collisions with He at low temperature. *MNRAS*, 421:1891–1896, April 2012.

[28] Francois Lique, Jacek Klos, and Majdi Hochlaf. Benchmarks for the generation of interaction potentials for scattering calculations: applications to rotationally inelastic collisions of c4 (x3[capital sigma]-g) with he. *Phys. Chem. Chem. Phys.*, 12:15672–15680, 2010.

[29] J. Kłos and F. Lique. The rotational excitation of SiS by para- and ortho-H_2. *MNRAS*, 390:239–244, October 2008.

[30] N. Troscompt, A. Faure, L. Wiesenfeld, C. Ceccarelli, and P. Valiron. Rotational excitation of formaldehyde by hydrogen molecules: ortho-H_2CO at low temperature. *A&A*, 493:687–696, January 2009.

[31] D. Rabli and D. R. Flower. The rotational structure of methanol and its excitation by helium. *MNRAS*, 403:2033–2040, April 2010.

[32] YUAN TSEH LEE. Molecular beam studies of elementary chemical processes. *Science*, 236(4803):793–798, 1987.

[33] Yuval Shagam and Edvardas Narevicius. Sub-kelvin collision temperatures in

merged neutral beams by correlation in phase-space. *The Journal of Physical Chemistry C*, 117(43):22454–22461, 2013.

[34] Samuel A Meek, Gabriele Santambrogio, Horst Conrad, and Gerard Meijer. Taming molecular beams; towards a gas-phase molecular laboratory on a chip. *Journal of Physics: Conference Series*, 194(1):012063, 2009.

[35] W. F. Drake Gordon. *Handbook of Atomic, Molecular, and Optical Physics*. Springer, January 2006.

[36] A. McKellar. Evidence for the Molecular Origin of Some Hitherto Unidentified Interstellar Lines. *Astronomical Society of the Pacific*, 52:187, June 1940.

[37] W. S. Adams. Some Results with the COUDÉ Spectrograph of the Mount Wilson Observatory. *ApJ.*, 93:11, January 1941.

[38] A. M. Ritchey, S. R. Federman, and D. L. Lambert. Interstellar CN and CH^+ in Diffuse Molecular Clouds: $^{12}C/^{13}C$ Ratios and CN Excitation. *ApJ.*, 728:36, February 2011.

[39] P. Hily-Blant, M. Walmsley, G. Pineau Des Forêts, and D. Flower. CN in prestellar cores. *A&A*, 480:L5–L8, March 2008.

[40] J. H. Kastner, P. Hily-Blant, D. R. Rodriguez, K. Punzi, and T. Forveille. Unbiased Millimeter-wave Line Surveys of TW Hya and V4046 Sgr: The Enhanced C_2H and CN Abundances of Evolved Protoplanetary Disks. *ApJ.*, 793:55, September 2014.

[41] G. I. Boger and A. Sternberg. CN and HCN in Dense Interstellar Clouds. *ApJ.*, 632:302–315, October 2005.

[42] E. Falgarone, T. H. Troland, R. M. Crutcher, and G. Paubert. CN Zeeman measurements in star formation regions. *A&A*, 487:247–252, August 2008.

[43] N. S. Hakobian and R. M. Crutcher. Structure and Composition of Molecular Clouds with CN Zeeman Detections I: W3(OH). *ApJ.*, 733:6, May 2011.

[44] S. Harrison, A. Faure, and J. Tennyson. CN excitation and electron densities in diffuse molecular clouds. *MNRAS*, 435:3541–3546, November 2013.

[45] G. Pineau des Forets, E. Roueff, and D. R. Flower. The formation of nitrogen-bearing species in dark interstellar clouds. *MNRAS*, 244:668–674, June 1990.

[46] E. F. van Dishoeck and J. H. Black. Comprehensive models of diffuse interstellar clouds - Physical conditions and molecular abundances. *ApJS.*, 62:109–145, September 1986.

[47] Ralf I. Kaiser. Experimental investigation on the formation of carbon-bearing molecules in the interstellar medium via neutralneutral reactions. *Chemical Reviews*, 102(5):1309–1358, 2002. PMID: 11996539.

[48] Sidaty Cheikh Sid Ely, Sbastien B. Morales, Jean-Claude Guillemin, Stephen J. Klippenstein, and Ian R. Sims. Low temperature rate coefficients for the reaction CN + HC_3N. *The Journal of Physical Chemistry A*, 117(46):12155–12164, 2013. PMID: 24047203.

[49] L. E. Snyder and D. Buhl. Observations of Radio Emission from Interstellar Hydrogen Cyanide. *ApJL*, 163:L47, January 1971.

[50] H. Liszt and R. Lucas. . *A&A*, 370:576–585, May 2001.

[51] T. Hirota, S. Yamamoto, H. Mikami, and M. Ohishi. Abundances of HCN and HNC in Dark Cloud Cores. *ApJ.*, 503:717–728, August 1998.

[52] G. van der Plas, S. Casassus, F. Ménard, S. Perez, W. F. Thi, C. Pinte, and V. Christiaens. Spatially Resolved HCN J = 4-3 and CS J = 7-6 Emission from the Disk around HD 142527. *ApJL*, 792:L25, September 2014.

[53] D. Talbi. An extensive ab initio study of a process of astrophysical interest: the $N^+(N)+CH_3(CH_3{}^+)$ reaction. *Chemical Physics Letters*, 312:291–298, October 1999.

[54] M. B. Mendes, H. Buhr, M. H. Berg, M. Froese, M. Grieser, O. Heber, B. Jordon-Thaden, C. Krantz, O. Novotný, S. Novotny, D. A. Orlov, A. Petrignani, M. L. Rappaport, R. Repnow, D. Schwalm, A. Shornikov, J. Stützel, D. Zajfman, and A. Wolf. Cold Electron Reactions Producing the Energetic Isomer of Hydrogen Cyanide in Interstellar Clouds. *ApJL*, 746:L8, February 2012.

[55] E. Herbst, R. Terzieva, and D. Talbi. Calculations on the rates, mechanisms, and interstellar importance of the reactions between C and NH_2 and between N and CH_2. *MNRAS*, 311:869–876, February 2000.

[56] A. Fuente, J. Martin-Pintado, J. Cernicharo, and R. Bachiller. A chemical study of the photodissociation region NGC 7023. *A&A*, 276:473, September 1993.

[57] P. M. Solomon and P. A. Vanden Bout. Molecular Gas at High Redshift. *ARA&A*, 43:677–725, September 2005.

[58] L. M. Ziurys, C. Savage, J. L. Highberger, A. J. Apponi, M. Guélin, and

J. Cernicharo. More Metal Cyanide Species: Detection of AlNC (X $^1\Sigma^+$) toward IRC +10216. *ApJL*, 564:L45–L48, January 2002.

[59] L. M. Ziurys and A. J. Apponi. Confirmation of Interstellar HOC +: Reevaluating the [HCO +]/[HOC +] Abundance Ratio. *ApJL*, 455:L73, December 1995.

[60] M. Guelin, J. Gomez-Gonzalez, J. Cernicharo, and C. Kahane. A new free radical in IRC + 10216. *A&A*, 157:L17–L20, March 1986.

[61] L. N. Zack, D. T. Halfen, and L. M. Ziurys. Detection of FeCN (x $^4\Delta_{\ i}$) in IRC+10216: A New Interstellar Molecule. *ApJL*, 733:L36, June 2011.

[62] R. L. Pulliam, C. Savage, M. Agúndez, J. Cernicharo, M. Guélin, and L. M. Ziurys. Identification of KCN in IRC+10216: Evidence for Selective Cyanide Chemistry. *ApJL*, 725:L181–L185, December 2010.

[63] J. L. Highberger, C. Savage, J. H. Bieging, and L. M. Ziurys. Heavy-Metal Chemistry in Proto-Planetary Nebulae: Detection of MgNC, NaCN, and AlF toward CRL 2688. *ApJ.*, 562:790–798, December 2001.

[64] J. L. Highberger and L. M. Ziurys. Detection of MgNC in CRL 618: Tracing Metal Chemistry with Asymptotic Giant Branch Evolution. *ApJ.*, 597:1065–1069, November 2003.

[65] S. Petrie. On the formation of metal cyanides and related compounds in the circumstellar envelope of IRC+10216. *MNRAS*, 282:807–819, October 1996.

[66] R. C. Dunbar and S. Petrie. Interstellar and Circumstellar Reaction Kinetics of Na^+, Mg^+, and Al^+ with Cyanopolyynes and Polyynes. *ApJ.*, 564:792–802, January 2002.

[67] M. Guélin, S. Muller, J. Cernicharo, A. J. Apponi, M. C. McCarthy, C. A. Gottlieb, and P. Thaddeus. Astronomical detection of the free radical SiCN. *A&A*, 363:L9–L12, November 2000.

[68] M. Guélin, S. Muller, J. Cernicharo, M. C. McCarthy, and P. Thaddeus. Detection of the SiNC radical in IRC+10216. *A&A*, 426:L49–L52, November 2004.

[69] M. Guelin, R. Lucas, and J. Cernicharo. MgNC and the carbon-chain radicals in IRC+10216. *A&A*, 280:L19–L22, December 1993.

[70] Joel M. Bowman, Bela Gazdy, Joseph A. Bentley, Timothy J. Lee, and Christopher E. Dateo. Ab initio calculation of a global potential, vibrational energies, and wave functions for hcn/hnc, and a simulation of the x emission spectrum. *J. Chem. Phys.*, 99(1):308–323, 1993.

[71] M. L. Senent, F. Dumouchel, and F. Lique. Cyanide/isocyanide abundances in the interstellar medium - I. Theoretical spectroscopic characterization. *MNRAS*, 420:1188–1194, February 2012.

[72] W. M. Irvine and F. P. Schloerb. Cyanide and isocyanide abundances in the cold, dark cloud TMC-1. *ApJ.*, 282:516–521, July 1984.

[73] P. Schilke, C. M. Walmsley, G. Pineau Des Forets, E. Roueff, D. R. Flower, and S. Guilloteau. A study of HCN, HNC and their isotopomers in OMC-1. I - Abundances and chemistry. *A&A*, 256:595–612, March 1992.

[74] H. Ungerechts, E. A. Bergin, P. F. Goldsmith, W. M. Irvine, F. P. Schloerb, and R. L. Snell. Chemical and Physical Gradients along the OMC-1 Ridge. *ApJ.*, 482:245–266, June 1997.

[75] Evelyne Roueff and Franois Lique. Molecular excitation in the interstellar medium: Recent advances in collisional, radiative, and chemical processes. *Chemical Reviews*, 113(12):8906–8938, 2013.

[76] M. Lanza, Y. Kalugina, L. Wiesenfeld, A. Faure, and F. Lique. New insights on the HCl abundance in the interstellar medium. *MNRAS*, 443:3351–3358, October 2014.

[77] F. Lique, R. Toboła, J. Kłos, N. Feautrier, A. Spielfiedel, L. F. M. Vincent, G. Chałasiński, and M. H. Alexander. Can we estimate $H_2(j = 0)$ rate coefficients from He rate coefficients? Application to the SiS molecule. *A&A*, 478:567–574, February 2008.

[78] M. Wernli, L. Wiesenfeld, A. Faure, and P. Valiron. Rotational excitation of HC_3N by H_2 and He at low temperatures. *A&A*, 475:391–391, November 2007.

[79] F. Lique. *Collisional excitation of interstellar molecules: theory and observations interpretations.* PhD thesis, LERMA - Observatoire de Meudon 5 Place Jules Janssen 92195 Meudon cedex, 2006.

[80] Otoniel Denis-Alpizar, Thierry Stoecklin, Philippe Halvick, and Marie-Lise Dubernet. Rotational relaxation of cs by collision with ortho- and para-h2 molecules. *J. Chem. Phys.*, 139(20):–, 2013.

[81] Max Born and Robert Oppenheimer. Zur Quantentheorie der Molekeln. *Annalen der Physik*, 84:457–484, 1927.

[82] D. R. Hartree. The wave mechanics of an atom with a non-coulomb central field. part i. theory and methods. *Mathematical Proceedings of the Cambridge*

Philosophical Society, 24:89–110, 1 1928.

[83] J. C. Slater. The theory of complex spectra. *Phys. Rev.*, 34:1293–1322, Nov 1929.

[84] C. David Sherrill and Henry F. Schaefer III. The configuration interaction method: Advances in highly correlated approaches. 34:143 – 269, 1999.

[85] Paolo Celani and Hans-Joachim Werner. Multireference perturbation theory for large restricted and selected active space reference wave functions. *The Journal of Chemical Physics*, 112(13), 2000.

[86] Chr. Møller and M. S. Plesset. Note on an approximation treatment for many-electron systems. *Phys. Rev.*, 46:618–622, Oct 1934.

[87] Bogumil Jeziorski, Robert Moszynski, and Krzysztof Szalewicz. Perturbation theory approach to intermolecular potential energy surfaces of van der waals complexes. *Chemical Reviews*, 94(7):1887–1930, 1994.

[88] F. Coester and H. Kmmel. Short-range correlations in nuclear wave functions. *Nuclear Physics*, 17(0):477 – 485, 1960.

[89] Ji ek. On the correlation problem in atomic and molecular systems. calculation of wavefunction components in urselltype expansion using quantumfield theoretical methods. *The Journal of Chemical Physics*, 45(11), 1966.

[90] Trygve Helgaker, Poul Jorgensen, Jeppe Olsen . *Molecular electronic-structure theory.* Wiley, January 2013.

[91] C. Hampel, K. A. Peterson, and H.-J. Werner. A comparison of the efficiency and accuracy of the quadratic configuration interaction (QCISD), coupled

cluster (CCSD), and Brueckner coupled cluster (BCCD) methods. *Chemical Physics Letters*, 190:1–12, February 1992.

[92] J. D. Watts, J. Gauss, and R. J. Bartlett. *J. Chem. Phys.*, 98:8718, 1993.

[93] Thom H. Dunning. Gaussian basis sets for use in correlated molecular calculations. i. the atoms boron through neon and hydrogen. *J. Chem. Phys.*, 90(2):1007–1023, 1989.

[94] FuMing Tao and YuhKang Pan. Mo/llerPlesset perturbation investigation of the He2 potential and the role of midbond basis functions. *J. Chem. Phys.*, 97(7):4989–4995, 1992.

[95] HuanC. Chang, FuMing Tao, William Klemperer, Catherine Healey, and Jeremy M. Hutson. The arhf intermolecular potential: Overtone spectroscopy and abinitio calculations. *J. Chem. Phys.*, 99(12):9337–9349, 1993.

[96] Heike Fliegl, Wim Klopper, and Christof Httig. Coupled-cluster theory with simplified linear-r12 corrections: The ccsd(r12) model. *J. Chem. Phys.*, 122(8):–, 2005.

[97] Thomas B. Adler, Gerald Knizia, and Hans-Joachim Werner. A simple and efficient CCSD(T)-F12 approximation. *J. Chem. Phys.*, 127(22):–, 2007.

[98] I. T. Iakubov and V. V. Pogosov. Toward the theory of the electron affinity of large dielectric clusters: Quantum size correction. *J. Chem. Phys.*, 106(6):2306–2310, 1997.

[99] I. C. Percival and M. J. Seaton. The partial wave theory of electron-hydrogen atom collisions. *Mathematical Proceedings of the Cambridge Philosophical Society*, 53:654–662, 7 1957.

[100] J M Launay. Body-fixed formulation of rotational excitation: exact and centrifugal decoupling results for co-he. *Journal of Physics B: Atomic and Molecular Physics*, 9(10):1823, 1976.

[101] Russell T Pack. Spacefixed vs bodyfixed axes in atomdiatomic molecule scattering. sudden approximations. *J. Chem. Phys.*, 60(2):633–639, 1974.

[102] Michael L. Klein, John D. Goddard, and David G. Bounds. An abinitio molecular orbital study of nacn and kcn. *J. Chem. Phys.*, 75(8):3909–3915, 1981.

[103] T. Hirano, K. Ishii, T.E. Odaka, and P. Jensen. . *Journal of Molecular Spectroscopy*, 215(1):42–57, 2002.

[104] A. J. Apponi, M. C. McCarthy, C. A. Gottlieb, and P. Thaddeus. The Radio Spectra of SICCH, SICN, and SINC. *ApJL*, 536:L55–L58, June 2000.

[105] J. H. He, Dinh-V-Trung, S. Kwok, H. S. P. Mller, Y. Zhang, T. Hasegawa, T. C. Peng, and Y. C. Huang. A spectral line survey in the 2 and 1.3 mm windows toward the carbon-rich envelope of irc +10216. *The Astrophysical Journal Supplement Series*, 177(1):275, 2008.

[106] John M. Brown and Alan Carrington. *Rotational Spectroscopy of Diatomic Molecules*. Cambridge University Press, 2003. Cambridge Books Online.

[107] Millard H. Alexander. Rotationally inelastic collisions between a diatomic molecule in a $^2\Sigma^+$ electronic state and a structureless target. *J. Chem. Phys.*, 76(7):3637–3645, 1982.

[108] G. C. Corey and F. R. McCourt. *J. Chem. Phys.*, 87(6):2723–2730, 1983.

[109] Millard H. Alexander, Jane E. Smedley, and Gregory C. Corey. On the physical origin of propensity rules in collisions involving molecules in $^2\Sigma$ electronic states. *J. Chem. Phys.*, 84(6):3049–3058, 1986.

[110] Alexander, Millard H. and Dagdigian, Paul J. Collisioninduced transitions between molecular hyperfine levels: Quantum formalism, propensity rules, and experimental study of CaBr($X^2\Sigma^+$)+Ar. *J. Chem. Phys.*, 83(5):2191–2200, 1985.

[111] D. A. Neufeld and S. Green. Excitation of interstellar hydrogen chloride. *ApJ.*, 432:158–166, September 1994.

[112] F. Daniel, M.-L. Dubernet, and Markus Meuwly. Selective hyperfine excitation of N_2H^+ by He: Potential energy surface, cross sections, and propensity rules. *J. Chem. Phys.*, 121(10):4540–4549, 2004.

[113] Nancy A. Richardson, Yukio Yamaguchi, and Henry F. Schaefer. Isomerization of the interstellar molecule silicon cyanide to silicon isocyanide through two transition states. *J. Chem. Phys.*, 119(24):12946–12955, 2003.

[114] Millard H. Alexander. Quantum treatment of rotationally inelastic collisions involving molecules in {II} electronic states: New derivation of the coupling potential. *Chemical Physics*, 92(23):337 – 344, 1985.

[115] W. Kol/os and L. Wolniewicz. Accurate adiabatic treatment of the ground state of the hydrogen molecule. *J. Chem. Phys.*, 41(12):3663–3673, 1964.

[116] W. Kol/os and L. Wolniewicz. Potentialenergy curves for the x1g+, b3u+, and c1u states of the hydrogen molecule. *J. Chem. Phys.*, 43(7):2429–2441, 1965.

[117] W. Kolos and L. Wolniewicz. Improved theoretical groundstate energy of the hydrogen molecule. *J. Chem. Phys.*, 49(1):404–410, 1968.

[118] Alice M. Smith, Kevin K. Lehmann, and William Klemperer. The intensity and selfbroadening of overtone transitions in hcn. *The Journal of Chemical Physics*, 85(9):4958–4965, 1986.

[119] H. Meyer, E. R. Th. Kerstel, D. Zhuang, and G. Scoles. Subdoppler rotationally resolved overtone spectroscopy of the hcn dimer. *J. Chem. Phys.*, 90(8):4623–4625, 1989.

[120] Alice M. Smith, Uffe G. Jo/rgensen, and Kevin K. Lehmann. The intensities of hcn overtone transitions from 1260018400 cm1. *The Journal of Chemical Physics*, 87(10):5649–5656, 1987.

[121] Isaac F. Silvera. The solid molecular hydrogens in the condensed phase: Fundamentals and static properties. *Rev. Mod. Phys.*, 52:393–452, Apr 1980.

[122] Otoniel Denis-Alpizar, Thierry Stoecklin, Philippe Halvick, and Marie-Lise Dubernet. The interaction of he with vibrating hcn: Potential energy surface, bound states, and rotationally inelastic cross sections. *J. Chem. Phys.*, 139(3):–, 2013.

[123] Franois Lique, Pascal Honvault, and Alexandre Faure. Orthopara-h2 conversion processes in astrophysical media. *International Reviews in Physical Chemistry*, 33(1):125–149, 2014.

[124] D. R. Flower, G. Pineau Des Forêts, and C. M. Walmsley. The importance of the ortho:para H_2 ratio for the deuteration of molecules during pre-protostellar collapse. *A&A*, 449:621–629, April 2006.

[125] M. A. Thompson N. Lo B. ODwyer M. R. Cunningham R. M. Loughnane, M. P. Redman. Observations of hcn hyperfine line anomalies towards low and highmass starforming cores. *Monthly Notices of the Royal Astronomical Society*, (2):13671383, 2012.

[126] Mathieu Lanza, Yulia Kalugina, Laurent Wiesenfeld, and Franois Lique. Near-resonant rotational energy transfer in hclh2 inelastic collisions. *J. Chem. Phys.*, 140(6):–, 2014.

[127] G.-J. van Zadelhoff, C. P. Dullemond, F. F. S. van der Tak, J. A. Yates, S. D. Doty, V. Ossenkopf, M. R. Hogerheijde, M. Juvela, H. Wiesemeyer, and F. L. Schöier. Numerical methods for non-LTE line radiative transfer: Performance and convergence characteristics. *A&A*, 395:373–384, November 2002.

[128] F. F. S. van der Tak, J. H. Black, F. L. Schöier, D. J. Jansen, and E. F. van Dishoeck. A computer program for fast non-LTE analysis of interstellar line spectra. With diagnostic plots to interpret observed line intensity ratios. *A&A*, 468:627–635, June 2007.

[129] V. V. Sobolev. *Moving envelopes of stars. Translated by Sergei Gaposchkin.* Harvard University Press Cambridge, 1960.

[130] D. Ben Abdallah, F. Najar, N. Jaidane, F. Dumouchel, and F. Lique. Hyperfine excitation of HCN by H_2 at low temperature. *MNRAS*, 419:2441–2447, January 2012.

[131] Fabien Dumouchel, Jacek Klos, and Francois Lique. The rotational excitation of the interstellar hnc by para- and ortho-h2. *Phys. Chem. Chem. Phys.*, 13:8204–8212, 2011.

[132] E. Sarrasin, D. B. Abdallah, M. Wernli, A. Faure, J. Cernicharo, and F. Lique. The rotational excitation of HCN and HNC by He: new insights on the HCN/HNC abundance ratio in molecular clouds. *MNRAS*, 404:518–526, May 2010.

[133] B. E. Turner, T. C. Steimle, and L. Meerts. Detection of sodium cyanide (NaCN) in IRC 10216. *ApJL*, 426:L97, May 1994.

[134] N. Mauron and P. J. Huggins. Gas phase atomic metals in the circumstellar envelope of IRC+10216. *A&A*, 513:A31, April 2010.

[135] Flower, D. R. and Pineau des Forts, G. Time-dependent modelling of the molecular line emission from shock waves in outflow sources. *Monthly Notices of the Royal Astronomical Society*, 421(4):2786–2797, 2012.

[136] D. E. Manolopoulos. An improved log derivative method for inelastic scattering. *J. Chem. Phys.*, 85(11):6425–6429, 1986.

[137] B.R Johnson. The multichannel log-derivative method for scattering calculations. *Journal of Computational Physics*, 13(3):445 – 449, 1973.